Dynamics of the Antarctic Mesosphere and Lower Thermosphere

by

A.Phillips. B.Sc(Hons).

A thesis presented

for the degree of

DOCTOR OF PHILOSOPHY

in the

UNIVERSITY OF ADELAIDE

Mawson Institute for Antarctic Research

July 1989

Contents

List of Figures

List of Tables

Abstract

A new spaced-antenna partial-reflection (SAPR) radar was established at Mawson, Antarctica (67° S, 63° E) in June 1984. From that date it has been used to measure horizontal winds (and other data) in the height range 70–108 km. Wind measurements are made at time intervals of 5–15 min and at 2 km height intervals, with a height resolution of approximately 4 km. Using a three year continuous set of data, studies of the mean winds, atmospheric tides, planetary waves and ionospheric echo strengths have been made.

The mean winds from Mawson are presented and compared with those of the SAPR radar at Adelaide, South Australia, as well as with those from similar-latitude northern hemisphere radar stations. The mean wind data are also compared with recent satellite-based climatologies and are found to differ significantly.

The diurnal atmospheric tides are found to be largely dominated by evanescent (non-vertically propagating) tidal modes, as expected from theoretical considerations. Some results suggest that they may be driven (in part) by Joule heating from energetic particle precipitation in the lower thermosphere. The semidiurnal tides are found to have comparatively large amplitudes and are formed from a mixture of propagating modes. Tidal data are compared with recent semi-empirical models and found to be in moderate (to poor) agreement.

Planetary wave activity is found to be as expected for a high-latitude site, with the notable exception of the quasi 2-day wave which, for a period during January, usually dominates the mean wind and tidal wind fields. Analysis of the amplitude and phase relationship between Mawson and Adelaide supports current theories on the wave structure in the southern hemisphere.

The high-latitude ionospheric environment is substantially different from that at mid-latitudes. Some results of ionospheric echo strength measurements (at the operating frequency of the radar) are presented and compared with those at Adelaide.

A brief investigation is made of the possible relationship between geomagnetic activity (expressed by the geomagnetic Kp and local-K indices) and the winds. A relationship between the amplitude of the diurnal tide and the Kp index is found.

To the best of this author's knowledge, this thesis contains no material previously published or written by another person, except where due reference is made in the text. It contains no material which has been submitted or accepted for the award of any other degree or diploma in any University. I consent to this thesis being made available for photocopying and loan by the librarian at the University of Adelaide on acceptance of the degree.

Andre Phillips.

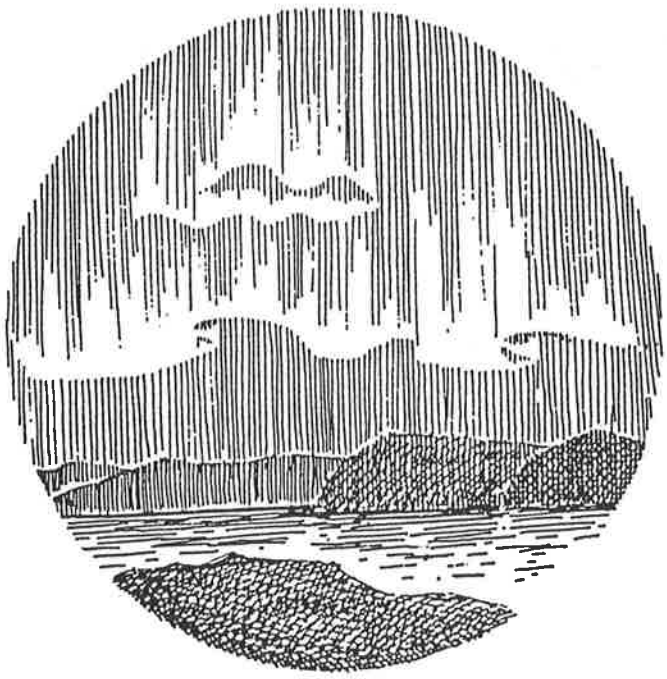

ACKNOWLEDGEMENTS

Thanks are due to my supervisors, Drs F. Jacka and R.A. Vincent for their great assistance and invitation to participate in this project. In addition, thanks are due to my colleagues for many useful conversations and suggestions, particularly with Drs W.K. Hocking, B.H. Briggs, D. Olsson-Steel, W.G. Elford and Mr's D. Murphy, L. Hettner, L. Campbell, S. Eckermann, D. Creighton and Miss M. Strain. Very special thanks are extended to Dr Briggs, whose enthusiasm, optimism, wisdom and kindness will be remembered always.

Thanks are due to Janet Camac for drafting services and to many members of the 1984 wintering ANARE[1] personnel at Mawson, Antarctica, whose considerable assistance contributed to the establishment of the radar facility at Mawson. The successful operation of the radar hardware was largely due to the technical skills of Don Creighton, whose extraordinary skill in anticipating electrical faults (and including ample spare parts and technical information) saved the day on many occasions.

This research was supported by the Australian Research Grants Scheme and by the Australian Antarctic Division. The work at Mawson formed part of the program of the Australian National Antarctic Research Expeditions.

[1] Australian National Antarctic Research Expeditions

M.V. Nella Dan. Launched Aalborg, Denmark, June 13, 1961.
Scuttled near Macquarie Island, December 24, 1987.

Chapter 1

INTRODUCTION AND LITERATURE SURVEY

1.1 Mean winds and planetary scale waves in the upper middle atmosphere and lower thermosphere

One of the interesting aspects of studies of the atmosphere in the height range 70–110 km is the similar magnitudes of the mean winds, planetary-scale waves, atmospheric tides and gravity waves (see figure 3.19, page 119). This is complicated further by the way in which these interact with each other. This is especially the case with the study of the mean winds and planetary scale wave propagation where it is difficult (and often impossible) to distinguish the two if only single-station ground-based observations are available. The degree to which the mean circulation in the middle atmosphere is directly attributable to forcing by the vertical transport of horizontal momentum by gravity waves and other wave processes has only recently been appreciated. Thus

to describe atmospheric dynamics by partitioning wind and wave effects into separate bands of frequency (ie. mean/planetary/tidal/gravity and acoustic waves) is somewhat superficial, but this separation is useful to gain an understanding of what is a very complex interrelation. The following section briefly summarizes some of the key points in our understanding of the mean flow and planetary wave perturbations, particularly in the upper mesosphere and lower thermosphere.

1.1.1 The mean flow

The derivation of mathematical expressions for the mean circulation in the atmosphere is approached through a series of approximations and assumptions. The basic equations of fluid flow, embodying conservation of momentum, energy and mass, must be tailored to suit the particular conditions and height range.

Atmospheric motion at lower levels is a response to the differential solar heating which occurs over the surface of the Earth (except for solar and lunar gravitational tides which are usually negligible in amplitude). Different temperature regimes give rise to pressure gradients (primarily meridional) and meridional circulation cells develop in response to these. However, meridional motion on a rotating sphere causes an acceleration of the wind through the effect of the Coriolis force. The wind which results when the Coriolis and pressure gradient forces are in approximate balance is known as the **geostrophic** wind and is expressed by the familiar equations

$$fv = \frac{1}{\rho}\frac{dp}{dx} \quad and \quad -fu = \frac{1}{\rho}\frac{dp}{dy},$$

where the Coriolis parameter $f = 2\Omega \sin\phi$ (where Ω is the angular velocity of the Earth's rotation and ϕ is latitude), ρ is the density, u and v are the zonal and meridional wind, and $\frac{dp}{dx}$, $\frac{dp}{dy}$ are the zonal and meridional pressure gradients respectively.

For some purposes it is more useful to consider the zonal winds in terms of meridional temperature gradients rather than pressure gradients. Satellite-borne instruments measure radiances from which one can infer vertical and meridional temperature gradients; winds can then be estimated from the thermal wind equation

$$\frac{\partial}{\partial z}\left[\frac{u_z}{T}\right] = \frac{-g}{fT^2}\int_0^z \frac{\partial T}{\partial y} dz \tag{1.1}$$

where z is the altitude and g is the acceleration due to gravity. This equation assumes a steady state, non-viscous, frictionless and horizontally stratified atmosphere. At extra-tropical latitudes, tropospheric and stratospheric winds may be estimated by this equation, but in the mesosphere, neglect of friction leads to winds which are much too large. Friction (or 'stress') terms, which arise from a number of processes, are often collectively parameterized into a single term known as Rayleigh friction. Inclusion of Rayleigh friction into a more complex wind model leads to more realistic wind profiles. However, consideration of friction alone fails to explain the way in which the zonal winds usually steadily decelerate in the mesosphere above (approximately) 60 km and often *reverse* direction somewhere in the height range 85–100 km. This effect is illustrated in figure 3.1 (results section 3.1, page 83) where it can be seen that (at Adelaide) the westward winds which occupy the summer mesosphere reverse to become eastward at 85–88 km. During the winter the zonal wind shear (above ≈60 km) is the opposite of that during the summer and the zonal wind reverses direction at a height of 95–100 km.

Another perplexing observation for early researchers was the relatively hot polar winter mesopause and cold polar summer mesopause; the latter gives the coldest temperatures observed anywhere in the atmosphere (see figure 1.1). As it turned out, the zonal wind reversals and anomalous temperatures were not unrelated effects (Holton, 1982). The widely held view is that the convergence of the vertical flux of horizontal

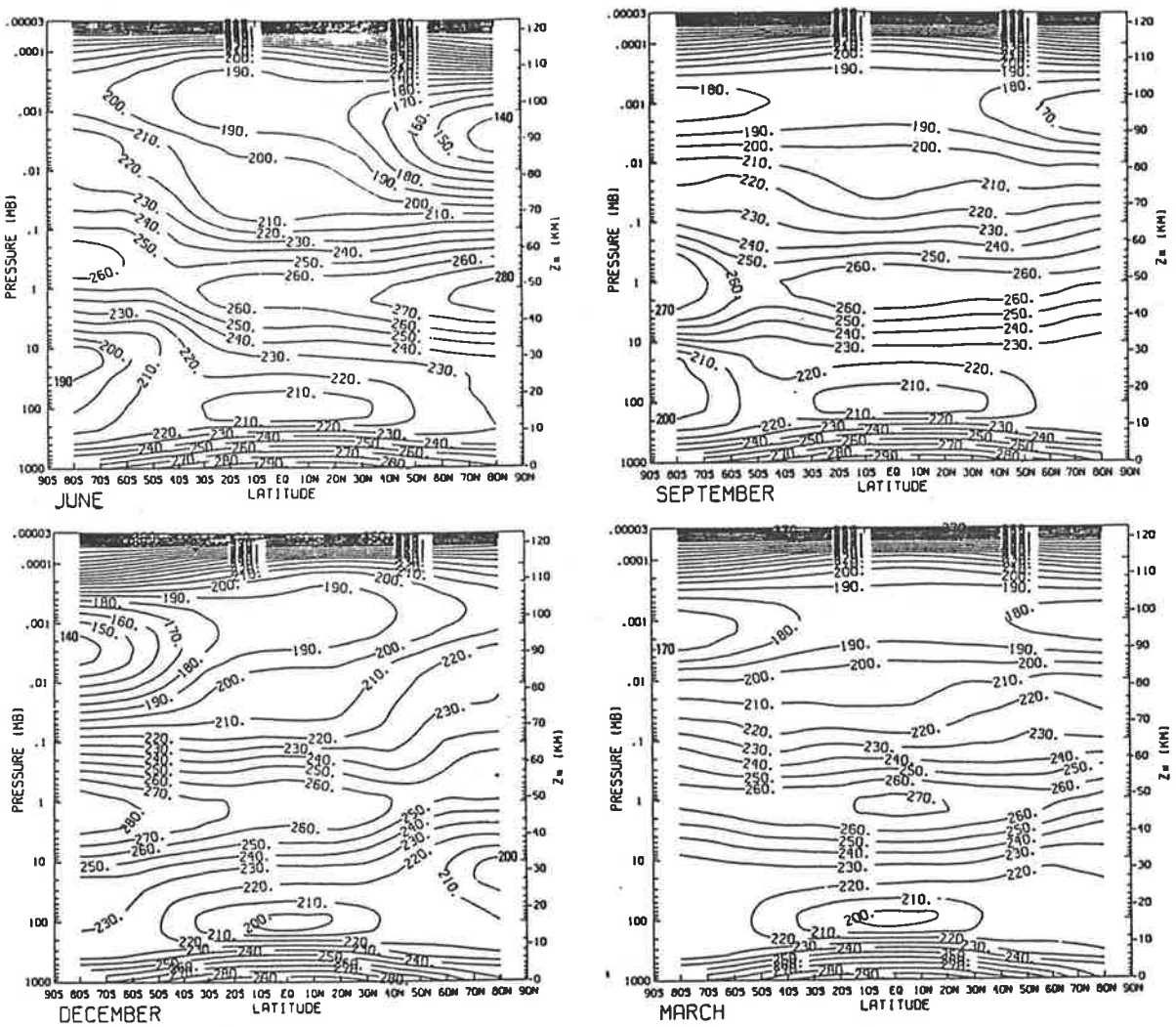

Figure 1.1: **Monthly averages of the global temperature distribution, from Fleming et al. (1988).**

momentum carried by breaking internal gravity waves accelerates the mean flow in the mesosphere and lower thermosphere (Lindzen, 1981; Vincent and Reid, 1983; Fritts, 1984). The direction of the acceleration is opposite to that of the geostrophic winds in the mesosphere (which have their maximum velocities at approximately 60 km). This is due to wind shears in the stratosphere which act as a filter so that only gravity waves with a relatively strong westward component of propagation will propagate vertically into the mesosphere during the summer (and vice-versa in the winter). Gravity wave drag on the mean zonal wind drives a meridional flow which is in the reverse direction to that at lower levels in the atmosphere and results in adiabatic heating (due to a sinking motion) over the winter pole and cooling over the summer pole (mainly in the height range 80–100 km). Thus a complete study of the circulation in the height range 70–110 km requires an understanding of gravity wave generation and propagation from the troposphere and stratosphere (which is outside the scope of this brief discussion).

Current mean wind models such as those of Groves (1985), Koshelkov (1985), Barnett and Corney (1985) and Fleming et al. (1988) are all of a semi-empirical type, drawing on data from many techniques. Middle atmosphere mean winds in the Barnett and Corney (1985) and Fleming et al. (1988) models (discussed in the results section of this thesis) are computed by taking balloon/rocket measurements of the temperature field at the 30 hPa level and using satellite radiance measurements to estimate geopotential heights above that level, to a maximum altitude of approximately 80 km. Geopotential height data are then differentiated to compute the 'geostrophic' winds; for example Fleming et al. (1988) use the equation,

$$[u] = \frac{-g}{2\Omega \sin\theta} \frac{\partial [z]}{\partial y} \tag{1.2}$$

where $[z]$ is the zonally averaged geopotential height and $[u]$ is the zonally averaged

geostrophic wind at a fixed pressure. This equation breaks down at very low and high latitudes and various approximations are used. For heights above 80 km, temperature and wind models must rely on empirical thermospheric models. For instance, in Fleming et al. (1988), winds in the height range 65–120 km used a model known as 'MSIS-86' (Hedin, 1987). *Precisely* how model, satellite, radar and synoptic data are merged is usually difficult to ascertain from published information. The differences between various models (which draw on very similar observational data) is very probably due (in part at least) to the preferences modellers have for merging different observational techniques.

1.1.2 Planetary waves

Planetary waves occur because of the variation of the Coriolis parameter with latitude and they are commonly known as Rossby waves. These are strikingly visible in satellite photographs of clouds taken at high latitudes, where the wavelike circumpolar patterns are very distinct. Depending on their period, planetary waves fall into two categories; 'travelling' (or 'transient') and 'quasi-stationary'. Waves with a period in excess of (approximately) 30 days are referred to as 'quasi-stationary' and, in the absence of satellite data (or a considerable number of radar stations distributed longitudinally) it is difficult to distinguish the 'mean' wind from the effects of quasi-stationary waves.

For the most part, planetary waves do not propagate vertically but remain trapped in the troposphere and stratosphere, but vertical propagation is possible under certain conditions. Using the β-plane approximation (where the Coriolis parameter f is set equal to $f_0 + \beta y$, and y is the latitude) it may be shown (Houghton, 1977) that vertical

propagation is possible when

$$0 < \overline{u} < \frac{\beta}{k^2 + l^2} \tag{1.3}$$

where k and l are the zonal and meridional wavenumbers respectively (ie. $k = \frac{2\pi}{\lambda_x}$). Hence equation 1.3 implies that with a westward or a large eastward zonal wind, no vertical propagation will occur. Also, vertical propagation will be more likely for those waves with very large horizontal wavelengths. This explains why the quasi-stationary waves, with their very large horizontal wavelengths, are a regular feature of the upper mesosphere in winter whereas the presence of travelling waves (such as the quasi 2-day wave) is associated with the occurrence of particular wind profiles in the stratosphere and mesosphere. This was shown by Charney and Drazin (1961), who investigated vertical propagation of planetary waves into the mesosphere and concluded that either strong eastward or westward stratospheric winds would trap the waves and that vertical propagation could only take place during the equinoxes.

As with gravity waves, there are a number of possible sources of planetary waves in the troposphere and stratosphere, including orographic forcing, land/sea differential heating and baroclinic or barotropic instabilities in the mean flow. The mathematical description of "free" planetary waves with periods less than (approximately) two weeks, is similar to that of the atmospheric tides, where solutions to the linearized Laplace tidal equations yield solutions known as Lamb modes (reviewed in Salby, 1984). Unlike the case for the atmospheric tides, the solutions are 'normal modes', which may be thought of as resonances determined by the spherical geometry, rotation and stratification of the atmosphere. Like the atmospheric tides, particular modes of oscillation are described by a 'zonal wavenumber' (ie. 1,2,3....), which is equal to the number of complete cycles around a circle of longitude (this zonal wavenumber should not be confused with the physical wavenumber which is equal to $\frac{2\pi}{\lambda}$). Theoretical studies and observations yield a

predominance of westward propagating modes (at extratropical latitudes). Commonly reported observations of travelling planetary wave oscillations identify the so-called 2, 5, 10 and 16-day waves. With the possible exception of the 2-day wave, the periods of these oscillations are not integral numbers of days and typically the observed periods fall in the period ranges 1.9–2.2, 4–7 and 10–20 days (Vincent, 1985).

Observational studies by Barnett and Corney (1985) show that the amplitudes of the quasi-stationary waves achieve maximum values at latitudes of 60–70° in the winter hemisphere. Although the amplitudes are largest in the stratosphere, they remain 'relatively large' up to 80 km (the top level of the Barnett and Corney planetary wave climatology for the interim CIRA). Although the horizontal wavelengths are of the order of the scale of the Earth, the vertical wavelengths can be relatively small (several tens of km).

Observations show that the amplitudes of the travelling planetary waves are similar in both hemispheres but the quasi-stationary waves are significantly stronger in the northern hemisphere. This is understandable since the travelling waves are thought to arise mainly from hydrodynamic instabilities whereas the quasi-stationary waves arise from zonal asymmetry in heating and orographic forcing. Quasi-stationary waves play a principal role in the development of stratospheric warmings, which occur more frequently and with more effect in the northern hemisphere.

Vertical and meridional propagation of quasi-stationary planetary waves is inhibited by the summertime westward (easterly) stratospheric winds (Charney and Drazin, 1961).

The quasi-stationary and travelling waves are usually strongly attenuated in the mesosphere. Miyahara (1985) suggests that, in addition to attenuation by Rayleigh friction and radiative damping, the interaction of stationary waves with internal gravity

waves will lead to enhanced attenuation. The deposition of momentum in the mean flow by planetary waves is often discussed in terms of the 'Eliassen–Palm (EP) flux' (Eliassen-Palm, 1960; Edmon et al. , 1981). The EP flux can be defined (approximately) by the equation

$$\vec{F} = \left[-\rho\overline{u'v'}, f\rho\frac{v'\theta'}{\frac{\partial\theta}{\partial z}} \right]$$

where f is the coriolis parameter and θ is the potential temperature. The first component of $\vec{F}$ is the northward flux of eastward momentum and the second component relates to the vertical flux of eastward momentum. The EP flux is a particularly useful tool in theoretical studies of the vertical and horizontal transport of momentum by planetary waves. Moreover, the divergence of the EP flux is a direct measure of force per unit mass, (Andrews and McIntyre, 1976; Boville, 1987) and thus the acceleration of the mean flow may be directly plotted (for instance) in units of $\mathrm{ms^{-1}day^{-1}}$.

1.1.3 The quasi two-day wave

A ubiquitous feature of the summer hemisphere middle atmosphere is the presence of a quasi 2-day period oscillation. This phenomenon has been observed in both hemispheres by rocket, radar and satellite techniques for over 20 years (Muller, 1972; Kingsley et al., 1978; Muller and Nelson, 1978; Rogers and Prata, 1981; Craig et al., 1980; Craig and Elford, 1981; Craig et al., 1983; Vincent, 1984; Tsuda et al., 1988) but there is still no universally accepted explanation of the driving force. There are a number of interesting differences in behaviour between the two hemispheres. In the northern hemisphere (NH) the period of the wave is frequently given as 51 ± 2 h, whereas in the southern hemisphere (SH), the period is usually very close to (if not exactly) 48 h (Muller and Nelson, 1978; Craig et al., 1980). Also, both satellite and ground-based radar observations show significantly larger amplitudes in the southern hemisphere (Rogers and Prata, 1981;

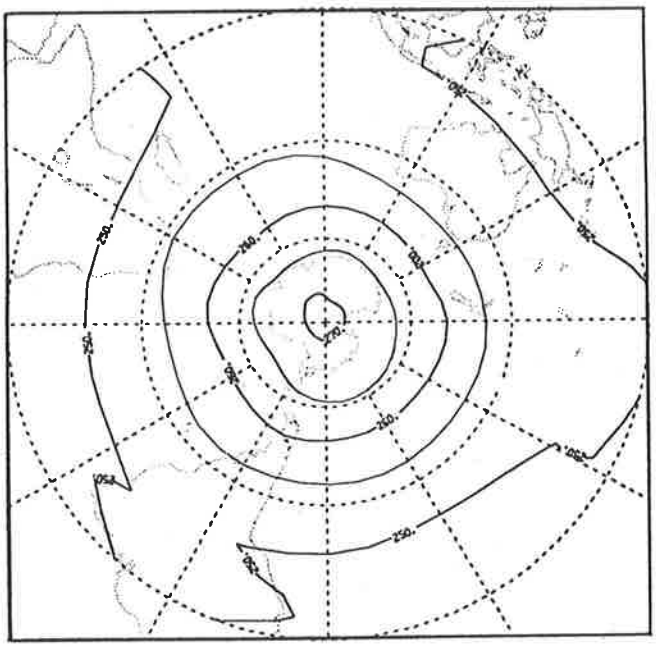

Figure 1.2: **Stratospheric temperature at ≈40 km measured by satellite, January 16 th 1973, showing a wavenumber 3 pattern (Rogers & Prata, 1981).**

Vincent, 1984; Plumb et al. , 1987). Satellite measurements of thermal radiance in the stratosphere (Rogers and Prata, 1981) show that the 2-day period temperature perturbations maximize just after the summer solstice and that the largest measured perturbations occur at a height of 70 km at 40°S. Figure 1.2 illustrates the wavenumber 3 structure observed in these satellite observations.

Since the wave appears to be almost solely confined to the summer hemisphere, interhemispheric comparisons are difficult to obtain. However, Craig et al. (1983) simultaneously observed the wave at Sheffield (53°N,2°W) and Townsville (19°S, 147°E) during July–August 1980. The amplitudes at Townsville were approximately half of those at Sheffield and no fixed phase relationship was found. This leakage of the wave from the NH summer was not detected at Adelaide (35°S, 138°E). In a similar study, Tsuda et al. (1988) made simultaneous measurements of the wave at Adelaide and Kyoto (35°N, 136°E) during January 1984. These showed that the amplitudes at Kyoto were approximately 0.25 of those at Adelaide and that the zonal components were in approximate antiphase. The period of the wave at Kyoto appeared to show a systematic

variation of 2.1–2.5 days during [local] summer, reducing to approximately 2 days in autumn. Tsuda et al. tentatively suggested that these period changes coincide with the disappearance of a core of eastward mean winds in late summer.

Vertical wavelengths of the wave are usually reported to be in excess of 100 km and the relationship of the phase with height indicates downward propagation of phase consistent with upward propagation of energy (Craig et al. 1980, Craig and Elford, 1981). On other occasions the wave appears to be evanescent in the vertical. A curious feature of the observations at Adelaide is the way in which the period is normally observed to be (within experimental error) *exactly* 48 h, and the phase has approximately the *same* local time from year to year. Craig and Elford (1981) found, after 9 years of observation, that the time of the maximum northwards wind (at a height of 90 km) occurred just after local noon. Vincent (1984) suggests that subsequent observations are in agreement with these earlier results.

Perhaps the most rigorous theoretical study conducted so far is that of Salby (1981). This suggested that the wave may be a westward propagating Rossby-gravity (3,3) normal mode. He examined propagation in a windless isothermal atmosphere, of the normal modes corresponding to solutions of the Laplace tidal equation with a 10 km equivalent depth. For each wavenumber m there exists a discrete set of Rossby normal modes corresponding to $n=m$, $n=m+1$,.... When $n=m$ the mode is conventionally termed the 'Rossby-gravity mode' because of its mixed character. The normalized Hough functions[1] for this mode are shown in figure 1.3.

The propagation of a (3,3) mode in more realistic conditions, (ie. with wind and temperature structure) leads to a wave with an expected period of 2.1 days and allows

[1]ie. solutions to the Laplace tidal equation, described in more detail in section 1.2.1

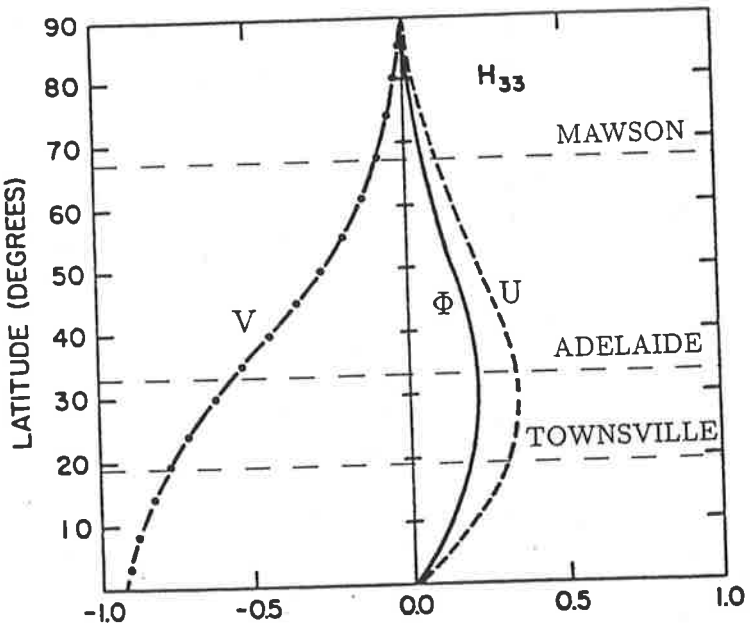

Figure 1.3: **Geopotential(Φ), zonal(U) and meridional(V) Hough functions for the third Rossby-gravity normal mode of a windless isothermal atmosphere (Salby, 1981).**

modelling (quantitatively) of the latitudinal and vertical structure (Salby, 1981). Figure 1.4 illustrates the amplitude of the components of the wave in summer and shows how amplification occurs at mesospheric heights. This figure also suggests there is a secondary peak in amplitude centred at the latitude of Mawson at a height of 10–11 scale heights. Because there are no energy sources with a period of two days known to exist, the forcing of the wave is thought to be by tropospheric 'noise'. Salby proposed that a combination of weak eastward winds (*relative* to the wave) and an equatorward temperature gradient lead to the amplification of the wave at mesospheric heights. Since these conditions are met during the summer this accounts for the regularity of the appearance of the wave.

An alternate theory by Plumb (1983) suggests that the '2-day wave' is due to a baroclinic instability of the westward jet in the summer mesosphere. Plumb suggests that the instability occurs when the vertical windshear of the zonal wind is in excess of 6 $ms^{-1}km^{-1}$ in the lower mesosphere.

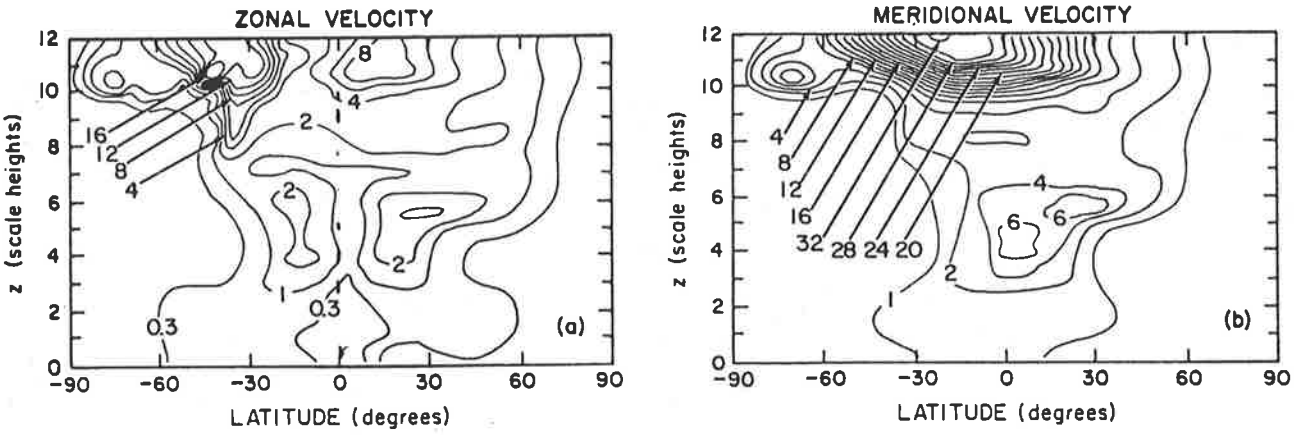

Figure 1.4: **Normalized amplitudes of the (3,3) Rossby-gravity normal mode modelled with realistic wind and temperature conditions, for the southern hemisphere summer solstice (Salby, 1981).**

1.2 Atmospheric tides

Periodic tidal oscillations in ground-level barometric pressure have been observed since last century. While these effects are quite small (eg. at Adelaide the amplitude is approximately 0.5 hPa), tidal oscillations of temperature, pressure and wind motion are considerably larger in the mesosphere and thermosphere with the amplitude of the wind oscillations often exceeding the magnitude of the mean wind. The following section briefly reviews some of the theory, observations and models used to describe tidal phenomena in the upper mesosphere and lower thermosphere.

1.2.1 Classical tidal theory

Atmospheric tidal oscillations with the solar period of 24 h and its harmonics are excited by insolation at different levels of the atmosphere. The gravitational effects of the sun and moon are negligible by comparison and will not be discussed further in this thesis. Absorption of infra-red radiation by water vapour in the troposphere, ultra-violet by

ozone in the stratosphere, and absorption of EUV(20–100 nm)/UV(120–200 nm) (by many molecular species) in the thermosphere are known to provide most of the forcing for the solar atmospheric tides.

To a first approximation, tidal motion in the middle atmosphere (10-100 km) may be modelled by using the 'classical' method of Laplace (Chapman and Lindzen, 1970; Lindzen, 1974). With this model, the Earth is assumed to be a smooth sphere, and the atmosphere to be a hydrostatic, non-viscous, shallow gas of uniform temperature. By considering equations of momentum, energy and mass conservation and by considering tidal motions to be small perturbations of the basic state, the Laplace tidal equations may be linearized and solved analytically (the reader is assumed to be familiar with the basic theory (Chapman and Lindzen, 1970) which will not be reproduced here).

The solution of the linearized tidal equations yields a set of eigenvalues and eigenfunctions which correspond to different modes of oscillation. Throughout this work, each mode is described by the symbol S_m^n (or simply (n, m)) where n represents the zonal wavenumber (ie. the integral number of oscillations in 24 h) and m is usually called the mode number. Positive values of m represent propagating modes which transport energy vertically. Negative values of m represent evanescent (cf. 'trapped' or 'rotational') modes which do not freely propagate vertically and whose amplitude decays exponentially away from the height of excitation.

A mode may be described as *symmetric* or *anti-symmetric* (about the equator). For example the symmetric diurnal propagating modes are the (1,1), (1,3), (1,5)... and the anti-symmetric modes are the (1,2), (1,4), (1,6)... For the semidiurnal tide, the symmetric modes are the (2,2), (2,4), (2,6).. and the anti-symmetric are the (2,3), (2,5), (2,7)...etc.

Each eigenvalue/eigenfunction solution to the Laplace tidal equation may be used to

Table 1.1: **Approximate vertical wavelengths (λ_z) of the diurnal and semidiurnal propagating tidal modes,** computed for Mawson at 90 km (using figures from CIRA 1988.) Equivalent depths (h_e) are taken from Chapman and Lindzen, (1970).

	Diurnal		Semidiurnal	
Mode	h_e/km	λ_z/km	h_e/km	λ_z/km
1	0.69	25	-	-
2	0.24	14	7.85	150
3	0.12	10	3.67	85
4	0.07	8	2.11	50
5	0.05	6	1.37	37
6	0.03	5	0.96	30

determine a vertical wavelength (in the case of the propagating modes (ie. positive m)) and the amplitude structure as a function of latitude. Table 1.1 shows the eigenvalues (or 'equivalent depths' - h_e) of the first six diurnal and semidiurnal modes. The equivalent depth may be used to estimate the vertical wavelength λ_z which is given by

$$\lambda_z \approx 2\pi \left(\frac{N^2}{g h_e} - \frac{1}{4H_\rho^2} \right)^{-\frac{1}{2}} . \tag{1.4}$$

N is the Brunt-Vaisala frequency, g is the acceleration due to gravity, H_ρ is the density scale height.

Table 1.1 uses equation (1.4) to estimate the vertical wavelengths at Mawson. With the exception of the semidiurnal (2,2) mode the vertical wavelengths remain fairly constant throughout the year and these figures are almost identical to those for Adelaide. It should be emphasized that these estimates are for the idealized[2] atmosphere and that vertical wavelengths of the propagating tides in the atmosphere may be affected by many

[2]as defined by Chapman and Lindzen (1970), pp 106–108

factors, including mean winds and dissipation, departure from hydrostatic equilibrium, surface topography etc.

Figure 1.5 from Forbes (1982a,b) shows the normalized diurnal and semidiurnal eigenfunctions for a classical atmosphere. These functions give an indication of how the amplitude of a given mode is likely to vary with latitude, but in the middle atmosphere they do not give any indication of absolute (or relative) amplitude or of which mode will dominate. Precisely which mode will dominate at a given time, place or height is dependent on many factors, some of which are discussed later in this section.

1.2.2 Tidal winds in the mesosphere and lower thermosphere

Although solutions to the Laplace tidal equations are only a first approximation to atmospheric tidal phenomena, they do provide a framework to describe the general features. Therefore, in tidal work, oscillations are usually described in terms of the associated 'modes'. However, in a realistic atmosphere, the effects of background winds, temperature variation, Newtonian cooling, electrodynamic forces, molecular/eddy diffusion (of heat and momentum) and composition must be considered. The addition of any (or all) of these effects into the tidal equations renders the equations inseparable and solutions must be obtained numerically. The difference between realistic mode structure and theoretical mode structure (of a classical[3] atmosphere), is usually described by the term *mode coupling* or *mode distortion.* Higher order modes are called 'coupled' modes, as distinct from 'direct' (ie. classical) modes. Background winds often lead to mode coupling.

[3]ie. windless, isothermal and homogenous

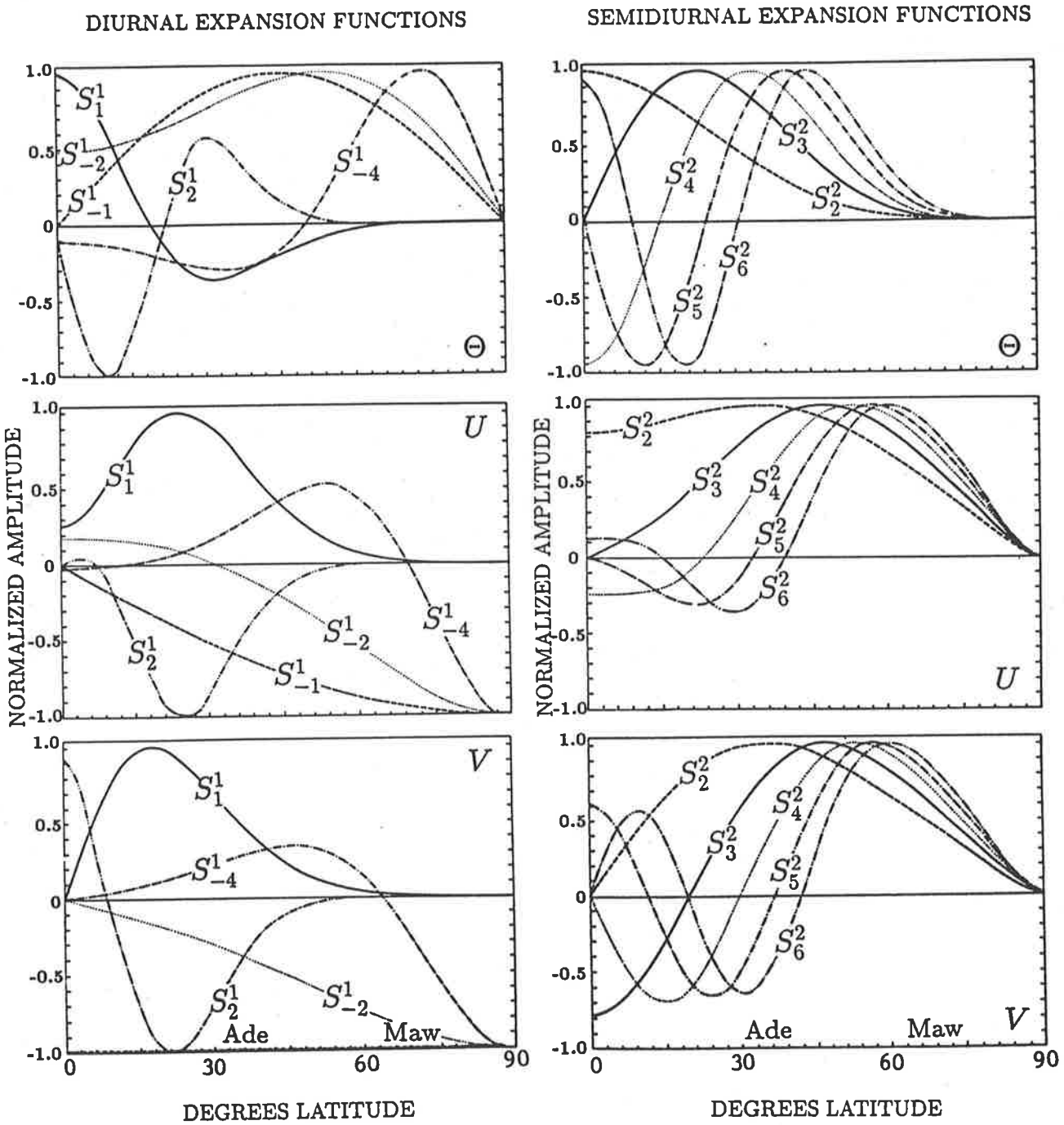

Figure 1.5: **Diurnal and semidiurnal expansion functions.** Normalized Hough (Θ) and velocity expansion functions for the zonal (U) and meridional (V), diurnal and semidiurnal tides (from Forbes, 1982a,b)). Normalization factors for the zonal diurnal modes are as follows: S^1_1–0.038, S^1_{-1}–0.130, S^1_{-2}–0.100, S^1_{-4}–0.024, S^1_2–0.018 and for the meridional diurnal modes 0.026, 0.126, 0.100, 0.024 & 0.015 respectively. Normalization factors for the zonal semidiurnal modes are as follows:S^2_2–0.355, S^2_3–0.182, S^2_4–0.115, S^2_5–0.081, S^2_6–0.062 and for the meridional semidiurnal modes 0.326, 0.171, 0.110, 0.078 & 0.060 respectively.

Forcing and damping

As stated earlier, atmospheric tides are primarily excited through heating by insolation due to absorption by atmospheric constituents. In addition, clouds (Lindzen, 1978) and coupling from the magnetosphere to the lower thermosphere are possible additional sources of excitation. Figure 1.6 shows where the main heating occurs in the troposphere and stratosphere. The heating function in figure 1.6 is represented by several curves, each one describing the amount of energy which drives a particular tidal mode. Because heating occurs in layers which are 10–30 km thick, modes with longer vertical wavelengths will suffer less destructive interference and so will be preferentially excited. This explains why the amplitude of the semidiurnal tidal modes (which, in general have longer vertical wavelengths) are comparable to (and can often exceed) the diurnal amplitudes at different levels in the atmosphere. However, because of the growth and dissipation of individual tidal modes (away from the height of excitation) the relative contribution from each mode (at a given height) shows considerable variation.

Observations of tidal winds in the height range 80–100 km usually show a downward progression of phase corresponding to an upward propagation of energy. It is probable that tides generated by sources in the thermosphere transport energy downwards but this is rarely observed as the amplitude will decrease with increasing density according to $\rho^{-\frac{1}{2}}$ (where ρ = atmospheric density). Upward propagating tidal modes will grow approximately according to $\rho^{-\frac{1}{2}}$ until heights where appreciable damping takes place. Significant damping of upward propagating tides usually occurs at 100-160 km and modes with vertical wavelengths less than approximately 30 km will be strongly damped above 100 km (Forbes and Hagan, 1982). Because of its long vertical wavelength the (2,2) mode is considerably less attenuated and may penetrate into the thermosphere

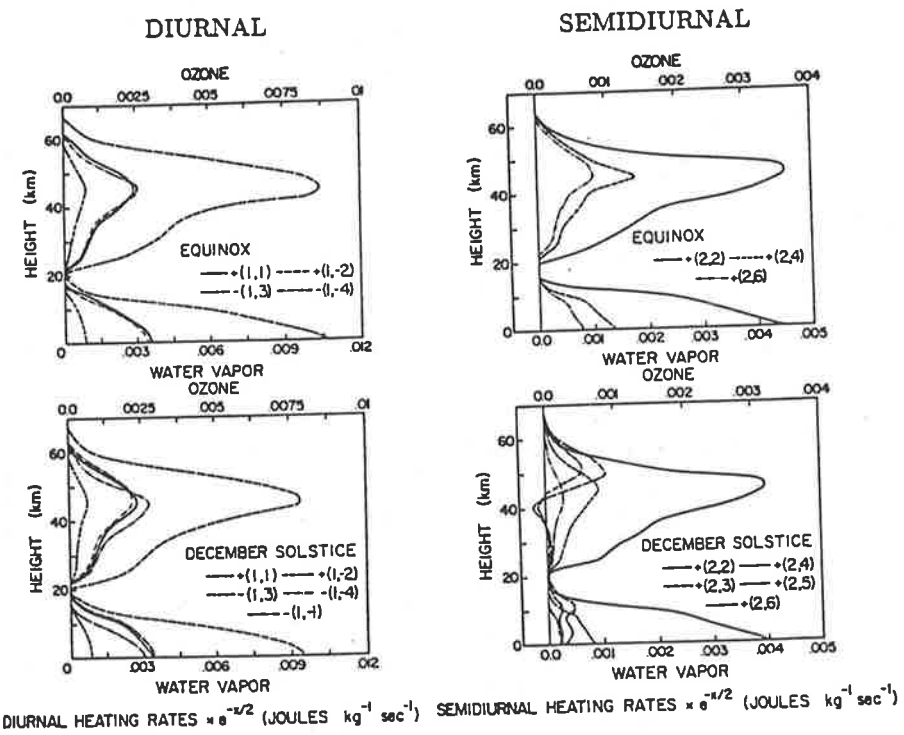

Figure 1.6: **Hough decomposition of diurnal and semidiurnal heating rates at equinox and (December) solstice due to insolation absorption by water vapour and ozone, and multiplied by the factor $e^{x/2}$, where $x = -\ln(p/p_o)$. (Forbes, 1982a,b)**

(Groves, 1983). Diurnal thermospheric tides are excited almost exclusively in-situ and are strongly influenced by high-latitude particle precipitation and Joule heating processes (Forbes and Garrett, 1979); this has particularly important consequences at the latitude of Mawson.

Vertical structure

In the height range 70–110 km considerable changes in modal composition may occur, so that precisely which mode will dominate at a given height and time is difficult to predict. However, one of the advantages of high-latitude observations, is that (on theoretical grounds at least) only the diurnal evanescent modes are likely to be present with significant magnitude (see figure 1.5) and of these the (1,–2) mode will probably strongly dominate. This is an unusual situation where a single mode can be observed in isolation

(there is a possibility however, that due to mode distortion, propagating modes *may* be present and it is one of the aims of this study to attempt to identify these). Usually, when a number of tidal modes are present, identifying modal composition from vertical wavelength is unreliable especially when complicated by the fact that meridional and zonal tidal components often display different vertical structure.

In the southern hemisphere, the phase of the zonal winds will usually lead that of the meridional winds by approximately 90°. This follows from tidal theory applied to the case where energy is moving upwards and phase is moving downwards.

Latitude structure

The symmetry (or anti-symmetry) of the Hough functions about the equator will cause the different modes to be driven with varying efficiency as the seasons change. Symmetric modes will be favoured at the equinoxes and anti-symmetric modes may be expected to increase at the solstices. This is only approximate as, even at the equinoxes, the global distribution of water vapour and ozone is asymmetric (Teitelbaum and Cot, 1979).

Figure 1.5 suggests that the diurnal (1,1) and (1,–2) modes are likely to be present, with significant amplitude, at equatorial-to-mid latitudes and that propagating modes are unlikely to be measured at latitudes greater than 60°. Forbes (1984) suggests that most vertical structure variations of the diurnal tide (at mid-latitudes) are due to superposition of the (1,1) and (1,–2) modes and that at high latitudes the (1,–2) mode will dominate.

Figure 1.5 suggests that semidiurnal tides will be present at all latitudes (except at the poles) and that all semidiurnal modes will reach peak amplitudes at mid-to-high latitudes.

Variability of the diurnal and semidiurnal tides

The amplitude and phase structure of the tidal winds in the height range 80–100 km shows pronounced variability, both seasonally and from day to day. Seasonal variations in tidal mode composition are mostly due to changes in the shape of the vertical heating profile and to the distribution of heating over the globe. Also seasonal changes of zonal winds may cause mode coupling.

The causes of the observed short-term variations (approximately less than 3 days) in tidal amplitudes and phases are not well understood, although there are a number of plausible explanations; Forbes (1985) summarizes some of the possibilities which include variations in thermotidal heating by varying ozone and water vapour concentrations, instability and non-linear interactions (for the diurnal tide) and modulation of gravity wave deposition into the mean flow. Forbes' preferred explanation for short term variations is the interference between several tidal modes, where comparatively small changes in one modal component can result in significant variation of the total tidal amplitude and phase. Bernard (1981) suggests that the variations of the semidiurnal tide are mainly associated with the winds and irregularities in the middle atmosphere. Vial et al. (1985) suggest that partial reflections of tidal waves (by steep temperature gradients in the lower thermosphere) may explain the tidal variability observed at the mesopause level.

1.2.3 Tidal modelling

Foremost among current tidal models are those of Forbes and Hagan (1988) and Vial (1986) (for the diurnal tide) and Forbes and Vial (1989) (for the semidiurnal tide); comparisons are made between observed data and these models in the results chapter

of this thesis. A tidal model must account for effects not considered in the idealized atmosphere such as background winds, temperature variation, composition, hydromagnetic coupling, Newtonian cooling, eddy and molecular diffusion and the sources of tidal forcing; a formidable task! Most of these effects must also be parameterized as a function of season. Normally tidal models are computed for solstice or equinox conditions. However, the semidiurnal model of Forbes and Vial (1989) attempts to model the tides at all times of the year (see figure 3.41 on page 154).

As later work will show, contemporary models are still only moderately (to poorly) accurate at predicting the amplitude and phase of the tidal wind structure in the height range 70-110 km. However, it must be emphasized that model tides are being compared with data derived from long-term (usually monthly) averages and that instantaneous measurements of tides can show very large deviations from mean results. Variations arise from a number of factors that are difficult to parameterize. For instance, variations in mesospheric turbulence, longitudinal variations in tidal forcing, lunar gravitational tides, and mode distortion by the background winds (Forbes, 1982a) will cause difficulty in attempts to model the tides. For instance, the lunar (gravitational) component of the semidiurnal tide may be 20% of the total in the lower thermosphere (Forbes, 1982b) and for short periods of observation, this will be indistinguishable from the solar thermal tide. Although tidal models may never provide perfect predictions, they are useful in describing the 'average' state and the likely effects of short term disturbances (such as stratospheric warmings or solar activity).

1.3 Geomagnetic and high-latitude effects

Although the study of the high-latitude ionosphere and geomagnetic effects is incidental to the main body of this work, it is worthy of brief mention because the radar's performance is affected by its high-latitude location. It is also possible that the horizontal wind data may be influenced by ionospheric effects not encountered at mid-latitudes. In the upper thermosphere at high latitudes winds are strongly affected by electric fields which are generated by the interaction of the solar wind with the geomagnetic field and approximately mapped down the magnetic field lines to the ionosphere; this effect is generally thought to diminish rapidly in the lower thermosphere.

At F-region heights ,where the electron and ion collision frequencies (ν_e, ν_i) are very much less than the gyro frequencies (Ω_e, Ω_i), the combined influence of the electric field **E** and magnetic field **B** on electrons and ions, will cause them to move in the **E**×**B** direction. In the high-latitude thermosphere, the magnetospheric electric field combined with the geomagnetic field causes a large-scale circulation of plasma. The circulation is anti-sunward across the pole with return flows in the dawn and dusk sectors (an approximate representation of this flow is shown in figure 3.43, page 163). Because of collisions between the ions and neutral particles, the motions of ions and neutral winds become coupled. Transfer of momentum between the two is known as 'ion drag'. At around 140 km, $\Omega_i \simeq \nu_i$ and at around 80 km, $\Omega_e \simeq \nu_e$. This means that in the E-region ($\approx$110 km), ions become more coupled to the neutral wind than the electrons, with the result that a polar current system develops (with flow lines described in figure 3.43).

Although geomagnetic variations have profound effects in the magnetosphere and thermosphere, the effects on the winds in the SAPR observing range (70–108 km) are usually assumed to be small. However, since MST radars (which also make use of

the motions of ionized irregularities) are operated at high-latitude, there is a continuing interest in possible electric field and geomagnetic effects at D/E-region heights. Johnson and Luhmann (1985b) correlated 3 years of summertime magnetometer data with horizontal winds at 87 km measured by the Poker Flat MST (65°) radar, but did not find a conclusive relationship. In a similar study (Johnson and Luhmann, 1985a) changes in wind spectra at 86 km were compared with magnetometer data but nothing significant was found. Johnson et al. (1987), using winds from the Chatanika radar, did find a significant relationship between geomagnetic activity (expressed by the Kp index) and tidal amplitudes, and the observed heights of 107 and 115 km are sufficiently far into the lower thermosphere that a correlation might be expected. They found an increase in the amplitude of the diurnal tide and a reduction in the amplitude of the semidiurnal tide during more active (Kp>2) periods. They tentatively attributed this effect to ion-drag forcing with the change in tidal amplitudes due to the relative phase relationship between the normal tides and the diurnal variation in the direction of flow of the ions. If effects of ion drag are to be investigated, then Mawson is well placed to observe them. That is, although Poker Flat is at a similar geographic latitude to Mawson, it is somewhat removed from the auroral electrojet, while Mawson is under it at midnight.

Reid (1983), in studies of electric field induced drift of ionospheric irregularities (for Poker Flat) suggests that under disturbed conditions ($|\mathbf{E}| \geq 50$ mVm^{-1}) drift velocities of 1 ms^{-1} are possible at 90 km, and up to 10 ms^{-1} at 100 km. While these drift figures are somewhat larger than those normally cited, they must be borne in mind when interpreting SAPR winds from high-latitude sites, especially from heights above 90 km. Until wind measurements can be continuously compared with other co-located observing techniques, an element of doubt will remain as to precisely what is being

measured.

Energetic particle precipitation into the ionosphere

Through a number of processes, energetic particles (mostly e^-, H^+ and He^+) precipitate into the ionosphere, especially at high geomagnetic latitudes. These particles may also be of direct solar origin or may arrive indirectly via processes within the plasmasphere/magnetosphere; they have energies in the range from a few to a few hundred keV. Although the energy flux from these particles may be small compared with the solar photon flux ($\approx$1%), the effects on the D and E regions may be profound.

Usually energetic particle precipitation into D/E-region is considered to be significant only in auroral regions; however, it may be a contributor to the maintenance of the structure of the mid-latitude ionosphere. Evidence for this comes from the existence of the *night-time* E-region. At mid-latitudes, night-time decrease of free electrons is much less than predicted from theory. Some of the night-time E-region may be caused by ionization of NO by $L_{\alpha,\beta}$ scattered from the hydrogen geocorona, but it has been suggested by Chamberlain and Jacka (1979) that the (mid-latitude) night-time ionization may be due, in part at least, to particle (mainly electron) precipitation. At mid-latitudes, Chamberlain and Jacka found a correlation between the intensity of 427.8 nm airglow emission (from excitation of N_2^+) and the geomagnetic Kp index. Since this emission is due to collisions with energetic protons or electrons, and since the H_β emission (caused by protons) was low, they concluded that the dominant source was energetic electrons, with an energy of around 10 keV.

Additional confirmation of mid-latitude particle precipitation comes from satellite and rocket observations. Avdyushin et al. (1981) give a particle energy flux (over mid/equatorial latitudes, with moderate geomagnetic activity) of $2-3\times10^{-3}\mathrm{Wm^{-2}sec^{-1}sr^{-1}}$.

During disturbed periods, this flux may increase by 1-2 orders of magnitude. Wagner and Ranta (1983) describe what they term the 'mid-latitude post-storm precipitation belt'. They attribute increases in absorption that occur in areas with geomagnetic-L[4] values of 2-4.5, (which is distinctly separated from the auroral absorption zone) to precipitating high-energy electrons (ie. >40 keV). These particles have 'leaked' from the reservoir of trapped particles in the plasmasphere by the process of pitch-angle diffusion. For this type of precipitation, the poleward boundary of the precipitation belt is closely correlated with the plasmapause position.

Penetration of ionizing particles to heights where the collision frequency is high leads to strong attenuation of MF and HF radio waves. This is especially true at high latitudes where extremely high levels of precipitation can lead to **P**olar **C**ap **A**bsorption events (PCA's), causing a shortwave communication blackout which may last for several days. PCA's are often associated with certain characteristic solar disturbances known as **S**olar **P**roton **E**vents (SPE's). Proton precipitation is now assumed to be small except during SPE's. The amount of absorption and the heights at which it occurs will be related to the spectrum and flux of the particles. Simultaneous observations from the satellite Geos-2 (Collis et al. 1986) and with ground-based riometers show that absorption of HF radio waves is most effectively caused by precipitating electrons with energies in the range 15-80 keV, with 40-80 keV electrons contributing to 70% of the absorption. In the D-E region, absorption will be proportional to the square root of the electron flux, which follows from the usual assumption of dissociative recombination as the main loss mechanism.

While most particle precipitation is of electrons, proton precipitation may dominate in certain regions at auroral latitudes. Francis and Jacka (1969), observing H_β emissions

[4]for a definition see appendix A.1, page 186.

(486.1 nm) from Mawson Station (L=8.7) found evidence of an H_β oval which, in general, lay equatorward of the visible aurora. They also found a poleward bulge in the H_β oval near geomagnetic midnight. These early ground-based measurements agree with recent satellite observations (of H_β emission) by Ono and Hirasawa (1987), who also find a proton-dominant region equatorward of the duskside auroral oval.

Rocket measurements above Kiruna (northern Sweden) by Kopp et al. (1985) show that precipitating electrons have a maximum energy deposition at 100-110 km. Torkar et al. (1985) suggest a figure of 90-110 km. Birkland currents (as the flows of precipitating particles are known) which are capable of sustaining a visible aurora deposit a power of approximately 10^{11} Watts (Brekke 1983). On the dayside of the auroral zone, this energy input represents approximately 1% of solar heating (in the lower thermosphere), and Brekke concludes that Joule heating by horizontal ionospheric currents appears to be a more important heat source than the heating from precipitating electrons. However, at greater heights in the ionosphere, the relative amount of heating by precipitating electrons becomes much greater. A simultaneous observation from the AUREOL-3 satellite and the EISCAT radar (Stamnes et al. 1986) shows that the energy from precipitating electrons is greater than the solar EUV input by a factor of 5-10 and that this precipitation enhances Pedersen and Hall conductivities by approximately five times compared to the solar EUV contribution.

Results later in this work show that at Adelaide (35° S) the diurnal variation in D-E region ionization is mostly under solar control with possible influences from mid-latitude particle precipitation, but that at Mawson electron precipitation and processes associated with the plasmasphere/magnetosphere have a significant effect on the structure of the D-E region ionosphere.

1.3.1 The winter anomaly

The term *winter anomaly* usually refers to the increase in electron concentration in the lower D-region (60–70 km) during the wintertime. The increased ionization at lower levels where the collision frequency is large, leads to an increase in HF radiowave absorption. Additionally, the increase in ionization will permit reflections or scatterings from lower heights. This effect probably contributes (in part) to the descent of the minimum observing height of the SAPR radar (at Mawson) from approximately 80 km during the summertime, to approximately 70 km during the wintertime (Schwentek, H., 1963). However, depending on context, *winter anomaly* may also refer to short-term enhancements (usually lasting a few days) which tend to occur more frequently in the wintertime. Except where stated otherwise the former interpretation will be used in this work.

Wintertime increase in D-region ionization is usually attributed either to an increase in the D-region concentration of NO (which is readily ionized by L_α), or to a temperature rise of a few tens of degrees (which alters the chemical reaction rates that control electron production/loss). Also the ionization of $O_2(^1\Delta_g)$ by solar UV is frequently cited as a smaller, but significant contributor to enhanced electron concentrations.

In the high-latitude D-region, [NO][5] is large and short term changes in HF radio wave absorption at mid-latitudes may be due to rapid equatorward transport (the lifetime of NO at D-region heights is several days). Mid-latitude absorption has been associated with stratospheric warmings and large amplitude planetary waves (Gregory and Manson 1970, Kawahira 1982), but the nature of the relationship is a subject for further research.

[5] [ ]≡"The concentration of..."

Offermann (1979) has suggested that the short-period increases in absorption may be correlated with increases in stratospheric temperature (this is not the kind of warming related to large-scale circulation breakdown). Ranta and Ranta (1977) showed that the (short period) winter anomaly also occurs at high geomagnetic latitudes but at L values greater than (approximately) 4.4, D-region changes are highly correlated with geomagnetic activity.

Often the winter anomaly is discussed in relation to the *transition height*, which (in this context) refers to the altitude level where the densities of NO^+ and water cluster ions are equal. Rocket data described by Offermann (1979) show that this height descends from 83-85 km to approximately 77 km (and occasionally lower) during the winter anomalies (this lowering of the transition height also occurs during PCA's and D-region disturbances, such as follow solar flares).

The shorter period winter anomaly can appear relatively suddenly; within perhaps 24 hours. Koshelkov (1987) has attributed this phenomenon to meteorological and aeronomical processes and has produced a model whose equations govern temperature and the concentration of ions and neutral particles. In terms of this model, several changes take place when an anomaly is in progress,

- D-region electron concentration increases by $\approx$10 times
- [NO] increases between $\approx$ 75-95 km
- Temperature increases between 75-90 km
- $[H^+]$ increases 2-3 times.

Koshelkov argues that the cause of these effects is temperature change and vertical/horizontal transport, which may be triggered by a period of strong turbulence in the

mesosphere and lower thermosphere. Although Koshelkov is referring to short period anomalies, it is often suggested that the longer-term seasonal variation is due to some kind of turbulent mixing associated with the breaking of gravity waves, planetary waves or tides, or changes in global dynamics which result in enhanced vertical/horizontal motions.

Recent computer modelling of $[NO^+]$ transport processes support the strong relationship between $[NO^+]$ and the winter anomaly. Garcia et al., (1987) show that the winter anomaly can be understood in terms of auroral production of $[NO^+]$ by electron precipitation. Transport of $[NO^+]$ from a polar night 'reservoir' can account for both the short- and long term variation in the winter anomaly.

The ongoing discussion in the literature and the difficulty in unequivocally defining a *fundamental* cause of the winter anomaly underscore the complexity of the interrelation of dynamical and chemical processes in this region of the atmosphere.

1.4 Ground based techniques for remote sounding of the middle atmosphere

Ground-based probing of the atmosphere with radio waves began with ionospheric sounding soon after the advent of radio transmission. Questions arising from the long-distance propagation of radio waves led to the discovery and structure of a multi-layered ionosphere. Technological developments in the wake of the Second World War, particularly in radar, rocketry and satellites, have dramatically improved our capacity to make observations of the Earth's atmosphere from ground level to interplanetary space and even to study the atmospheres of other planets. Although this thesis is largely concerned with horizontal winds in the D-region (acquired by the SAPR method), it is

useful to review briefly some of the sounding techniques in current use to assist in the intercomparison of results from different sources.

The ionosonde

The ionosonde was the first widely used atmospheric remote sensing technique enabling continuous observation of electron density structure. An ionosonde typically sounds the height range 0–1000 km with significant ionization usually commencing at around 60-70 km. Although the maximum height of the observations is usually in the range 300-400 km, the ionosonde also detects apparent reflections from much greater heights, caused by multiple reflections between layers and the ground, and sometimes between the different ionospheric layers. The technique is still widely used with a large array of stations worldwide. Prediction of long-range HF radio propagation still relies on continuous data from many widely-separated stations. Appleton first named the two main ionospheric layers (E,F) from observations of discreet reflecting layers in the height range 100-500 km.

Typically an ionosonde scans a frequency range 0.5–20 MHz. Radiowave penetration of each ionospheric layer occurs for signal frequencies greater than the plasma frequency f_N, which can be determined from electromagnetic theory, viz.

$$f_N = \frac{1}{2\pi}(\frac{Ne^2}{m_e\epsilon_0})^{\frac{1}{2}},$$

where e=electronic charge, m_e=mass of electron, ϵ=permittivity of free space and N=electron number density. Therefore the electron number densities of the different ionospheric layers can be estimated from the frequencies f_N at which those layers are penetrated.

The riometer

A riometer (an acronym for **R**elative-**I**onospheric-**O**pacity-meter.) usually consists of a receiver with a bandwidth of a few MHz operating at around 30-50 MHz, connected to a vertically pointing low-gain antenna. Cosmic radio noise (of mainly galactic origin) usually passes through the ionosphere unattenuated at these frequencies except for times of unusual electron concentration in the D-region, where the high rate of electron-neutral collisions will absorb energy from electrons set into motion by the passage of electromagnetic waves. By comparing the strength of the galactic noise with that measured during times of no absorption, estimates can be made of the rate of ionization and hence the flux of precipitating energetic particles. This instrument is especially useful at high geomagnetic latitudes where D-region absorption is strongly correlated with PCA's (polar cap [HF] absorption events), solar flares and auroral/geomagnetic phenomena.

Wave-wave interaction and heating of the ionosphere

Probing the ionosphere by using high-power low-frequency transmitters to elevate ionospheric temperatures arose in 1933 out of what was dubbed the *Luxemburg effect*. This was caused by a powerful transmitter in Luxemburg (operating at 250 kHz) whose transmissions modulated the temperature of the electrons at D-E region heights. Since radio wave absorption on the D-region is related to electron collision frequency, medium frequency signals ($\approx$ 1 MHz) propagating through the D-region and reflecting from the E-region became cross modulated with the Luxemburg signal.

Wave interaction, or *heating* as this technique is usually known, is used at a number of stations, especially at Arecibo, Puerto Rico and Tromsø in Northern Scandanavia. The heating transmitter (operating on LF to HF frequencies) usually has a peak power

of several megawatts and is normally pulsed synchronously with a 'probe' signal transmitted on an HF or VHF carrier frequency. If the probing signal is pulsed at twice the frequency of the heater, pairs of probe pulses will give a reflection profile with heat-on and heat-off. Also the heater may be switched on for longer periods to study longer term changes to the ionosphere caused by artificially elevated temperatures. At Tromsø these changes can be monitored by incoherent scatter radar.

A heater may also generate VLF radio waves because in the E-region the conductivity is related to the temperature of the electron gas. If the heater is modulated at VLF frequencies, the E-region DC current will be modulated, leading to the generation of artificial VLF waves.

The measurement of electron density by the differential-absorption method

Due to the presence of the geomagnetic field, the ionospheric plasma is a birefringent medium, and oppositely-rotating circularly-polarized waves will experience different refractive indices and absorption coefficients. Since a linearly polarized electromagnetic wave can be thought of as two equal and oppositely rotating circular waves (designated **O** for **O**rdinary or right-hand polarized and **E** for **Ex**traordinary or left-hand polarized), ionospheric reflections from such a wave will be 'split' as the two components propagate with different velocities and attenuations in the ionospheric plasma. Since the relative attenuations and reflection coefficients are related to the electron density ($[e^-]$), a profile of E and O reflected signal strengths can be used to deduce a height profile of electron concentration (Belrose, 1970).

In the low D-region, the measured amplitude ratio of the reflected signals $\frac{A_X}{A_O}$ is approximately the same as the ratio of the reflection coefficients $\frac{R_X}{R_O}$ at a given height. However, because of absorption, $\frac{A_X}{A_O} \neq \frac{R_X}{R_O}$ at greater heights and $\frac{R_X}{R_O}$ must be determined

by integrating from lower heights. Consequently, the method becomes more unreliable with increasing height and is usually only useful in the range 70-90 km. Before incoherent scatter radars, rocket and differential absorption were the main techniques for studying electron density in the D-region.

MST radar

MST or Mesosphere-Stratosphere-Troposphere radars are usually high-power VHF Doppler radars that utilize weak reflections from refractive index irregularities which have a scale size of about one half of the radar wavelength (however, some UHF incoherent scatter radars are also described as 'MST' radars). Some well known examples of these radars are at Poker Flat in Alaska, the SOUSY radar in West Germany and the MU radar in Kyoto, Japan. By using steerable narrow beams, 3-dimensional winds may be measured in the height range (approximately) 2–20 km and 70–100 km with a typical height resolution of 300m–2 km.

Although called Mesosphere-*Stratosphere*-Troposphere radars, they are (usually) only effective in the troposphere, lower stratosphere and ionospheric D-E regions, but performance is largely dependent on power. In the troposphere, the effects of turbulence and atmospheric wave motion on gradients of temperature and water vapour lead to perturbations in the density. VHF scattering from these perturbations is most effective within the first few km and to get much higher than the tropopause requires high power and narrow beam widths. However, at D-region heights, perturbations in electron density (due to turbulence, probably caused by breaking gravity waves in a region of a vertical gradient in electron density) produce sufficient backscatter to measure the winds.

Most MST radars operate at around 50 MHz and so optimum scatter will occur at

the Bragg length ($\frac{\lambda}{2}$) when the spatial scale of the scatterers is approximately three metres. This is inside the so called *inertial* scale of turbulence in the troposphere but is usually considered to be within the *viscous* range at D-region heights. However, recent work by Kelley et al. (1987) suggests that in the mesosphere, the turbulence scales of neutral particles and the electron gas may not *necessarily* be the same. They suggest that in the very cold summer polar mesosphere higher concentrations of water cluster ions may cause the ionization irregularities to be of a smaller scale than the scale of the turbulence in the neutral gas. They further suggest this would take the Kolmogorov microscale for the electron gas to within the inertial range and possibly explain the enhanced VHF backscatter from the summer polar D-region.

Meteor radars

Meteor radars determine winds in the middle atmosphere by measuring the Doppler shift of the signal reflected from ionized meteor trails. Generally meteors enter the atmosphere at velocities of 10–70 kms^{-1} and vaporize at heights between 80 and 100 km. These trails of ionization persist for approximately 1 second, which is sufficient for a wind measurement to be made.

Generally meteor radars operate at VHF frequencies of 30–50 MHz and employ CW (continuous wave) or pulse techniques. With CW, the range is determined by using more than one frequency or by phase-shifting the transmitted signal. The direction of the meteor is located by using narrow beams or receiver arrays arranged to determine the inclination of the incoming wavefront.

MST and incoherent scatter radars are often operated as meteor radars. Although there are diurnal and sporadic variations in the rate of incoming meteors, meteor radars can provide neutral wind measurements in the height range 80–100 km with a time

resolution comparable to the SAPR radar. At present, the upper height limit is imposed by lack of signal and the possibility that $\mathbf{E}\times\mathbf{B}$ drift of the ions may be included in the wind measurement. Recent work by Olsson-Steel and Elford (1987) suggests that the majority of meteors occur *above* 100 km and work is currently in progress to detect these with the VHF radar at Adelaide.

Incoherent scatter radar

Another type of MST radar are the Incoherent (or Thomson) scatter radars (ISR's) which are very large and powerful UHF radars. They operate with enormous ERP (effective radiated power) and deliver a wealth of information. These instruments, of which the best known are located at Jicamarca in Peru, Aricebo in Puerto Rico, Millstone Hill in the U.S.A. and EISCAT in Scandanavia, make use of extremely weak scattering which comes from free electrons. The scattering cross-section from a single free electron is

$$\sigma_e = [\frac{\mu e}{4\pi m_e} \sin\psi]^2,$$

where μ is the permeability of free space, e and m_e are the charge and mass of an electron and ψ is the polarization angle (the angle between the direction of vibration of the incident field, and the direction from the scatterer to the receiver). This is a very small figure indeed, being approximately equal to $8\times10^{-30}\sin^2\psi$ m^2. Random fluctuations in the electron density due to thermal motion of ions and electrons cause fluctuations in the index of refraction, even though the mean electron density is constant. These refractive index fluctuations must not be confused with those due to variations of mean electron density which cause the coherent scatter with the SAPR radar. Note that these coherent effects do not operate at UHF because there are no Fourier scales equal to half the radar wavelength. The electron scatter reflects a very small fraction of the

power of the incident waves. Therefore the height range for observations commences where appreciable ionization begins (≈50 km) but extends to the outer limits of the magnetosphere/plasmasphere (and even to the measurements of the atmospheres of other planets).

In the ionosphere, electrons and ions have different temperatures (T_e, T_i), implying different Maxwellian velocity distributions. The shape of the Doppler-broadened frequency spectrum is related to $\frac{T_e}{T_i}$ and once this ratio is known, electron density can be determined from echo power. (electron density can also be measured from the Faraday rotation of the echoes). The Doppler shift of the reflected signal gives the drift velocity. The separate velocities of the ions and of the electrons and the mass of the ions can also be inferred from distortions to the Doppler spectrum.

With very high spatial and temporal resolution, ISR's can measure electron density, electron and the ion temperatures, ionic composition, neutral species density and temperature, drift motions and the orientation of the geomagnetic field. Because of their enormous height range, ISR's lend themselves to the study of high latitude auroral and magneto/plasmaspheric interactions and they can measure auroral ionization.

Judging by the number of recent papers describing new applications for the technique, the full power of the ISR is yet to be realised.

Light radar (LIDAR) and Fabry–Perot spectrometer (FPS)

Although not currently in widespread use, it is likely that lidars will become a major tool for continuous observations of tropospheric/mesospheric temperature and density. In the D-region, two techniques are used; resonant and Rayleigh scattering. Resonant scattering occurs from the low concentrations of metals (probably of meteoric origin) in the height range 80-100 km. Tunable lasers can detect abundances of Na, K, Li and

(very recently) Ca. The prominent sodium layer which exists at approximately 90 km can be studied by this technique.

Lidars using Rayleigh scattering can measure height profiles of density (and therefore infer temperature) in the range 30-90 km with an accuracy of better than 10K in the mesosphere (Chanin, 1984). Since observations can be made continuously, this can provide considerably better temporal resolution than rockets or satellites. If operated in conjunction with a radar, the winds, temperature and density could be measured simultaneously, which would be of great benefit in the study of wave motion in the atmosphere. (To this end, a lidar is currently under construction at the Mawson Institute).

By measuring the Doppler-shift and Doppler-broadening of atomic spectral-line emissions in the atmosphere, the scanning Fabry-Perot spectrometer (of the kind currently operated by the Mawson Institute at Mawson, Antarctica) is capable of measuring the temperature and radial velocity of the atmosphere (Jacka 1984). The source of the emissions may be airglow or auroral emissions. While temperature and velocity may be measured accurately, the height of the source region must be assumed. For example, it is hoped that measurements of the sodium layer at approximately 90 km may be used to confirm the accuracy of the horizontal winds determined by the spaced-antenna technique.

The spaced-antenna partial-reflection radar

The spaced-antenna, partial-reflection technique is a relatively simple and inexpensive method of making continuous measurements of horizontal winds in the middle atmosphere and lower thermosphere. These radars operate in a pulsed-mode at 2–6 MHz and make use of scattering from quasi-isotropic irregularities with a scale size of ap-

proximately one half wavelength. In the case of the radar at Mawson, the size of the scatterer would be around 75 m, which is within the inertial range of turbulence. Signals are partially reflected by the ionization (free electrons) of the ionospheric D and E regions in the height range 60–100 km (although reflection from near the bottom of this range is determined by time of day and ionospheric conditions). These scattered signals produce a far-field diffraction pattern at the ground which moves at twice the horizontal velocity of the scattering layer. The exact cause and nature of the irregularities is still a topic for research and is the subject of the substantial Ph D. thesis of Hocking (1981).

The upper limit for observations is normally at the level of the ionospheric E-region. That is, radars that operate at around 2 MHz are unlikely to be able to penetrate this region, but even if they can there is another more important reason why 100 km is the upper limit for observations. In the D-region the ionization is so weak that there is no significant change in the mean refractive index and the speed of propagation of the signal is near the speed of light. When ionization becomes appreciable the speed of propagation decreases and the apparent height (as measured by the radar) and true height begin to differ significantly. Wind measurements at large heights are still possible, but without some method of knowing the distribution of free electron concentration, there is no way of knowing from what height the signal was scattered.

Because the ionosphere is a birefringent medium, magneto-ionic splitting takes place, and this can affect the operation of a SAPR radar. That is, the splitting of a plane-polarized wave into **O** and **E**[6] circularly polarized waves can cause problems when the two waves interfere with each other, giving the impression of fading. More importantly, at all times the E-mode is more efficiently scattered but during the day is attenuated more than the O-mode. Therefore, to maximize the strength of the signals scattered

[6]defined and discussed in sections 2.2.3 (page 69) and 3.3.2 (page 168)

from the D/E-regions, it is desirable to transmit in the mode which is most efficiently returned. At Adelaide the best performance comes from transmitting O-mode during the day and E-mode during the night.

Analysis of the moving HF diffraction patterns over the ground has become a well established technique, lending itself well to computer analysis, and is described in detail in the theory and equipment sections of this thesis.

Chapter 2

THEORY AND EXPERIMENTAL DETAILS OF THE SAPR RADAR AT MAWSON

2.1 Moving pattern analysis; theory and practice

The moving pattern analysis used throughout this work is that developed by Briggs et al. (1950) and reviewed by Briggs (1984). Although this method is commonly used, this section reviews some of the basic ideas which may assist later with the interpretation of the results. Later sections discuss the application of this theory to physical data and show the limits and potential errors of the technique in practice.

2.1.1 Describing moving patterns - some basic ideas

The apparent velocity

There are many kinds of moving patterns one observes frequently. For example, ripples on the surface of a stream and moving clouds are patterns which evolve as they move. Trying to determine the **systematic motion** of an evolving pattern is the aim of moving pattern analysis.

Partial reflections of high frequency radio waves from the ionosphere produce a moving diffraction pattern of signal strength over the ground. The speed and direction of this pattern is related to winds in the ionosphere, being twice the wind speed because of the point source effect (Felgate, 1970). It is the aim of the SAPR technique to infer wind speeds and directions from analysis of these diffraction patterns. Such a pattern can be conveniently described by a contour diagram, where the contours represent equal signal strength. A contour diagram will have the appearance of hills and valleys and, if the pattern is moving, signals detected by a single radio receiver will correspond to a cross-section through the 'hills' and 'valleys'. 2 MHz radio wave reflections from the ionosphere will produce a diffraction pattern which is of large scale and a very large array of detectors (such as the Buckland Park 2 MHz filled array - 1 km in diameter) will be required to visualize the moving pattern. Fortunately a large filled array is not necessary to measure the speed of the pattern and in fact a minimum of three (non-colinear) detectors can be used to determine the speed and direction and also to derive a measurement of how fast the pattern is evolving with time. The following discussion follows that presented by Briggs (1984).

Although the three (or more) detectors may be arranged in any configuration, it is easier to consider first the case of three detectors arranged in a right angled tri-

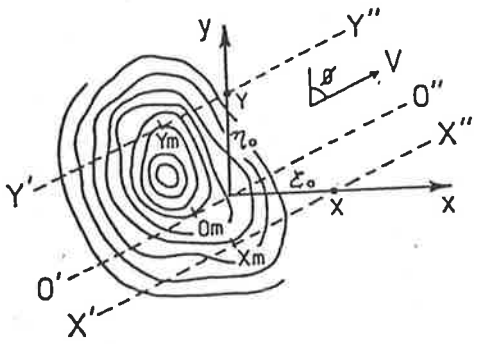

Figure 2.1:

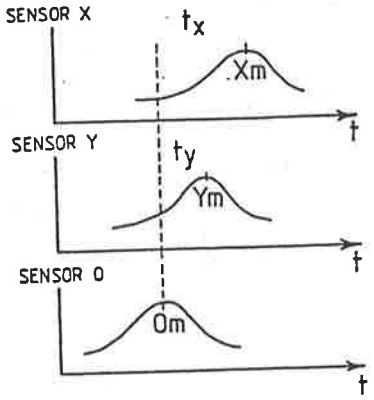

Figure 2.2:

angle XOY (figure 2.1) with an x-axis separation of ξ_0 and y-axis separation of η_0. When a hill-shaped pattern passes over the sensors XOY, each one will record a similar but time-shifted function corresponding to cross-sections through the 'hill'. If the pattern is roughly circular, then a 'line-of-maximum' drawn between the maximum points $X_m, 0_m, Y_m$ will be approximately perpendicular to the direction of motion. Figure 2.2 shows the signals from the X and Y detectors which have time lags of t_x and t_y compared with that of the origin.

From this information an apparent velocity of pattern motion may be determined by simple geometry. Figure 2.3 shows the direction of a line-of-maximum with a velocity V; the time lags t_x, ty being related by

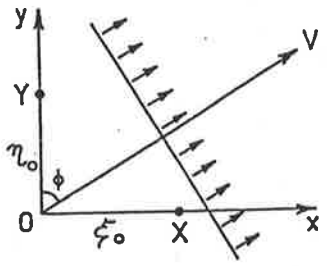

Figure 2.3:

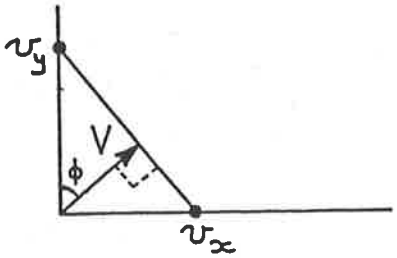

Figure 2.4:

$$t_x = \frac{\xi \cos\theta}{V} \qquad and \qquad t_y = \frac{\eta \sin\theta}{V}.$$

If v_x and v_y are defined:

$$v_x = \frac{\xi_0}{t_x} \quad and \quad v_y = \frac{\eta_0}{t_y}$$

then

$$v_x = \frac{V}{\cos\theta} \quad and \quad v_y = \frac{V}{\sin\theta}.$$

Note that v_x and v_y are **not** the components of the velocity V, but may be used to compute V geometrically; figure 2.4 shows how the apparent velocity vector is perpendicular to a line joining v_x and v_y.

Thus the calculation of an apparent velocity and direction from three detectors is a straight-forward task (and indeed apparent velocity is one of the first results actually

computed by the SAPR analysis program). However the pattern described in figures 2.1–2.4 is a special case where the pattern does not change shape with time and the contours are (on average) circular. When the pattern *evolves with time* and is *systematically elongated in one direction*, assessment of the pattern velocity requires a more rigorous treatment, usually known as **full correlation analysis** (FCA).

Full Correlation Analysis

FCA begins by first considering the 2-dimensional cross-correlation $\rho(\xi,\eta)$ of a random pattern described by the function $f(x,y)$:

$$\rho(\xi,\eta) = \frac{< f(x,y).f(x+\xi,y+\eta) >}{< [f(x,y)]^2 >}$$

where $\overline{f(x,y)} = 0$ and $<>$ denotes an average over all values x, y.

If the 2-dimensional (2D) function is random and isotropic then the cross-correlation function (CCF) $\rho(\xi,\eta) = constant$ will form a set of concentric circles. Therefore $\rho(\xi,\eta)$ is only dependent on the radial displacement from the origin and we may write,

$$\rho(\xi,\eta) = \rho(A\xi^2 + B\eta^2)$$

If however, a systematic stretch is applied to the random 2D function, the CCF becomes a set of concentric ellipses which may be described by,

$$\rho(\xi,\eta) = \rho(A\xi^2 + B\eta^2 + 2H\xi\eta)$$

When the function evolves with time (but shows no systematic movement), a 3-dimensional CCF may be drawn with axes of ξ,η and τ. In this coordinate system, surfaces of constant correlation will form concentric ellipsoids aligned with the τ axis. Now the CCF may be described by

$$\rho(\xi,\eta,\tau) = \rho(A\xi^2 + B\eta^2 + K\tau^2 + 2H\xi\eta)$$

Having produced a spatio-temporal CCF, the basis of the FCA may now be understood. Firstly, consider a temporal auto-correlation determined for a fixed point in space. Since time is the only variable,

$$\rho(0,0,\tau) = \rho(K\tau^2)$$

Similarly, at a fixed time a spatial auto-correlation may be described by

$$\rho(\xi,0,0) = \rho(A\xi^2)$$

Both the spatial and temporal auto-correlations have the *same functional form*, and therefore, *constants relating to the spatial correlation functions may be deduced from the temporal correlation functions*. This *assumption* forms the basis of the FCA technique.

The final step in modelling the CCF of a time varying function, is to consider systematic motion in the X, Y plane. Now the surfaces of constant correlation in the 3D CCF will be concentric ellipsoids tilted with respect to the τ axis. However, to an observer *travelling with the function*, there is no systematic motion and the function is changing randomly. Therefore in the moving coordinate system x', y', t the CCF becomes,

$$\rho(\xi',\eta',\tau) = \rho(A\xi'^2 + B\eta'^2 + K\tau^2 + 2H\xi'\eta'). \tag{2.1}$$

The moving and stationary frames of reference are related by,

$$x = x' + Vt\sin\phi = x' + V_x t$$

$$y = y' + Vt\cos\phi = y' + V_y t.$$

Substituting these into (2.1), the equation becomes,

$$\rho(\xi,\eta,\tau) = \rho(A(\xi - v_x\tau)^2 + B(\eta - v_y\tau)^2 + K\tau^2 + 2H(\xi - v_x\tau)(\eta - v_y\tau) \tag{2.2}$$

which has the form,

$$\rho(\xi,\eta,\tau) = \rho(A\xi^2 + B\eta^2 + C\tau^2 + 2F\xi\tau + 2G\eta\tau + 2H\xi\eta). \tag{2.3}$$

Therefore coefficients A,B,C,F,G,H completely describe the spatio-temporal CCF of any systematically elongated, randomly changing, moving function (ie. pattern). All these coefficients can be evaluated experimentally and used to derive the components of the 'corrected' (ie. systematic) velocity V (also sometimes called the 'true' velocity).

Calculating the true velocity and other useful information from experimental observations

Recall figure 2.1 showing three sensors arranged on a right angle triangle. The CCF of the sensors on the x-axis will be,

$$\rho(\xi_0, 0, \tau) = \rho(A\xi_0^2 + C\tau^2 + 2F\xi_0\tau + 2G\eta\tau).$$

To find the time lag τ_x' at which this auto-correlation is a maximum, set $\frac{\partial \rho}{\partial t} = 0$, which gives,

$$\tau_x' = -\frac{F}{C}\xi_0.$$

Similarly, the time lag for the y-axis sensors is

$$\tau_y' = -\frac{G}{C}\eta_0.$$

τ_x' and τ_y' may be easily calculated on a computer. Assuming that the pattern is random, then theoretically the auto-correlations of all three sensors will be identical. In practice they are not and a mean auto-correlation is computed and used in the analysis. This auto-correlation $\rho(0, 0, \tau)$ will be (from equation (2.3)), purely a function of τ. That is,

$$\rho(0, 0, \tau) = \rho(C\tau^2).$$

Now the simple cross-correlation of the x-axis sensors $\rho(\xi, 0, 0)$ may be equated with the auto-correlation $\rho(0, 0, \tau_x)$ where τ_x is the time shift for the auto-correlation to fall

to a value of $\rho(\xi, 0, 0)$. Hence from equation (2.3),

$$\rho(A\xi_0^2) = \rho(C\tau^2) \Longrightarrow \frac{A}{C} = \frac{\tau_x^2}{\xi_0^2}.$$

Similarly for the sensors on the y-axis,

$$\frac{B}{C} = \frac{\tau_y^2}{\eta_0^2}$$

and for the sensors at ξ_0, η_0,

$$\frac{H}{C} = \frac{\tau_{xy}^2}{2\xi_0\eta_0} - \frac{A\xi_0}{2C\eta_0} - \frac{B\eta_0}{2C\eta_0}.$$

The cross-correlations $\tau_x^2, \tau_y^2, \tau_{xy}^2$ are easily calculated on a computer and therefore the ratios $\frac{A}{C}, \frac{B}{C}, \frac{F}{C}, \frac{G}{C}, \frac{H}{C}$ are known. Only C (the *scale*) is required to fully describe the CCF $\rho(\xi, \eta, \tau)$. Again using equation (2.3), define $t_{0.5}$ as the time for the mean auto-correlation to fall to 0.5. Therefore,

$$\rho(0, 0, \tau_{0.5}) = \rho(C\tau_{0.5}^2) = 0.5.$$

Now that the CCF is fully described by the coefficients $A - G$, these may be used to evaluate the true velocity of the pattern and other useful information. Equating coefficients of $\xi\tau$ and $\eta\tau$ between equations (2.2) and (2.3) gives a pair of simultaneous equations in V_x and V_y which uniquely determine the true velocity:

$$AV_x + HV_y = -F \tag{2.4}$$

$$BV_y + HV_x = -G$$

In addition to the true and apparent velocity, other useful information may be derived from coefficients $A - H$. If a *characteristic ellipse* is defined as the CCF for which $\rho(x, y, 0) = 0.5$ then the spatial dimensions and orientation of that ellipse give a measure of the physical size and elongation of the pattern. Similarly, by defining a time $T_{0.5}$ at

which the mean auto-correlation falls to 0.5 (for an observer moving with the pattern) a measure of the time-scale of the random changes within the moving pattern is obtained. Another useful measure of random changes is a quantity V_c with the dimensions of velocity, defined as V_c = (pattern scale in direction of motion)/$T_{0.5}$.

2.1.2 Application of the theory to physical data

Computer software used in SAPR analysis

Computer software used in SAPR analysis follows closely the theory presented in the previous section. During the data-acquisition phase, the computer stores a time series of the complex signal amplitude from each of the three spaced receivers. The transmitter is pulsed at 20 Hz and reflections are coherently averaged over eight pulses. This gives an effective sampling interval of 0.4 s. The *in-phase* and *quadrature* amplitudes from each receiver (for a given height) are digitized into 8–bit signal levels and sampled at each 0.4 s for a period of 102.4 s (ie. 256 data points).

After the data-acquisition phase, the computer begins analysis by cross-correlating the time series between each of the three receivers. Because the time series are complex[1] the complex cross-correlation

$$\mid \rho(\xi) \mid = \frac{< f(x).f^*(y+\xi) >}{< [f(x)f(y)] >},$$

is formed (and similarly for the complex auto-correlation). Note that the modulus of the correlation coefficient is used in subsequent analysis. The cross-correlation functions usually have maxima within a few seconds of the zero time shift. By interpolation between computed points these time differences (or 'lags') $\tau_{i,j}$ can be found and, using

[1] see section 2.2.4, page 76

the simple algebra described in section 2.1.1, the apparent velocity may be computed. This process is repeated for each height level.

To calculate the 'true' velocity using full correlation analysis, the computer begins by calculating the auto-correlation for each receiver and averaging these to form the mean auto-correlation function. This is used, along with the three cross-correlation functions to calculate the true velocity (using the equations described in section 2.1.1).

In addition, as a by-product of FCA, other potentially useful data are produced. The power signal-to-noise ratio is calculated by measuring the size of the 'spike' which occurs (at zero time shift) in the auto-correlation function. The ratio of the amplitude of the spike, to the amplitude of the cross-correlation (near the zero time shift) is equal to the reciprocal of the power signal-to-noise ratio (Hocking, 1981). This figure is used by the computer to assess whether the signal is of sufficient quality to proceed with analysis. Also the systematic pattern size, orientation and elongation are recorded.

The programs have been written in the (Data General) FORTRAN language with ASSEMBLER language subroutines. ASSEMBLER is used to communicate with the experiment interface and to do high-speed tasks such as the calculation of complex auto/cross-correlation functions. The current computer program running the SAPR experiment (at Adelaide and Mawson) has evolved from software used when the analysis was conducted remotely on a main-frame computer. The advent of economic mini-computers allowed this data reduction to be done in-situ. The actual program listings are not reproduced in this thesis but are available from the Atmospheric Physics Group at the University of Adelaide on request.

Errors and limitations of the FCA method

The several assumptions made for FCA must be tested when physical data are used. For instance, when the 2 MHz SAPR (at Mawson) was operating normally, under normal ionospheric conditions, the number of wind measurements successfully passing all the quality checks accounted for only 20-40% of the total data acquired. Briggs (1984) has discussed the rejection criteria, which are briefly listed below. Also included is an estimate of the percentage of data rejected for each type of 'error' (where the assumptions of FCA were not satisfied).

- **Shallow fading** The data is rejected if the standard deviation of the signal level is $\leq$ 2% of the mean level. This occurs when the signal strength remains nearly constant during data acquisition. This condition can also occur when the receivers become saturated and with equipment failure. (Occurrence $\ll$1%)

- **Signal to noise level below –6dB** Coherent averaging is conducted during data acquisition (over a set of eight sequential data points) and this improves the signal to noise ratio (S/N) by about 9dB. When, after averaging, the S/N drops below –6dB, the data are rejected. Reflected signal strengths are usually too weak from heights below about 80 km but this situation varies regularly with the day and season and irregularly with ionospheric disturbances. During strong Polar-Cap-Absorption (PCA) events, reflections from the D and E regions may disappear completely for several days (The occurrence of this condition is largely a function of height, being virtually 100% at heights below 76 km, and only a few percent at heights above 86 km).

- **Mean auto-correlation did not fall below 0.5** This indicates extremely slow fading (ie. greater than $\approx$10 s – Occurrence 2-6%).

- **Cross-correlations have no well defined maxima or the cross-correlation maximum is greater than 1** Sometimes very noisy signals can cause this (Occurrence 1-2%).

- **Percentage time discrepancy (PTD)>0.3** Ideally the three time lags ($\Sigma\tau'_{ij}$) deduced from the three cross-correlation functions should sum to zero. In practice, this rarely occurs and a PTD 'quality figure' is defined as

$$\frac{\mid \Sigma\tau'_{ij} \mid}{\Sigma \mid \tau'_{ij} \mid} \times 100\%$$

  The PTD gives an indication of whether the assumptions of the moving pattern analysis are valid. Although data used throughout this work have a PTD<0.3, May (1988) suggests that PTD's up to 0.5 are acceptable. (Occurrence 10-20%).

- V_c^2 **<0** This implies V_c (defined earlier in this section) is imaginary. If $V_c \approx 0$, this indicates pure drift with negligible random change. Computational errors can sometimes make V_c^2 slightly negative, in which case the apparent and true velocities are very similar, because the true value of V_c is zero. This is a benign 'error' as the data are not rejected and, in fact, are probably of high quality (so long as V_c is only *slightly* negative). (Occurrence 10-20%).

- **Computed coefficients for the characteristic ellipse indicate hyperbolic rather than elliptical contours** (Occurrence 2-5%).

- **Corrections to the apparent velocity by FCA are too large**

  Data are rejected if:

  - $V_{apparent} \geq 3V_{true}$
  - $V_{apparent} \leq 0.5V_{true}$

– the apparent and true directions differ by more than 40°.

Even when the data have successfully passed all the rejection criteria, a few spurious wind figures may occasionally be produced. Incorrect figures can often be identified as 'spikes' or 'transients' in the data (ie. winds which imply impossibly large acceleration of the mean wind); they are usually referred to as 'outliers'. Most of these spikes can be removed by producing histograms of wind velocities and using these to determine limits at which velocities become unacceptably large. Care has to be taken to ensure that correct data is not also removed in this process.

With the wind data used throughout this thesis, the following method was used to remove outliers from the data. Data was separated into two-week intervals, and for each of these, velocity histograms (at each 2 km height interval) were produced. These histograms were approximately normally-distributed, but visual inspection showed that there were sometimes a number of unacceptably large velocities which fell outside the 'bell'-shape of the histogram. By choosing velocities which left out $2\frac{1}{2}\%$ of the data in each histogram tail, limits were determined which were then used to edit the data.

There is always some difficulty in justifying methods which remove suspect data points. In the above case, the decision to remove 5% of the wind data (ie. $2\frac{1}{2}\%$ from each tail) was empirically based and was fairly successful at removing obviously incorrect data points. However, while the high-velocity spurious data are removed, there are probably other false low-velocity data remaining. It is more difficult (or perhaps impossible) to detect these, but fortunately, for the purpose of this thesis, this is of small concern. That is, the SAPR collects data with (generally) a 5-15 min time resolution between each wind measurement (at each height level), and since hourly averages are usually employed, the low-velocity spurious data are less likely to cause problems when conducting spectral or harmonic analysis (ie. numerical methods which involve taking the square of a

wind velocity (such as harmonic analysis), and Fourier spectra (which can be seriously affected by transient spikes) will be relatively unaffected by the low-velocity spurious data). However, it must be acknowledged that this process of removing 'outliers' may bias the data toward lower velocities.

Precisely **why** incorrect wind figures can be produced (after carefully testing the assumptions of FCA) is unknown. However, it is a common problem when dealing with non-Gaussian statistics, to observe 'outliers' or 'glitches' in the data.

There are critics who question precisely what is being measured by the SAPR method. Clearly the wind measurements of the SAPR method are closely related to the actual winds in the mesosphere and lower thermosphere, but the degree of accuracy is occasionally questioned. Over the years several attempts have been made to compare the SAPR wind measurements with those from other techniques; for instance Hocking and Vincent (1982) made direct comparisons with rocket observations. More recently, May (1988) and Hocking et al. (1989) have discussed in great detail the accuracy and reliability of wind measurements (and other parameters) deduced by the spaced antenna method. Application of the technique to measure tropospheric and stratospheric winds (using VHF radars) permits direct comparison with radiosonde measurements. The conclusion drawn is that FCA provides accurate measurements of winds and this basic assumption is used throughout this thesis.

2.2 Equipment

This section describes the construction and general theory of the hardware used with the Mawson SAPR radar. Although an earlier version of the experiment operated at Mawson Station during the summer of 1981-2, (MacLeod and Vincent 1985, MacLeod

1986), all the equipment (excluding the towers) was returned to Adelaide in 1982 and substantially rebuilt. The original system had been designed for semi-mobile use and had been operated at Townsville (20°S 147°E) periodically between 1976-80.

The author, with considerable assistance from the Mawson Institute and many ANARE expeditioners, rebuilt the radar during his 1984 wintering at Mawson. The major part of the construction took around 6 months. After the writing of the first draft of this thesis, the author returned to Mawson (during the summer of 1988-89) and conducted a major overhaul of the radar, including the replacement of the computers, replacement of antenna feeders and a careful inspection of the electronics and antennas. This is briefly described in appendix A.2.

2.2.1 Factors to be considered when constructing an antenna array in the Antarctic

The radio frequency environment

From the point of view of radio communication, Mawson station can be divided into three distinct areas:

- an electrically quiet area for high frequency (HF) receiving antennas (West Bay),
- an area for the high-power HF transmitting antennas (East Bay),
- the main living area of the station itself.

Land area is at a premium at Mawson, so most of the large HF antenna arrays are very close to each other and sometimes overlapping. Short wave communications with Australia are conducted using 1 or 2 transmitters which send telemetry (by the *Frequency Shift Keying* (FSK) technique) or voice (by *Single Side Band* (SSB)). As FSK

requires a continuous carrier wave and as each of the communications transmitters produces 10 kW of radio frequency (RF) output, the RF energy density at the transmitter site is relatively high; so much so that inductive coupling between adjacent antennas (or even odd pieces of wire) can produce uncomfortably large RF voltages. Spurious emissions from the transmitters are relatively low, but in view of the large power being used, considerable undesirable noise is produced.

Other strong sources of RF noise are electrical generators, fluorescent lights, motors and the many computers and microprocessor controlled devices about the station. Static electrical discharges produced by blizzards often generate sufficient RF noise to halt HF communications (the drifting snow particles carry static charge and generate radio noise when they contact the antenna wires). The buildup of charge on antenna wires can lead to continuous arcing to [electrical] ground (and electric shocks for the unwary) if the feeders are not earthed. In summary, Mawson Station is an electrically noisy site for a 2 MHz SAPR radar and the desire to minimize interference has largely determined the present location of the receiver (Rx) and transmitter (Tx) arrays.

Notes on the physical environment

Mawson Station is an extremely windy place. The mean wind speed during 1985-87 was 11 ms^{-1} (21 knots). On average 27 days of each month experienced strong winds (>14 ms^{-1} or 22 knots) and of these, on 13 days the winds exceeded gale force (>17 ms^{-1} or 34 knots). Maximum wind gust velocities for any month were typically 40 ms^{-1} (80 knots) but sometimes exceeded 50 ms^{-1} (100 knots). Very few [inhabited] locations on the earth's surface consistently experience winds of such magnitude.

Mawson's unusually high winds are mainly *katabatic*, produced by a downwards flow of cool air off the Antarctic continent. In some places this wind becomes channelled

into a narrow region, giving rise to very strong winds which blow in an almost constant direction. This is the case at Mawson where the wind vector is usually within a few degrees of 312° [geographic] (ie. a south-easterly). This constant wind direction influences the design and orientation of buildings and largely determines where snow drift will build up around structures.

Temperatures range from +5°C in summertime to –35°C in wintertime, with usual wintertime temperatures below –20°C. Blizzards, which usually occur every few weeks (especially during the wintertime) often gust to 40-50 ms^{-1} (100 knots). During the winter, snow drift blown from inland, form hills around structures and may completely bury the smaller buildings.

The land surface at Mawson is undulating igneous rock (charnockite) strewn with moraine boulders. On the southern side of the station, rock gives way to hard ice which rises steeply inland. For about 9 months of the year, the sea surface around Mawson is frozen solid to a depth of about 3m extending out to a distance of several hundred kilometres from land.

2.2.2 Layout of the SAPR transmitter and receiver sites

Because of extremely limited space at Mawson and the large area of the SAPR transmitting antenna array, the antenna was rebuilt on the site of the earlier (1981-2) radar. This area in West Bay is one of the flattest on the station and is bordered by a communications log-periodic (transmitter) array (pointing directly towards the SAPR transmitter array), an IPSO (Ionospheric Prediction Service Organisation) ionosonde array, and the sea. Figure 2.5 shows the positions of the radar transmitter and receiver antennas relative to the main living area and to the communications transmitter antenna area (which is situated on the East Arm of Horseshoe Harbour).

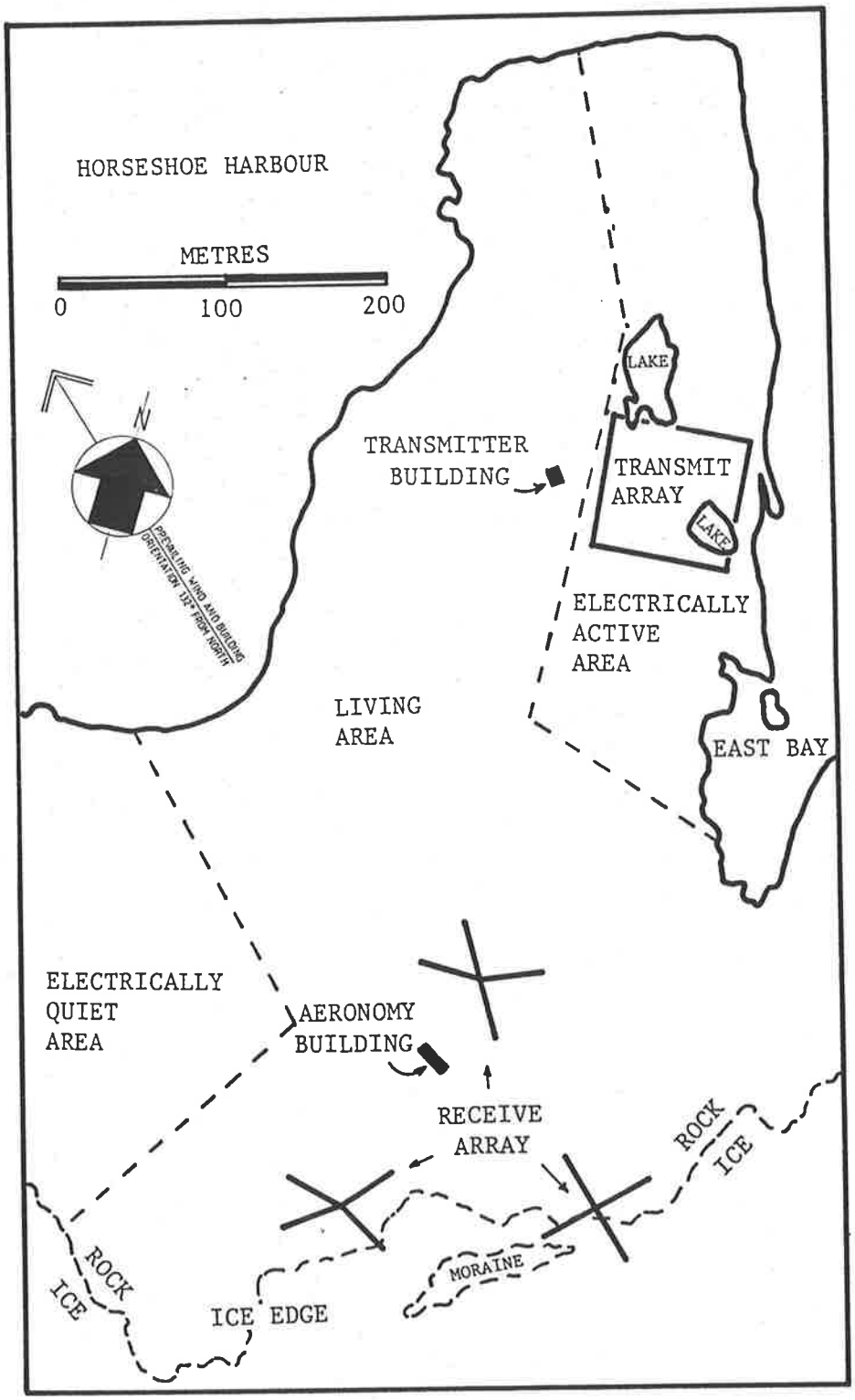

Figure 2.5: East Arm of Mawson Station - positions of the SAPR receiver and transmitter arrays

Figure 2.6 shows the many buildings dotted around the harbour but it does not show the intricate spider-web of antennas and feeders which covers them. Due to the difficulty in finding places to erect receiver towers and the desire to avoid interfering with existing antennas, compromises had to be made.

2.2.3 Construction of the SAPR radar

Construction took six months and the outside temperature largely determined the sequence of operations. Cranes, pneumatic rockdrills, and other essential machinery cease to work at low temperatures (<–15°C) so the work-plan required that outside work be completed first. Chronologically the work proceeded as follows:

- erection of the transmitter towers,
- erection of the receiver towers,
- rigging the transmitter and receiver arrays with antennas and feeders,
- tuning the antennas and servicing the transmitter,
- getting the computer hardware and software into operation.

The following sections describe these tasks in more detail.

Erection of the transmitter towers

The SAPR transmitter array consists of four 11m-tall towers arranged in a square and supporting four folded-dipole antennas (see Figures 2.7 and 2.9). This configuration is used at Adelaide and was used with the earlier mobile array at Townsville and Mawson. Each half-wavelength folded dipole is approximately 75m long, this being slightly shorter than the separation (80m) between the towers.

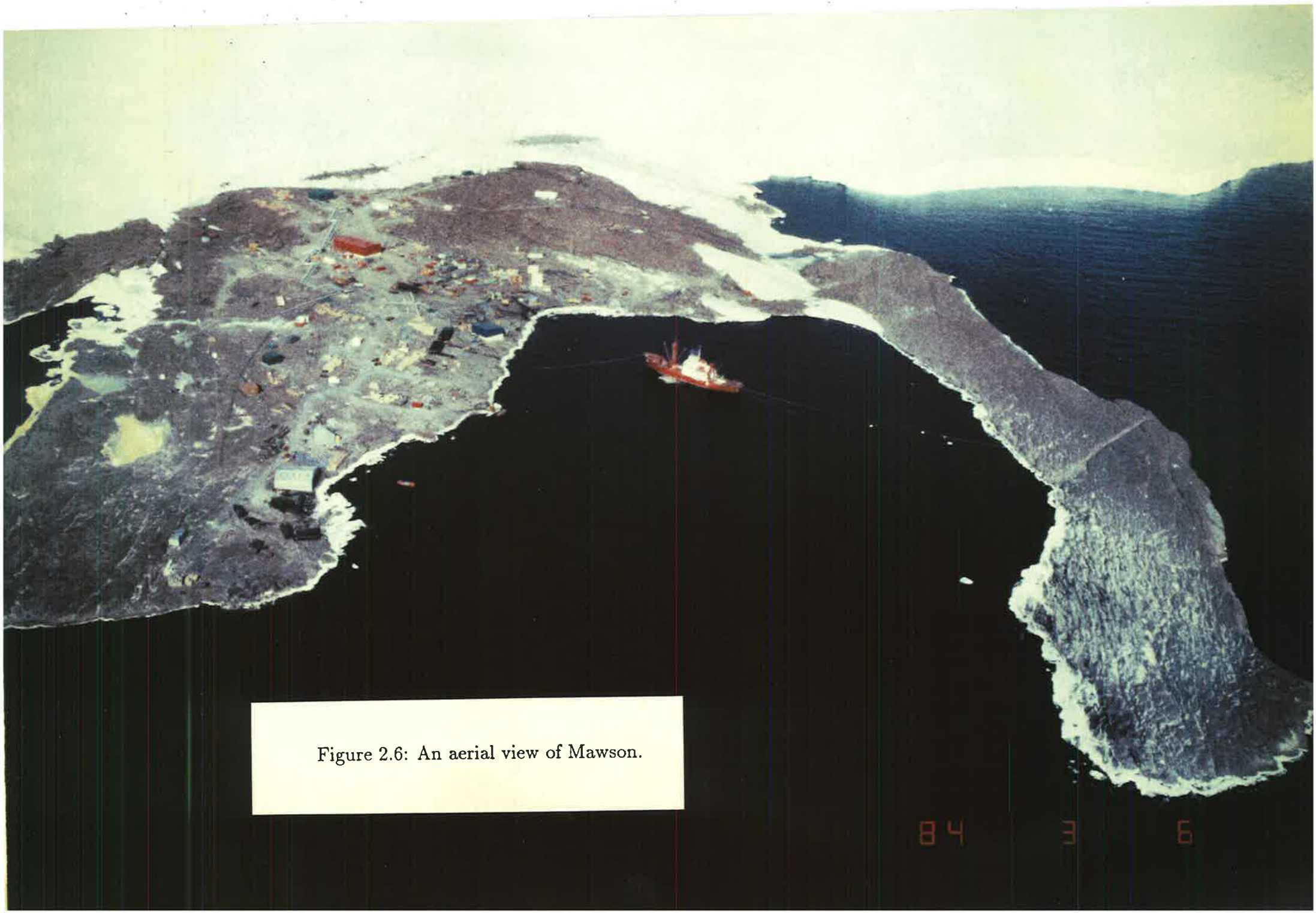

Figure 2.6: An aerial view of Mawson.

Before the new transmitter array could be erected the 4 old towers remaining from the 1981-2 radar had to be lowered and removed. These three-section telescoping towers were reconditioned and re-rigged for use as the new receiver aerial towers (18m tall).

The transmitter array site was re-surveyed and holes for new guy anchor points drilled. The hard charnockite rock surface is well suited to making extremely strong anchor points for the guys. Anchor points were made by drilling a 3 cm diameter hole 50 cm into the rock, and sledge-hammering in anchor pins. Figure 2.8 shows how a steel wedge at the bottom of the hole spreads the base of the split anchor-pin and holds it securely in position. For extra strength, molten sulphur was poured down the hole.

Bordering the area reserved for the SAPR transmitter array is a large vertical log-periodic antenna array and numerous open wire feeders conducting power from the 10 kW transmitters. Great care had to be taken when working near these feeders as they were live for most of the day. Surprisingly, despite the large flux of RF radiation in the area, there was a small pyramidal building at the centre of the radar transmitter site containing explosives and detonators and at the edge of the site there was a shipping container with more explosives. Although electrically operated detonators are not used at Mawson (because of the induced current hazard) it was requested that in the interests of safety the explosives be moved elsewhere, and they were subsequently moved to West Bay.

A small quantity of concrete was poured for the antenna base plates. With air temperatures of –10°C, the concrete had to be warmed with hot air (from a *Hermann-Nelson* kerosene powered heater) until it was sufficiently cured, which took about a day. Normal concrete would require several days of heating to fully cure, but the concrete used was a special fast setting type known as *Vertipatch.*

The transmitter towers were of standard triangular-section ANARE (Australian Na-

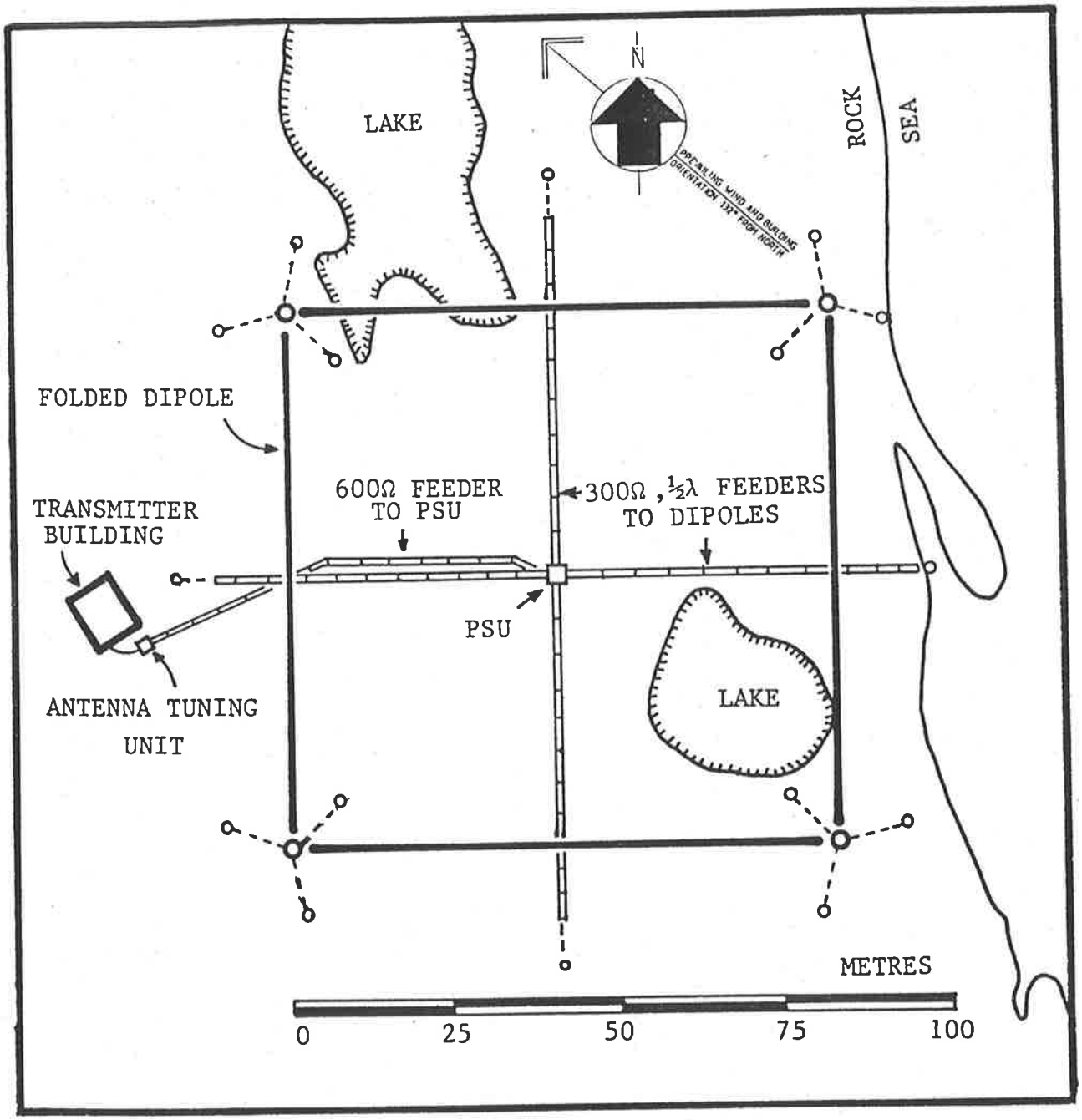

Figure 2.7: The transmitter array - plan view

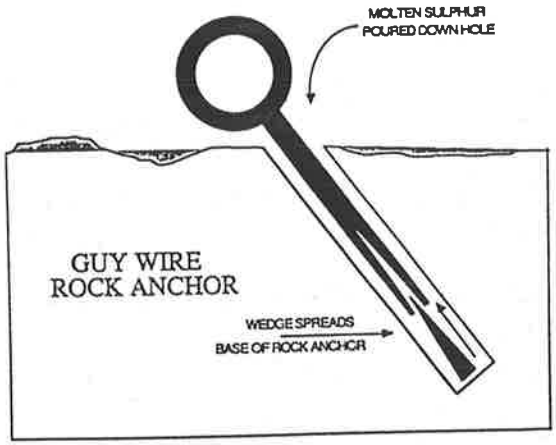

Figure 2.8: Guy wire rock anchor

tional Antarctic Research Expedition) type construction. These are supplied in 1.83m sections which may be bolted together to make a tower as tall as required. Our towers (made of 6 sections) were 11m tall and after some modifications to the top sections, were erected into position by a Grove crane (Figure 2.10).

Erection of the receiver towers

Finding satisfactory sites to erect the receiver towers required much thought and diplomacy. Over the last few years the outward appearance of Mawson Station (and the other Australian Antarctic stations) has changed dramatically with the construction of large new buildings, roads, pipelines and other structures. Building work is likely to continue for some years, and it has further decreased the already limited space available for new antennas. The receiver towers had to be sited such that they were clear of buildings (including proposed ones) and existing communications antennas and yet had to be spaced in an equilateral triangle with sides of 150-180m (1.0-1.2 λ). Also, at each tower the 2 dipoles had to be orthogonal to each other and preferably aligned in the same direction as the other dipoles.

The final positions of the receiver dipoles are shown in Figure 2.11. The skewness

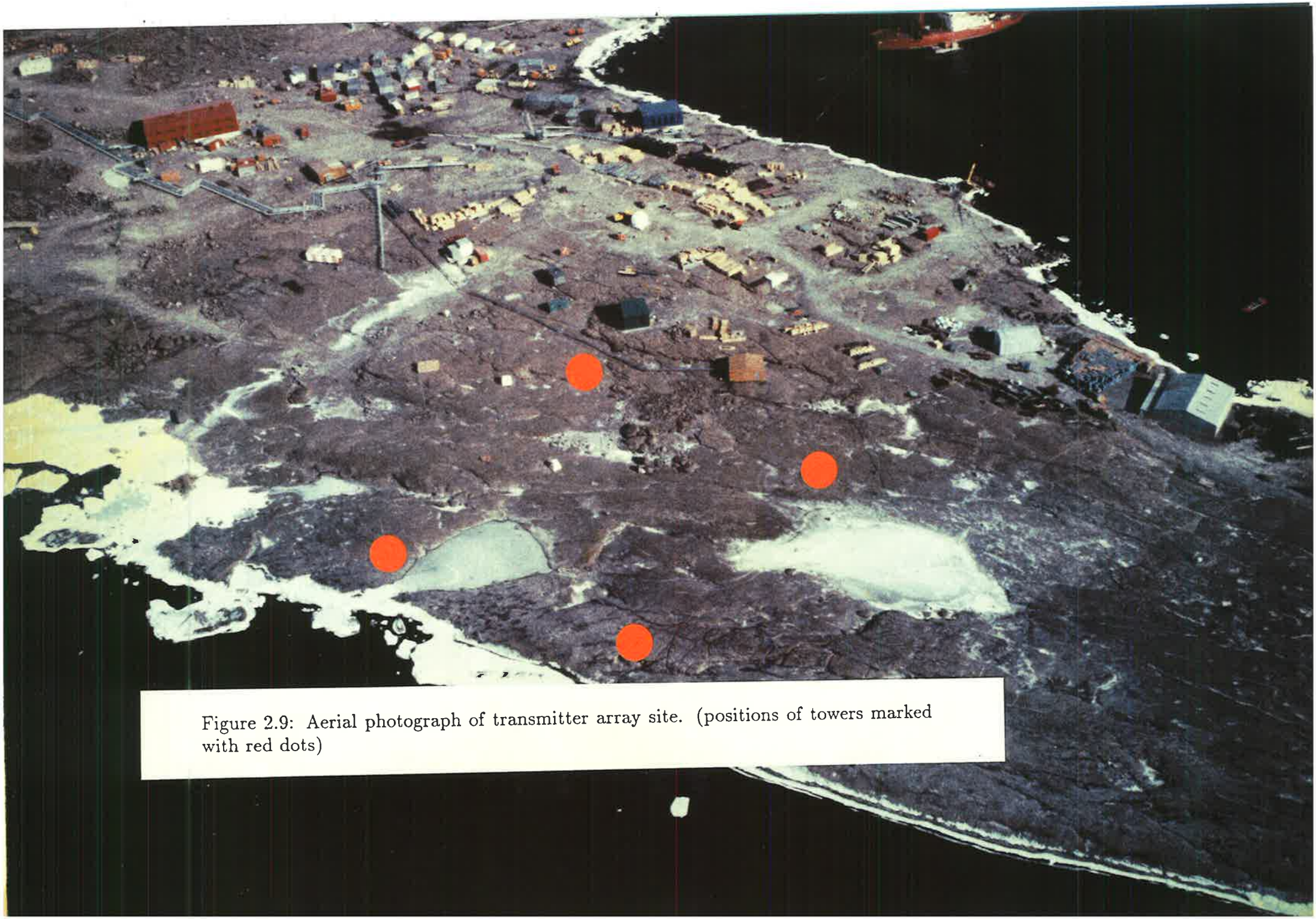

Figure 2.9: Aerial photograph of transmitter array site. (positions of towers marked with red dots)

Figure 2.10: Using a Grove crane to erect transmitter towers

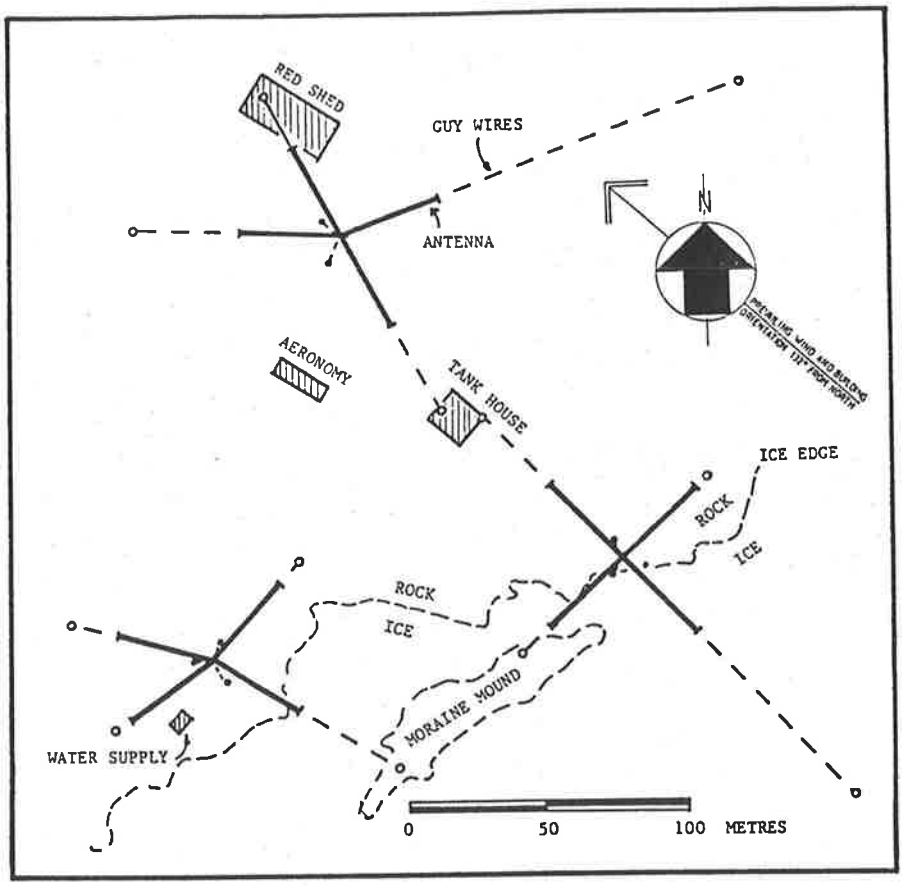

Figure 2.11: The receiver array - plan view

of some of the dipoles indicates the compromises which had to be made. The towers form a triangle which is nearly equilateral, having sides of 153, 156 and 163m. Also the aeronomy building which houses the receivers is conveniently central to the array, thus minimizing the length of coaxial feeders.

Rigging the antennas and feeders for the arrays

Rigging the antenna arrays in the extremely windy and cold conditions proved to be a very time consuming task taking about 6 months to complete. At Mawson, the high winds place substantial loading on towers and wires. Folded dipoles in the transmitter array have to be pulled taut between two masts 80m apart and so considerable tension is required. Because of the high tensile strength required, the wire used for antennas and feeders is hard-drawn copper-cadmium (3 mm diameter), of the type used by Australian

Telecom for long trunk routes and antennas. There is a further reason for using this wire. Mawson is subjected to frequent blizzards and the powdery drifting snow is surprisingly abrasive on thin metal wires. For example, during 1984, measurements on some 'soft' copper wire feeders showed that the wire diameter had decreased by a few percent over several months (this abrasion was first noticed when the characteristic impedance of an open-wire feeder mysteriously changed). After a blizzard the copper wires usually gleamed a coppery-pink colour, but resumed their tarnished green appearance after several days. The copper-cadmium wire was much less subject to this abrasion.

Copper-cadmium wire was used for the open wire feeders as these required tensioning to prevent vibration and fatigue caused by the strong winds. The feeders in the Tx array which connect the antenna to the phase shifter unit (at the centre of the array) are an electrical half wavelength ($\frac{\lambda}{2}$=75.8m) in length. A $\frac{\lambda}{2}$ length of feeder is sometimes known as a *load shifter* because the impedance measured at one end is equal to the impedance connected at the other end. This is useful for making precise measurements of antenna impedances and for ensuring that the feeders do not transform the antenna impedances to awkward values if the antennas and feeders are mismatched.

All the fittings and supports for the feeders were built in-situ using whatever materials were available. Over the years a surprising amount of antenna hardware (eg. guy wires, haulyards, rockbolts, insulators, pulleys etc.) has been left lying around the station and with the discontinuity caused by the annual replacement of technical personnel, much of this equipment has been forgotten. This was a great benefit as many fittings for the feeders were made from equipment salvaged from odd piles of 'junk'.

For high-power low-loss RF transmission, open wire feeders are nearly always used in the Antarctic. Conventional PVC sheathed coaxial cable becomes very stiff and hard at low temperatures and quickly abrades and cracks in Mawson's windy environment.

Where coaxial cable is used (as with our receivers) it is desirable that it be laid when the temperatures are 'warm' (>–10°C) and that it is securely tied down in a cable tray. Where there is no cable tray the coax has to be securely held down with rocks and snow.

Tuning the arrays

For the transmitter array, tuning was fairly straight-forward. Each folded dipole had an impedance, measured at the centre of the array, of around 200 Ω (cf. 300 Ω for free space). Inductive reactance in these dipoles was balanced out with the addition of parallel capacitance. Any other odd reactance and mismatched impedance was balanced out by the antenna tuning unit (ATU, a standard π-network) which transformed the impedance of the entire array into a resistive load of 77 Ω.

The phase-shifter unit (PSU) at the centre of the transmitter array delays half the power of the transmitted pulse waveform by a quarter of a cycle. Dipoles on opposite sides of the array are connected in parallel. When the original and phase-shifted signals are transmitted on the orthogonal dipole pairs, a circularly polarized wave is generated. A relay inside the PSU box switches between ordinary ('O', ie. right-hand) or extraordinary ('E' ie. left-hand) polarization by reversing the connections to one pair of dipoles. To check that the polarization switching of the array was working correctly, a dual-beam oscilloscope was used to confirm that the two dipole pairs were receiving voltages which were indeed 90° out of phase.

The receiver dipoles were trimmed to resonance, but in-situ measurements at the mastheads (see figure 2.12, page 71) indicated an impedance of around 70 Ω. Since the characteristic impedance of the coaxial feeder is 50 Ω, 50:70 Ω baluns (balanced-to-unbalanced transformers) were installed at the mastheads to optimize the matching. With a little re-trimming of the dipoles, the antenna impedance measured an ideal 50 Ω

(non-reactive) and was resonant at 1.94 MHz. Separate coaxial cables from each dipole are returned to the aeronomy building where an extra $\frac{\lambda}{4}$ length of coaxial cable is added, using relays, to one feeder or the other. As with the transmitter array, the addition of the original and 90° phase-lagged signal optimizes the reception of E or O circularly polarized signals.

Other control cables

The transmitter is approximately 400m distant from the aeronomy building where the receivers are located. Control signals to the transmitter are relayed via a coaxial cable which runs between the aeronomy and transmitter buildings. This cable, for the most part, runs inside electrical cable trays.

A twisted-pair cable runs from the transmitter building to the relays in the PSU box. Since this cable lies on the ground and runs 50m perpendicular to the prevailing wind, a problem was encountered with abrasion. This problem was solved by using surplus 100 ampere low-temperature wire which had sufficient weight to resist vibration and whipping by the wind.

2.2.4 Other hardware (excluding antennas)

For the most part, the Mawson SAPR radar hardware and software are very similar to those in operation at Adelaide. They have been extensively described by several authors including Hocking (1981), Ball (1981) and MacLeod (1986). Therefore, only a general functional description will be presented with special references to technical features specific to the Mawson SAPR radar. A summary of system specifications is presented in table 2.1, page 72.

Figure 2.13 presents a functional block diagram of the whole SAPR system. The

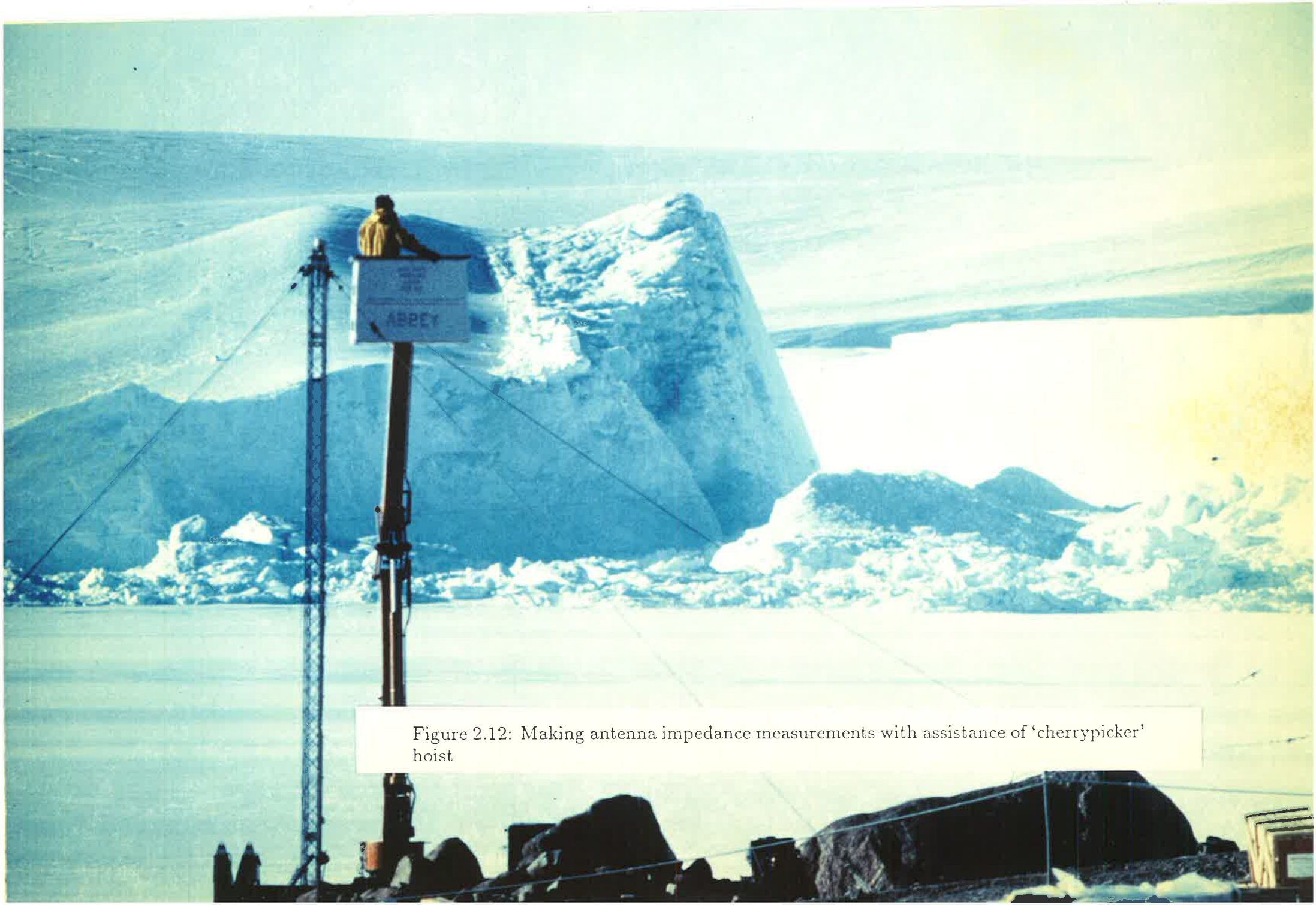

Figure 2.12: Making antenna impedance measurements with assistance of 'cherrypicker' hoist

Location:	Mawson Antarctica, 67° 36'S, 62° 53'E
Transmission Frequency:	1.94 MHz
Transmitting array:	$4 \times \frac{1}{2}\lambda$ folded dipoles arranged in a square with sides of length $\frac{1}{2}\lambda$ Dipoles phased to transmit E or O mode circular polarization Antenna elements elevated $\approx \frac{1}{4}\lambda$ above terrain Beam width (to -3dB points) ≈50 degrees
Receiving array:	3 pairs of horizontal droopy dipoles arranged in an approximate equilateral triangle with sides of 153, 156 & 163 metres($\equiv$ 1.0, 1.0, & 1.1λ) Antenna elements elevated $\frac{1}{10} - \frac{1}{14}\lambda$ above terrain Each dipole pair crossed and phased to receive E or O mode circular polarization
Transmitter :	Peak power 4 kW Pulse width 30 μs Pulse repetition frequency 20 Hz
Receivers:	Single conversion superhetrodyne with IF of 485 kHz Bandwidth ≈ 25 kHz Gain ≈ 100 dB Detector Phase-sensitive detection of *in phase* & *quadrature* signal
Data Acquisition:	Output from phase sensitive detectors (*in phase* and *quad* components) digitized into 8-bit words
Number of heights sampled	10
Width of height interval	2 km
Height resolution	≈ 4 km
Number of points coherently averaged	8
Effective sampling rate	2.5 Hz
Interval between successive wind measurements	5 minutes
Computer:	Data General NOVA 2 with 32K core-type memory
Terrain:	Antenna arrays built on bare rock (charnockite) adjacent to the ocean and less than 20m above sea level

Table 2.1: **A summary of system-specifications for the Mawson SAPR radar**

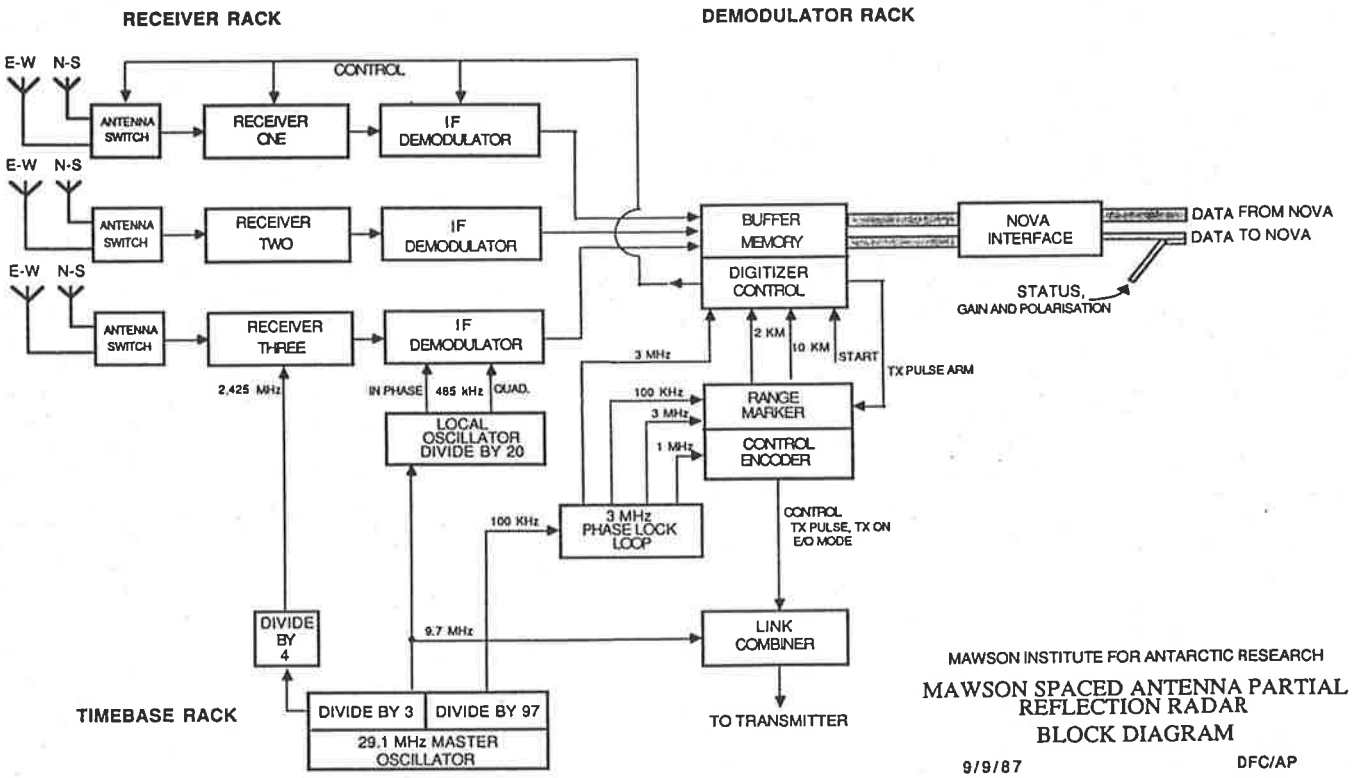

Figure 2.13: **Mawson spaced antenna partial reflection radar - block diagram**

equipment can be divided into 5 general areas which correspond to 5 separate pieces of hardware:

- the timebase rack,
- the receiver rack,
- the transmitter,
- the demodulator/digitizer rack,
- the computer.

Each of these units will now be described in further detail.

The timebase rack

Because the radar measures both the amplitude and phase of received signals (ie. phase relative to the transmitted signal), the whole system needs to be phase coherent and therefore signals to the transmitter, receiver local oscillators and digitizer control are obtained from a single 29.1 MHz master crystal oscillator. That frequency was chosen so that by simple integer division, all the required frequencies could be generated. The transmitter receives a 9.7 MHz signal ($\frac{29.1}{3}$) via coaxial cable and divides this by 5 to produce the carrier frequency of 1.94 MHz (ie. $\frac{29.1}{15}$). The receiver local oscillator frequency is 2.425 MHz ($\frac{29.1}{12}$) and the IF frequency is 485 kHz (ie. $\frac{29.1}{60}$). A 485 kHz signal from the master oscillator is required by the phase-sensitive detectors.

A 100 kHz signal ($\frac{29.1MHz}{291}$) from the master oscillator controls a 3 MHz phase lock loop (PLL) oscillator whose function is to produce range markers and timing for the digitizers. The choice of 3 MHz for use in the digitizer control circuitry is related to the speed of light. That is, at 3 MHz, radio waves (in free space) will travel almost exactly 100m per cycle (99.931m exactly) and therefore simple division of this signal can be used to measure distance in convenient units. For example, 30 kHz and 150 kHz signals derived from this oscillator provide the 2 and 10 km height markers when using a dual-beam oscilloscope to display the amplitude of the reflected signals as a function of height.

The transmitter

At Mawson, space limitations require that the transmitter be approximately 400m distant from the receivers and experiment controller. Previously, the antenna arrays were co-located and several cables were connected between the computer interface and the transmitter. In the earlier (1981-2) system at Mawson, three cables were used: one for

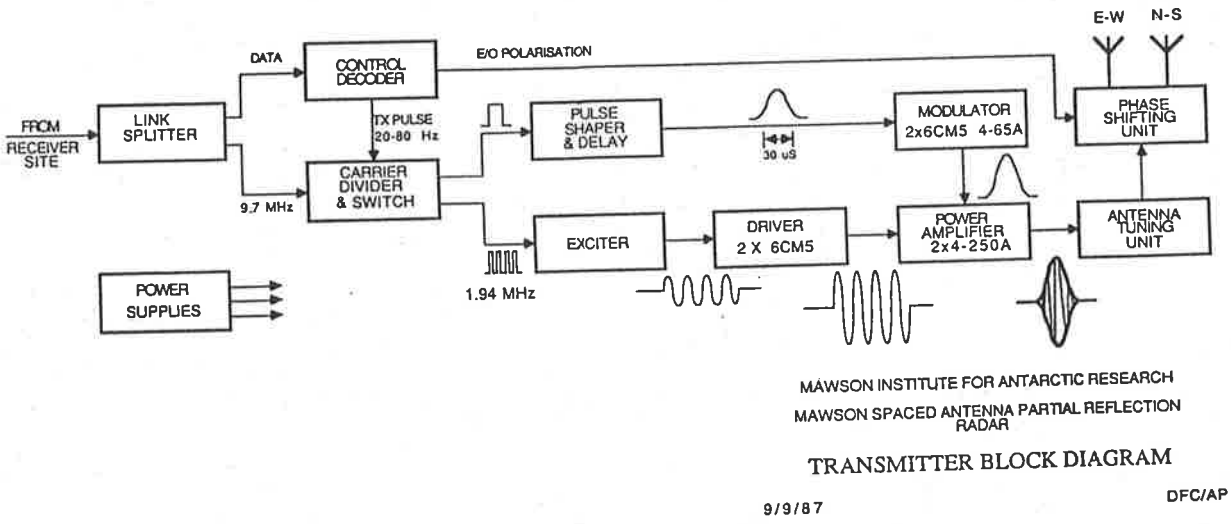

Figure 2.14: **Transmitter block diagram.**

the 1.94 MHz carrier, a second for the transmit trigger pulse and a third to the polarization relays. All three cables have now been combined into one coaxial cable, improving reliability and serviceability. This has been achieved by encoding the transmitter trigger pulse, the polarization and other information in a serial data-stream transmitted continuously along the coaxial-link cable. In addition 9.7 MHz is transmitted along the coaxial cable and both signals are separated at the link splitter (see Figures 2.13 and 2.14)

From the link splitter, the serial data is decoded and the 9.7 MHz is divided by 5. When a trigger pulse is received, a burst of 1.94 MHz digital signal is sent to the exciter and the pulse shaper produces a cosine-squared pulse (which approximates a Gaussian waveform). The filtered, amplified signal from the exciter is now a sine wave and is further amplified by the driver. After the [$\sin^2$] envelope is amplified by the modulator, the power amplifier multiplies the envelope and the RF pulse (a delay circuit ensures that both signals arrive at the power amplifier simultaneously). Typically the duration of the

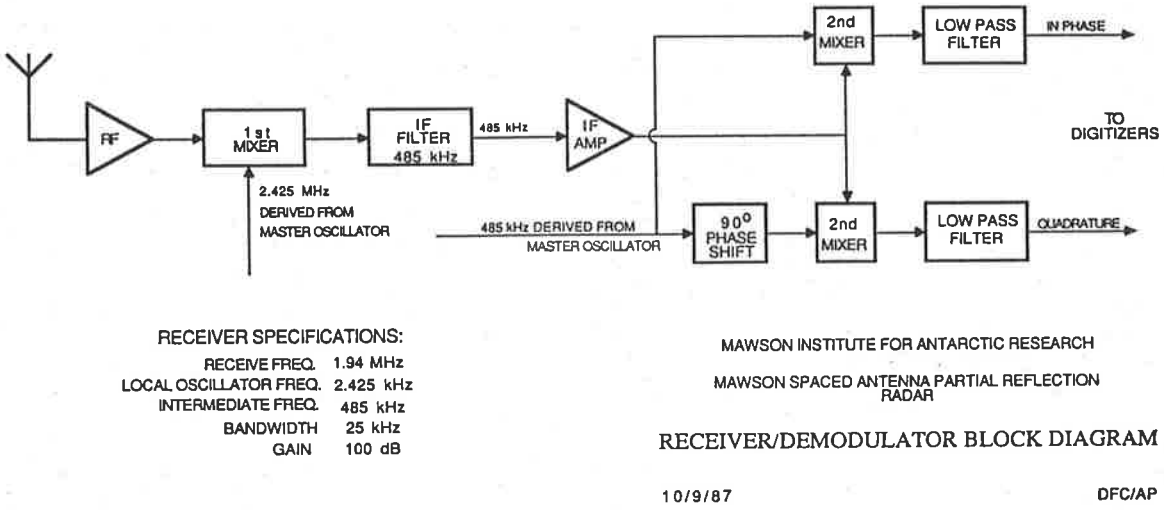

Figure 2.15: **Receiver block diagram**

pulse is 30 μs (between half power points) with an output voltage (at the transmitter) of 1000-1600 V peak-to-peak (ie. 2-4 kW into a 77 Ω load).

Relays in the PSU at the centre of the array determine the polarization (E or O mode) and are actuated by the control decoder.

The receivers

The receivers are conventional single-conversion superheterodynes with a local oscillator frequency of 2.425 MHz (from the master oscillator) and an intermediate frequency of 485 kHz. The gain is $\approx$100 dB and the bandwidth $\approx$25 kHz. Figure 2.15 shows the block diagram for the receivers. Earlier versions of this experiment (pre 1979) simply detected the signal after the IF stage, thereby obtaining a voltage which was proportional to the amplitude of the input RF signal. It was realised that significant improvement could be made to the signal-to-noise ratio and extra information obtained if the detectors were made *phase-sensitive*.

Phase detection is achieved in the following way. Consider the voltage of the IF signal to be of the form

$$A(t)cos[\omega_0 t + \Phi(t)]$$

where ω_0 is the IF carrier frequency (485 kHz). $A(t)$ represents the amplitude modulation of the signal and $\Phi(t)$ represents the phase (of the received signal relative to that of the transmitted). $\Phi(t)$ will include any constant and Doppler phase shift. Normal detection (or 'demodulation') will recover only the amplitude modulation $A(t)$. Complex numbers (of the form $I + iQ$ where $i = \sqrt{-1}$) are used to represent the output produced in phase-sensitive detection. Consider Figure 2.16 where some of the input signal, $A(t)cos(\omega_0 t + \Phi)$ is **multiplied** (the $\otimes$ symbol) by a reference signal $cos(\omega_0 t)$ (in phase with the transmitter) and then passed through a low-pass filter (LPF). The product of two cosine terms can be rewritten by the trigonometric identity

$$cosAcosB = \frac{cos(A+B)}{2} + \frac{cos(A-B)}{2}$$

and therefore it is clear that the voltage of the output signal (after removal of the high-frequency term by the LPF) will be proportional to

$$\frac{A(t)cos\Phi}{2}.$$

This is called the real (or *in-phase*) part of the signal. Similarly, since $cos(A - 90^o) = sin(A)$ and using the trigonometric identity

$$sinAcosB = \frac{sin(A+B)}{2} + \frac{sin(A-B)}{2},$$

the *imaginary* (or *quadrature*) component is equal to

$$\frac{A(t)sin\Phi}{2}.$$

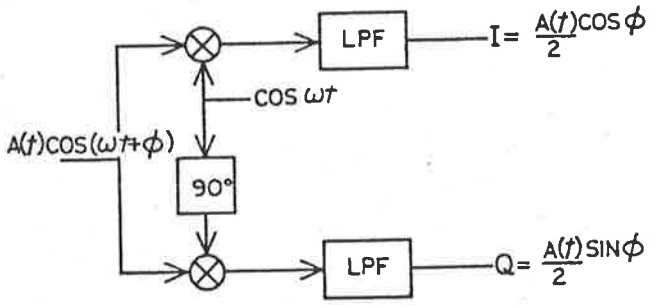

Figure 2.16: **Generation of the *in-phase* (I) and *quadrature* (Q) components**

This process is also shown on the right hand side of Figure 2.15. Phase-sensitive detection permits the measurement of Doppler shift and a significant improvement in signal-to-noise.

Digitization and computer control

In its current configuration, the experiment attempts a sounding every 5 minutes, spending the first 102.4 seconds acquiring data and the rest of the time analysing and recording it. During the data acquisition phase, the computer controls the receiver gain, polarization and the initial height for which data is recorded (and some other parameters) and every $\frac{1}{20}$ of a second it initiates a transmitter pulse. Once the transmitter trigger has been sent, the digitizer control board (DCB) momentarily takes control and determines the sequence of events to follow.

After the transmit pulse has been sent, the DCB commences timing and waits until reflections return from the start height requested by the computer (usually between 70-90 km). After this time has elapsed (4.7–6.0 ms) the DCB sends an impulse to the digitizers which then convert the *in-phase* and *quadrature* outputs from the three receivers into six 8–bit words. The DCB then stores these numbers in its own buffer

memory. This process is repeated 10 times at 6.7 μs intervals (corresponding to a change in height of 2 km), thus collecting data over a 20 km height range. Once the digitization process is complete the computer proceeds with a Direct Memory Access (DMA) high-speed transfer of data (sixty 8–bit words at a rate of $2x10^5$ words per second) from the DCB buffer memory to its own memory. Having completed this the DCB waits for the computer to trigger another transmitter pulse and the process is repeated.

The computer hardware and software

The computer is a Data General (DG) 16-bit NOVA 2 minicomputer running DG diskette operating system (DOS). Memory is limited to 32 K and is of the magnetic core type. By modern standards, this computer is limited in memory capacity, is a bulky size and requires a lot of maintenance, but its chief merits are its high speed DMA facility and its ability to compile FORTRAN language programs which may include high speed ASSEMBLER language subroutines.

Peripheral devices include a 9-track read/write tape recorder, a teletype/screen and dual diskette drives. With this system, in-situ analysis of recently collected data is possible, which is a significant improvement on earlier systems where data had to be returned to Adelaide for analysis.

Communication with the experiment is made through the interface board which is mounted inside the computer chassis. Through this board the experiment control information is transmitted and status information is returned. Transfer of receiver signal data is made through a direct-memory-access process, which means that the computer very rapidly places a sequence of data on the data-bus and this is written directly to the memory. It is this DMA facility which allows the computer to operate at the speed necessary for **real time** analysis.

Software used to run the experiment is written in Data General FORTRAN and ASSEMBLER languages. The main program which runs the experiment is written in FORTRAN with ASSEMBLER language subroutines. ASSEMBLER language is used where high speed is required (such as when performing complex auto-correlation functions) and where control words and data are being communicated via the NOVA interface board.

Data reduction occupies most of the computer's time and wind figures are produced within three minutes of the data acquisition. The software which makes these reductions is a development of software originally written for remote processing of SAPR data, but more powerful computers now allow this to be done in-situ.

The software used at Mawson is similar to that used in Adelaide, although at Mawson rewriting of some ASSEMBLER language subroutines was required.

Since the first draft of this thesis, the equipment at Mawson has been substantially upgraded. For more information the interested reader is directed to appendix A.2.

Notes on mains power supply

Mawson is reticulated with 230 Volt, 50 Hz mains power, produced by diesel-electric generators. However, the supply often failed (during 1984) and was subject to large variations in frequency (±5 Hz) and voltage (ranging from 200-230 volts). The large voltage drops were corrected by the addition of a 1 kW *Stabilac* AC voltage regulator, which supplied the equipment in the laboratory.

As described earlier, Mawson is electrically very noisy and much of that noise is propagated via the electrical distribution system. When the SAPR system first commenced operation, high voltage transients often stopped the computer several times a day. This unworkable situation was resolved by addition of low-pass mains filters on

all equipment. Even so, a certain amount of RF interference is still picked up from the mains and the computer still occasionally stops because of voltage surges and transient spikes.

Chapter 3

RESULTS

Chapter 3 draws on data from several sources. Data from Mawson, Antarctica were collected by the author during 1984, and by employees of the Australian Antarctic Division during 1985–88. Data from Adelaide was made available courtesy of the Atmospheric Physics Group of the University of Adelaide.

3.1 Mean winds and planetary waves

3.1.1 Introduction

This section presents observations of the mean circulation and planetary wave activity in the upper mesosphere and lower thermosphere at Mawson and Adelaide, and compares these with the results of recent models of winds for the southern hemisphere. Comparisons are also made with recent observations made at similar latitude stations in the northern hemisphere. Note that the quasi two-day wave is discussed separately in section 3.1.4 (see page 108).

3.1.2 Observations

Zonal Winds

Figure 3.1 shows the zonal mean (or 'EW') circulation at Adelaide constructed from three years of continuous data. The rms differences between the monthly means (eg. the differences from $\overline{January\ 85, 86, 87}$) may be taken as a measure of the interannual variability in the EW component. The time-height cross-section of figure 3.1 is very similar to that of Manson et al. (1985) which was made from observations taken at Adelaide during the period 1978-1983 (Although the data of Manson et al. cover a longer period than that shown in figure 3.1, they are from an assemblage of observational campaigns ranging from a few days to a few weeks in duration). The only significant difference between the present and earlier results (1978-83) is that the zonal flow is somewhat more westward at heights above 95 km in winter during the period 1984-1987. Otherwise the form of the zonal flow is similar during the ten year period between 1978 and 1987.

A time-height cross-section of the zonal flow at Mawson is shown in figure 3.2. It is apparent that the zonal mean circulation in winter at Mawson is considerably weaker than at Adelaide and that the summer westward flow extends to slightly higher altitudes. As with Adelaide, the interannual variability (as measured by the rms value of the monthly means) is about 5 ms^{-1}.

One interesting difference in the temporal behaviour of the zonal winds at Mawson and Adelaide concerns the relative timing and rapidity of the reversals of the flow at the two sites below 95 km. The change over from the summer to winter circulation commences at both locations is during February–March with the zero-wind contour descending rapidly. The reversal of the zonal winds in spring proceeds systematically at

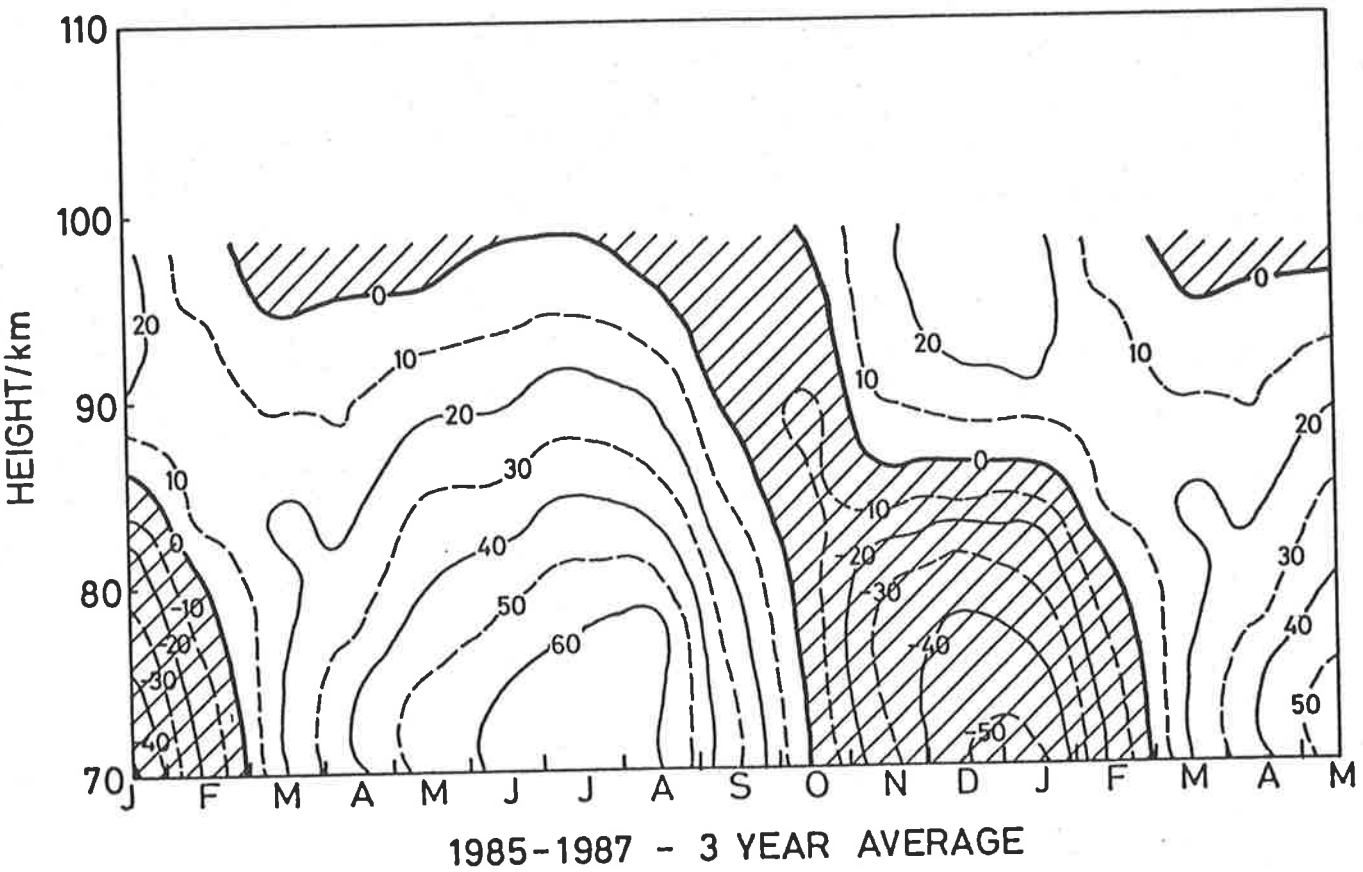

Figure 3.1: **Contours of zonal mean wind at Adelaide** in ms^{-1} constructed from three years of continuous data. Periods of westward flow are indicated by shading.

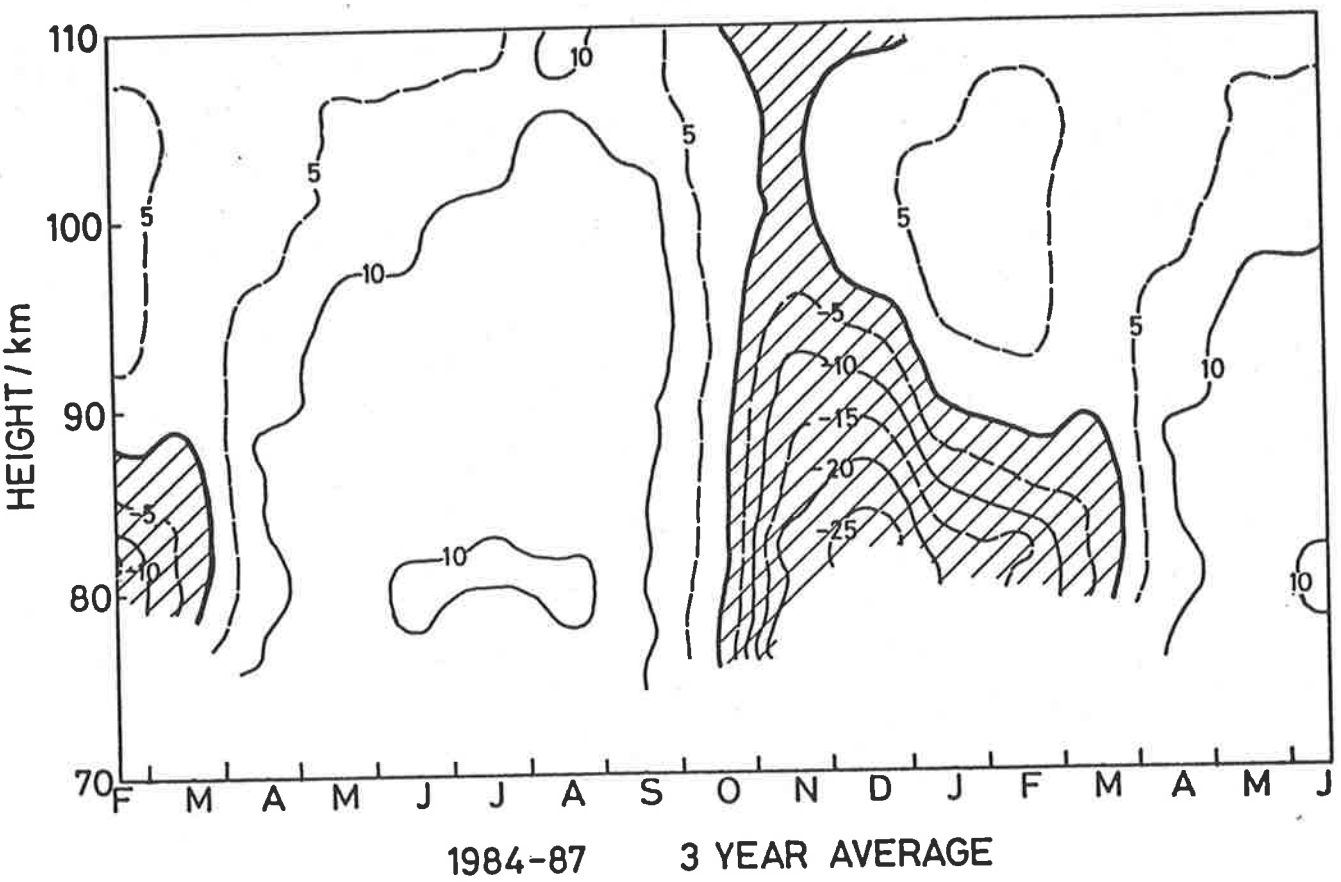

Figure 3.2: **Contours of zonal mean wind at Mawson** in ms^{-1} constructed from 3 years of continuous data. Shading as for Adelaide.

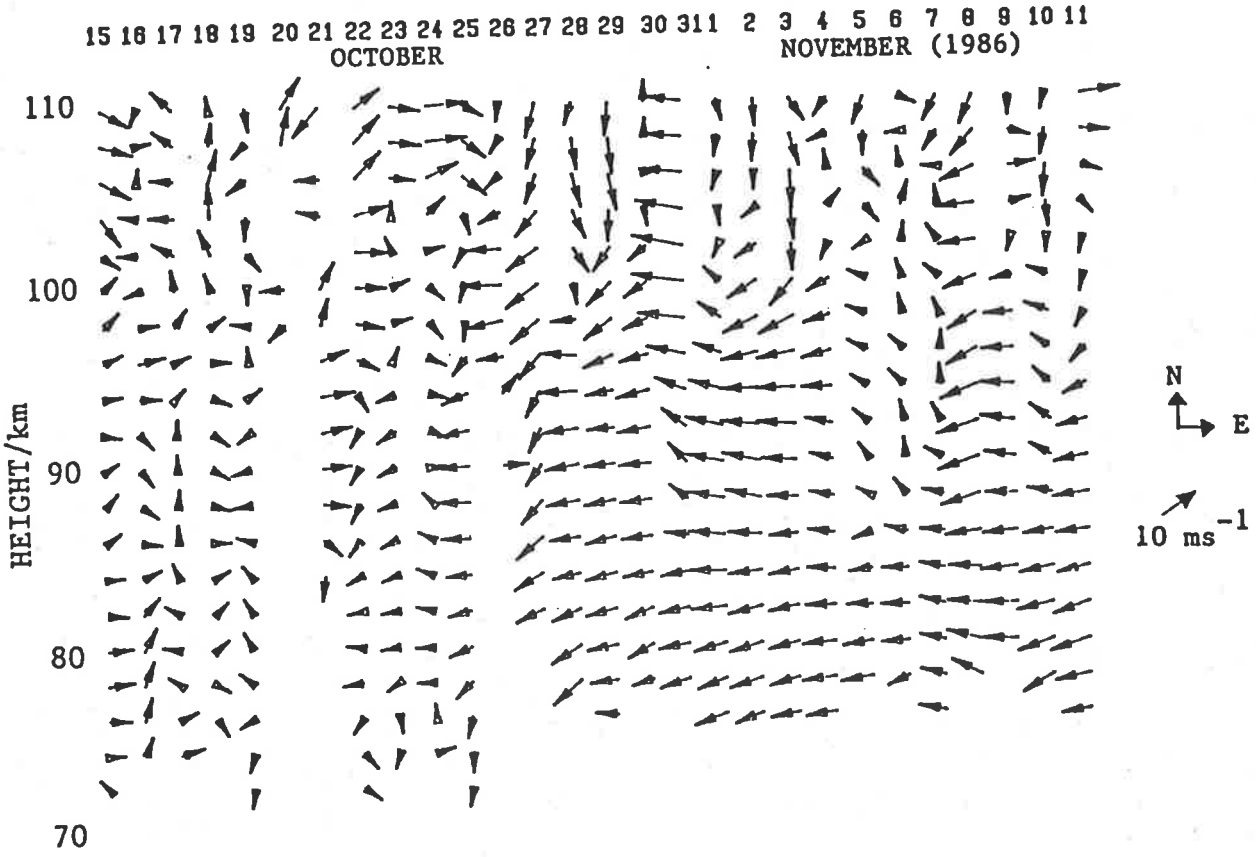

Figure 3.3: **Spring transition of wind vectors at Mawson.** Arrows represent unfiltered mean daily winds.

Adelaide with the zero-wind contour descending at a rate of about 10–20 km per month. The springtime reversal at Mawson however, occurs even more rapidly than indicated in figure 3.2. This is because figure 3.2 is constructed from monthly averages and this tends to disguise the abruptness of the reversal. Figure 3.3 illustrates more vividly the spring transition, with individual vectors indicating the direction and strength of the mean wind at each height on a daily basis in the period October 15 to November 19, 1985. During the first weeks of October, the winds are variable from day to day, probably reflecting propagation of planetary wave activity from below. However, in the 3rd week of October, this variability gives way to a strong westward flow below 95 km with the transition occurring almost simultaneously at all heights.

The Meridional Winds

The three-year meridional (or 'NS') mean winds, are shown in Figures 3.4 and 3.5. The rms monthly deviations are about 2-5 ms^{-1} so that, on a proportional basis, the meridional winds are much more variable than the zonal winds. At Adelaide the NS flow is essentially poleward at heights below about 85-90 km in all seasons except summer and equatorward at heights above this level. Only in mid-summer does an equatorward flow penetrate downward into the mesosphere. The meridional winds appear to behave in a less systematic manner at Mawson and in general they are also somewhat weaker than at Adelaide. One feature which appears to be common at both locations is a broad jet-like structure which occurs in mid-summer at or just above the height at which the EW winds reverse (approximately 90 km). Equatorward winds at Adelaide have been observed (in some years) to reach peak values of about 10 ms^{-1} about two weeks after the summer solstice.

Values in excess of 5 ms^{-1} in magnitude are also observed at heights near 80 km or below in February-March and in August to October at Adelaide. As described in figure 3.44 (top diagram), (page 166) echoes are not always observed continuously throughout the day, and below 80 km, are usually very much weaker at night. Therefore, at lower heights it is possible that incomplete removal of the diurnal tide might contaminate these results, especially as the diurnal tide attains its largest amplitudes at the equinoxes (Vincent et al., 1988). These authors show that at the equinoxes at 80 km, the time of maximum northward diurnal wind occurs near midnight with amplitudes of about 10–20 ms^{-1}. At Adelaide, the incomplete sampling at night at heights below 78 km causes a tendency for the diurnal tide to produce a net negative bias to the mean wind. Estimates of the possible bias, made by extrapolating downward the phase

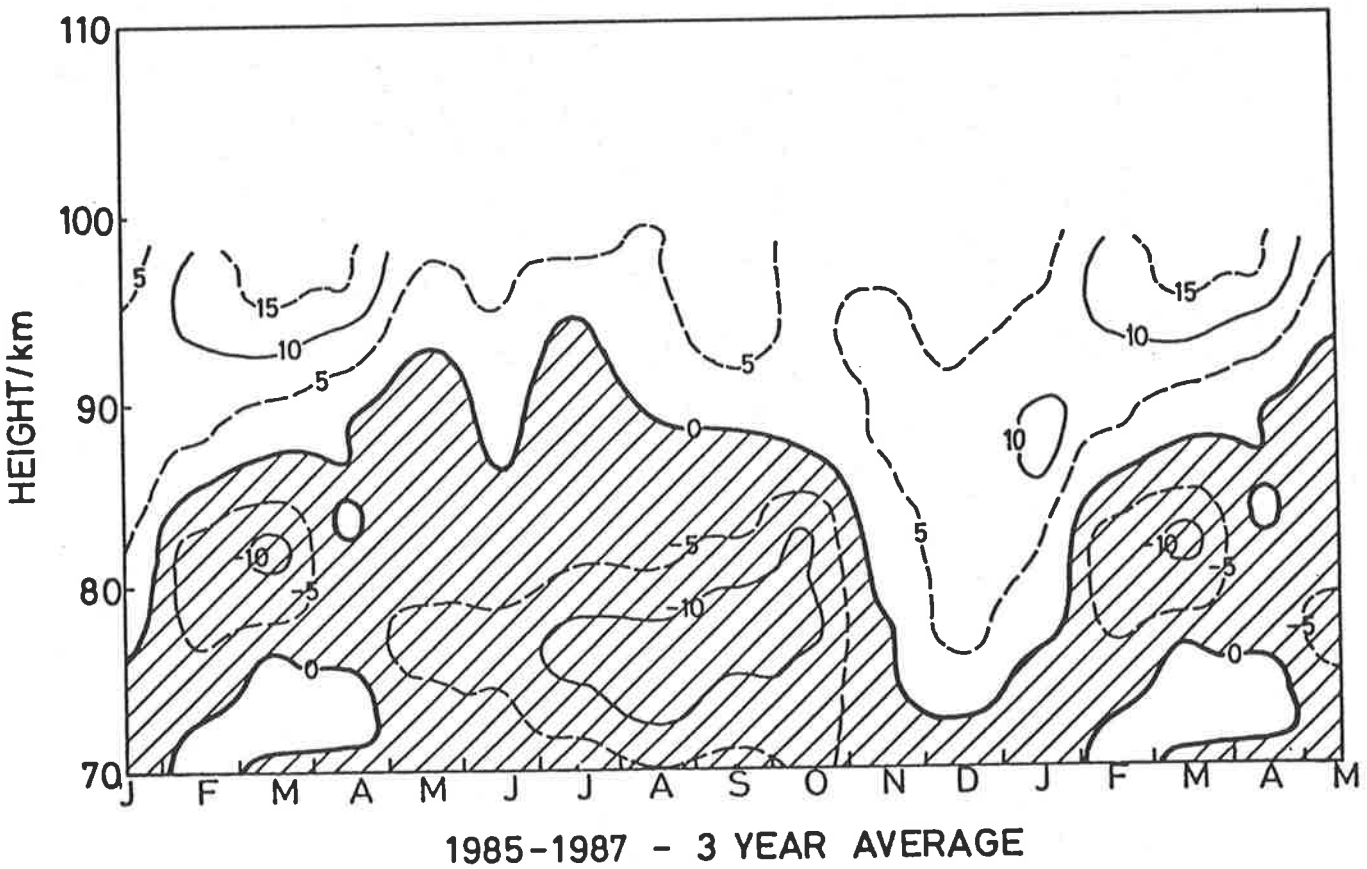

Figure 3.4: **Contours of meridional mean wind at Adelaide** in ms^{-1}. Regions of southward or poleward (negative) flow are denoted by shading.

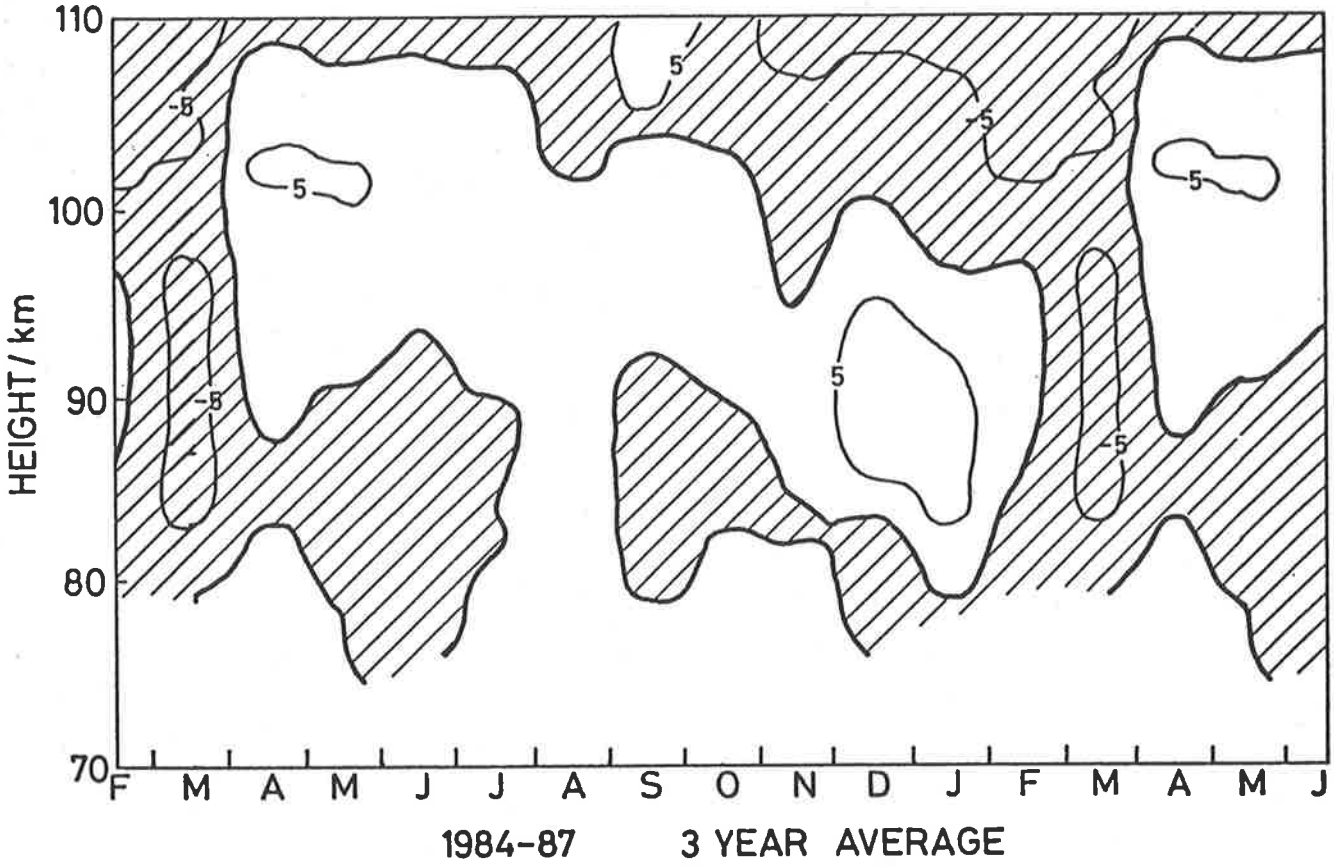

Figure 3.5: **Contours of meridional mean wind at Mawson** in ms^{-1}. Regions of southward or poleward (negative) flow are denoted by shading.

and amplitudes measured near 80 km to heights near 75 km, suggest that the diurnal tide produces a southward (negative) bias of about 2 ms^{-1}. While significant, this bias cannot account for the values of -10 ms^{-1} observed in August to October at 75 km. At Mawson, the much weaker diurnal tide and the capacity to acquire data over a complete day probably does not produce as much tidal bias as at Adelaide, but the considerably lower transmitter power and higher noise level mean that data below 76 km must be treated with caution.

Similar tidal bias effects may be expected for the zonal winds at Adelaide, although they will not be proportionately as large because of the greater magnitudes of the prevailing zonal winds. The phases of the zonal component of the tide are such that tidal bias will produce a net westward wind of less than 5 ms^{-1} at heights near 75 km during the period between March and September, i.e. the incomplete averaging of the diurnal tide causes the strength of the eastward winds to be slightly underestimated during the winter.

With the presence of travelling and quasi-stationary waves, it is improbable that single station observations of the winds (at a given time) represent the global (zonally averaged) circulation. In fact, it is possible that the pseudo-random structure of the meridional wind in figure 3.5 is largely due to travelling planetary wave activity, with contributions from quasi-stationary waves during the wintertime.

The annual wind oscillation

The annual oscillation in the zonal and meridional winds at each height may be harmonically analysed into mean, annual and semiannual components. Figure 3.6 presents the amplitude and phase of the annual oscillation at Mawson and Adelaide. The amplitude structure of the zonal components at the two locations is similar although the

amplitude at Adelaide is approximately 2.5 times that at Mawson. At Adelaide, lines of constant phase descend slowly over several months, except that at heights of 70–80 km, the phase is roughly constant. This descending structure is clear from inspection of the mean zonal winds in figure 3.1 (page 84) which shows the seasonal changes commencing at greater heights. At Mawson however, seasonal changes tend to be more abrupt and occur over a large height range simultaneously (for example the springtime zero-wind line in figure 3.2, page 85). This effect is reflected in the constant value of the zonal annual phase at Mawson.

Trying to determine consistent features of the meridional wind is difficult given its weakness and variability. However, the phase of the meridional wind at Adelaide does suggest an equatorward wind in summer which is consistent with the widely held view of an equatorward summer circulation in the upper mesosphere. At Mawson the phase structure is more complex, suggesting a different meridional circulation. Between 94–110 km there is a relatively strong (6–8 ms^{-1}) equatorward flow centred on mid-winter, but at 94 km there is an approximate 6 month jump in phase indicating maximum equatorward flow during midsummer. From 84–76 km there is a trend to earlier occurrence of maximum equatorward winds, although below 80 km, the data must be treated with caution due to the possibility of distortion caused by the low acquisition rate during the summer months.

The amplitude and phase of the annual zonal oscillation have been tabulated in the semi-empirical climatology of Fleming et al (1988). The model figures for Mawson are overlaid on the data in figure 3.6 and the agreement in amplitude and phase is excellent. Note however that figure 3.6 compares the amplitude of the annual component without the inclusion of the annually-averaged mean wind. In a similar fashion to figure 3.6, the amplitude and phase of the **semiannual** oscillation have been computed and are

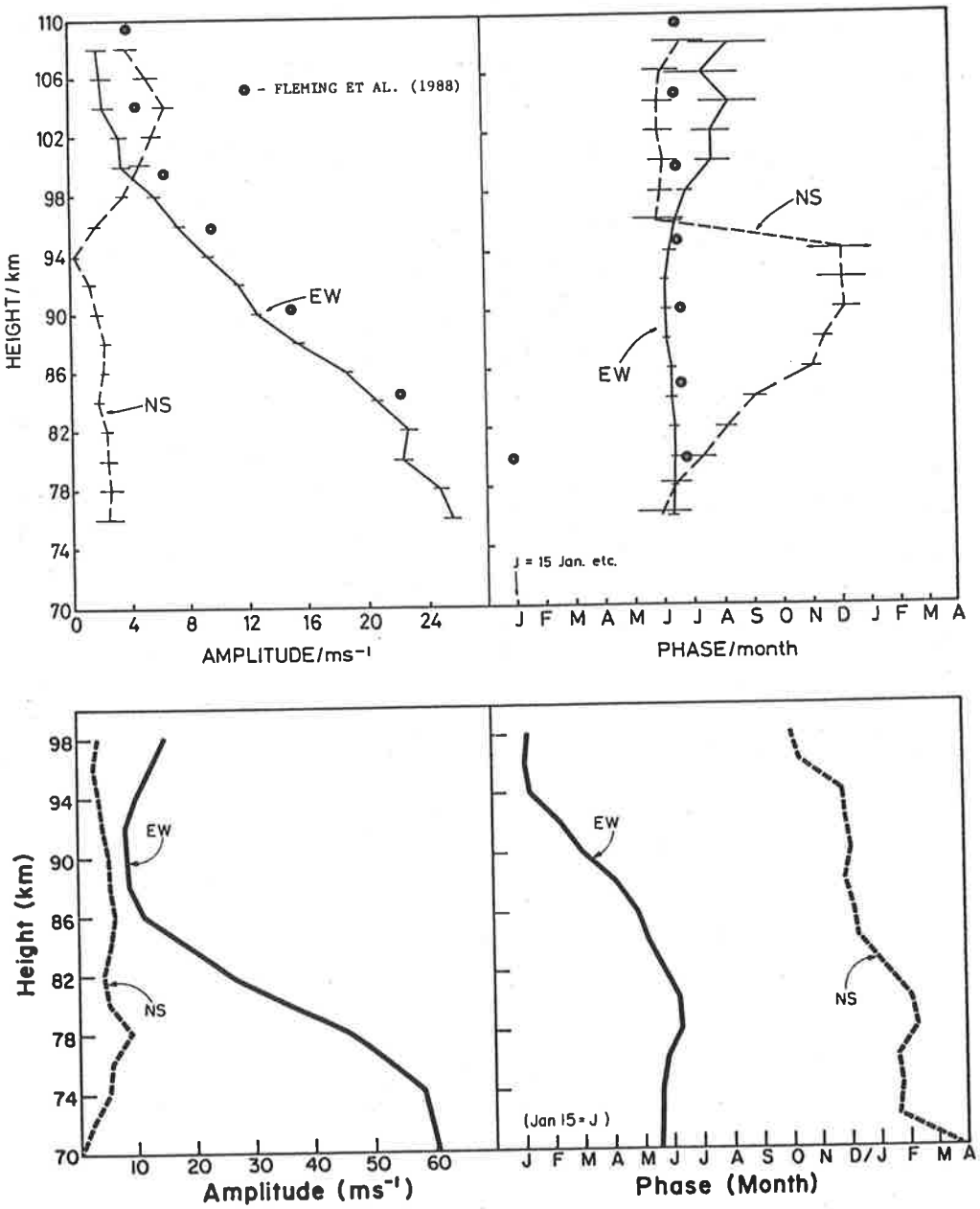

Figure 3.6: **Amplitude and phase of the annual wind oscillation as a function of height observed at Mawson (top) and Adelaide (bottom).** The Mawson figure was prepared by harmonically averaging three years of data from mid-1984–mid-1987. Note that the 'phase' is the time of maximum northward or eastward motion. The Adelaide figure was produced by R.A. Vincent and presented in Manson et al. (1985). Zonal amplitude figures from the semi-empirical model of Fleming et al. (1988) are shown for Mawson.

reproduced (for the interested reader) in figure A.3 (page 193).

Planetary Waves

The winds at Mawson and Adelaide often exhibit significant changes on a day by day basis, especially in winter. This behaviour suggests the presence of large scale travelling or quasi-stationary wave activity. In order to investigate how this activity varies as a function of season and altitude the data were band-pass filtered such that fluctuations with periods less than about 2 days and longer than about 30 days were removed. Note that the limits of the filter exclude the effects of the quasi 2-day oscillation[1] which is a well known feature of the mesopause region at Adelaide in mid-January (Craig and Elford, 1981;Plumb et al., 1987). Defining u and v as the zonal and meridional prevailing[2] wind and u' and v' as perturbations ftrom the mean, time-height contour plots of the mean square amplitudes $\overline{(u'^2 + v'^2)}$, provide a convenient measure of wave activity. Figures 3.7 and 3.8 show the mean square amplitudes at Adelaide and Mawson, respectively, for the years 1985 and 1986.

At Adelaide, most activity is concentrated in the lower mesosphere, peak values being reached near 70 km in mid-winter. A subsidiary maximum also appears in autumn (March/April) 1985. The maximum rms wind perturbation amplitudes are about 25 ms^{-1}. The planetary wave amplitudes for Mawson in figure 3.8 do not show Adelaide's prominent enhancement during winter and generally the amplitudes are smaller at heights up to 80–100 km. It is possible that wintertime amplitudes at low levels are larger than observed, but the lower equipment sensitivity at Mawson makes it more difficult to study planetary waves below 76 km, especially during the summer. Some

[1] described in detail in section 3.1.4, page 108

[2] ie. wind data smoothed by a 30-day moving average

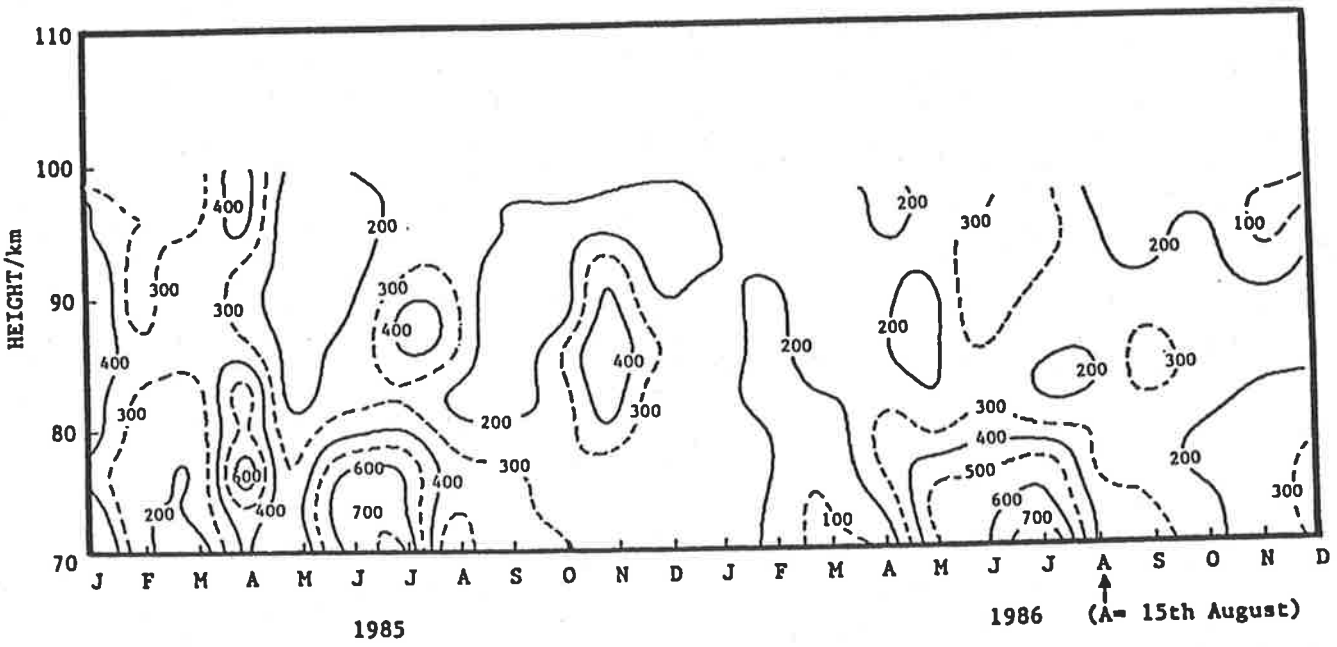

Figure 3.7: **Contours of mean square perturbations $\overline{(u'^2 + v'^2)}$ at Adelaide with 2-30 day period (m^2s^{-2}).**

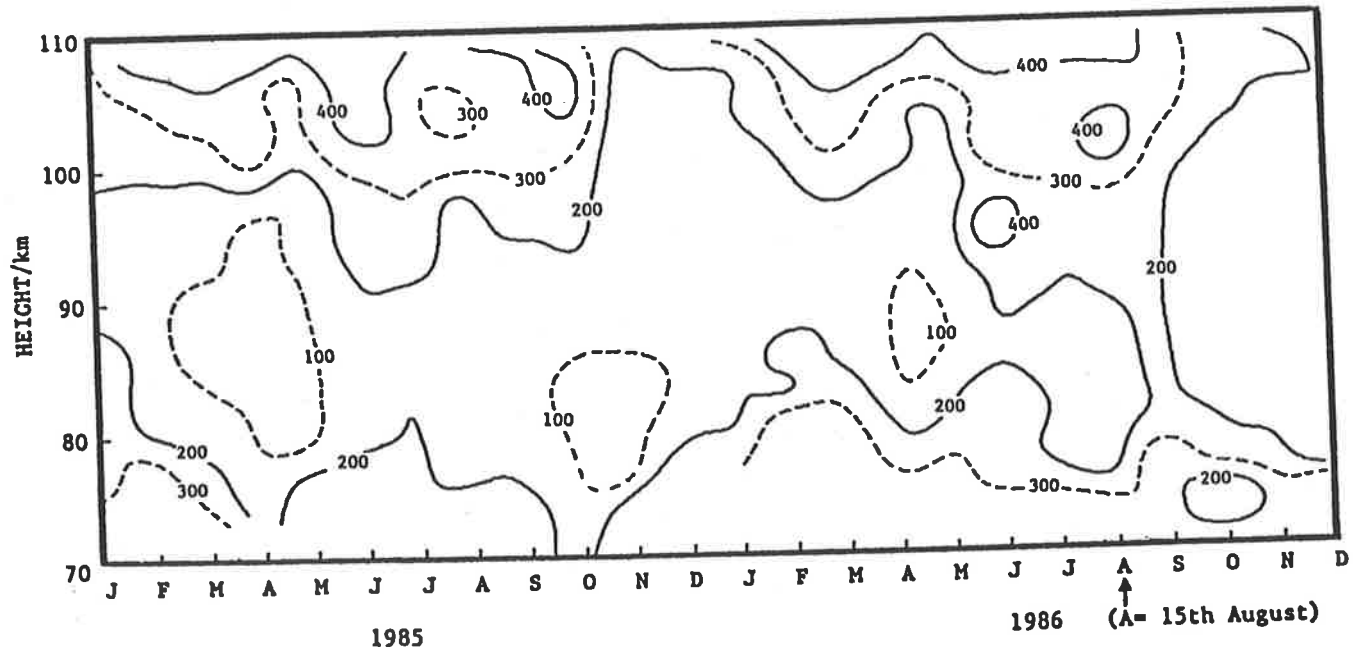

Figure 3.8: As for figure 3.7 but for **Mawson**.

interannual variability is evident, with larger amplitudes occurring in 1986 than in 1985.

Because of ionospheric differences the Mawson radar can probe 10 km higher than the Adelaide system. It is apparent from figure 3.8 that the wave amplitudes grow with altitude. It is possible that these disturbances are not associated with meteorological activity in the lower atmosphere but may be associated with auroral disturbances in the lower thermosphere. Mawson is in the auroral region and strong local heating by Joule dissipation of ionospheric currents and by particle precipitation can cause disturbances which persist for several days.

When working with daily averages of the winds, and observing the semi-regular way in which they change in response to the passage of planetary waves (for example, figure 3.3 on page 86), it is tempting to try and correlate these winds with the passage of synoptic systems, which have a similar period. It is known that high windshears associated with fronts and jet-streams at mid latitudes may generate gravity waves which propagate into the lower thermosphere (cf. Jacob and Jacka, 1985). And of course, the planetary waves generated in the troposphere do propagate into the mesosphere. Using charts published by the European Centre for Medium Range Forecast (consisting of a sea level pressure and 500 mb geopotential height chart) a comparison was made with the mesospheric disturbances. Comparisons were made with large changes in surface pressure, the passage of fronts, the presence of high or low pressure systems and windspeed/direction at the 500 mb level. In one study, two years of daily mean surface pressures (from Mawson) were cross-correlated with radar winds. To date, no significant connections have been found.

Examination of the individual fluctuations in u and v shows that at Adelaide the zonal perturbations tend to be larger by a factor of 1.5–2 on average at heights below 80-85 km, while the meridional fluctuations tend to dominate above 90 km. This does

not appear to be the case at Mawson where no component consistently dominates at any height or time. Calculation of the $\overline{u'v'}$ covariances shows that only in June/July do the zonal and meridional perturbations show significant correlation (figure 3.9). At Mawson, the $\overline{u'v'}$ covariances are small and probably not significant whereas at Adelaide they are almost invariably negative in sign. This means that usually a northward perturbation is associated with a westward perturbation and a southward perturbation with an eastward perturbation.

3.1.3 Discussion

The radar winds at Mawson (acquired between 1984-88) have been compared with earlier observations from Mawson taken during January 1981 (MacLeod and Vincent, 1985) and with SAPR radar measurements reported from Scott Base (78° S, 170° E) during December 1982 by Fraser (1984). Over this short period there is good agreement with the mean winds, especially in the magnitude and direction of the equatorward flow observed around 90 km.

With regard to northern hemisphere observations, a long sequence of wind measurements has been published by Tetenbaum et al. (1986) for Poker Flat (65° N, 147° W). Figures 3.10 and 3.11 show comparisons of the zonal and meridional winds observed at Mawson in the period 1984 to 1986 and at Poker Flat for the years 1983 to 1984 (note that the zonal winds at Mawson have been shifted by 6 months for ease of comparison). There are interesting similarities and differences. The zonal circulation exhibits reversals in February at Poker Flat, behaviour associated with minor stratospheric warmings in these years. As noted above however, the spring time reversal at Mawson is very abrupt and appears to occur a little later in spring than at Poker Flat. The summer-time winds show very similar patterns at both sites.

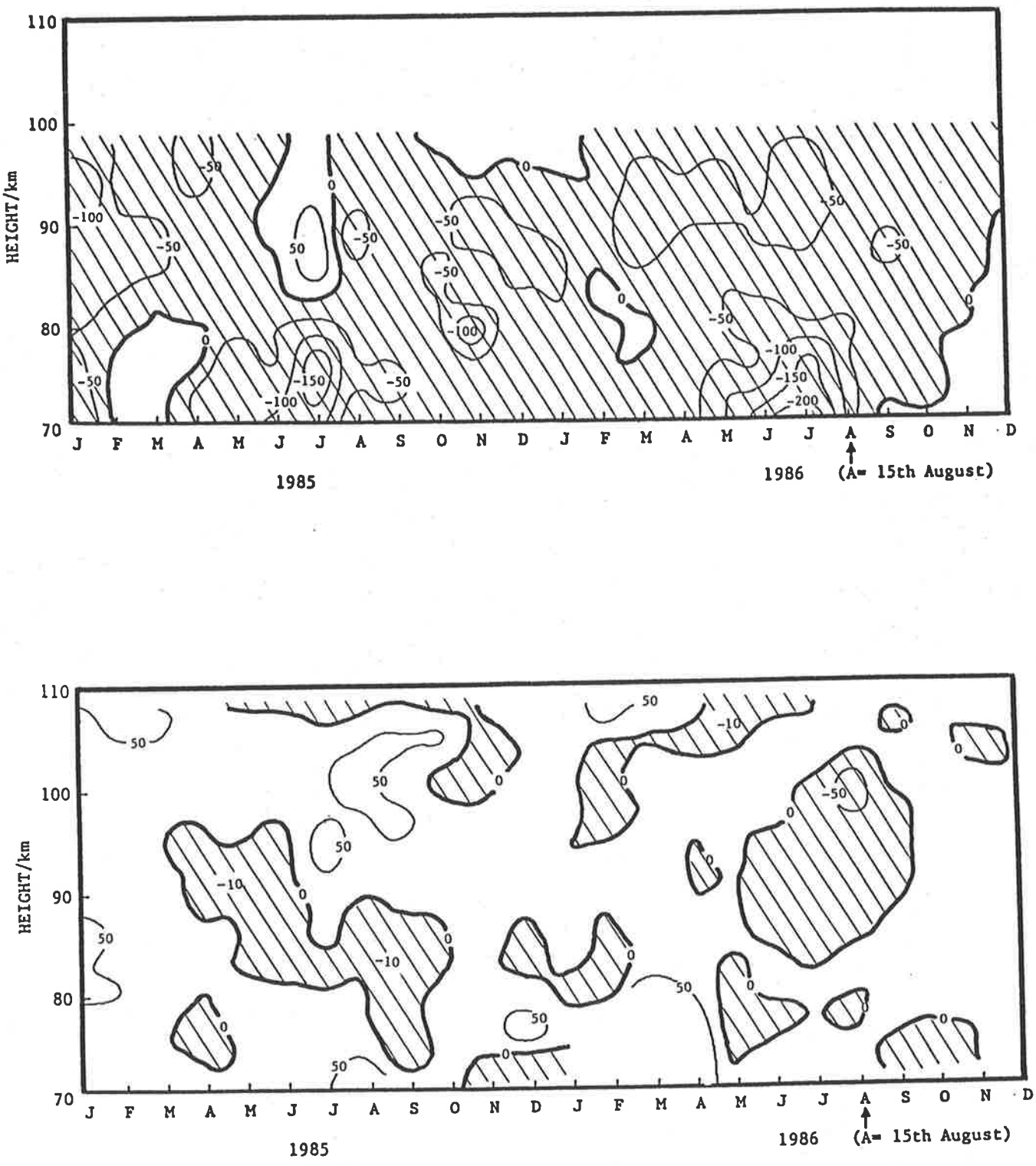

Figure 3.9: **Contours of covariance $\overline{(u'v')}$ at Adelaide (top) and Mawson (bottom)** (m^2s^{-2}). Negative values shaded.

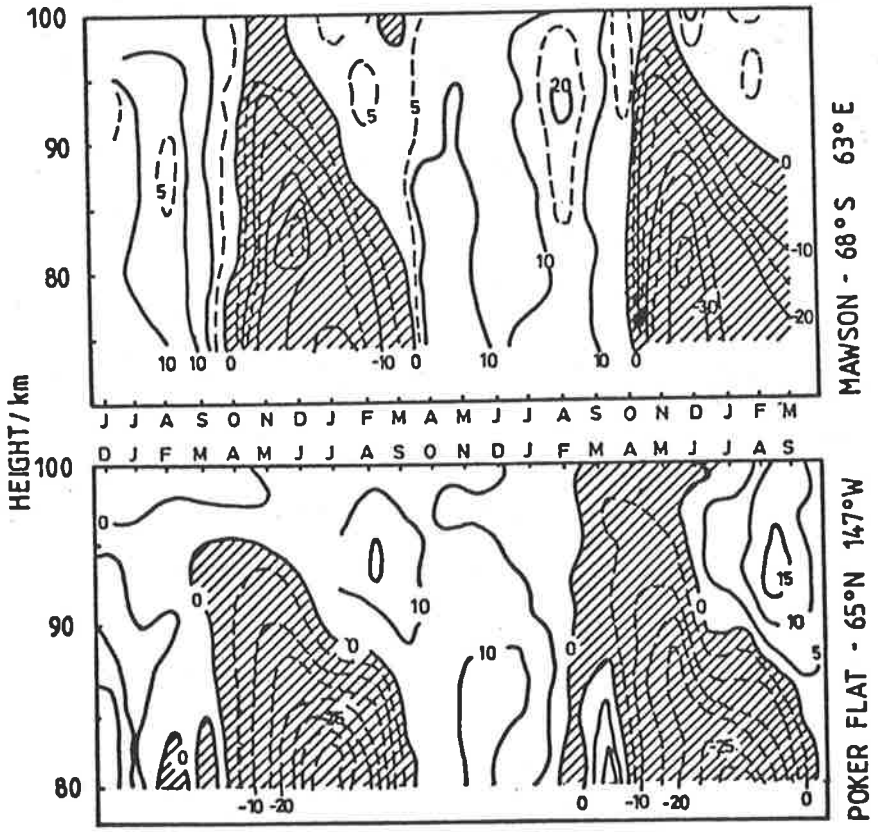

Figure 3.10: **Comparisons of zonal mean wind between Mawson and Poker Flat** (Tetenbaum et al., 1986). Mawson data extends from June 1984–March 1986 and Poker Flat from December 1982–September 1984. The timescales between the two sites have been displaced by six months so that seasons may be directly compared. Contour levels are in ms^{-1} with westward winds shaded.

Tetenbaum et al. (1986) note that the meridional winds at Poker Flat showed less year to year consistency than the zonal winds and figure 3.11 shows that significant interannual variability is also evident at Mawson in this wind component. Perhaps the most consistent feature at both locations is the weak summertime equatorwards flow which often peaks at, or just above, 90 km with peak equatorward velocities of approximately 10 ms^{-1} (see figure 3.11). Interestingly, the meridional shears are such that $\overline{v}$ becomes poleward at heights below about 85 km. Although the magnitude of the summer meridional winds are the same as the mid-latitude values, it should be noted that the Coriolis torques (given by $f\overline{v}$, where f is the Coriolis parameter) are 1.6 times larger at the high latitudes. This implies that the gravity wave body-forces, which are thought to drive the meridional circulation (e.g. Lindzen, 1981), are also correspondingly larger at 65-70° latitude (about 115 $ms^{-1}day^{-1}$ compared to 70 $ms^{-1}day^{-1}$ at 35° latitude).

Recently, satellite measurements have provided better models of the zonal circulation in the southern hemisphere middle atmosphere. The new interim CIRA (MAP Handbook, vol 16) contains estimates for mean winds in the southern hemisphere based on rocket and satellite observations collected during 1973–78, in the height range 20–80 km (Barnett and Corney, 1985). Koshelkov's (1985) southern hemisphere climatology is based on land and shipborne rocket data and also covers the range 20–80 km. Since the lowest continuous (reliable) observations of the SAPR radar at Mawson occur at approximately 75 km, these models are of limited usefulness for comparison. Fortunately, a very recent global climatology by Fleming et al. (1988) covers the height range 0–120 km. This empirically based model incorporates balloon, rocket, radar and satellite observations and includes an empirical thermospheric model for heights above 86 km. This climatology probably presents the best wind estimates currently available for the

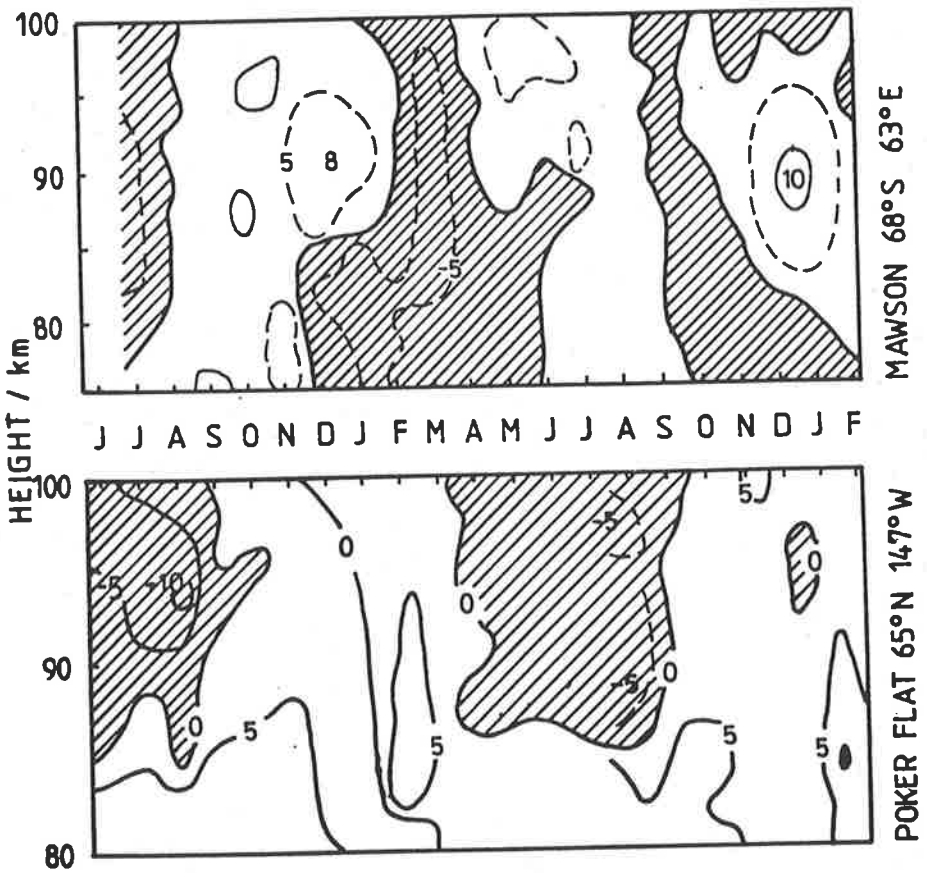

Figure 3.11: **Comparisons of meridional mean wind between Mawson and Poker Flat** (Tetenbaum et al., 1986). Mawson data extends from June 1984–February 1986. Contour levels are in ms^{-1} with southward winds shaded.

entire SAPR height range.

Figure 3.12 from Barnett (1987), is similar to that presented in MAP 16 except that it was computed (by Barnett) for the specific latitude and longitude of Mawson, and therefore incorporates the effects of travelling and quasi-stationary planetary waves (in this case wavenumbers 1 and 2 are included). The zonal and meridional winds are inferred from the model temperature profiles (based on satellite radiance measurements) via the geostrophic approximation. Comparison with the observed zonal winds (see figure 3.2, page 85) is only possible over the height range 75–85 km. In this height range there is a reasonable agreement between the model and observed winds. In particular, the timing and general structure of the seasonal changes are comparable, and show the sudden reversal during spring (from eastward to westward winds) and the more gradual reversal during autumn. However, in the model, the sudden descent of the zero-wind line (during spring) occurs in mid September, whereas it is usually observed during mid-to-late October. The position of the autumn zero-wind line in the model, is within a week of the position observed, which is quite reasonable considering the approximate two week variation in this transition. Amplitudes during the summer compare very well with both model and observations reaching a maximum of 20–25 ms^{-1} during December–January. Wintertime model amplitudes of 20–40 ms^{-1} during June–August are not observed; radar observations indicate typical wintertime eastward winds of 5–15 ms^{-1} in the height range 80–110 km.

The Barnett (1987) model meridional winds bear no apparent resemblance to the observations but this is entirely understandable given the relative weakness (normally $|v|<5\ ms^{-1}$) and considerable interannual variability of the meridional wind at Mawson. Although figure 3.5 is an average of three years of data the contours have a pseudo-random appearance and a much longer observing time will be required to establish a

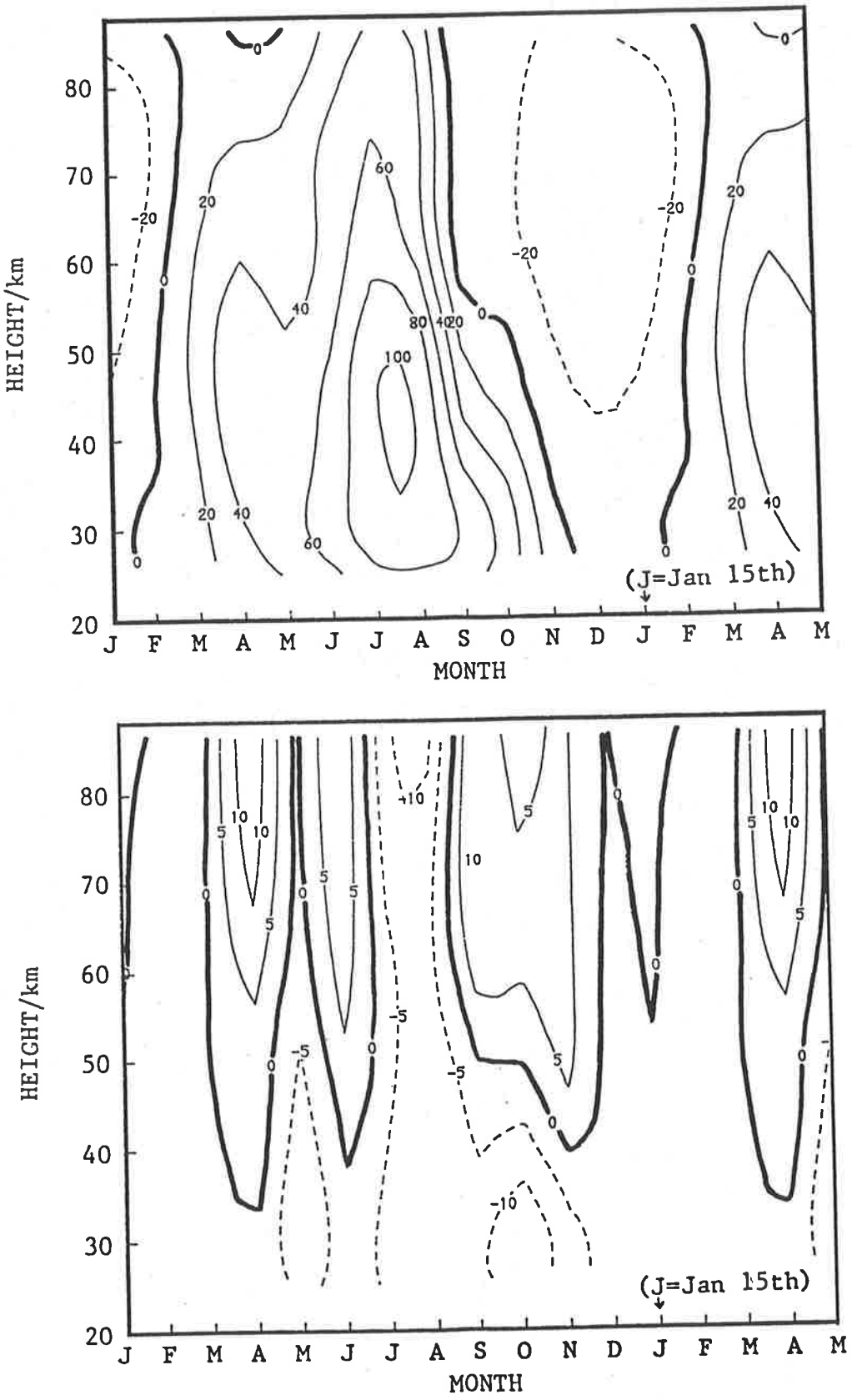

Figure 3.12: **Zonal (top) and meridional (bottom) mean winds for Mawson from the model of Barnett (1987)**, in ms^{-1}. These figures were derived from MAP Handbook 16 data using the zonal mean and wavenumbers 1 and 2 to obtain the values at the particular latitude and longitude of Mawson with the geostrophic wind approximation.

'background' state (if one exists at all). Also, the meridional winds in figure 3.12 are derived from model (satellite-based) zonal temperature variations (by the geostrophic approximation) and therefore are a function of the vagaries of planetary wave activity and gravity wave drag. However, the fact that satellite-based geostrophic winds and observed winds often differ, can lead to some interesting results. Labitzke et al. (1987) discuss the ageostrophic winds and use these to study the seasonal fluctuations in planetary wave and gravity wave drag.

For interest, the Barnett (1987) winds have also been computed for Adelaide and are shown in figure A.4 (page 194). The magnitude and seasonal changes of the zonal winds compare extremely well with figure A.5, which is derived from an average of rocket winds collected at Woomera (31° S,137° E) during 1962–72.

The model of Fleming et al. (1988) is probably the most comprehensive available which covers the entire SAPR observing range. The zonally averaged mean zonal winds from this semi-empirical model are presented in figure 3.13. Broadly speaking, the model correctly estimates the general features of the observations (note that figure 3.13 and the three-year mean zonal winds (in figure 3.2, page 85) are drawn on identical axes). However, closer inspection reveals some important differences. As was the case with the Barnett (1987) model, the model summer winds (October–March) in the height range 70–90 km are in excellent agreement with the Mawson observations but the wintertime winds (over virtually the entire height range) are 2–3 times larger than those observed. Given that the contours in the model winds were drawn from monthly averages, the agreement of the zero-wind lines is good. However, the 15 ms^{-1} 'jets' which occur in the model at 95–105 km during October–November and March have not been observed during 1984–87. In fact, over this height range, at these times, the winds are normally weak and sometimes westwards ($\mid v \mid < 5$ ms^{-1}). The model winds show a sudden

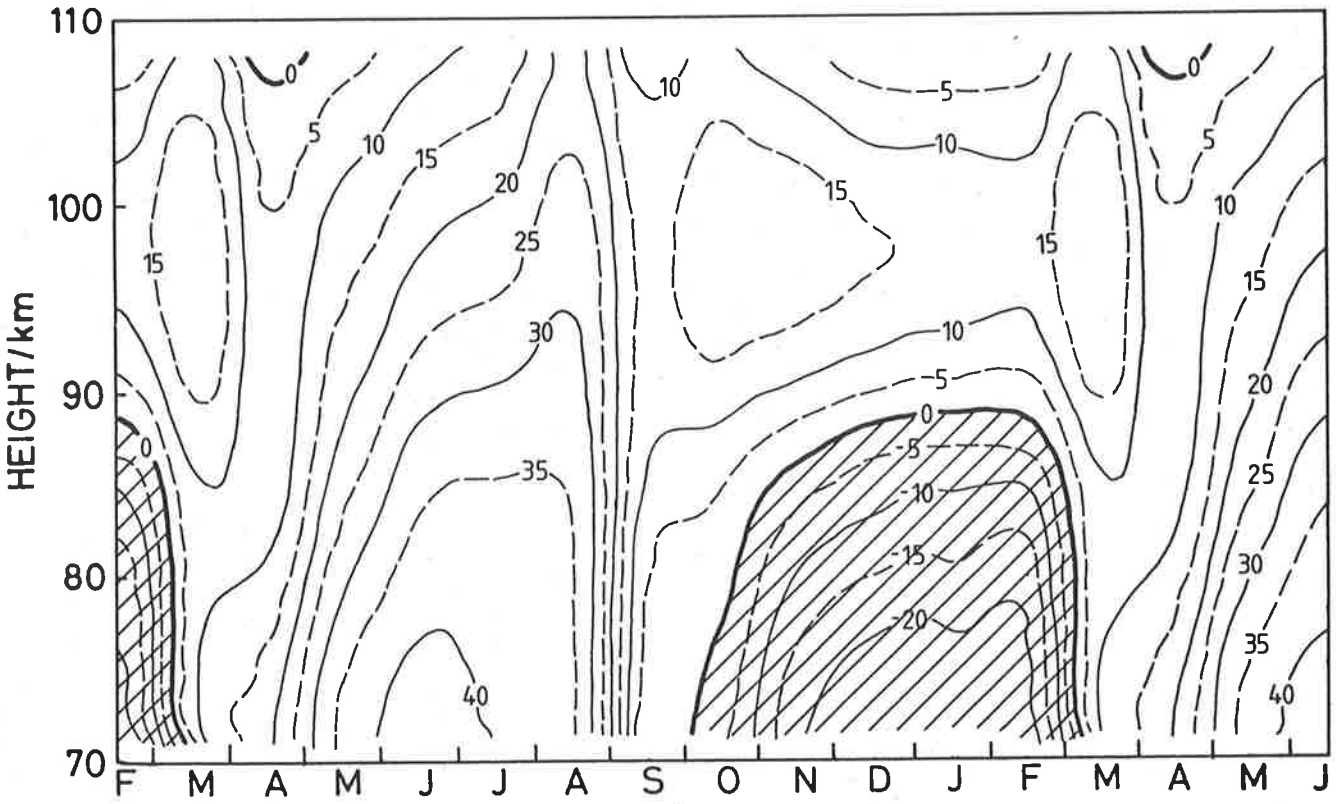

Figure 3.13: **Contours of zonal mean winds from the model of Fleming et al. (1988) for 70°S.** Contours are in ms^{-1} and regions of westward (or negative) flow are denoted by shading.

deceleration during late August through to early September, whereas observations suggest that the deceleration is greatest during mid-October. However, in figure 3.13, the contours were drawn around data points derived as monthly means. This may slightly distort the spacing of the contours and it is likely, for instance, that the deceleration during late August–early October, is much more realistic than that shown.

Koshelkov (1985) has made an extensive collection of more directly measured (rocket) winds and temperatures in the southern hemisphere which have provided the base for a specific southern hemisphere model. Groves (1985) combined both rocket and satellite temperature observations to generate winds using the geostrophic equation. Like Bar-

Table 3.1: **Comparison of monthly mean zonal winds (ms^{-1}) at a height of 80 km observed at Mawson (M)** with model results from Fleming et al (1988) (F), Barnett and Corney (1985)(B), Groves (1985)(G) and Koshelkov (1985)(K). The last column (RMS) is the rms value of monthly difference between the model and radar winds.

	J	F	M	A	M	J	J	A	S	O	N	D	RMS
M	-20	-14	-10	10	10	10	10	10	10	4	-20	-21	
F	-15	-18	9	10	29	38	36	35	4	2	-9	-13	14
B	-15	-16	10	10	31	41	40	38	10	3	-10	-20	17
G	-22	-4	11	11	31	46	47	52	21	4	-12	-23	22
K	-29	-26	-17	0	12	4	14	13	5	-9	-30	-36	9

nett and Corney (1985) and Barnett (1987), these models have upper limits at about 80 km so that they only partly overlap the radar winds discussed here.

Table 3.1 compares the model zonal winds and the Mawson winds at a height of 80 km. Agreement with the models is better for Adelaide than for Mawson, where the differences are especially significant in winter.

These comparisons must however, be treated with some caution because the model winds are zonal means whereas the radar observations are confined to a single location and were made in a later epoch than the satellite measurements. However, it is clear that, while the model and radar winds agree well for most of the year, the models show larger eastward winds in mid-winter (especially at the latitude of Mawson). While it is possible that some other (as yet unresolved) factor may be causing the radars to slightly underestimate the winds, it seems that it must operate only in mid-winter since there is good agreement at other times of the year. Furthermore, it is not due to the radars being incapable of measuring large wind speeds since it is not uncommon for zonal wind speeds in excess of 50 ms^{-1} to be measured for several hours at a time

at Mawson during the passage of planetary waves. It is interesting to note that the amplitude of the annual zonal oscillation in Fleming et al. (1988) agrees very well with the observations (cf. figure 3.6, page 92) but the annual mean (zonally averaged) zonal winds are consistently biased 10–20 ms^{-1} eastward of the observations.

Labitzke et al. (1987), using 4 years of satellite observations, compared the derived geostrophic winds with those from the MF radar at Saskatoon (52° N,107° W). This study, like our own, suffered the disadvantage that the techniques overlapped only in the height range 78–80 km. As with the results from Adelaide and Mawson, they found good agreement in the summer but significant ageostrophic motion was observed in the autumn and winter. Interestingly though, the disagreements at Saskatoon were generally because the radar winds were *stronger* than the geostrophic winds. This contrasts with Adelaide and Mawson where the radar winds are significantly weaker than the Barnett and Corney (1985) winds (especially at Mawson). Possible explanations for the discrepancy between the observations are gravity wave induced drag or gravity wave interaction with planetary waves (Miyahara, 1985). This may assist in explaining the weaker winds at Mawson, but not the larger winds at Saskatoon.

When considering the mismatch between the models of Barnett and Corney (1985), Barnett (1987), Groves (1985) and Fleming et al. (1988) it is noteworthy that the common characteristic of these models is that the winds are derived by applying the geostrophic approximation to the rocket and satellite measured temperatures and radiances. Recently, Boville (1987), for example, has pointed out that the geostrophic winds can significantly exceed the true winds in the winter upper stratosphere because of curvature of the streamlines due largely to the presence of waves. It is possible therefore that the radar and model wind differences which are apparent in mid-winter are caused by overestimated model winds; as noted in section 3.1.2, it is in this period that

the planetary waves in the lower mesosphere attain their largest amplitudes at Adelaide, so that the flow curvature will be largest, at least locally. Koshelkov (1986) also finds marked discrepancies between the geostrophic and actual wind patterns, and in particular with the wintertime eastward winds in the 80–90 km height range. Clearly geostrophic winds do not accurately model the actual winds but as Labitzke et al. (1987) point out, the discrepancies are a useful indicator of atmospheric processes.

In addition to problems with application of the geostrophic approximation, the errors in base-level meteorological data, from which satellite-derived data are extrapolated, may lead to significant error in satellite based wind models. Grose and O'Neill (1989) recommend "....it is prudent to advise caution in drawing inferences, particularly quantative ones, from meteorological fields derived from satellite data. Such counsel is certainly apt for the southern hemisphere where coverage of data from sources other than satellites is limited."

The large planetary wave activity which is observed in June/July at Adelaide is consistent with the analysis of the circulation of the upper stratosphere in the southern hemisphere by Hartmann (1976) and Hirota et al. (1983). They found that transient planetary waves of wavenumber 2 and periods of the order 10 days exhibit a change in their location during winter, following the latitudinal march of the core of the stratospheric eastwards jet which attains its most equatorward position near 40° S in June and July. The upper limit of these observations was near 50 km in altitude, so considering the data of figure 3.7, it appears that the wave amplitudes maximize at some height below 70 km. The rapid decrease in wave amplitude with height between 70 and 80 km is probably due to gravity wave drag effects (Miyahara, 1985). The negative $\overline{u'v'}$ fluxes (figure 3.9) are also consistent with what is known about the planetary waves since they correspond to an equatorward Eliassen-Palm flux (proportional to $-\overline{u'v'}$) which

is characteristic of waves in the southern hemisphere mid-winter (Shiotani and Hirota, 1985). In their height-latitude analysis of the variations of the zonal wind and wave activity with time, Shiotani and Hirota (1985) showed that in late winter the jet shifts poleward and downward and that quasi-stationary wavenumber 1 activity is enhanced. Improvements in the sensitivity of the Mawson radar are required to study winds and waves at heights below 75-80 km.

3.1.4 The quasi 2-day wave at Mawson and Adelaide

The present study draws mainly on data collected at Adelaide and Mawson during the SH summer months of December, January and February for the years 1985–86 and 1986–87. For the purposes of the present analysis, the winds were averaged over the height range 87.5–97.5 km in order to minimize errors and reduce the number of record gaps. This should have little effect on the 2-day wave because of its large vertical wavelength, but it may have reduced the tidal amplitudes. Also, one hour averages were formed in Universal Time (U.T.), and are used throughout the present analysis.

Although the wave is present for most of the summer months (and may have a few 'bursts' of activity lasting for a few cycles) it usually reaches maximum amplitude during the latter part of January, whereupon it may abruptly diminish (as was the case in 1987). Maximum amplitudes in excess of 40 ms^{-1} are often observed in the meridional wind component at Adelaide. Figure 3.14 shows that the amplitude structure is similar at the two sites but the amplitude at Mawson is approximately 0.3 of the amplitude at Adelaide. Note that in Figure 3.14 occasional gaps in the wind data were filled (to avoid spurious 'ringing' in the filtered data) by taking an average of the wind 48 h before and after the missing data point. While it may be argued that this process could introduce a fictitious 48 h component, it is acceptable in this case as the true frequency is very

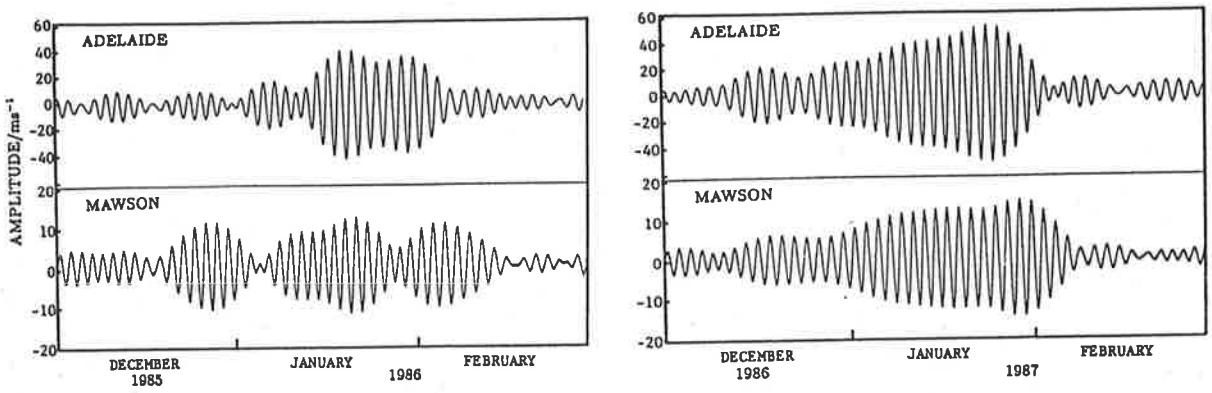

Figure 3.14: **Comparison of the meridional components of the wind at Adelaide and Mawson during December–January 1985–86 (left) and 1986–87 (right). Wind data have been band-pass filtered by a square filter of period range 1.8–2.2 days.**

close to 48 h, and the data gaps very few.

Figure 3.15 shows *amplitude* spectra for the last two weeks of January in 1986 and 1987, when the 2-day wave amplitude is a maximum. These diagrams have been arranged to allow comparison of spectral amplitudes between the zonal and meridional wind components of the 2-day wave at each station. At Adelaide the amplitude of the meridional component averaged 33 ms^{-1} in 1986 and 45 ms^{-1} in 1987, with the zonal components approximately 0.3 and 0.5 (respectively) of the meridional. At Mawson, the meridional amplitudes for the two years were both about 12 ms^{-1}, with the zonal amplitudes approximately 0.25 of the meridional in 1986 and 0.9 of the meridional in 1987. During the last two weeks of January 1985 (not shown in Figure 3.15) the component amplitudes at Mawson were again comparable and averaged 10 ms^{-1} for the meridional component and 8 ms^{-1} for the zonal.

The geographic separation of Mawson and Adelaide is 33° in latitude and 75° 35′ in longitude. If the 2-day wave is assumed to be due to a westward travelling wave of zonal wavenumber 3, and assuming there is no phase change with latitude, the 2-day

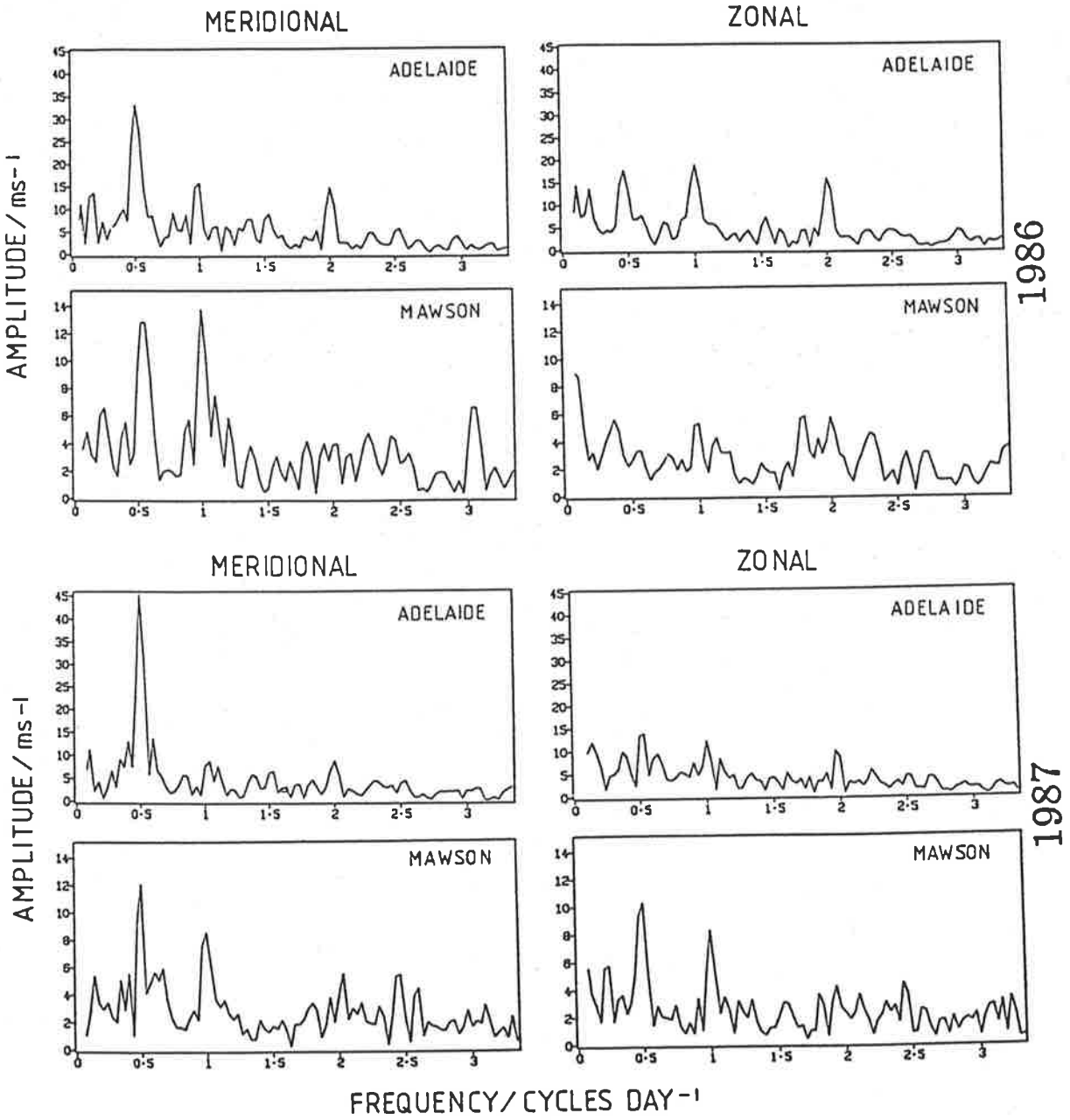

Figure 3.15: **Spectra for the mean wind components (87.5-97.5 km) for the periods January 15-26 1986 (top) and January 15-31 1987 (bottom)** – note that the amplitude scale at Mawson has been expanded by three times. The ordinates of the amplitude spectra have dimensions of $ms^{-1}Hz^{-1}$. However, in these diagrams, they have been multiplied by a normalizing constant (with dimensions of Hz) in such a way that a sinusoid of amplitude A occupying the entire record length will appear in the spectrum as a 'line' of peak height A ms^{-1}, and the spectra may be used to estimate the amplitudes of any purely sinusoidal components which are present in the records analysed.

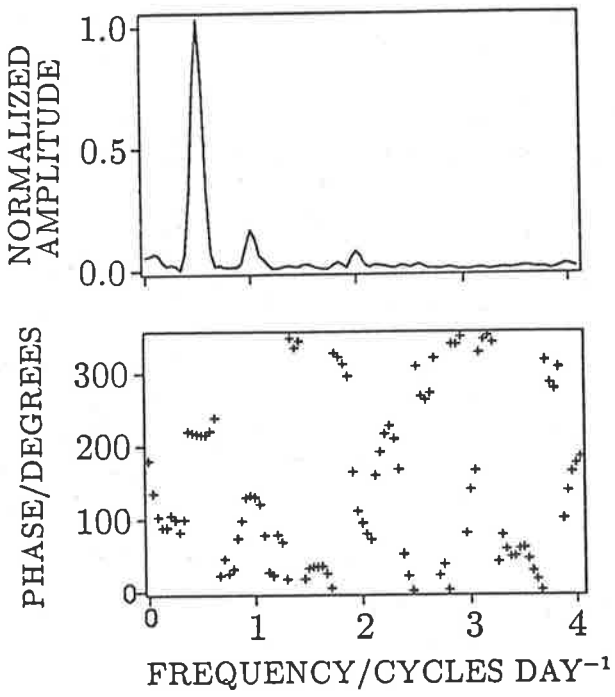

Figure 3.16: **Normalized cross-spectrum of the meridional wind component (averaged over the height range 87.5–97.5 km) between Adelaide and Mawson during January 1987.** The *Phase* is the number of degrees by which Mawson lags Adelaide.

wave at Mawson should lag that at Adelaide by 30.23 h. In order to estimate the actual time differences between the stations, cross-spectral techniques were employed. Figure 3.16 shows a normalized cross-spectrum between the meridional winds at Adelaide and Mawson for January 1-31 1987. The spectrum has been smoothed with a window of 0.2 cycles day^{-1} to show trends in phase difference. At the 2-day period the phase difference is approximately 215° or 28.6 h. While the 2-day wave dominates the diurnal and semidiurnal tides over this period, in this diagram the tides may be underestimated due to height-averaging of the data.

Table 3.2 shows the apparent phase lag between the stations for several independent periods during 1986 and 1987. These estimates were determined by computing a cross-spectrum for the interval and measuring the phase at a frequency of $\frac{1}{2}$ cycle day^{-1}. Given variations in the quality of the data, it is difficult to create a reliable error estimate for

Table 3.2: **Phase relationship of 2-day wave components between Mawson and Adelaide. Universal time has been used and figures shown are the number of hours by which Mawson lags Adelaide.**

Interval	Zonal	Meridional
January 17-22 1986	17.8	21.5
January 1-8 1987	22.3	24.2
January 9-16 1987	26.9	26.5
January 17-22 1987	19.6	24.8
January 23-31 1987	32.0	32.3
average	24±8	26±6
January 1-31 1986	18.7	21.1
January 1-31 1987	24.6	28.6

the cross-spectral phase. Therefore phase differences from several independent periods are presented to demonstrate any trends. Intervals were chosen to be at times when the 2-day wave was large (see Figure 3.14). Over these periods the phase of the meridional wind component at Mawson lags that at Adelaide by approximately 26±6 h (150°–240°), and the zonal by 24±8 h (120°–240°).

Figure 3.17 shows a cross-spectrum of the wind components at Mawson. Note that phase is approximately 90° at the $\frac{1}{2}$,1,2,$\frac{5}{2}$ and 3 cycle day^{-1} frequencies (where significant peaks in amplitude occur). Table 3.3 shows the phase relationship of the zonal and meridional wind components of the 2-day wave between each station. These figures were obtained by taking the cross-spectrum of the wind components and measuring the phase at a frequency of $\frac{1}{2}$ cycle day^{-1} and, as with table 3.2, several independent periods are presented. In the SH, the circular polarization of vertically propagating atmospheric

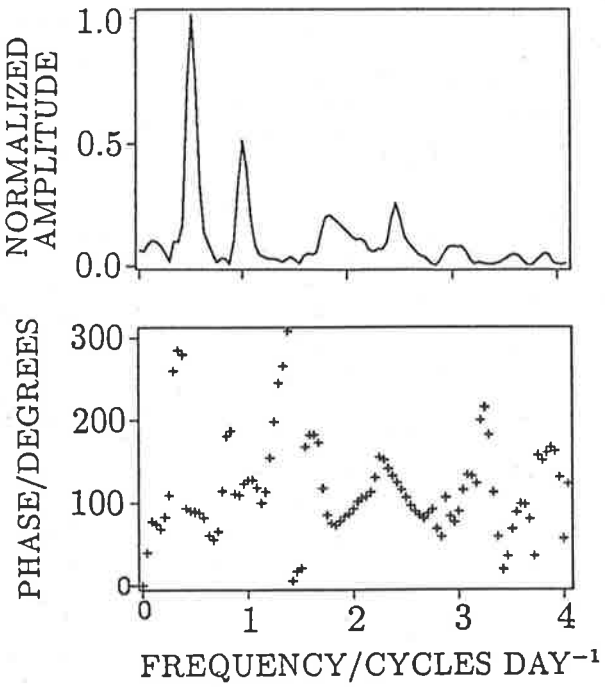

Figure 3.17: **Normalized cross-spectrum of the meridional and zonal wind components (averaged over the height range 87.5–97.5 km) for Mawson during January 1987.**

tides and long-period waves is normally anticlockwise (ie. the zonal leads meridional by approximately 90°) and therefore it may be expected that for the 2-day wave the zonal component will lead the meridional by 12 h. Phase relationships between the 2-day wind components given in table 3.3 show that generally this is the case. However it is interesting to note that at Mawson the phase difference of the components of the 2-day winds is usually close to 90° and at Adelaide often closer to 45° (previous data from Adelaide gave phase differences in the range 6–12 h (Craig et al., 1980).

Figure 3.18 shows the phase relationship of the [filtered] meridional winds at Mawson and Adelaide during January 1987. The average period of oscillation during this period is 47±1 h at Adelaide, and 48±1 h at Mawson. Due to this slight difference in frequency, the two oscillations are approximately in antiphase at the beginning of the month and in quadrature toward the end. While it is clear that the two stations do not have a

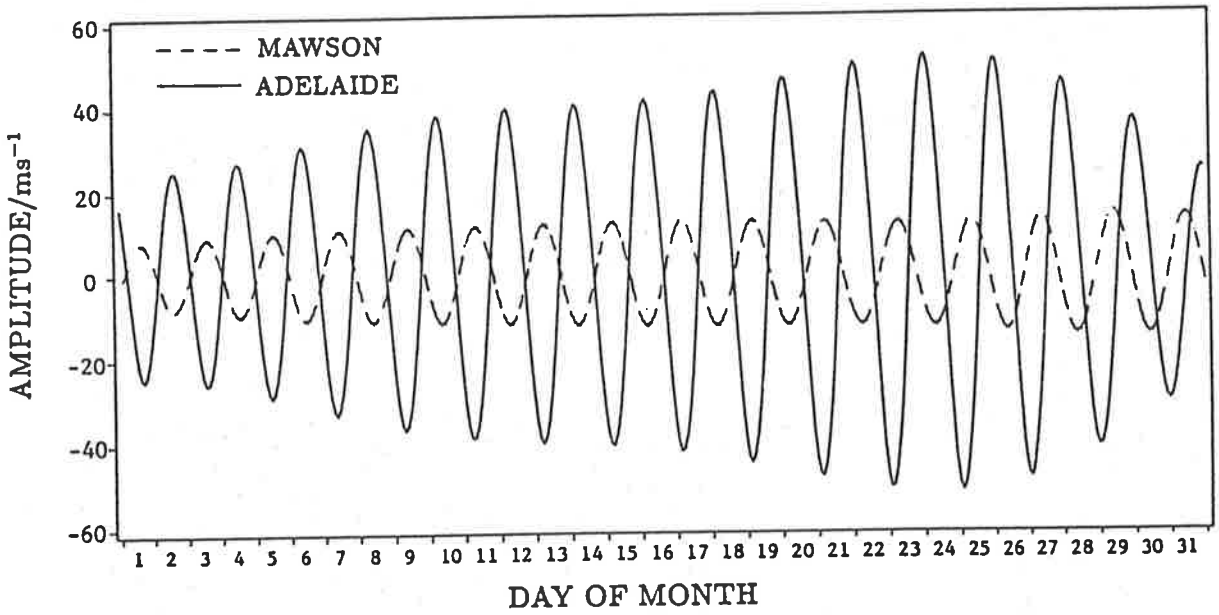

Figure 3.18: **Comparison of the meridional component of the 2-day oscillation between Mawson and Adelaide during January 1987 (an expanded section of figure 3.14).** Wind data have been filtered by a square band-pass of period range 1.8–2.2 days.

constant phase relationship, other observations (e.g. Table 3.2) indicate that the phase usually remains within the range of that shown in Figure 3.18.

Use of data for individual heights shows that, within the height range being sampled (80–100 km), amplitudes at both stations maximize at 92±6 km with no measurable vertical phase variation (although, within the errors of these measurements, vertical wavelengths >60 km may well exist). Craig et al.,(1983) find vertical wavelengths of 50±10 km at low latitude (ie. Townsville - 19°S) but wavelengths >100 km are usual at Adelaide and are also consistent with the present observations at Mawson.

3.1.5 Discussion

During all summers (from mid-1984 to the present) 2-day wind oscillations have been measured at Mawson with typical amplitudes (during January) of 10–15 ms^{-1}, and reaching a maximum in late January. The simultaneous onset and development of

Table 3.3: **Phase relationship of 2-day wave wind components.** Figures show the number of hours by which the zonal leads the meridional component.

Interval	Mawson	Adelaide
January 17-22 1986	11.0	6.9
January 1-8 1987	10.0	8.2
January 9-16 1987	7.9	3.4
January 17-22 1987	10.8	5.3
January 23-31 1987	13.0	12.1
average	11±2	7±4
January 1-31 1986	10.0	5.7
January 1-31 1987	11.9	7.9

the 2-day disturbance at Mawson and Adelaide suggests that the wave is global and persistent to high southern latitudes.

In the northern hemisphere, the 2-day wave is also observed at fairly high latitude. A study by meteor winds at Garchy, France (49°N) and Obninsk, U.S.S.R. (55°N) (Glass et al. 1975) showed 51 h-period oscillations of 13 ms^{-1} (at both sites) which persisted for two weeks in July/August. This amplitude compares well with Mawson, but Carter and Balsley (1982) observe only weak 2-day winds with the meteor radar at Poker Flat (65°N, compared with 67°S at Mawson). Although more quantative data is required, a weaker 2-day wave in the high-latitude NH is consistent with the generally weaker 2-day wave amplitudes observed at mid-latitudes in that hemisphere (Craig and Elford, 1981; Vincent,1984).

At Adelaide the disturbance is predominantly meridional with the zonal amplitudes approximately 0.3 of the meridional. During 1985 and 1987 wind component amplitudes

at Mawson were comparable but in 1986 the meridional strongly dominated. In 1985 and 1987 the meridional amplitudes were still slightly stronger (10–15%) but further data will be required positively to establish a trend.

Using satellite observations of the stratosphere (40±20 km), Rogers and Prata (1981) found a 2-day-period temperature perturbation maximum (of 0.6K) at 20°S. The perturbations become immeasurable outside the latitude range 20°N–50°S which is interesting, as mesospheric wind observations from Mawson showed that the 2-day winds occur with significant amplitude at higher latitudes than these satellite observations would suggest.

Earlier studies by pairs of similar-latitude stations show good agreement with the theory of a wave travelling westward at approximately 60° longitude per day (Craig et al., 1980). The phase differences of the wind components between Adelaide and Mawson are 24±8 h for the zonal and 26±6 h for the meridional (cf. Table 3.2). These are less than the 30.23 h which would have been expected if the wave was of precisely 2-day period and the stations were of comparable latitude. This suggests that the phase may have changed by around 5 h (≈40°) over the 33° latitude separation between the stations. Salby (1981) has modelled the amplitude and phase structure for the 2-day wave at 'midsummer' (ie. using a wind model which draws no distinction between the hemispheres) but only up to 12 scale heights (84.5 km - CIRA 1988). At this level, there is 65±20° (4.3 h) phase difference between the waves at the latitudes of Mawson and Adelaide, but it is not clear [from Salby, 1981] which location leads or lags. It is probable that there is a phase variation with latitude and this may account for Mawson's approximate 5 h phase lead (ie. Mawson is approximately 5 hours 'early') seen in both the zonal and meridional wind components. However, because the phase relation is not fixed, times can be found when the phase difference is very close to the 30.23 hours which would be expected for similar latitude stations (eg. January 23–31, 1987).

This variable phase relationship also suggests that the global structure of the wave region may be changing, with the mid and high-latitude parts of the wave propagating at different velocities (in this case, assuming that wave velocity is related to observed frequency, the mid-latitude part of the wave is propagating faster). Similar behaviour has also been observed between mid-NH and low-latitude SH parts of the wave. For example, simultaneous observations at Sheffield (53°N) and Townsville (19°S) by Craig et al. (1983) gave periods of 51±1 h at Townsville and 49±1 h at Sheffield. Also meteor radar observations from Kyoto (Tsuda et al. 1988) showed that the period of the 2-day wave may vary from 2.1–2.5 days during summer and may become 2 days during the autumn. These changes were tentatively correlated with the disappearance of eastward mean winds at around 95 km, which may be related to changes in zonal circulation at a lower level. Considerably improved satellite observations or an array of radars will be required to fully resolve the latitude and time-dependent amplitude and phase structure of the mesospheric 2-day wave.

3.2 Atmospheric Tides

3.2.1 Introduction

This section presents observations of the tidal winds from Mawson, Antarctica, acquired at various times during 1984–87. The diurnal and semidiurnal tides are discussed separately and these are compared with results from the northern hemisphere (from Poker Flat, 65° N) and with the tidal wind models of Vial (1986, 1988) and Forbes and Hagan (1982, 1988).

Figure 3.19 is presented to demonstrate the comparable magnitude of the tides and mean winds (in the height range 70–110 km) observed at Mawson and Adelaide. In

this diagram, individual vectors represent monthly averages of the winds over intervals of 2 km of height and 1 h of local time. (Figure 3.19 groups together the autumn months; similar diagrams for summer, winter and spring are presented in appendix A.4 on pages 197–199). The mean wind circulations described in section 1.1 are clearly displayed and Adelaide's prominent diurnal tide is clearly visible with the diagonal patterns of arrows indicating downward phase propagation. At Mawson, a diurnal tide cannot be detected by eye but closer inspection shows a propagating semidiurnal tide (especially conspicuous during May). This figure also demonstrates the different observing conditions at Mawson and Adelaide. At Adelaide, prevailing ionospheric conditions do not normally permit observations below 80 km by night, and data is not collected at heights above 100 km. However, at Mawson, ionized particle precipitation (and other phenomena) permit 24 h observation at lower levels although data-acquisition rates below 80 km are normally very low (especially during the summer).

In the following sections, several graphs of long-term tidal averages (ie. a month or greater) are presented. These figures have been produced by placing the wind data into month-long data-sets and conducting an harmonic analysis. Since it is unlikely that the phase of a tide will remain constant over a month, amplitude figures presented may well be smaller than those from shorter-period observations. Because of ambiguities which can be produced in this way, there are a number of conflicting views on how long-term tidal averages should be determined. Throughout this work averages for intervals greater than one month are formed by taking the vector average of the monthly means.

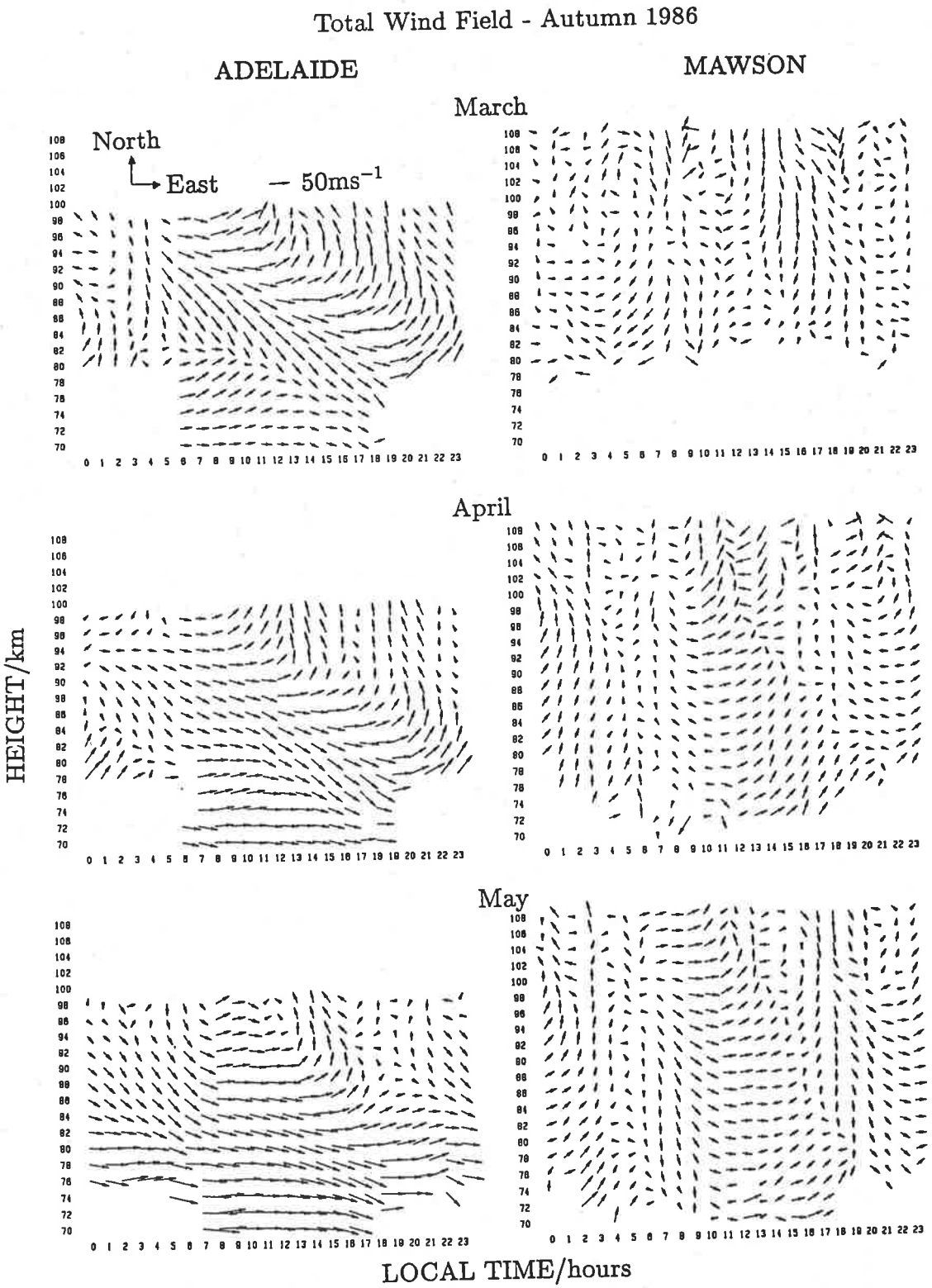

Figure 3.19: **Hourly mean winds measured at Adelaide (35° S) and Mawson (67° S).**Winds are averaged for the **autumn months** of 1986. Note that wind values plotted at **12** h (for example) on the time axis, are the averages taken between 12:00-13:00 h local time. Similar diagrams for the summer, winter and spring seasons are presented in appendix A.4, pages 197–199

3.2.2 The diurnal tide

Observations at Mawson

Figures 3.20 and 3.21 present the mean behaviour, as a function of height, of the amplitude and phase of the diurnal tide at Mawson. These data from 1985 have been analysed into summer, winter and equinox 'seasons' and in addition, an annual average ($\overline{1985}$) has been computed. Unlike the mean wind, the amplitudes of the meridional components of the tides (both diurnal and semidiurnal) at Mawson are usually greater than those of the zonal components. This effect is demonstrated in figure 3.20 where the annual average meridional amplitudes (above 90 km) are approximately twice as large as the zonal amplitudes. The equinoctial and winter amplitudes are comparable with the annual average, but during the summer, the amplitudes of both components are 30–50% greater than the average.

In the height range between 75 and 90 km amplitudes are generally small ($<5 ms^{-1}$) except in summertime when the amplitude of the zonal component is 4–5ms^{-1} and the meridional component is 7–10ms^{-1}. Above about 90 km (during all seasons) the amplitudes show an approximately linear increase with height. The maximum amplitude values occur at the top of the observing range (108 km) and are (during all seasons) $15\pm2 ms^{-1}$ for the meridional and $7\pm2 ms^{-1}$ for the zonal component. Figure A.9 (in appendix A.4, page 200) shows the diurnal amplitudes during the solstitial months of June and December and these are very similar to the seasonally averaged summer and winter plots in figure 3.20. The diurnal tidal amplitudes at Mawson show only small and gradual changes with season.

The vertically oriented phase profiles of the diurnal tide (figure 3.21) suggest the presence of purely evanescent tidal modes, as expected at high latitudes (see the Hough

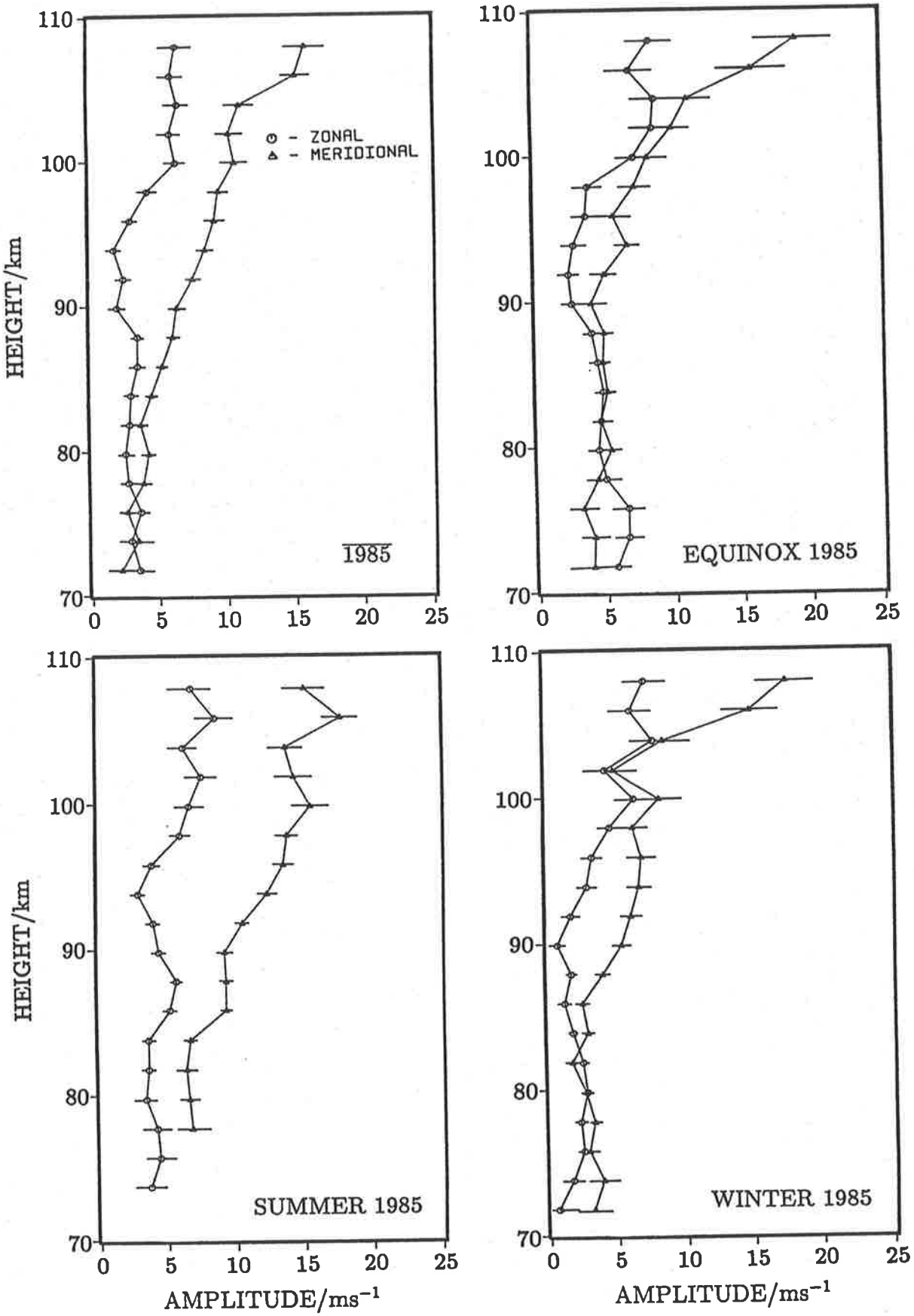

Figure 3.20: **Amplitude of the diurnal tidal component of the wind at Mawson** averaged over a whole year ($\overline{1985}$) and by season. (Summer = Nov, Dec, Jan, Feb; winter = May, Jun, Jul, Aug; Equinox = Mar, Apr, Sep, Oct)

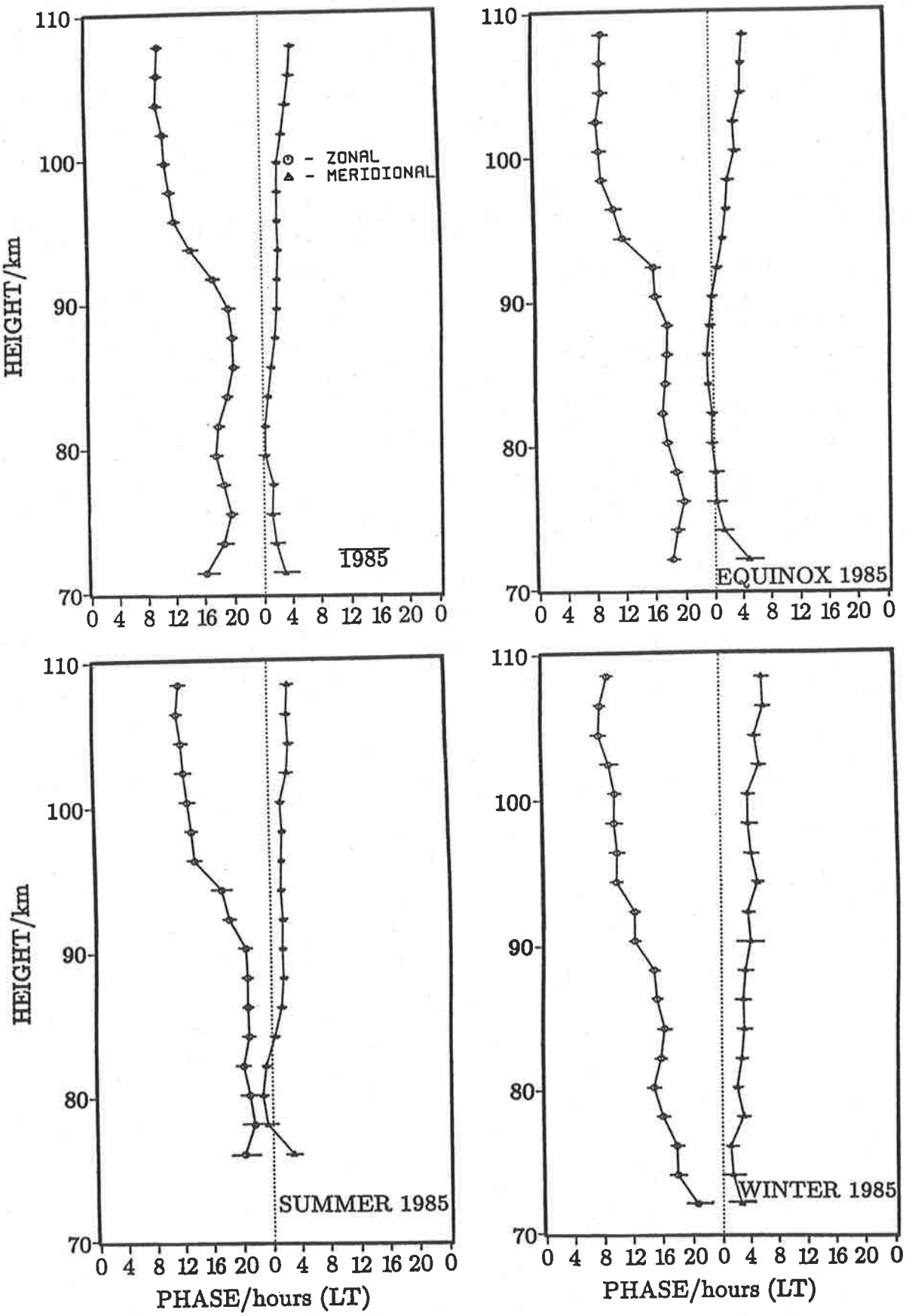

Figure 3.21: **Phase of the diurnal tide at Mawson** - details as for figure 3.20.

functions of the diurnal tide figure 1.5 on page 17). That statement applies particularly to the meridional phase profiles which are almost constant with height and throughout the year; however the zonal phase profiles typically undergo a smooth change of 6-8 h between 85-95 km with an earlier phase occurring at greater heights. This may be due to mode superposition or reflection, but it is interesting to note that above 100 km, not only is the meridional phase slope positive (ie.the time at which the maximum wind occurs advances with increasing height) but the phase of the meridional component leads that of the zonal component by approximately 6 h, indicating *clockwise* rotation of the wind vector. Between 80-90 km the rotation of the wind vector is anti-clockwise (zonal leads meridional) which is the usual case in the southern hemisphere. During the winter, above approximately 90 km, the rotation of the wind vector is clockwise but below 90 km it ceases to rotate and the two components are out of phase by approximately 12 h.

The constancy of the meridional phase profile is an interesting feature of the diurnal tide at Mawson. The slight (but consistent) phase tilt, with later phase occurring with decreasing height implies a vertical wavelength is of 100–200 km. This effect may be due to interference between evanescent modes or perhaps the presence of a small component of a propagating mode which is transporting energy downwards from the thermosphere.

Figures 3.22 and 3.23 more concisely describe the annual variation in the amplitude and phase of the diurnal tides at Mawson. These plots have been generated by contouring monthly means from three years of data from 1984–87 Figures A.11 and A.12 (see appendix A.4, pages 202–203) show similar contour diagrams for the diurnal tide at Adelaide).

The diurnal amplitude at Mawson is seldom more than 5-10 ms^{-1} (and then usually only above 100 km) and shows gradual change with season, although figure 3.23 suggests the meridional amplitudes reach a broad minimum during winter and peak during

February.

Monthly mean diurnal phase is quite variable from month to month and it is only when several years of data are averaged that consistent phase diagrams can be produced. Even then, phase diagrams such as those in figures 3.22 and 3.23 must be interpreted with caution.

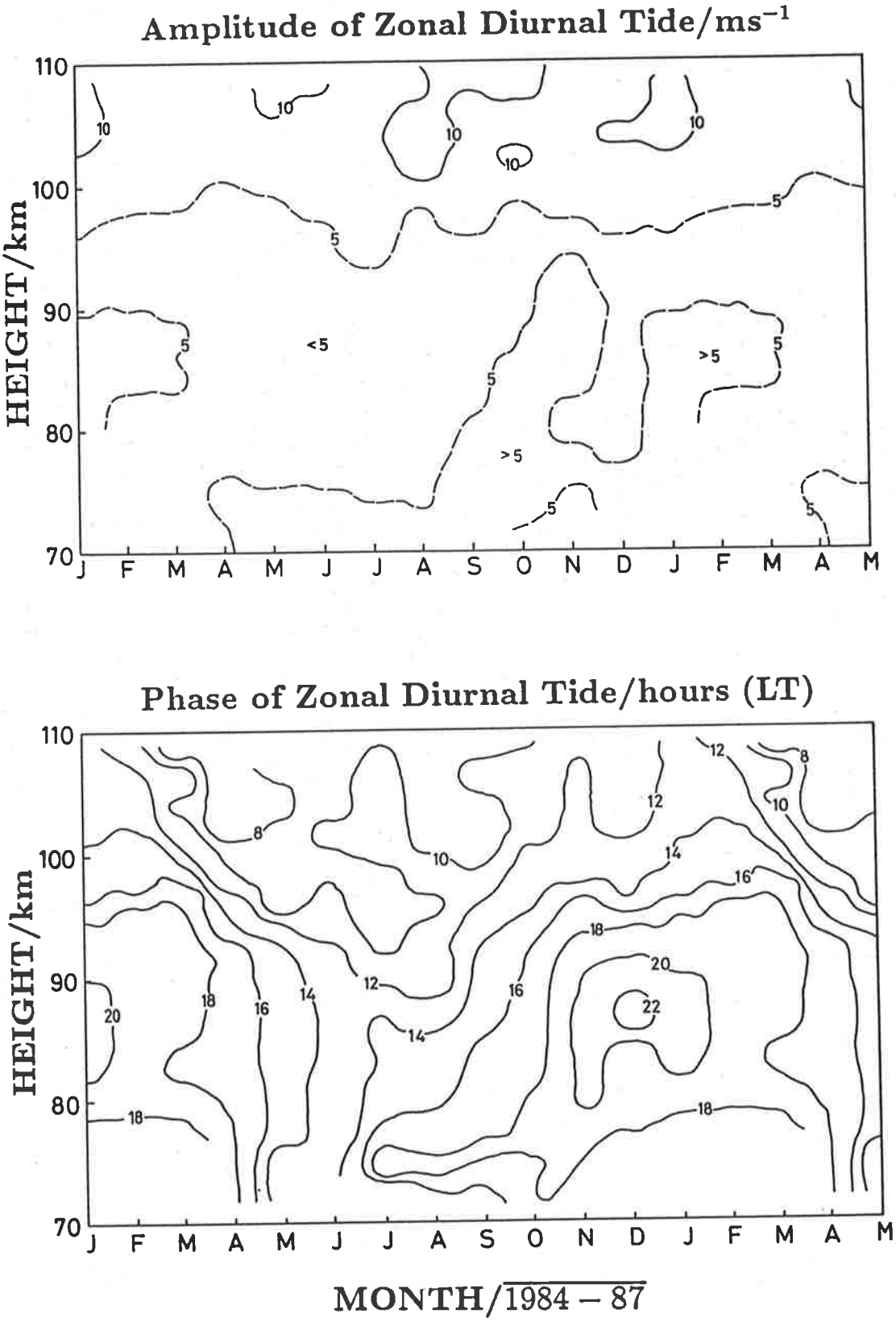

Figure 3.22: **Contours of amplitude and phase of the mean zonal diurnal tide at Mawson (67° S).** 3 years of data (1984-87) are combined to produce a mean year. Note that time marks on the x-axis indicate the middle of a month and the months January–May are repeated on the right hand side of the plot.

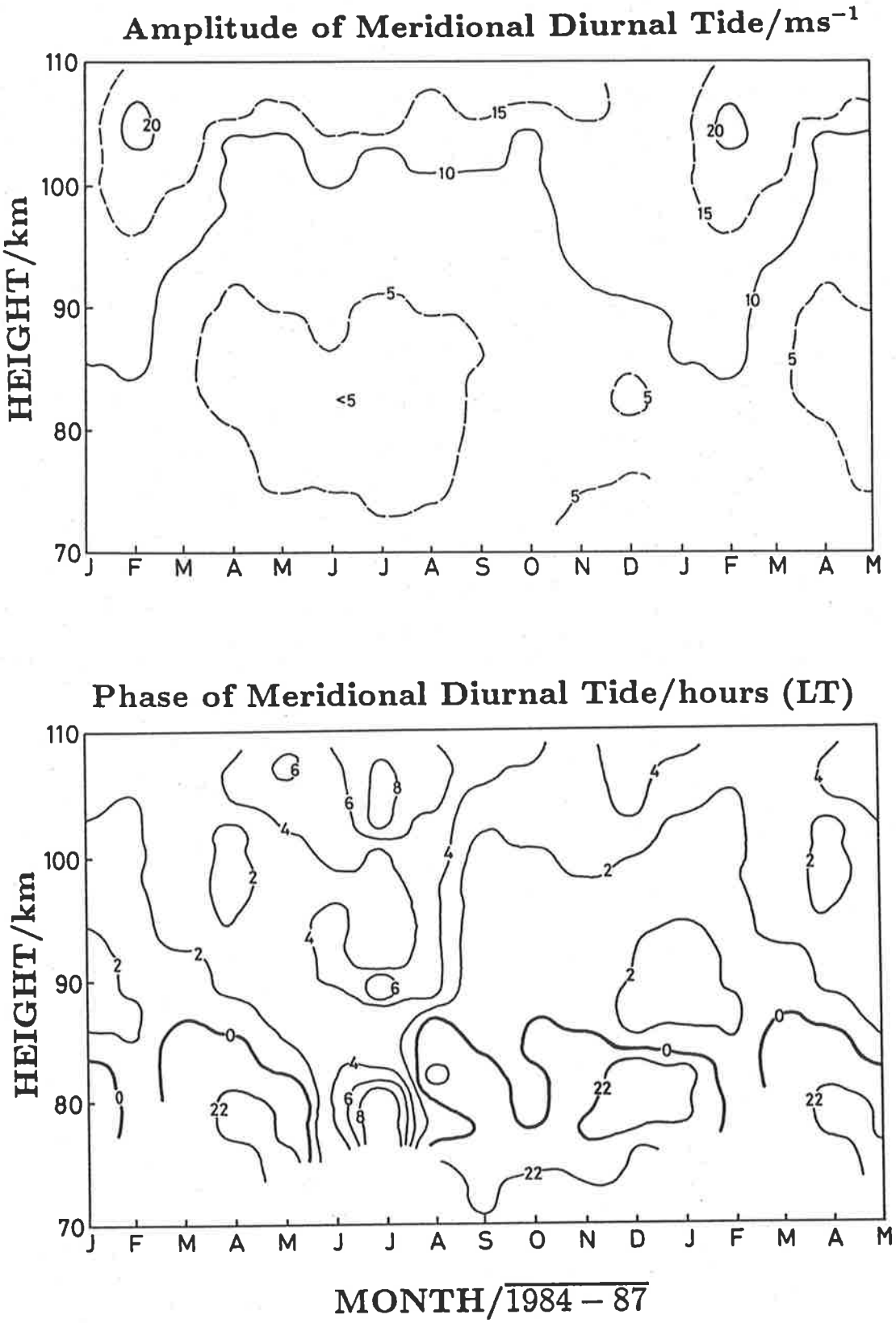

Figure 3.23: **Contours of amplitude and phase of the mean meridional diurnal tide at Mawson (67° S)** - details as for figure 3.22.

Comparison of the diurnal tide with Poker Flat, 65° N

Figures 3.24 and 3.25 compare seasonal averages of the diurnal amplitude and phase at Poker Flat and Mawson. The Poker Flat tidal winds have been measured by using the Poker Flat MST radar to infer winds from the Doppler shifts of meteor reflections. The averages at Mawson have been calculated by taking the vector average of the monthly means. When local seasons are compared, the amplitude profiles at the two sites have a similar shape, but apparently the amplitudes are 20-30% greater at Mawson, especially at heights above 100 km. The phase profiles of the zonal component of the diurnal tide at both sites are similar in shape and the local times often agree within the error bars. The zonal component phase profiles at Poker Flat usually have a 'negative' slope (ie. the time of the maximum wind occurs earlier with increasing height). The phase profile at Mawson usually undergoes a sudden transition at around 85–95 km, but this is not evident in the data from Poker Flat. The meridional components at the two sites are generally in antiphase. This phase relationship suggests that symmetric tidal modes such as the (1,–2) or (1,–4) are possibly dominant at these latitudes.

It is interesting to note that the dominance of the meridional component evident at Mawson is not so marked at Poker Flat. With the notable exception of the northern hemisphere summer months (JJA) above 85 km, the meridional and zonal component amplitudes at Poker Flat are comparable.

The tides at Mawson show a significant increase in amplitude at heights above 100 km. This is not apparent at Poker Flat (see figures 3.24 and 3.25).

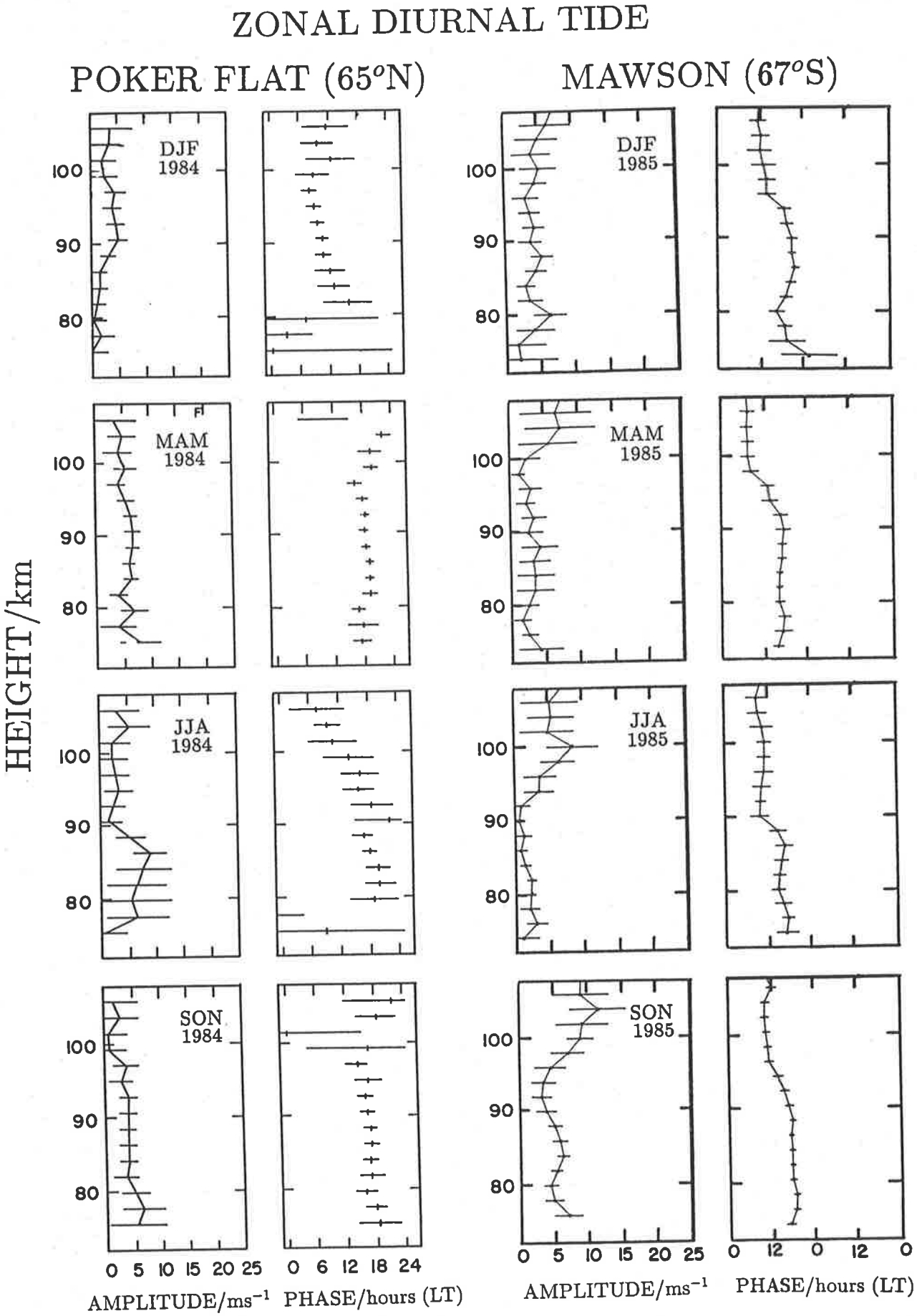

Figure 3.24: **Comparison of seasonal averages of amplitude and phase of the zonal diurnal tide at Poker Flat, Alaska (Tetenbaum et al. 1986) and Mawson, Antarctica.** 'DJF'=Dec, Jan, Feb etc. Note the difference in phase scale between the two sites.

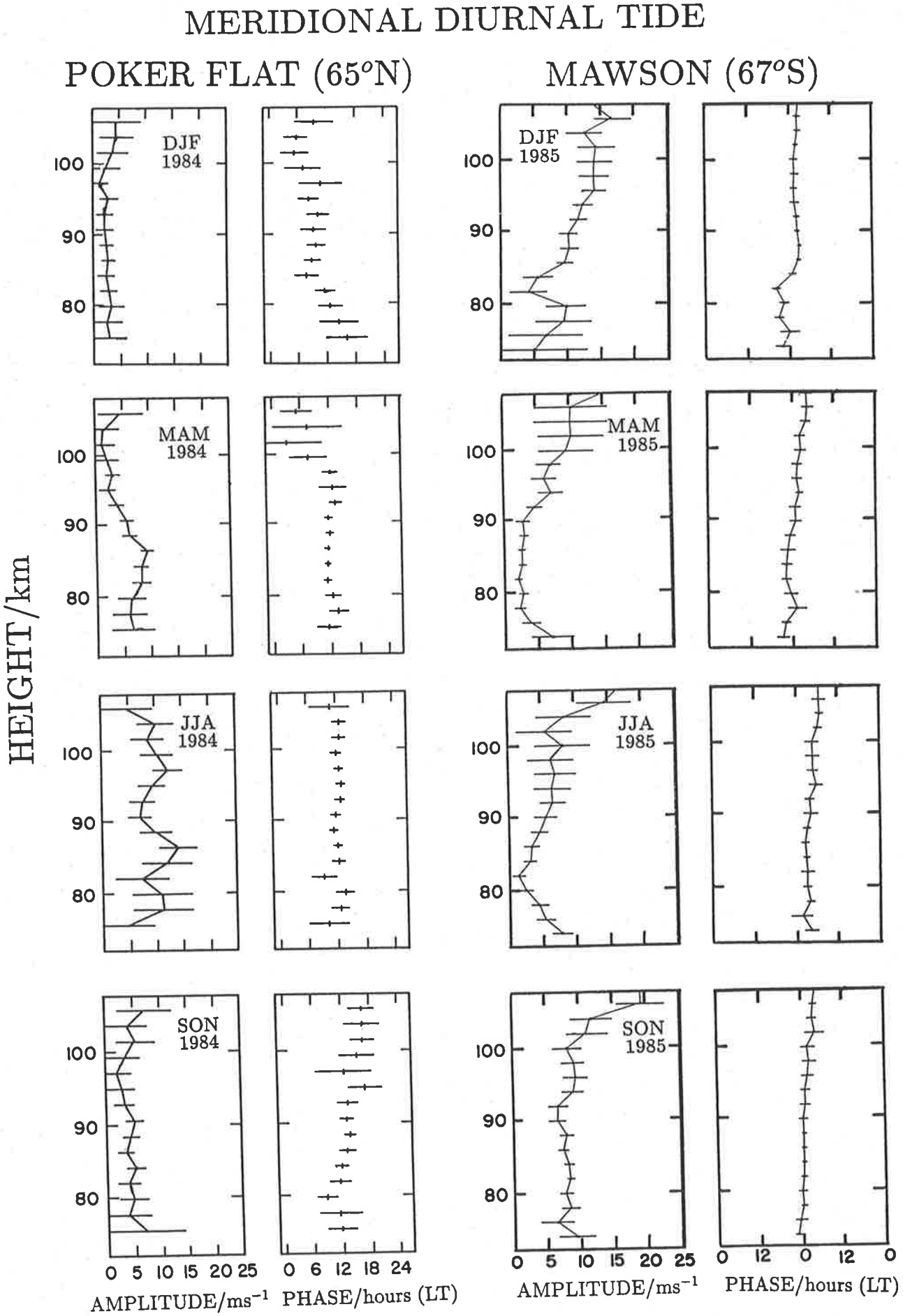

Figure 3.25: **The meridional diurnal tide** - details as for 3.24

Figure 3.26 is taken directly from Tetenbaum et al. (1986) and summarizes the monthly average amplitude and phase of the diurnal tide at Poker Flat during 1983–84, at selected heights (82, 92 and 102 km). For ease of comparison, figure 3.27 uses identical axes to figure 3.26 and shows two years (1985–86) of tidal data from Mawson. At 82 and 92 km amplitudes of the diurnal tide at both sites are comparable. However, at 102 km the amplitudes at Mawson are 50-100% greater than at Poker Flat and the phase structure is the reverse of that at lower levels (ie. meridional leads zonal by 6 h).

At 82 and 92 km, the phase of the zonal component is comparable between the two sites (both usually 16±4 h local time). At Poker Flat the meridional component usually leads the zonal component by approximately 6 h and at Mawson it lags by approximately 6 h. At 102 km, the phase structure at Poker Flat is highly variable but at Mawson it appears to be much more stable, with the zonal phase usually 10±4 h and lagging the meridional phase by approximately 6 h at most times. The phase diagram in figure 3.27 implies that the clockwise rotation of the wind vector is a regular feature at Mawson at the 102 km level.

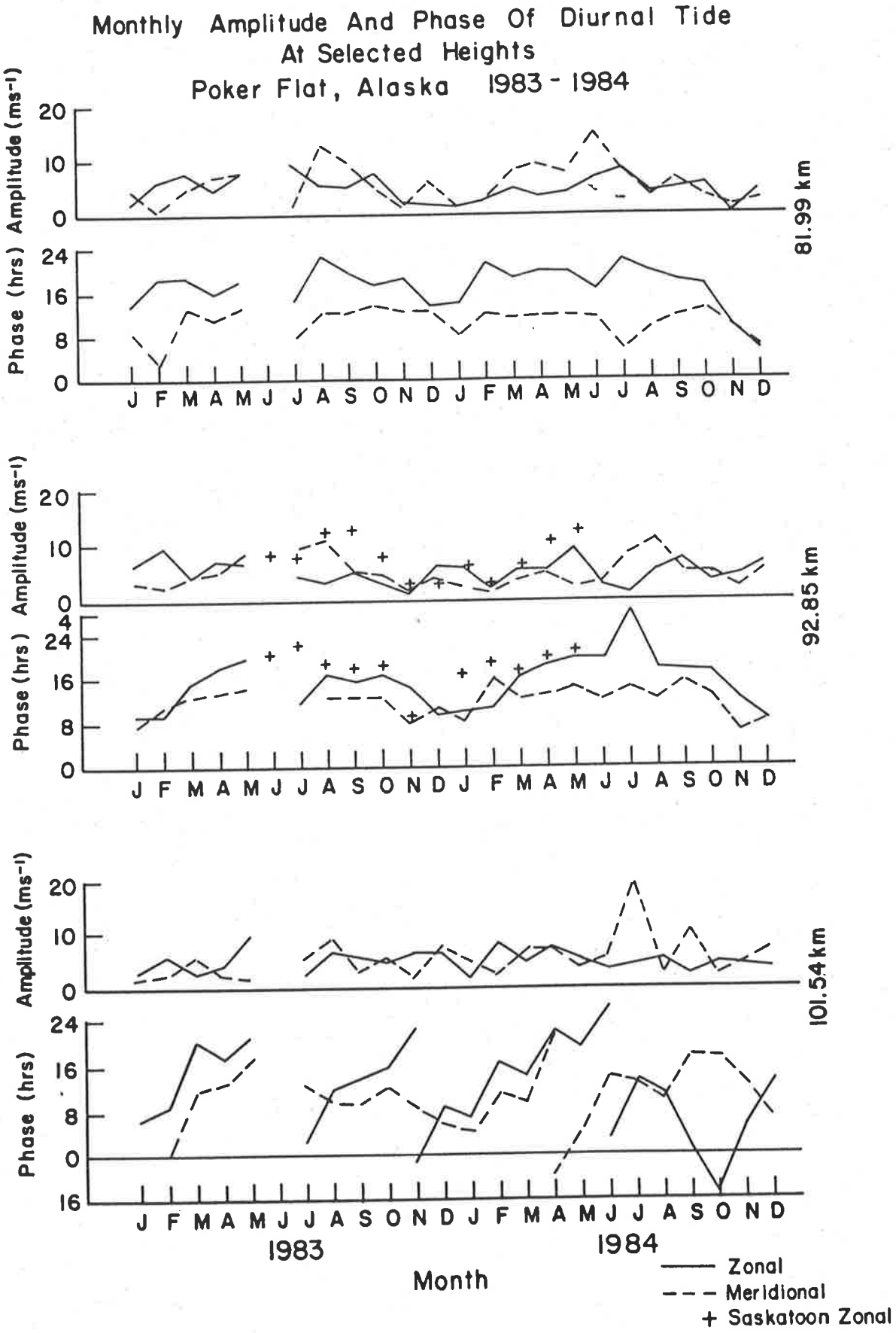

Figure 3.26: **Monthly averages of amplitude and phase of the diurnal tide at Poker Flat, Alaska** (Tetenbaum et al. 1986).

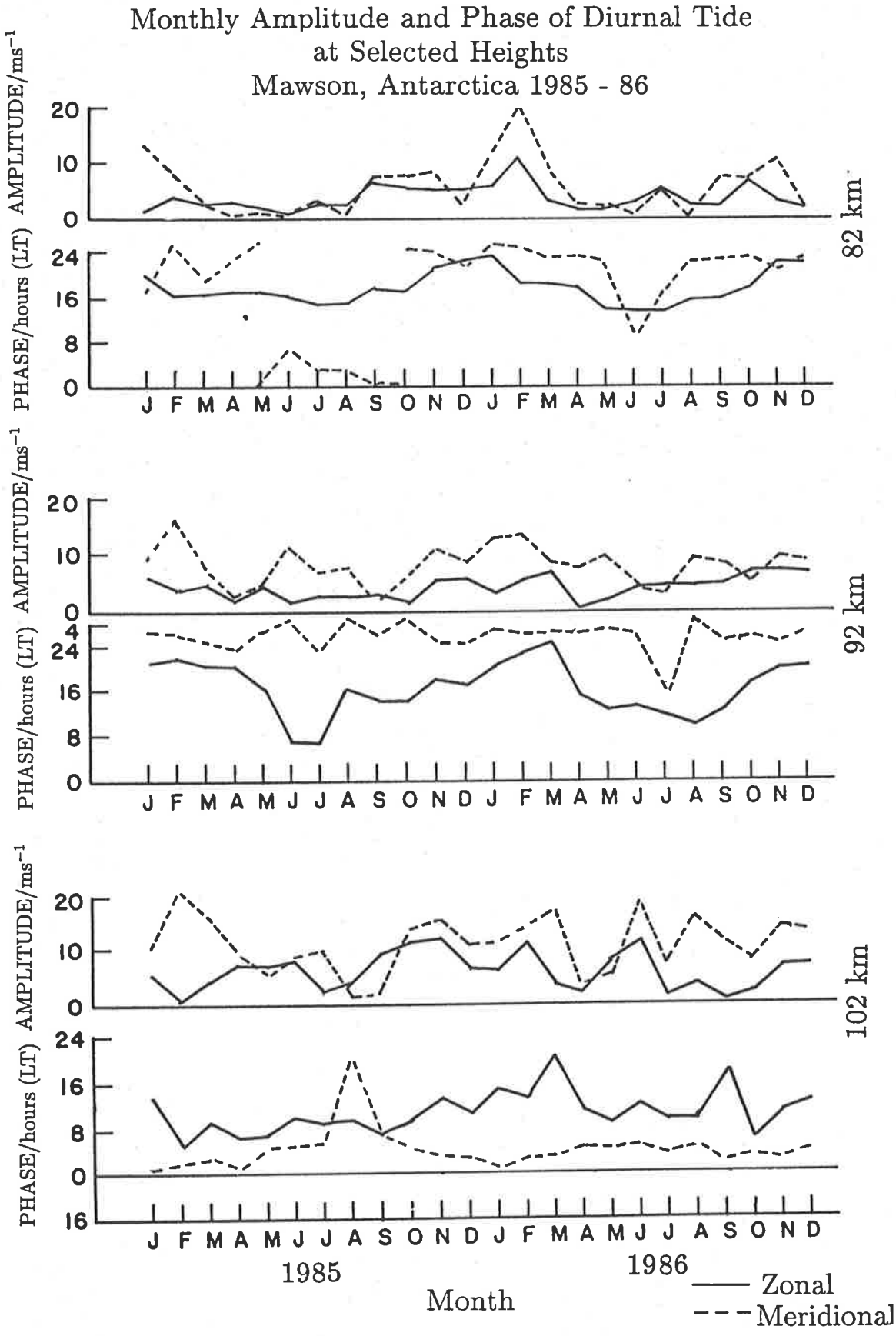

Figure 3.27: **Monthly averages of amplitude and phase of the diurnal tide at Mawson, Antarctica.**

Contour plots in figures A.15, A.16, A.17 and A.18 (in appendix A.4, pages 206–209) juxtapose 2 years (1983-84) of data from Poker Flat with $2\frac{1}{2}$ years (mid-1984–early-87) of data from Mawson. Data from the two sites overlap in time for the last six months of 1984, but the plots have been displaced horizontally to conserve space and directly compare seasons. (The contour plots of Poker Flat data are taken directly from Tetenbaum et al. (1986) but have been stretched horizontally by 60% to equalize the height scales). Comparison of figures A.15 and A.17 show that the amplitude of the diurnal tide is similar at both sites except above about 100 km, where it is 50-100% greater at Mawson. The diurnal phase at Mawson is so variable (even when averaged over a month) that a reasonably consistent picture can only be obtained by averaging several years of data. Hence figures A.16 and A.18 show a three year average for the phase at Mawson. At both sites the contours of phase are often vertically orientated, indicating mainly evanescent phase structure.

3.2.3 The semidiurnal tide

Observations at Mawson

Figures 3.28, 3.29 and 3.30 present the amplitude and phase and vertical wavelength of the semidiurnal tide at Mawson. As was the case for the diurnal tide, these data have been split into summer, winter and equinox 'seasons' and an annual average has been calculated.

Amplitudes of the semidiurnal tide (figure 3.28) are generally larger than those of the diurnal tide, especially in the height range 80-90 km. Unlike the diurnal amplitude, which increases approximately linearly with height (above about 90 km), the semidiurnal amplitudes reach a broad maximum at 90 km (±5 km). As was the case with the diurnal

tidal amplitudes, the meridional component is usually larger than the zonal (by 20-80%) and during the summertime the meridional component becomes very much larger above 100 km.

Below 100 km the phase of the semidiurnal tide (figure 3.29) shows the classical form of a propagating tide, with the zonal component leading the meridional by 3 h and phase propagating downward. Above 100 km the meridional component becomes evanescent.

The stability of this phase structure is indicated by the very small error bars on the seasonal averages. However, the vertical wavelength increases markedly in the wintertime.

The annual variation in the vertical wavelength of the semidiurnal tide (in the 80–100 km height range) is shown in figure 3.30. The vertical wavelengths were calculated by applying linear regression to the semidiurnal phase profiles in the height range 80–100 km. With superposition of several tidal modes, a curved phase profile might be expected. However figure 3.28 demonstrates that the semidiurnal phase profiles are usually very linear in the 80–100 km height range and linear regression is a suitable method to estimate the vertical wavelength. There is an annual variation in the vertical wavelength with the shortest values (20–30 km) occurring during January and the longest (70–80 km) during wintertime. Table 1.1 on page 15 shows the vertical wavelengths of some of the common semidiurnal tidal modes. With reference to these figures, it is possible that the short summertime wavelengths (in the height range 80-100 km) may be due to the joint presence of the (2,6) and (2,7) modes and the longer wintertime wavelengths due to the (2,2) and (2,3) mode. Also, the steep (apparently evanescent) phase slopes often seen at 100-108 km (figure 3.29) are probably due to the (2,2) symmetric mode.

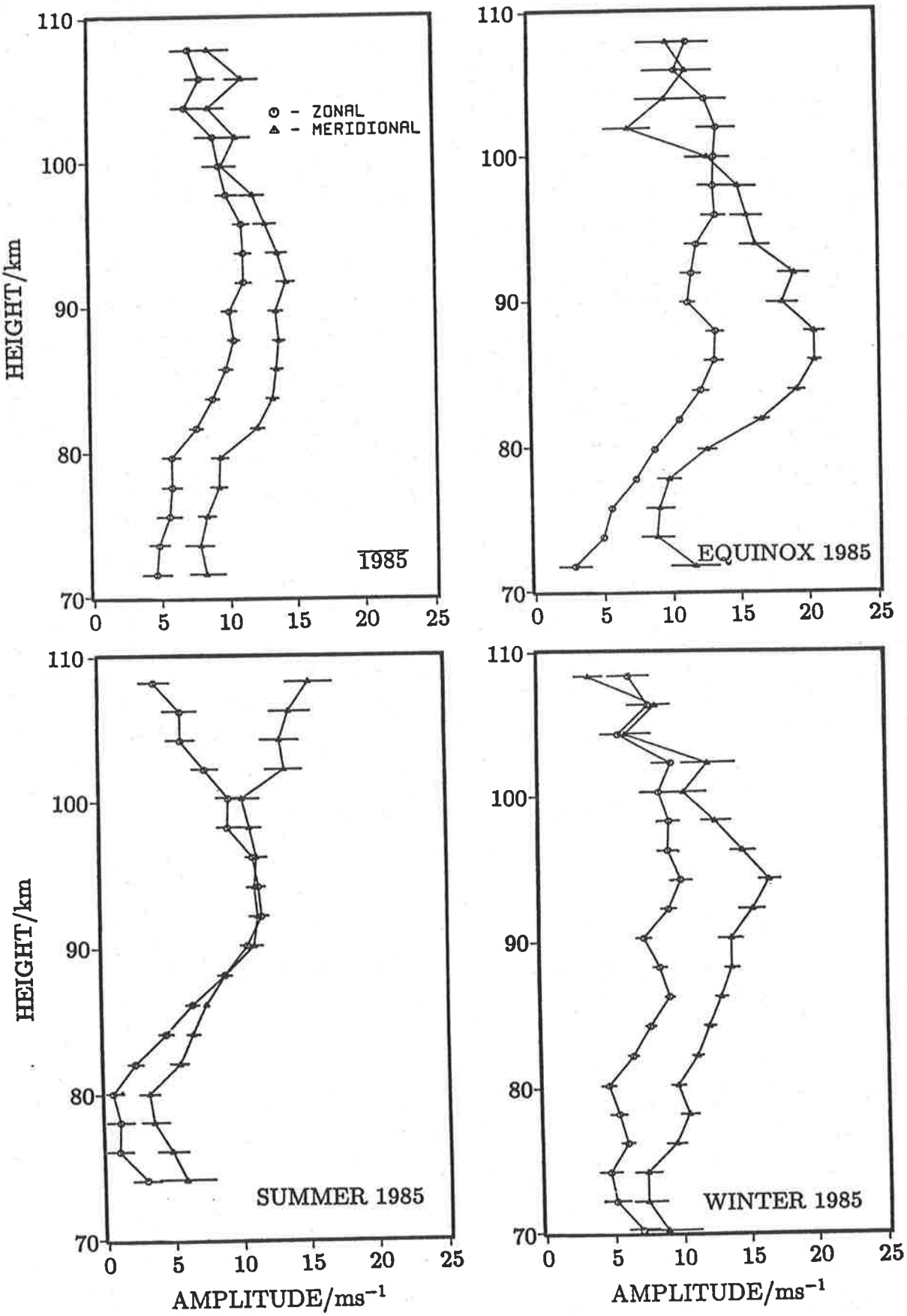

Figure 3.28: **Amplitude of the semidiurnal tidal component of the wind at Mawson** averaged over a whole year ($\overline{1985}$) and by season. (Summer = Nov, Dec, Jan, Feb; winter = May, Jun, Jul, Aug; Equinox = Mar, Apr, Sep, Oct)

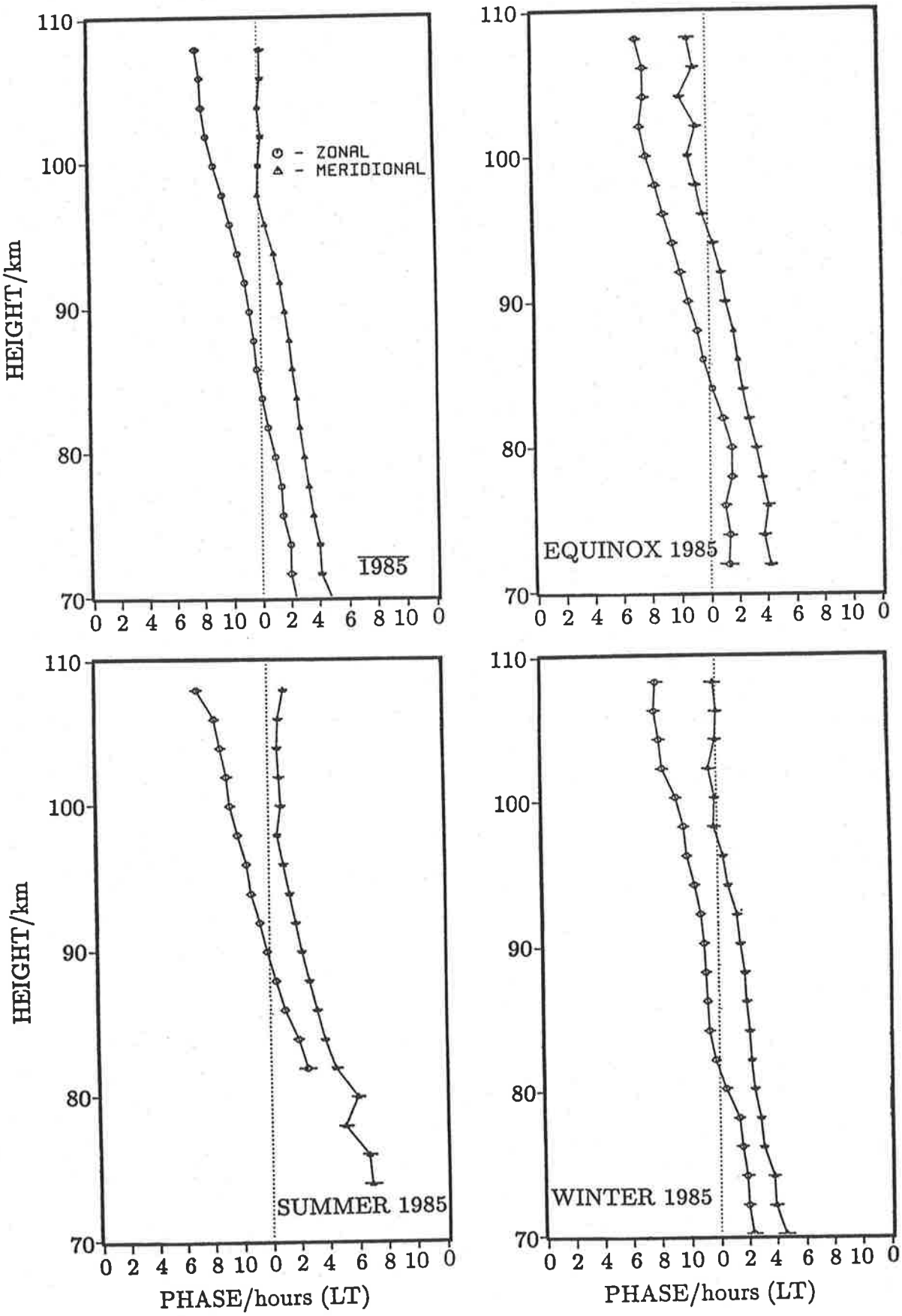

Figure 3.29: **Phase of the semidiurnal tide at Mawson** - details as for figure 3.28.

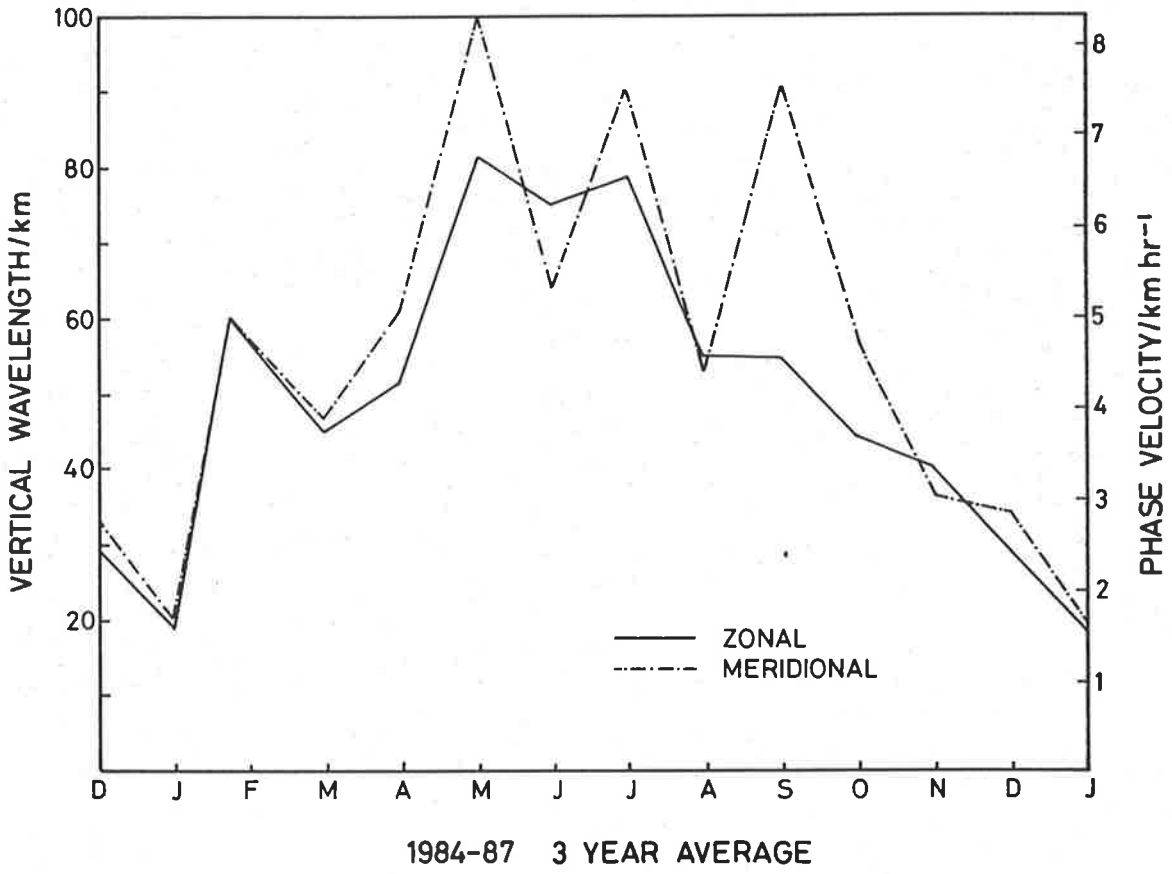

Figure 3.30: **Mean vertical wavelength of the semidiurnal tide in the height range 80-100 km at Mawson.** Wavelengths were calculated by linear regression of phase data.

Figure A.10 (in appendix A.4, page 201) is a vector average of 3 years of data from the solstitial months of June and December. The solstitial semidiurnal tide appears to be much the same as the seasonal averages in figures 3.28 and 3.29. However, figure A.10 highlights the very short summertime vertical wavelength ($\lambda_z \approx$20-25 km) at 80-96 km and the sudden transition to evanescence (of the meridional component) above this height.

The contour diagrams in figures 3.31 and 3.32 describe more concisely the annual variation in the amplitude and phase for the semidiurnal tides at Mawson. These plots have been generated by contouring a vector average of the monthly means from 1984-87. The semidiurnal tide at Adelaide (in appendix A.4, pages 204–205) is typically 10-15 ms^{-1} in amplitude and characterised by abrupt changes in the phase structure during the equinoxes. At Mawson the semidiurnal tide is a little weaker but with a smooth phase structure which is less inclined to suffer abrupt changes with change of season. Summertime phase contour lines tend to bunch together as the wavelengths shorten.

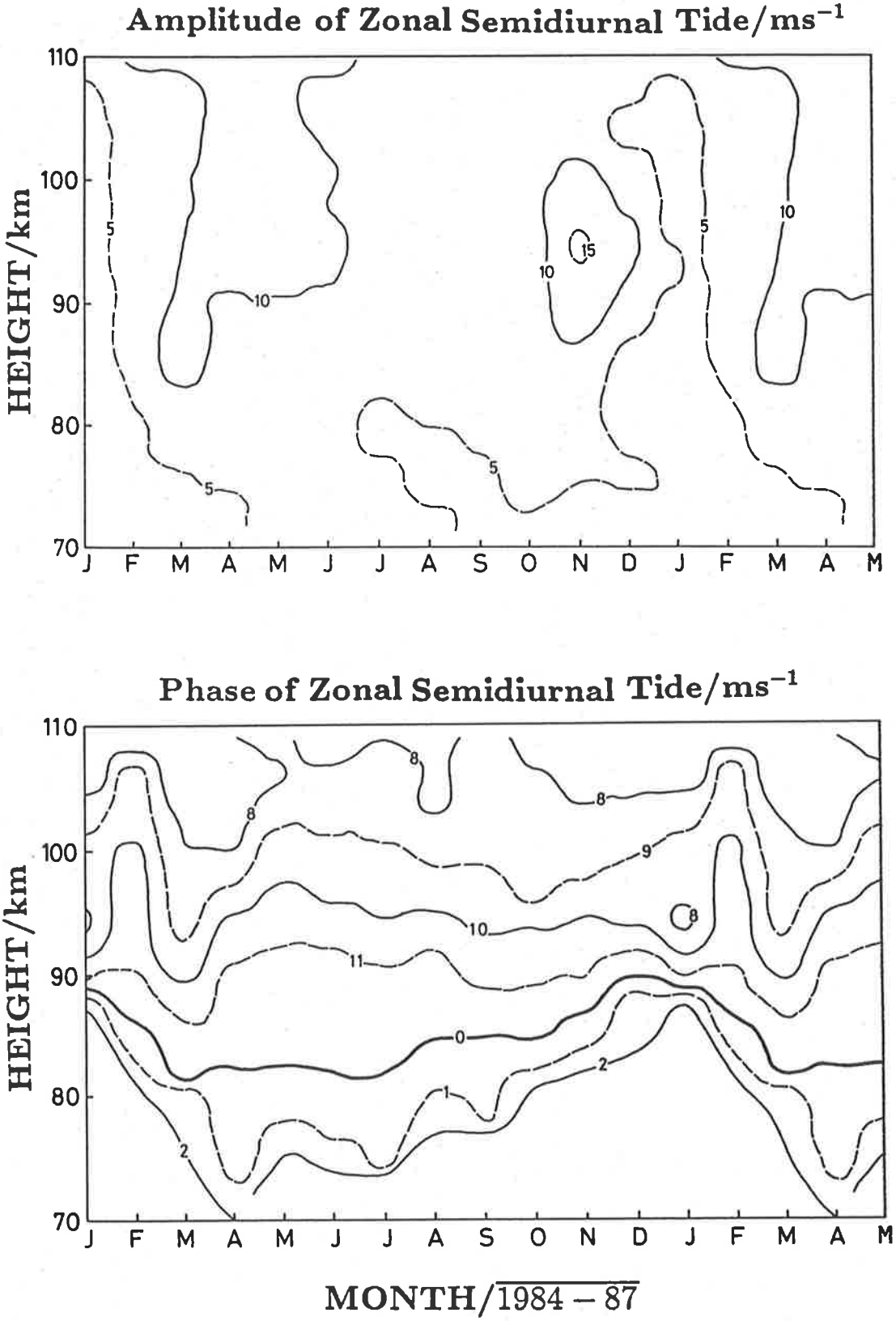

Figure 3.31: **Contours of amplitude and phase of the mean zonal semidiurnal tide at Mawson (67° S).** 3 years of data (1984-87) are combined to produce a mean year. Note that time marks on the x-axis indicate the middle of a month and the months January–May are repeated on the right hand side of the plot.

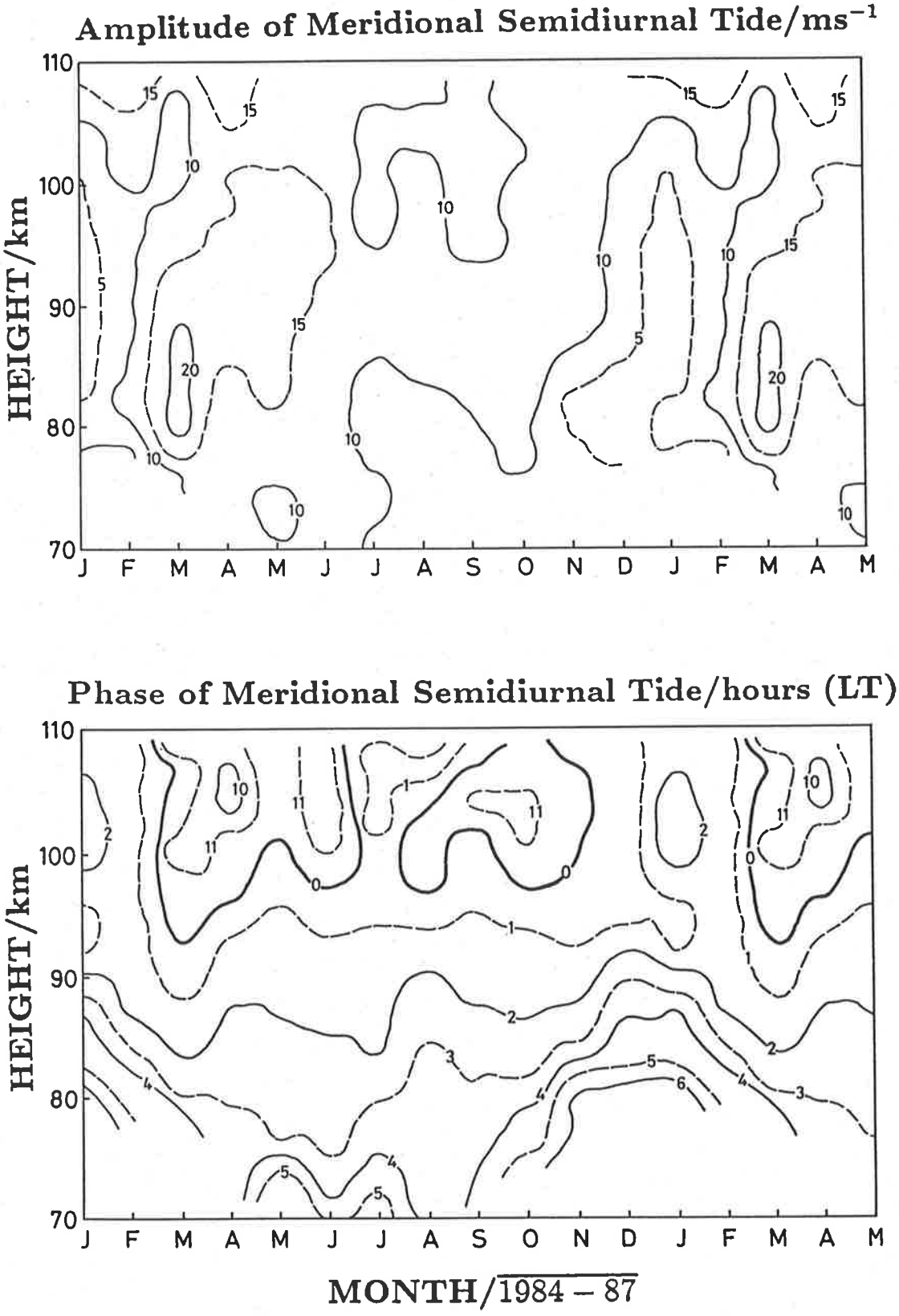

Figure 3.32: **Contours of amplitude and phase of the mean meridional semidiurnal tide at Mawson (67° S)** - details as for figure 3.31.

Comparison of the semidiurnal tide with Poker Flat, 65° N

In figures 3.33 and 3.34 seasonal averages of the tidal amplitude and phase at Poker Flat and Mawson are compared. The amplitude of the semidiurnal tide appears to be significantly larger (50-100%) at Mawson than at Poker Flat, especially during the equinoxes. Unlike the diurnal tide there is no consistent phase relationship apparent between the two sites. This is probably due to the joint presence of several symmetric and anti-symmetric modes of comparable amplitude.

As was the case for the diurnal tide, the amplitude ratio of the tidal components is a conspicuous feature of the semidiurnal tides at Mawson, with the meridional amplitudes typically 50–100% larger than the zonal. The large enhancement in the tides during the equinoxes at Mawson (in particular during the spring) is not so apparent in the Poker Flat data. In fact the greatest amplitudes at Poker Flat appear to occur during the summertime.

At most times, and especially during the equinoxes, at Mawson, semidiurnal amplitudes reach a broad maximum between 80–100 km; this effect is much less apparent at Poker Flat.

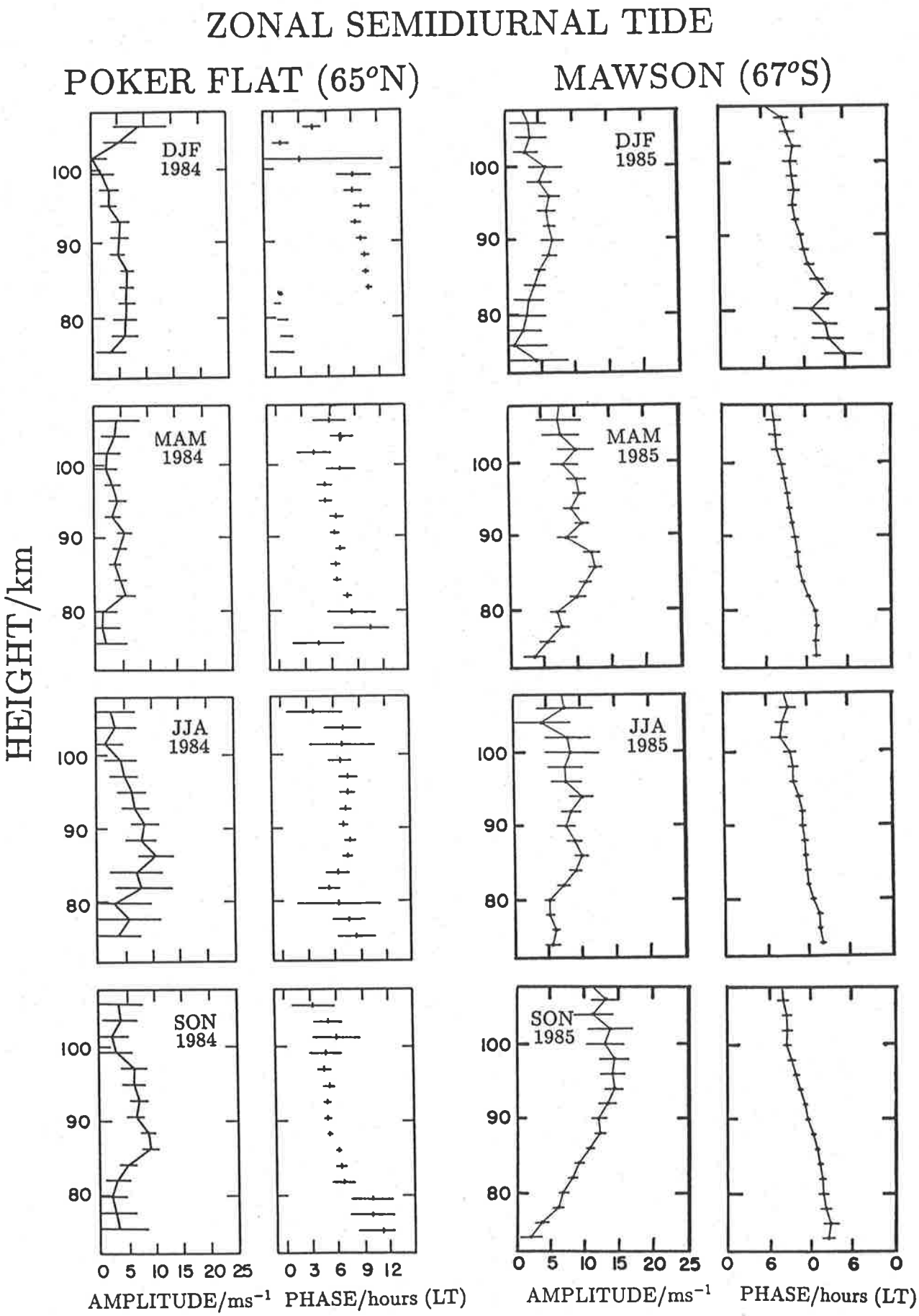

Figure 3.33: **Comparison of seasonal averages of amplitude and phase of the zonal semidiurnal tide at Poker Flat, Alaska (Tetenbaum et al. 1986) and Mawson, Antarctica.** 'DJF'=Dec, Jan, Feb etc. Note the difference in phase scale between the two sites.

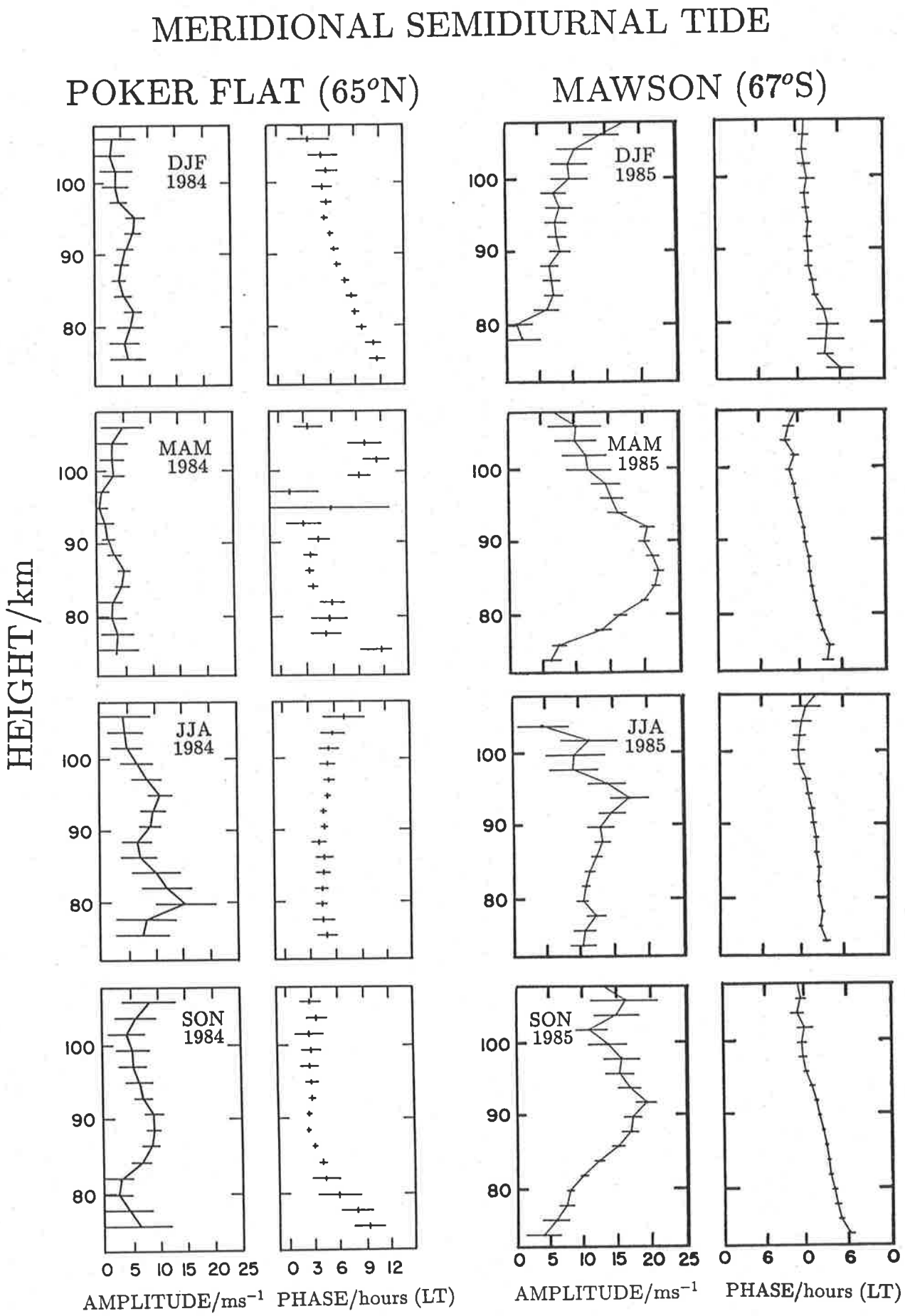

Figure 3.34: **The meridional semidiurnal tide** - details as for 3.33

Figures 3.35 and 3.36 compare the monthly averages of the semidiurnal tidal winds at Poker Flat and Mawson at heights of 82,92 and 102 km. Semidiurnal amplitudes tend to be larger at Mawson, especially at 102 km. At all levels, the meridional component leads the zonal at Poker Flat and the zonal leads the meridional at Mawson (by approximately 3 h). Annual variations in the semidiurnal phase at Mawson appear to be smaller than at Poker Flat, especially at 102 km. From these diagrams, no definite phase relationship of the tides (between the two sites) can be inferred.

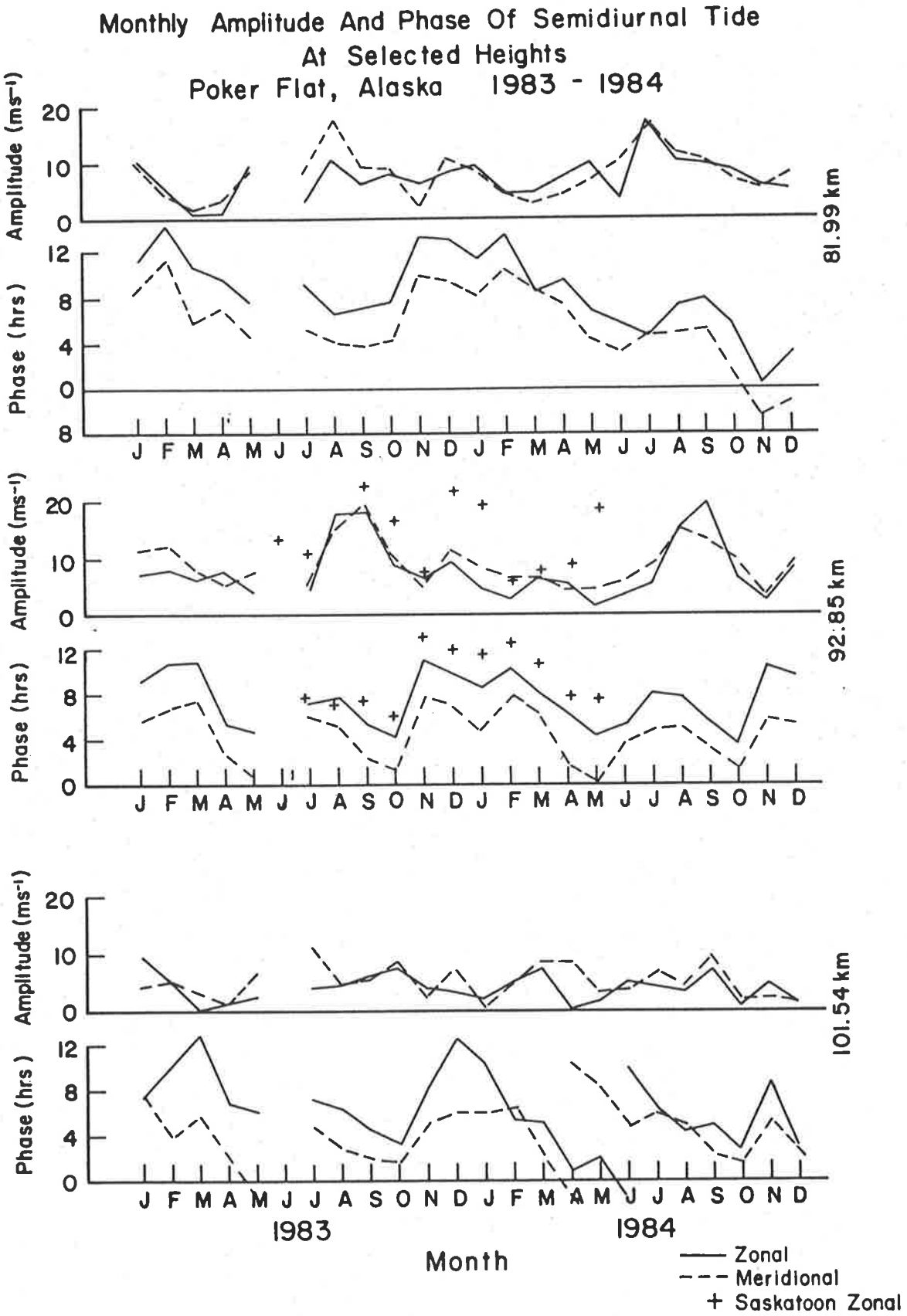

Figure 3.35: **Monthly averages of amplitude and phase of the semidiurnal tide at Poker Flat, Alaska** (Tetenbaum et al. 1986).

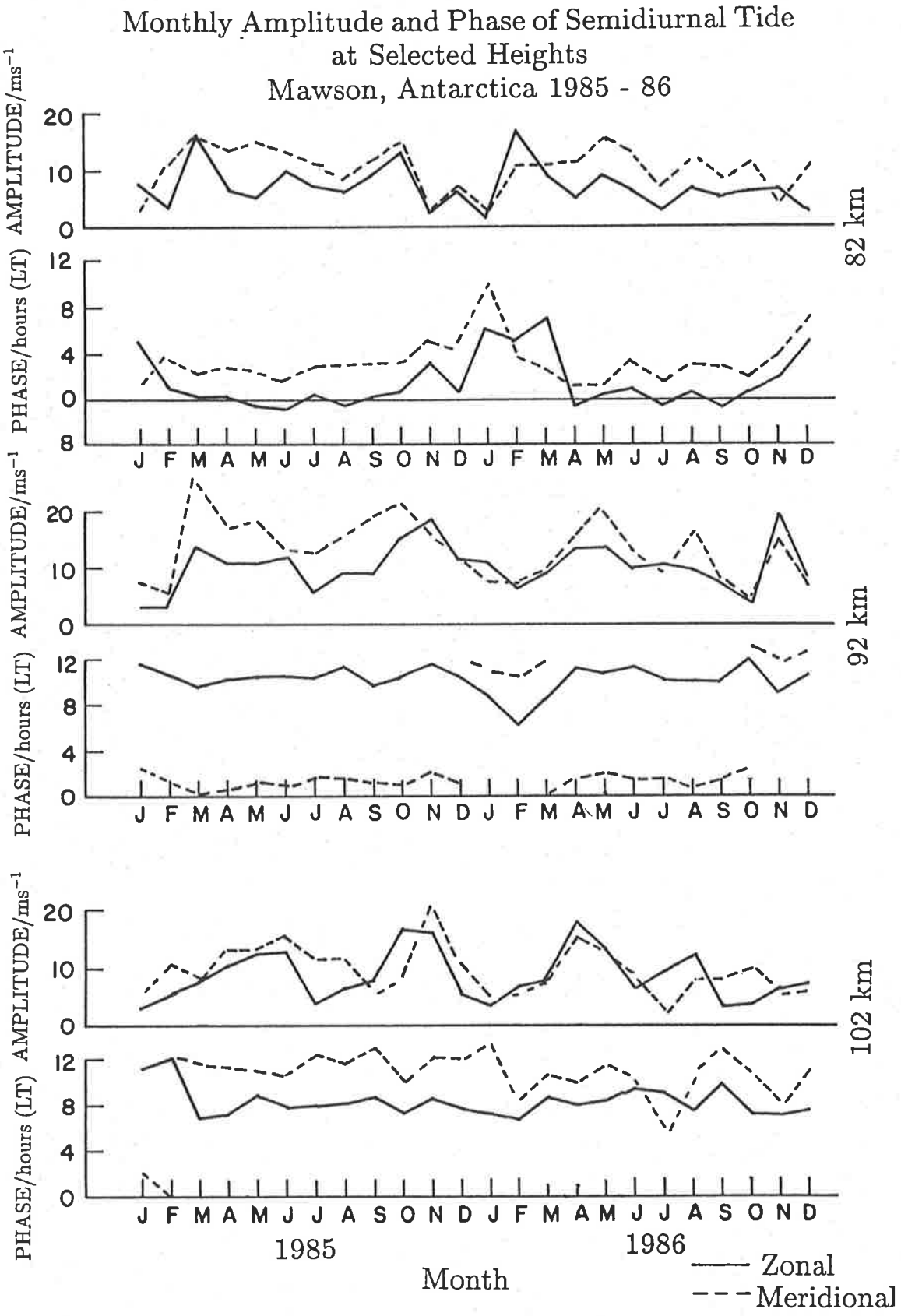

Figure 3.36: **Monthly averages of amplitude and phase of the semidiurnal tide at Mawson, Antarctica.**

Contour plots in figures A.19, A.20, A.21 and A.22 (in appendix A.4, pages 210–213) juxtapose 2 years (1983-84) of data from Poker Flat with $2\frac{1}{2}$ years (mid-1984–early-87) of data from Mawson. The data overlap in time for the last six months of 1984, but the plots have been displaced horizontally to conserve space and directly compare the seasons. (The contour plots of Poker Flat data are taken directly from Tetenbaum et al. (1986) but have been stretched horizontally by 60% to equalize the height scales).

In the semidiurnal amplitudes (figures A.19 and A.21) there is an enhancement at both locations during autumn near the 85-95 km level. At Mawson, a similar increase also appears during the local spring equinox but this does not appear at Poker Flat during 1983-84.

If the diagrams of semidiurnal phase in figures A.20 and A.22 (pages 211 and 213) are truly representative of the data, then there are substantial differences in the phases of the semidiurnal tide between Mawson and Poker Flat. It should be emphasized however, that drawing phase diagrams requires careful judgement and different approaches to drawing contours can give a different appearance to the final product. In particular sudden changes of phase (which often occur at Mawson during January/February) must be treated with caution. However, these changes are not apparent in the Poker Flat diagrams, where the vertically oriented contours suggest more evanescent phase structure than at Mawson, where phase contours are usually (approximately) horizontal.

3.2.4 Comparison of Mawson data with recent tidal wind models

Recent tidal model predictions from Forbes and Vial (1989), Forbes and Hagan (1988) and Forbes (1982b) are compared with tidal winds data from Mawson in figures 3.37,

3.38, 3.39 and 3.40. Since most of the model predictions are specifically for the solstices, 'mean solstice' conditions have been estimated by taking a vector average of the monthly mean tides during June and December for the three years between 1984–86.

The diurnal tide

The largely evanescent nature of the diurnal tide at Mawson (figures 3.37 and 3.38) has been correctly predicted by the models of Vial (1986) and Forbes and Hagan (1988). Although the model amplitudes below 90 km approximate the generally small ($<5 ms^{-1}$) observed tidal amplitudes, neither model predicts the approximately linear increase in amplitude which takes place above (approximately) 90 km. During December, both models show an increase in amplitude between 90–100 km but then a decrease above this height. Neither model, except that of Vial (1986) for the zonal component in June, predicts the large increase in amplitude which usually occurs at heights above 100 km. In both models, the component amplitudes are almost identical, whereas with real amplitude data, the meridional component is usually significantly larger.

Although the model phase profiles are of near-constant value (for the most part), the prediction of the absolute phase is usually approximate. Neither model predicts the change of phase which usually occurs in the zonal component at heights between 90–96 km; a regular feature at Mawson (see figure 3.21 on page 122).

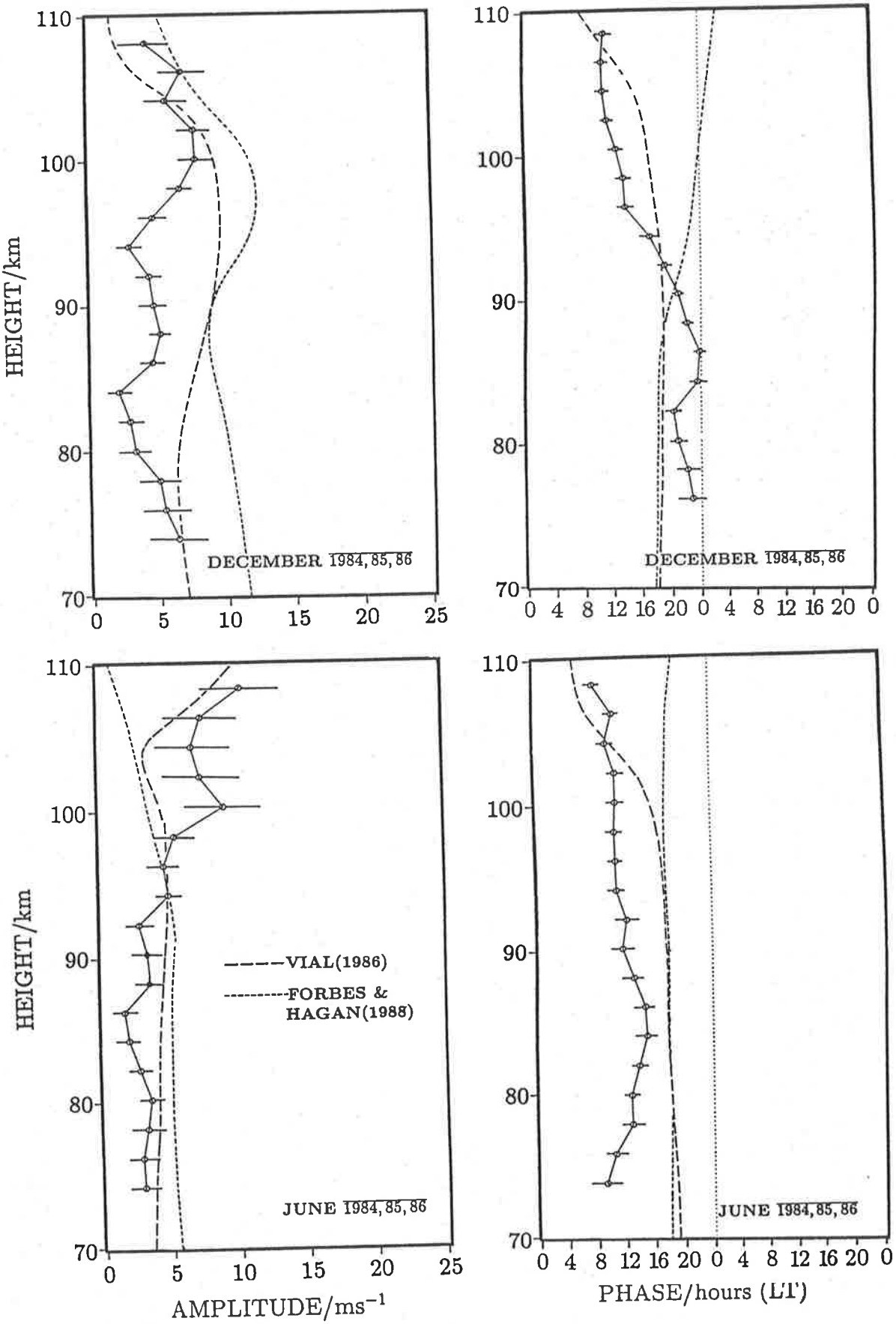

Figure 3.37: **Comparison of the amplitude and phase of the mean zonal diurnal tide at Mawson, with the tidal models of Vial (1986) and Forbes and Hagan (1988).** Data is averaged over the solstitial months of June and December for the years 1984-87.

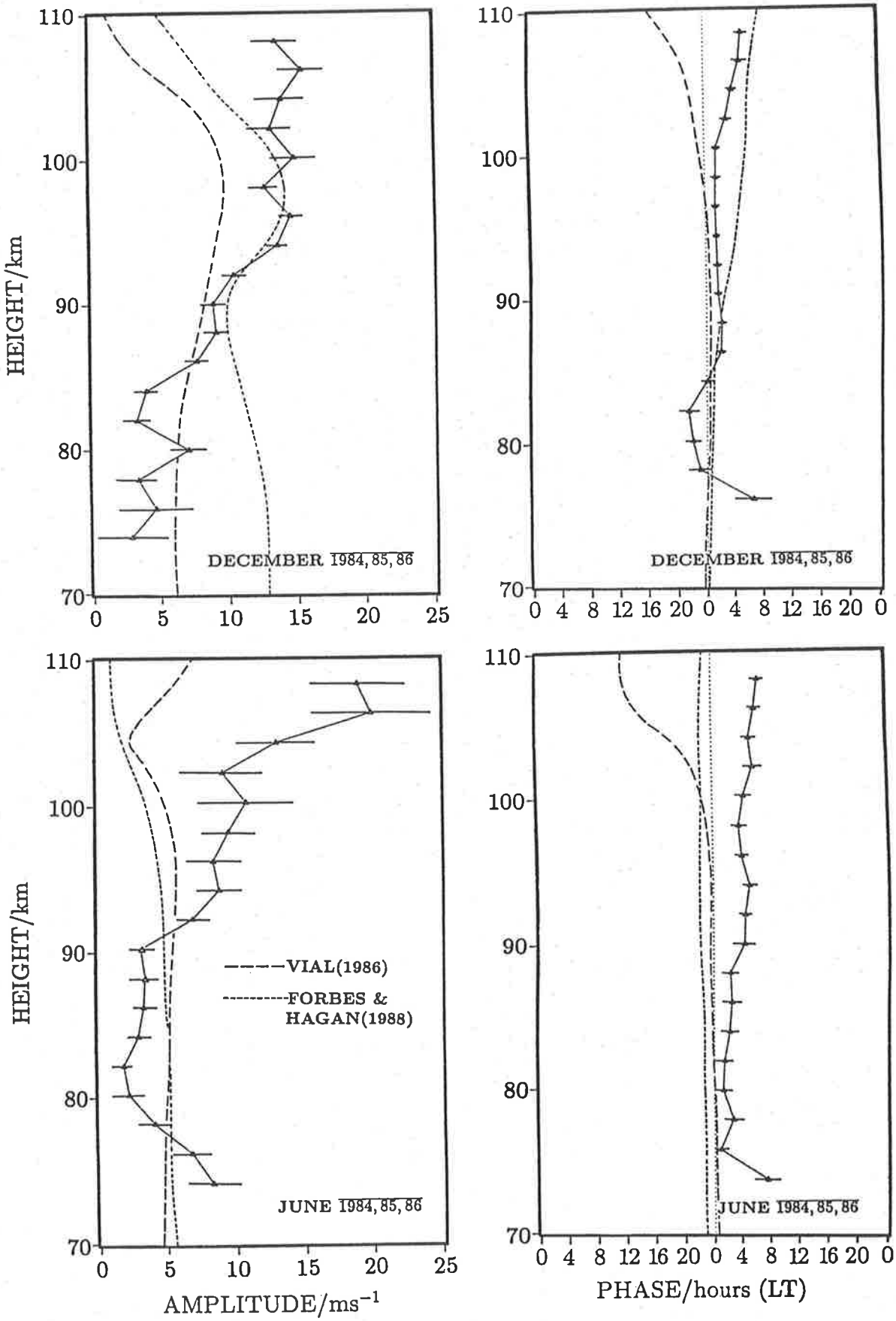

Figure 3.38: **Comparison of the amplitude and phase of the mean meridional diurnal tide at Mawson, with the tidal models of Vial (1986) and Forbes and Hagan (1988)** - details as for figure 3.37.

The semidiurnal tide

In figures 3.39 and 3.40 the semidiurnal tidal winds at Mawson are compared with the models of Forbes and Vial (1989) and Forbes (1982b) (Forbes, 1982b has been included to demonstrate how semidiurnal models have evolved in recent times). Both models predict amplitude profiles which are considerably different from what is observed. During June both models predict a sudden increase in amplitude at around 90 km, which is not observed. In fact, the amplitude of the semidiurnal tide usually peaks at approximately 90 km and then decreases above that height (cf. figure 3.28 on page 135). During December, the Forbes (1982b) model gives a sudden increase in amplitude at 85–90 km whereas the Forbes and Vial (1989) (abbreviated 'FV') gives a minimum. Neither of these changes are observed in the data. Both models fail to account for the dominance of the meridional component.

The model phase profiles show better agreement with the data than do the amplitudes. In the height range 80–100 km, the FV model is good at predicting the slope of the phase profile, and during June the comparison is excellent (FV is within an hour of the actual phase). Although the sudden phase transition at around 90 km in December (in the FV model) is not observed in the data, the sudden steepening in the model phases (at about 90 km) is observed. Above 90 km the FV models agreement with phase data is good, but below 90 km it is poor.

Clearly these diagrams indicate that semidiurnal tidal modelling at high southern latitudes requires much refinement, especially for the amplitude predictions. These diagrams suggest that damping processes, far larger than those being modelled, are present in the height range 90–110 km.

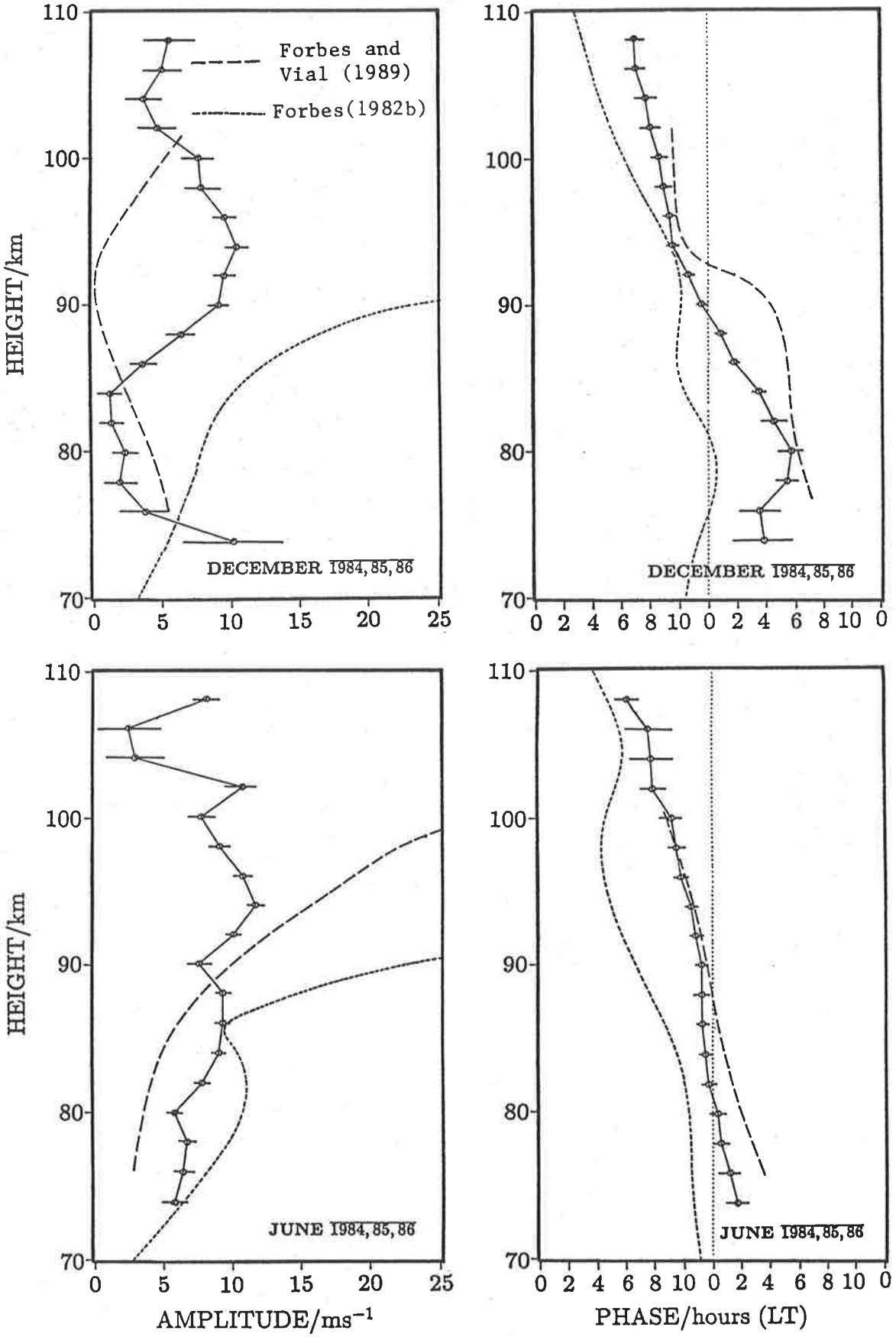

Figure 3.39: **Comparison of the amplitude and phase of the mean zonal semidiurnal tide at Mawson, with the tidal models of Forbes and Vial (1989) and Forbes (1982b).** Data is averaged over the solstitial months of June and December for the years 1984-87.

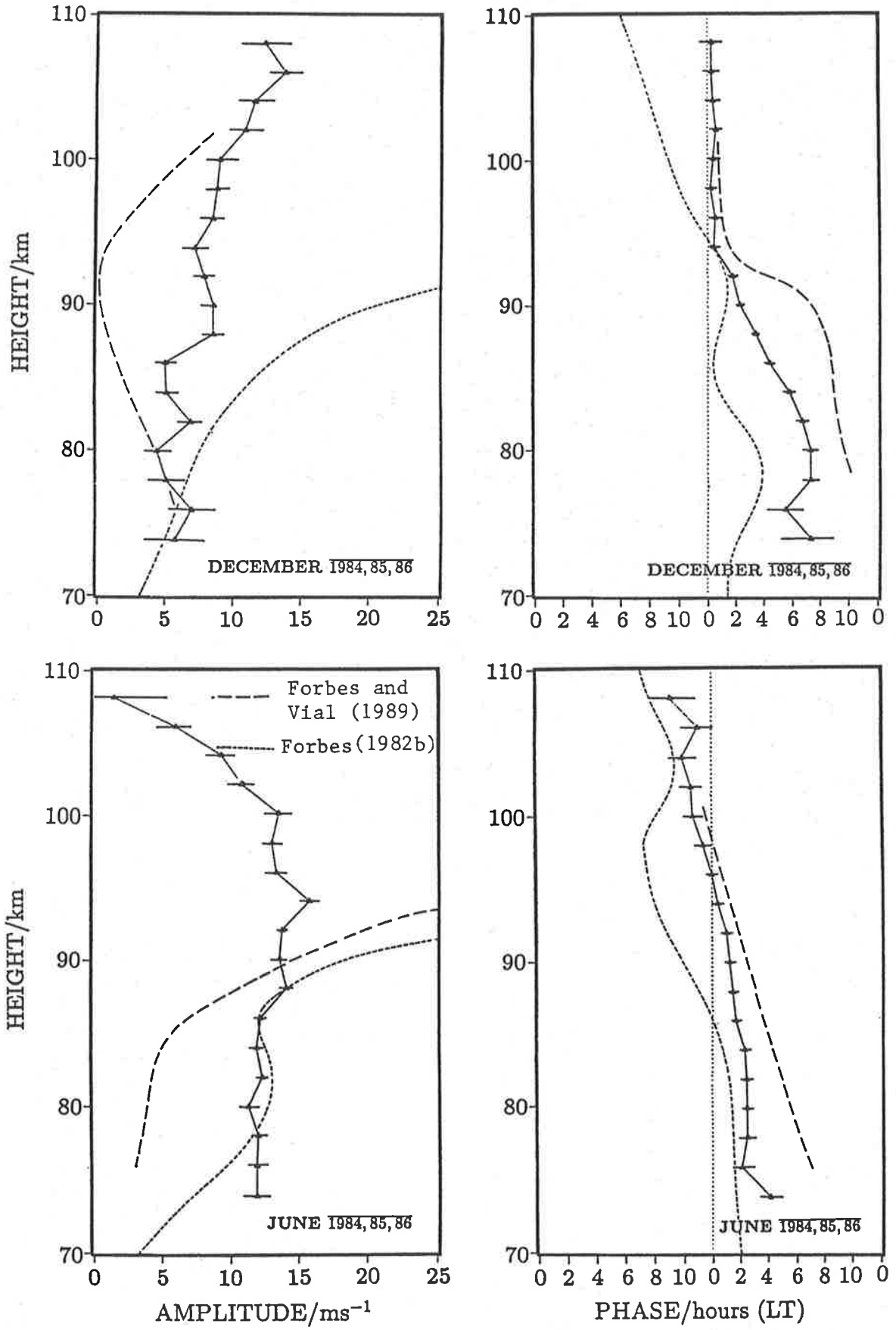

Figure 3.40: **Comparison of the amplitude and phase of the mean meridional semidiurnal tide at Mawson, with the tidal models of Forbes and Vial (1989) and Forbes (1982b)** - details as for figure 3.39.

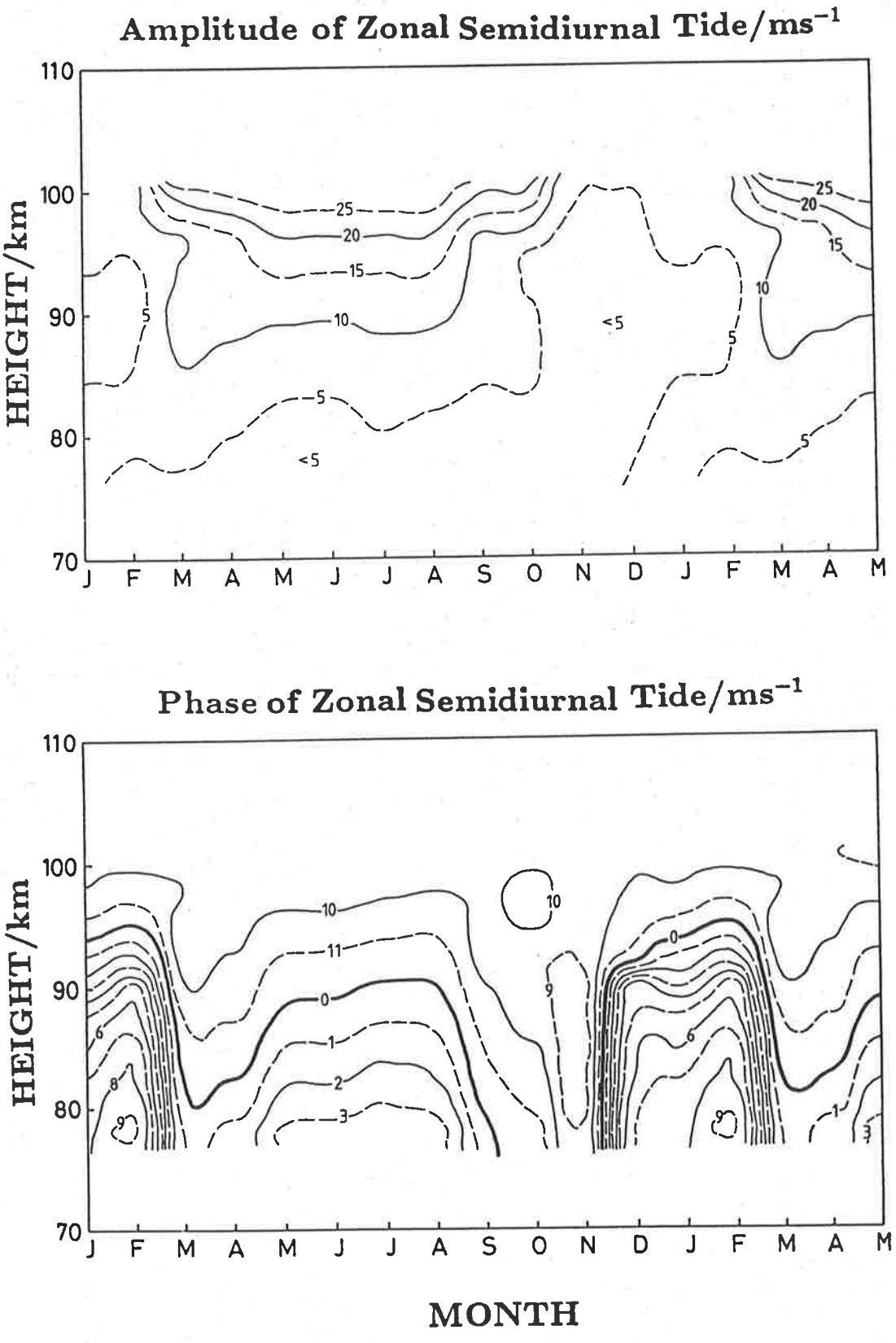

Figure 3.41: **Contours of amplitude and phase of the mean zonal semidiurnal tide at 66° S from the model of Forbes and Vial (1989).** This figure may be directly compared with semidiurnal tidal data from Mawson in figure 3.31 on pages 139.

3.2.5 Discussion

At Mawson, the amplitude of the meridional component of the diurnal and semidiurnal tides is usually significantly larger (often up to 100%) than that of the zonal component and this is generally the case at all heights and during all seasons. This is not the case at Adelaide where the tidal components are usually of comparable magnitude, with neither component dominating at all times and heights (see pages 202 and 203). At Poker Flat there is some evidence that the meridional components are stronger (especially for the summertime diurnal and semidiurnal tide) but the effect is small compared with that at Mawson. This dominance of the meridional component could not be anticipated from the Hough velocity expansion functions (and their normalizing factors (figure 1.5, page 17)). Moreover, the amplitudes of the components in both the Vial and Forbes models are almost identical and hence this very prominent effect is not explained by the existing theories.

Tidal data from Scott base, Antarctica (78°S) (Taken by G. Fraser and presented in Avery et al. (1989)) do not show any enhanced wind component but long term averages (1967–73) from Molodezhnaya (68°S) (Avery et al., 1989 - reproduced in figure A.23, page 214) show a distinct enhancement of the semidiurnal meridional component at all times of the year (at 90 km). However this is not the case for the diurnal tide where no component dominated consistently.

There is the possibility that this dominance of the meridional component could be generated by the SAPR radar technique. The 'winds' measured in the D-region may be distorted by charged-particle drift (in a meridional direction) which is not tightly coupled with the neutral wind. There is some evidence to suggest that the orientation of the characteristic ellipses measured by the SAPR are aligned with the local magnetic

field (MacLeod, 1986) and that the fading time ($\tau_{0.5}$) can be affected during times of geomagnetic disturbance. Until there is some way of comparing SAPR measured winds with another co-located method (such as lidar, Fabry–Perot spectrometer or rocket) an element of doubt will remain with the SAPR method. To remove this uncertainty, research is currently being planned (by the Mawson Institute) to simultaneously measure winds with the Fabry–Perot spectrometer (FPS) installed at Mawson. The FPS will measure temperatures and line-of-sight velocities of the sodium layer at approximately 90 km.

At Mawson, the phase structure of the diurnal tide implies that evanescent tidal modes dominate. Between Mawson and Poker Flat, the zonal diurnal components are approximately in-phase (in local time) and the meridional diurnal components are approximately in anti-phase, implying that symmetric trapped modes such as the (1,–2) or (1,–4) are probably dominant. Enhancement of the diurnal tide during local summer is possibly due to increased excitation of anti-symmetric modes or perhaps simply due to increased insolation leading to greater in-situ forcing. At heights between 90-100 km, sudden changes in the phase of the zonal diurnal component suggest that mode superposition and interference may be occurring. This may be caused by the joint presence of two or more modes or by tidal reflections taking place due to large temperature or density gradients (Vial et al. 1985). Alternately, it is equally plausible that the main source for this tide occurs in the thermosphere and the amplitude and phase profiles are a consequence of the downward propagation of energy. This is consistent with the clockwise rotation of the wind vectors with height and with the approximately linear increase in amplitude (with height) which occurs above 90 km. In addition, figure 3.42 (on page 162) shows that the amplitude of the diurnal tide at Mawson is closely related to the geomagnetic Kp index, which is closely related to Joule heating in the auroral

ionosphere.

Another plausible source of diurnal excitation, characteristic of Mawson's geographic position, is ion drag in the lower thermosphere in response to the magnetospheric electric field (Phillips and Jacka, 1987). It was suggested, on the basis of the simple model represented by figure 3.43 (page 164), that this drag could drive a diurnal variation in the wind with a maximum northward forcing at about dawn, with enhancement at times of high Kp. Interestingly, the observed maximum meridional velocities usually occur (at the 108 km level) at 4–6 h local time. The available evidence supports the idea that the diurnal tides are being driven in the lower thermosphere either by Joule heating or by ion drag associated with magnetospheric electric fields.

The semidiurnal phase profiles imply that the semidiurnal tides at Mawson are propagating modes, but because several symmetric and anti-symmetric modes reach their peak at a latitude of about 60° S (implied from the Hough functions (page 17)), it is unlikely there will be an unequivocal general phase relationship between the northern and southern hemisphere data. This is confirmed by the observations. Short summertime vertical wavelengths in the height range 80–100 km are possibly due to a combination of the (2,6) or (2,7) tidal modes and the longer wintertime wavelengths may be due to the (2,2) and/or (2,3) mode. Between 100-108 km the (2,2) mode is probably dominant, especially in the summer months. The large amplitude and normalization factors for the (2,2) eigenfunctions (figure 1.5, page 17) also suggest this mode should be strong at Mawson.

During the equinoxes, the semidiurnal amplitudes at Mawson substantially increase, typically reaching maximum velocities (for the meridional component) of 20 ms^{-1} at about the 90 km level. Given that the vertical wavelengths (at the heights 80–100 km) are approximately 50 km, it is probable that the (2,4) symmetric modes is being en-

hanced at these times.

Diurnal amplitudes at Mawson tend to remain small ($<5 ms^{-1}$) below 90 km and then to increase linearly from approximately $5 ms^{-1}$ at 90 km to 10–$15 ms^{-1}$ at 108 km. Generally the meridional amplitude exceeds the zonal by 30-100%, especially above 90 km. Semidiurnal amplitudes at Mawson reach a peak at 90±5 km, and during the equinoxes they may average 20-25 ms^{-1}.

Directions of the tidal winds at Mawson (and in the southern hemisphere generally) rotate anticlockwise with the zonal component leading the meridional by approximately 90°. The exception is the diurnal tide, where between 96-108 km the direction tends to rotate clockwise with the meridional component leading the zonal by approximately 90°.

Compared with Adelaide, Mawson has a weak diurnal tide which is quite variable from day to day and month to month. Several years of data need to be averaged to obtain a consistent pattern. However, the amplitude of the semidiurnal tide is comparable with that at Adelaide (where it is typically 20-40% stronger). Semidiurnal phase structure at Adelaide is characterised by abrupt changes in phase during the equinoxes. This behaviour is generally not seen at Mawson, where the changes in the semidiurnal tidal phase tend to be gradual throughout the year (with the notable exception of January when the tidal phases may abruptly change).

Even with the considerable advances in recent years the predictions from tidal models (at high southern latitudes) are, at best, approximate. In the case of the diurnal tide, although the evanescent nature is correctly modelled the coincidence of model phase profiles with the data is very approximate. The large amplitudes observed above 100 km are not apparent in Forbes and Hagan (1988) and Vial (1986). However, diurnal wind measurements above 100 km (at the latitude of Mawson) must be treated with

caution because of the possibility of different drift velocities for charged and neutral particles, especially at times of high geomagnetic activity. For instance, at Mawson, the daily overhead passage of the auroral zone, with the associated particle precipitation, may lead to a diurnal variation in the E×B charged-particle drift occurring in the lower thermosphere. Not until collaborative studies are conducted between the SAPR technique and other methods (*at high latitude*) can full confidence be placed in these data (however, it should also be noted that wind data can only be acquired at relatively quiet auroral/geomagnetic times due to the effects of particle precipitation).

Model predictions for the semidiurnal amplitude (pages 152 and 153) are poor, probably because dissipation is not adequately accounted for in the high order modes. However, for the semidiurnal phase, Forbes and Vial's (1989) model is moderately successful during winter in the height range 80–100 km and during the summer from 94–100 km. The difficulty in predicting precise amplitudes and phases, given the large number of similar-amplitude tidal modes likely to be present, is understandable.

None of the models, either diurnal or semidiurnal, predict the dominance of the meridional amplitude which is perhaps the most conspicuous feature of the tides at Mawson. However it has not been proved conclusively that this effect is not a consequence of the local ionospheric environment. Further measurements by different techniques will be required to prove unequivocally that this effect is real.

3.3 Geomagnetic and high-latitude effects

3.3.1 Variation in the amplitude of the atmospheric tides with geomagnetic activity

In this study, the daily geomagnetic index Ap and the three-hourly index Kp have been used as measures of the degree of magnetic disturbance. Johnson and Luhmann (1985 a,b), and others have looked for a relationship between winds in the mesosphere and geomagnetic activity, but their results, as well as the results of others, show no conclusive correlation. Johnson et al. (1987) did find a relationship between tidal amplitude and geomagnetic activity, but their observation heights of 107 and 115 km are at the top of, and beyond, the range of the SAPR radar. It is therefore expected that the geomagnetic effect in the Mawson data will be small, if it exists at all. The Mawson radar has been operating continuously since July 1984; it records 3–4 data points per hour, at each 2 km height interval between 70–108 km. This is perhaps the most extensive data set for these heights at high southern latitudes currently available; it lends itself well to a search for small effects.

In these studies Kp < 2 is taken to indicate geomagnetic quiet and Kp ≥ 4 to indicate disturbed conditions. These disturbed periods are typically associated with intense auroral displays caused by greater than normal particle precipitation, when electrons penetrating downwards produce more ionization in the D-region; this sometimes improves the SAPR radar data acquisition rate at lower altitudes. However, during extremely disturbed conditions, absorption can be so great as to put the radar 'off the air' for up to several days.

Taking the entire 1985 data set, the wind components were first sorted into high,

medium and low Kp bins and then combined into an 'equivalent day'. An equivalent day is generated by averaging the data according to time of day. An harmonic analysis was carried out in which a least squares fit was made to the diurnal and semidiurnal components. These can be regarded as average diurnal and semidiurnal tides for the whole period.

This analysis shows that the amplitude of the meridional component of the diurnal tide has a distinct connection with Kp; the amplitude increases with increasing Kp as shown by figure 3.42. Between the heights of 75 and 95km the difference in amplitude between high and low Kp categories is 2–4 ms^{-1} but above 100 km it increases to 10–15 ms^{-1}. No such correlation could be found for the zonal component or for either component of the semidiurnal tide. There is also no significant change in the phase of the tides with geomagnetic activity.

The planetary Ap index is used to characterize the level of geomagnetic disturbance on a daily basis. If the data are sorted according to high, medium or low Ap the results show nothing of significance. The tentative conclusion is that whatever mechanism is relating the diurnal tide to geomagnetic activity, it is shortlived and lasts in the order of hours.

The Kp effect seems to be present only in the meridional component of the diurnal variation. At first glance this would suggest that a disturbance to the north or south of Mawson is propagating along the geographic meridian. If, for instance, the disturbance were caused by sudden heating from the auroral electrojet, it might be expected to propagate in a geomagnetic north-south direction. Working on this hypothesis, the coordinate axes were rotated to the invariant magnetic L-coordinate system[3], but the

[3]for a description of this coordinate system, see appendix A.1, page 187.

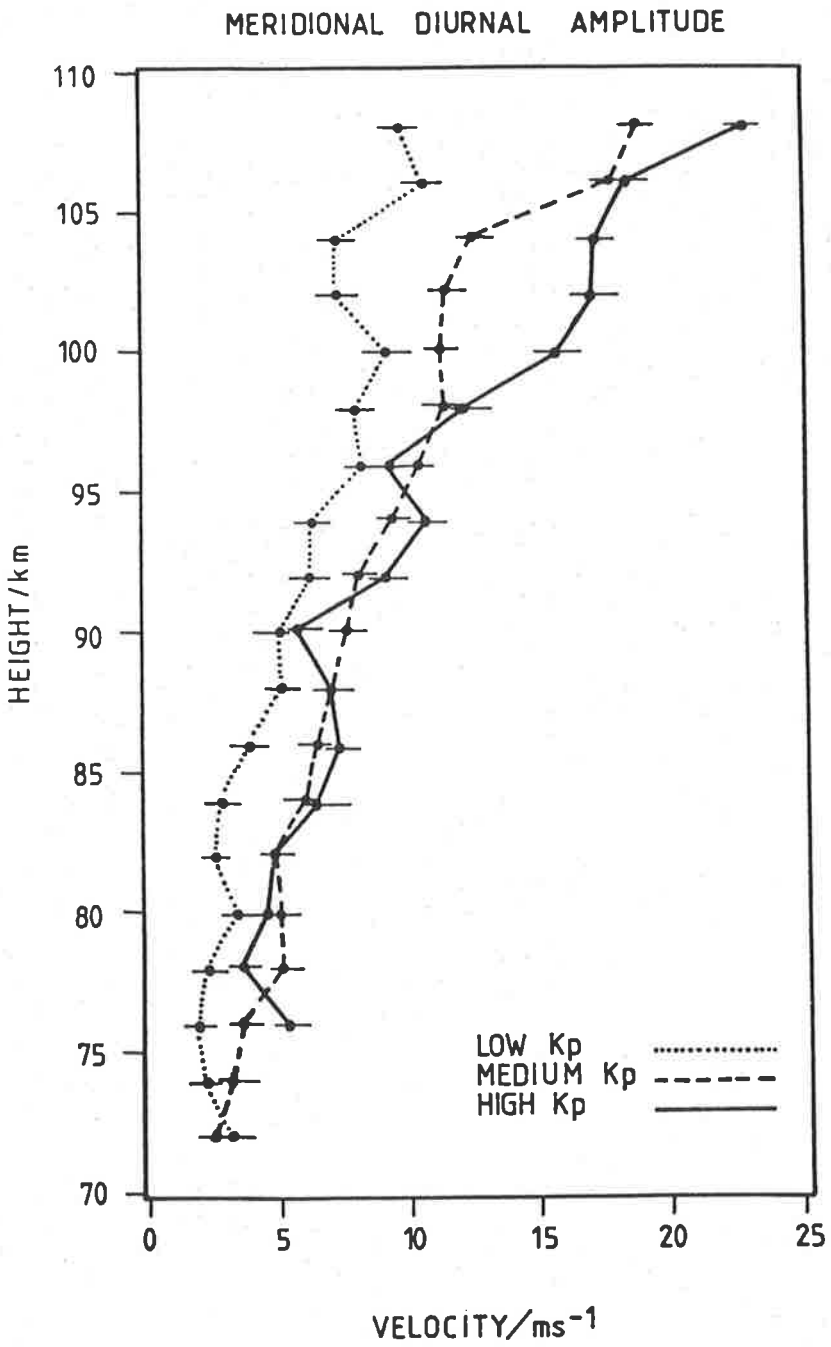

Figure 3.42: **Variation of the amplitude of the meridional component of the diurnal wind as a function of geomagnetic Kp index** (Phillips and Jacka, 1987). These curves were produced by harmonically averaging a complete year of data (all 1985) but separately analysing data according to the Kp figure ('low'=<2, 'medium'=≥2 and <4, 'high'=≥4).

effect of the disturbance on the magnetic meridional component was comparable with the geographic meridional component. Therefore, within the angular resolution of this technique, one can only say that the disturbance is propagating in an approximately meridional direction.

The tidal models of Forbes and Vial (1989), Forbes and Hagan (1988) and Forbes (1982a,b) often show significant (sometimes enormous) increases in the amplitudes of the tides in the lower thermosphere between heights of 100 and 110 km, probably because of inadequate dissipation in the model. This has not been observed in the data. However during the period 1984–87 the sun was in a quiet phase of its 11 year cycle and was not producing the intense prolonged activity required for large UV/EUV heating. But, as noted above, the geomagnetic effect is observed when the data are sorted according to 3-hour Kp, yet not observed when sorting according to daily Ap, suggesting that there is a rather rapid response to the forcing process. Forbes (1982a,b) notes the difficulty in trying to model for such a variable flux. For instance, when modelling the diurnal tide in the height range 90-200 km, the Forbes models are 'tuned' to yield observed diurnal temperature amplitudes under 'average'[4] conditions.

An alternative hypothesis to explain the significant increase in the meridional component of the diurnal variation with increases in Kp invokes ion drag. At the height of the observations, the gyro frequency is much less than the collision frequency, so the component of ion drift and drag in the $\mathbf{E}\times\mathbf{B}$ direction will be small. In the upper thermosphere this is dominant (cf. Wardill, Jones and Jacka, 1987). In the lower thermosphere the direction of motion lies between that of $\mathbf{E}$ and $\mathbf{E}\times\mathbf{B}$ (cf. Jones and Jacka, 1987). An idealised representation of the equipotentials of the electric field is shown in figure 3.43. As the Earth rotates under this pattern, Mawson Station moves

[4]using a global mean exospheric temperature of $\overline{T_0} = 1000^o$ K

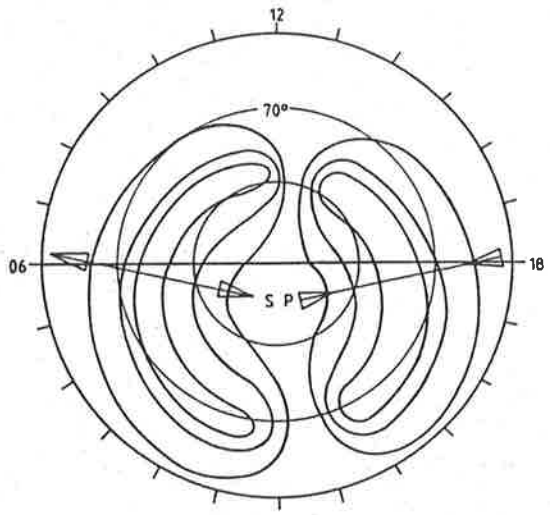

Figure 3.43: **Equipotentials of the high latitude magnetospheric electric field which is approximately mapped down into the thermosphere. The arrows indicate the approximate direction of the electric field across the dawn-dusk meridian. Coordinates are invariant latitude (see notes on page 187) and magnetic local time. Adapted from Heelis et al. (1982).**

around a circular path at 70° geomagnetic invariant latitude. The ion drag would be expected to be aligned in an approximately geomagnetic meridional direction, and with diurnal variation in the forcing, with the maximum northward component near the dawn sector and enhanced at times of high Kp. This is what is observed and illustrated in figures 3.42 and 3.43.

3.3.2 Variation in the strength of reflections at 2-MHz, as measured by the SAPR radar

Although the primary function of the SAPR radar is to measure D-region horizontal winds, a great deal of other information is also acquired, including reflected signal strengths and the mean shape, size and orientation of the diffraction pattern over the ground. This section describes an unexpected variation in the signal strength of the radio waves scattered from the D and E-regions.

During each sounding (which the SAPR radar performs every 5 min) a signal-to-noise

(S/N) figure is computed for each height observed. Because real-time coherent averaging is performed during the data acquisition phase, the radar is capable of detecting signals which are approximately 6 dB below the noise level. Thus the radar, in its simplest form, acts as a very sensitive, single-frequency (1.94 MHz) ionospheric sounder. If the noise is assumed to be constant, the S/N ratio (after averaging) can be taken to be an indication of the echo strength. Figure 3.44 shows the diurnal and height variation of the S/N ratio at Mawson and Adelaide, formed by averaging over all S/N data from 1985. Note that in figure 3.44, the S/N ratio is expressed as a ratio rather than in decibels (dB). This figure shows that there is a significant difference in the height structure of signal strength between the two sites but, before proceeding, further explanation of these S/N diagrams is required.

This study assumes that the 'noise' being measured in the S/N ratio is mainly receiver thermal noise and noise from natural and man-made sources that show no significant systematic diurnal variation. Some man-made noise sources at Mawson, in particular the IPSO ionosonde, produce high levels of pulsed broad-band noise. However, because the digitization of the received signals by the SAPR radar is gated over a very small time interval, the effects of pulsed type interference are negligible since the unwanted pulses very rarely occur at the relevant instant of time. Other electrical noise from motors, generators, computers and fluorescent lights is significant, and ultimately limits the performance of the experiment, but fortunately (for the purposes of this study) this noise level tends to be constant with no significant diurnal variation. Although there is a general problem of radio interference at Mawson, the harmonics of the SAPR radar are also often cursed! Frequencies around 1.94 MHz are used by international shipping but there is no detectable long-range propagation of these signals to Mawson.

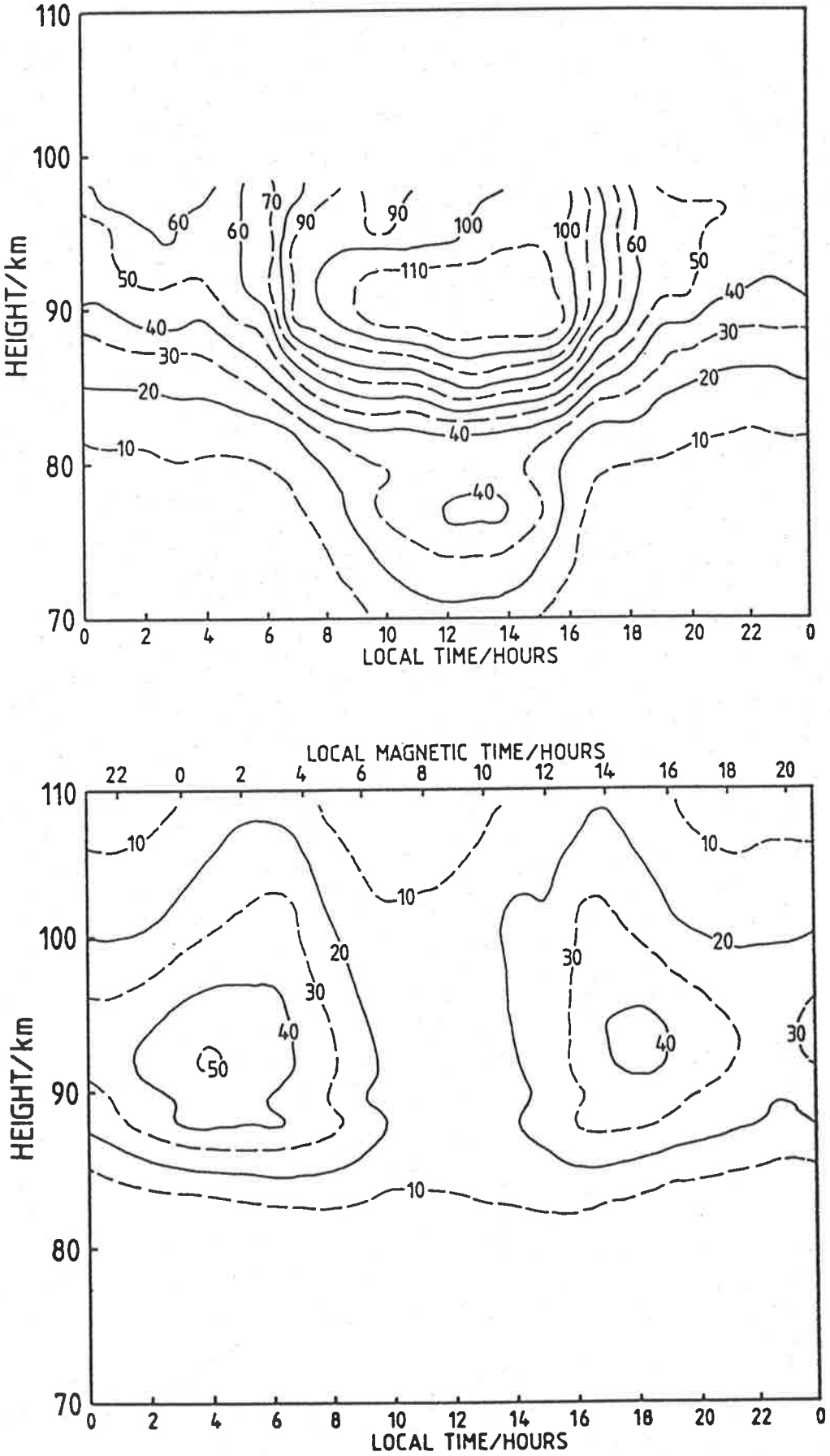

Figure 3.44: **Diurnal variation of the SAPR radar signal to noise ratio at Adelaide (top) and Mawson (bottom).** Note that the S/N ratio is expressed as a *ratio* (rather than in decibels) and that the local magnetic time scale is for Mawson only.

It is acknowledged that the use of S/N data to represent echo field strengths is less than ideal but, given the preceeding considerations, it is reasonable to assume that the averaged S/N ratios do give an indication of the *relative* power being reflected from various levels in the ionosphere. However, it should be noted that values of S/N for Mawson and Adelaide (in figure 3.44) cannot be compared directly as the larger transmitter power (and antenna systems) used at Adelaide will lead to larger S/N ratios. Also the noise level is probably different at the two sites. When calculating a 'mean' S/N ratio, care must be taken. Because the S/N ratio distributions are non-Gaussian, and S/N ratios can be enormous for short periods when signals are strong, a simple algebraic average of the S/N ratio can produce misleading values which are often far larger than those normally observed. Another alternative is to form the geometric mean $((x_1 \times x_2 .... x_n)^{\frac{1}{n}})$, which in fact was used in figure 3.44. This has the advantage that it is less influenced by short powerful bursts and is more representative of the 'typical' S/N values observed. Also, since the data-collecting efficiency of the SAPR radar is closely related to the S/N ratio, diagrams of geometrically averaged S/N ratio (such as figure 3.44) give an indication of the rate of data acquisition.

At Adelaide there is clearly strong solar control of the D-region ionization, with an almost total absence of reflections below a height of 80 km during nighttime. When the radar at Mawson commenced operation, the author was surprised at the pronounced semidiurnal variation in the data acquisition rate. During the early morning and mid-evening, the radar operated very efficiently and acquired large amounts of data. However, towards midday and midnight, the radar often went 'dead' due to an apparent total loss of reflected signal. The two periods of strong reflections which occur at Mawson are centred on a height of approximately 90 km at 5 and 20 h local time. At Mawson, acquisition of data below a height of 80 km is infrequent at the best of times, but in contrast

to Adelaide, the midday signals below 80 km are often weaker than in the morning and evening. If it were not for the large loss of signal around midday at Mawson, then the diagrams in figure 3.44 would probably be similar. This poses the question of whether there is a genuine 'semidiurnal' variation in echo signal strength at Mawson, or whether some effect, peculiar to the radar at Mawson, is leading to a loss of signal during the day. Possible explanations for this effect include the polarization of the radar signal, and ionization processes, such as particle precipitation or horizontal/vertical transport of ionization.

Figure 3.45**(bottom)** shows the total number of wind data points collected during 1985, as a function of season and time of day. The semidiurnal oscillation in acquisition rate is apparent during all seasons. Reflections from the height range 70–80 km are much stronger during the winter[5], therefore the total data acquisition rate during summer is smaller than in winter. However the effect is also exaggerated in figure 3.45 (bottom) due to increased system downtime (for maintenance) which occurred during the summer.

Perhaps the simplest explanation for the midday loss of echoes, is that the transmitted signal is incorrectly polarized (linearly, elliptically or circularly polarized in the wrong sense).[6] In fact (during 1985) the experiment operated in *only* the E-mode. However, the decision to operate the radar in only the E-mode was based on the observation that the data acquisition rate was not significantly affected by polarization (except that the acquisition rate was a often a little better in E-mode). There were none of the strong day/night polarization effects characteristic of Adelaide. This raises the possibility that something may have been wrong with the transmitting hardware and a circularly polarized signal was not being transmitted. This is plausible but during the summer of

[5]winter anomaly:see section 1.3.1, page 28

[6]the requirement for a circularly polarized signal is discussed in section 1.4 page 38

1988-89, the author returned to Mawson to work with the radar and care was taken to ensure that the polarization function of the transmitting and receiving arrays was working correctly. The midday loss of signal was still apparent when either polarization was used. Therefore, the author believes that the effect is not caused simply by an inappropriate polarization being used.

The present system now conducts (on the hour) a sounding in E-mode, followed by one in the O-mode. The most successful mode (measured by the number of data points and signal strength) is retained for the next hour. The author observed no consistent preference for one polarization during the day or night.

If polarization is not causing the midday loss of signal, then there are a number of other possible explanations peculiar to Mawson's geographic position. For instance, energetic particle precipitation processes may lead to increased ionization at lower, more dense regions of the atmosphere causing absorption at 1.94 MHz. Riometer records from Mawson show a significant increase in absorption around local midday and, to a lesser extent, around local midnight. Figure 3.45 (top) from Eather and Jacka (1966) shows a 0.5–1 dB attenuation at 27.6 MHz, observed around midday, especially during the winter months. The absorption measured by the riometer is occurring within the SAPR observing range (and below) and may well be greater at 1.94 MHz than at 27.6 MHz.

Since the data acquisition rate of the SAPR radar often showed marked variations during times of intense auroral/geomagnetic activity, a study was conducted to investigate the relationship between reflected signal strengths and geomagnetic activity. As with the earlier study of the geomagnetic effects on the tides, data were sorted according to the geomagnetic (3-hour) Kp index, with $Kp < 2$ taken to indicate geomagnetic quiet and $Kp \geq 4$ indicating disturbed conditions. Figure 3.46 presents height-time profiles of S/N ratio for the overall mean ($\overline{1985}$) and for 'low', 'medium' and 'high' Kp.

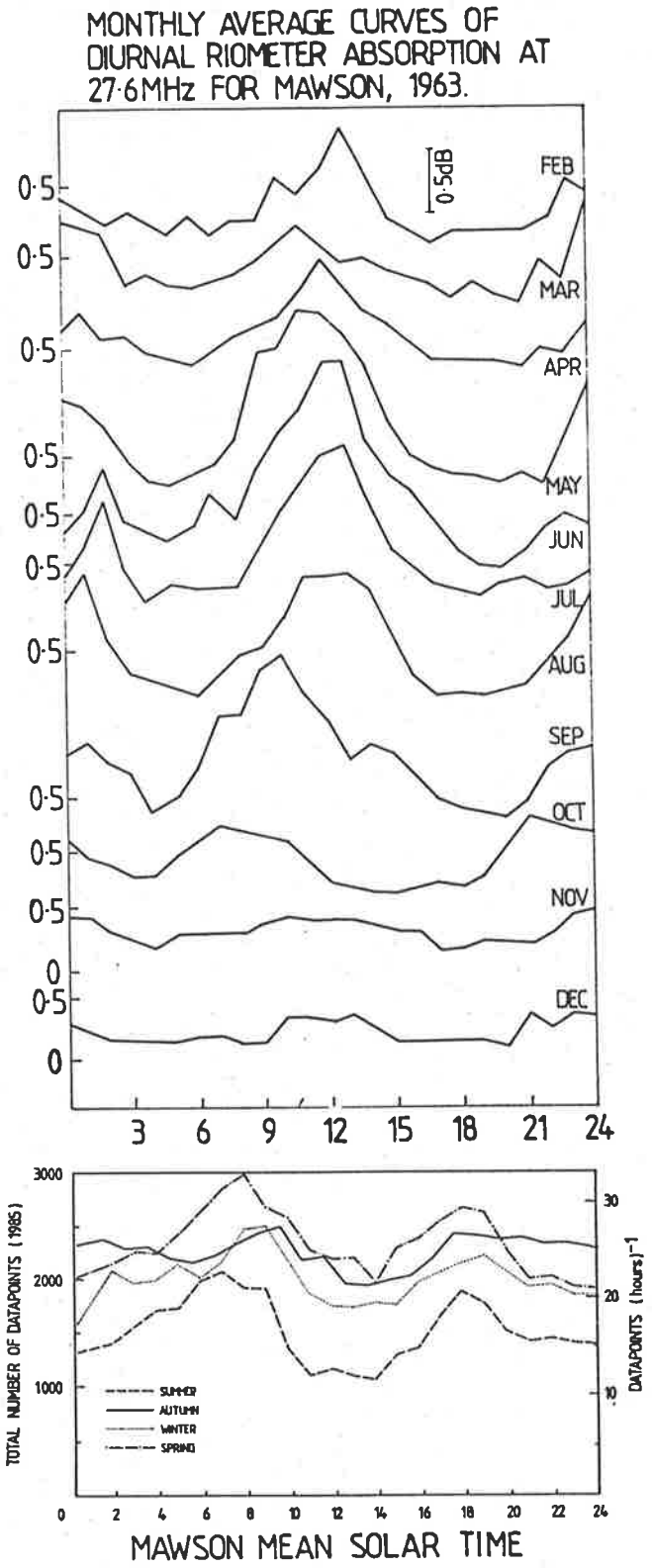

Figure 3.45: **(top) Monthly average curves of diurnal riometer absorption at 27.6 MHz for Mawson, 1963** (adapted from Eather and Jacka, 1966). The vertical axis is in units of dB. (bottom) The diurnal variation in the number of data points acquired during 1985.

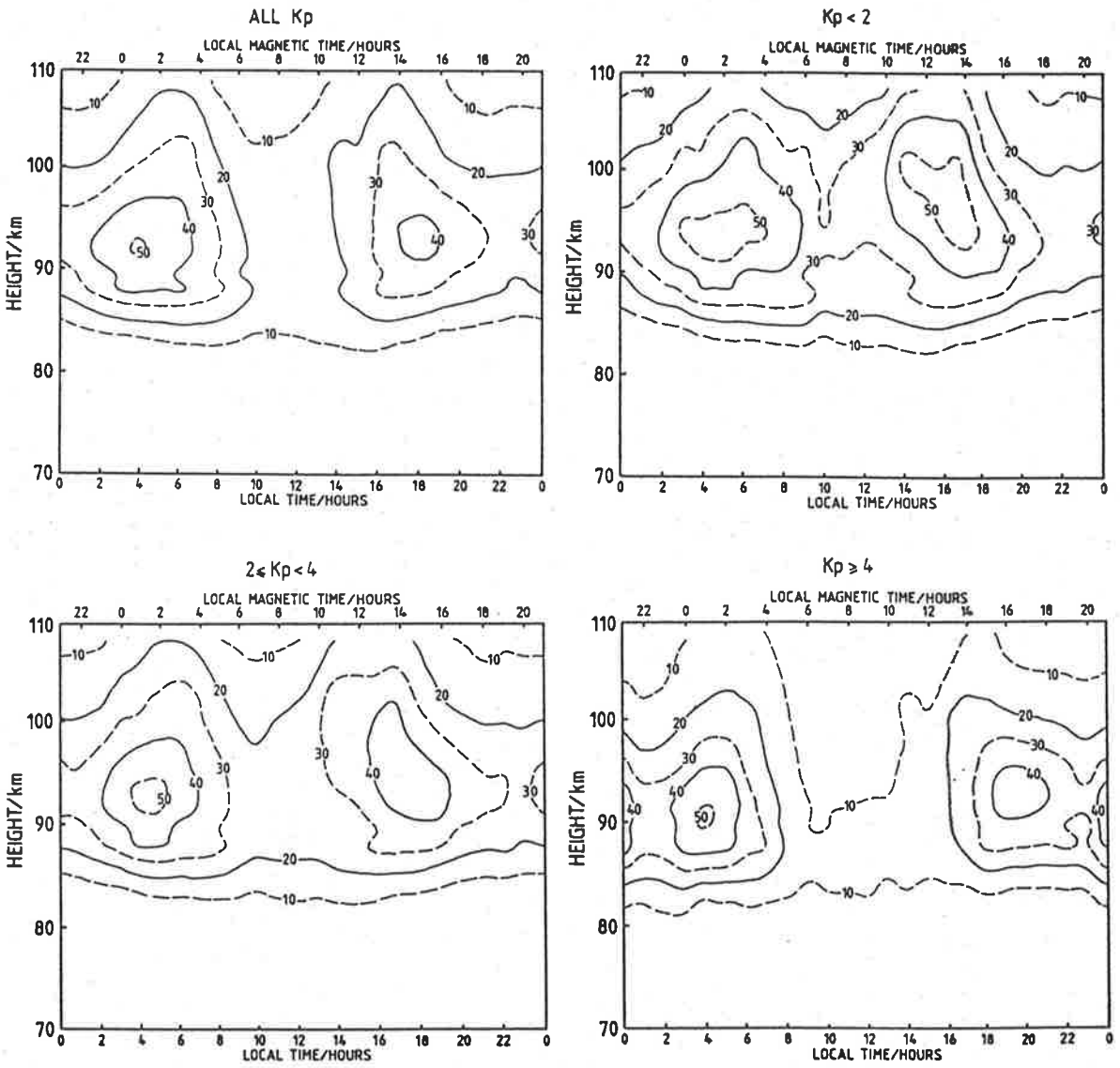

Figure 3.46: **Contours of mean signal-to-noise ratio, (at Mawson) for different values of the 3-hour Kp index. A complete year of data (1985) was used in the production of these diagrams. Note that the S/N ratio is expressed as a *ratio* (rather than in decibels).**

The most prominent feature is the greatly increased attenuation centred around midday during disturbed conditions. That is, at lower levels during quiet conditions, there is a tendency for echo strengths to increase around midday, whereas during disturbed conditions they tend to be reduced at midday. A similar study was conducted by sorting the data according to the local K-index, and precisely the same general features were observed as with the Kp index (For interest, the K-index plot is included in appendix A.5, page 215).

The absence of echoes around midnight may be due to a loss of ionization (as is

the case at Adelaide), but given the increase in riometer-measured absorption, particle precipitation may also be the cause. The *semidiurnal* variation in the riometer and SAPR records suggests that the atmospheric tides may be associated in some way. In the tides section of this thesis, the semidiurnal tide at Mawson was shown to be of comparable (or greater) strength than the diurnal tide, and the phase of the semidiurnal tide was shown to be relatively stable. In the ionosphere, it is known that the interaction of winds with an inclined magnetic field can place a vertical force on the ions, which are partially constrained to follow magnetic field lines. This effect is generally thought to diminish rapidly in the lower thermosphere and to be ineffective below about 90 km.

Figure 3.47 shows the variations in S/N ratio with height and time when the data are sorted according to the seasons. Two years (1985,86) of data are averaged. Seasonal trends include a lowering of the minimum observing height and a deepening of the midday 'trough' during winter. During summer consistently strong reflections occur centred around a height of 100 km at 7 and 16 h local time. It is interesting to note that the two lobed 'cats-eye' pattern frequently observed in these S/N diagrams also occurs in data collected during the winter solstice when the sun is below the horizon (at ground level). This is not really surprising as it must be remembered that at an altitude of 100 km (during the winter solstice) the sun will still rise approximately 10° above the horizon and therefore solar-induced ionization is anticipated.

At Mawson the magnetic inclination and declination are (approximately) 68° S and 63° W respectively. This means that winds in the ionosphere which blow towards magnetic north (297° geographic) will tend to lift the ions and vice-versa for magnetic southward winds. To investigate the possibility that this mechanism may (in part) explain the S/N observations, wind data from Mawson were rotated to magnetic coordinates and an harmonic analysis of the tides was conducted. In figure 3.47 the times of

maximum magnetic northward winds resulting from the semidiurnal tide are indicated by upward pointing arrows and similarly downward pointing arrows indicate southward wind. In this figure both S/N data and tidal data were sorted according to season. Several consistent (though possibly coincidental) features are apparent. The midday trough usually corresponds to times when winds are blowing magnetic eastward and therefore no vertical motion of the ionization would be expected. At heights of 70–80 km the ionization might be expected to be moving downwards around midday. The peak in reflected power which occurs at approximately 92 km and 3–5 h local time, corresponds to an upward flow of ionization whereas the second peak at 92 km and 17–19 h local time generally occurs with magnetic westward winds (ie. no vertical forcing of ionization). It has recently been suggested to the author, that the above study uses only the *semidiurnal component* of the wind and that an analysis of the total wind may lead to some interesting results. This study will be incorporated into a forthcoming paper.

Discussion

A relationship between geomagnetic activity and the amplitude of the diurnal tide is apparent in figure 3.42 (page 162). This may be due to the downwards propagation of thermospheric tides or to increased ion drag effects due to larger electric fields mapped downwards from the magnetosphere. This latter idea is supported by Johnson et al. (1988) who see a similar effect in tidal data observed by the MST radar at Chatanika, Alaska. In their observations of the wind at heights of 107 and 115 km, they find an increase in the diurnal tidal amplitude and a decrease in the semidiurnal amplitude during more active times (Kp>2). They attribute this to the relative phase of the background tides and the diurnal variation of the ion-drag forcing. However, it should be noted that an MST Doppler radar deduces wind by tracking ionospheric

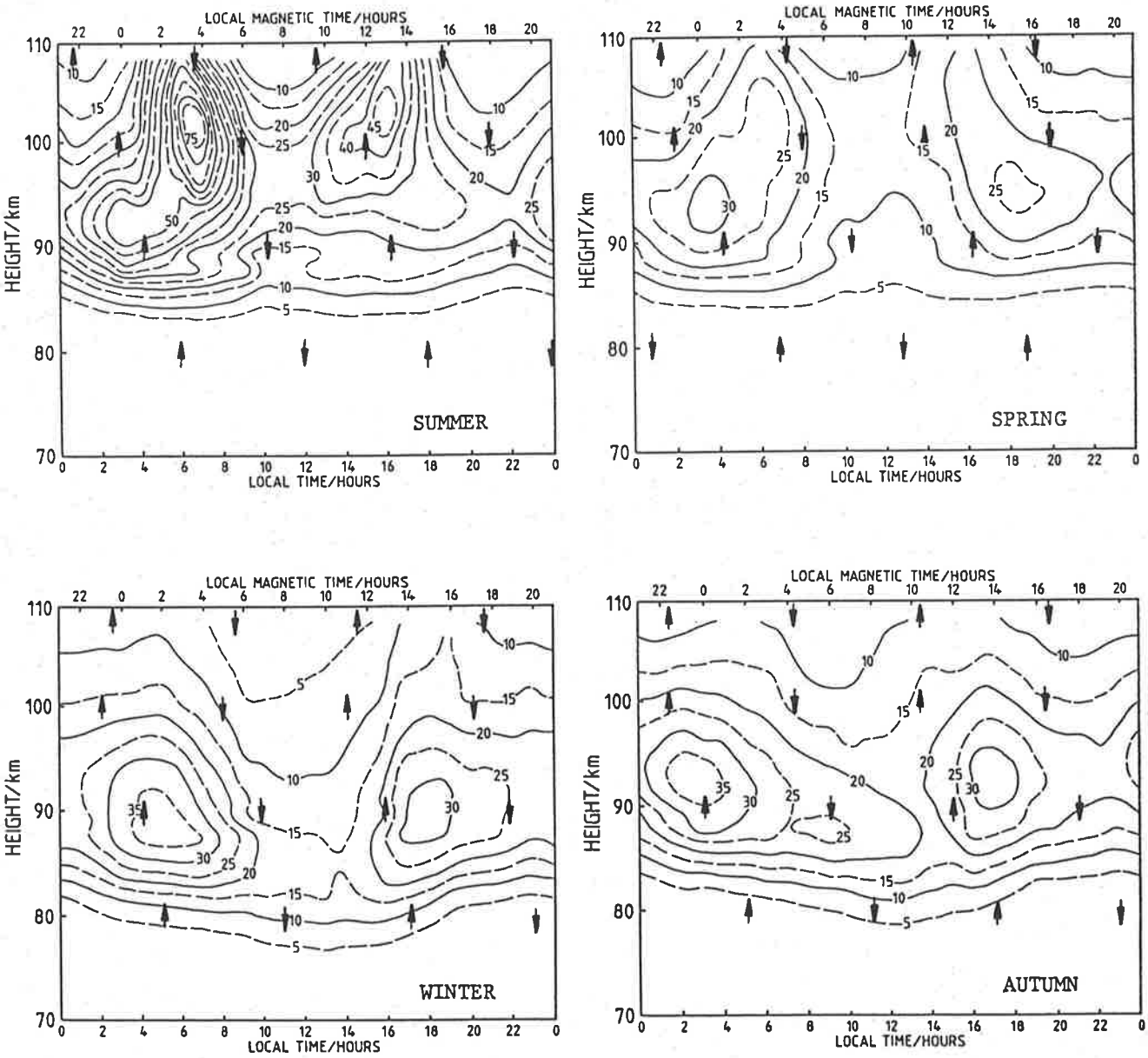

Figure 3.47: **Contours of mean signal-to-noise ratio (at Mawson) for different seasons.** Note that summer= the months of DJF, autumn=MAM, winter=JJA and spring=SON. Arrows indicate the time of maximum upwards or downwards forcing of charged particles, due to the interaction of the semidiurnal tidal wind with the local magnetic field. Two years of data (1985,86) were combined in the production of these diagrams. Note that the S/N ratio is expressed as a *ratio* (rather than in decibels).

irregularities and these results may be partly (or wholly) due to electric field induced ion drift (Reid, 1983) rather than ion drag on the neutral winds.

The D-region ionosphere at Mawson is significantly different from that at Adelaide. For instance the size of the pattern scale at Mawson (reflected from a height of 90 km) is typically 260 m whereas at Adelaide it is typically 360 m. These pattern scale sizes show pronounced diurnal, seasonal and (probable) geomagnetic variations. A full analysis of these pattern data, along with the dynamical inferences, is outside the scope of this discussion; they have been examined statistically by Price (1988), with an emphasis on the variation with geomagnetic conditions. Australia's Ionospheric Prediction Service Organization (IPSO) operates an ionosonde at Mawson. Ionograms from Mawson are characterised by greater D-region absorption and they tend to show fewer 'multi-hop' effects[7] than in Australia. This is the case at mid-latitudes but *especially so* at Mawson. It is interesting to note that the SAPR radar is considerably more sensitive than the ionosonde at Mawson. For example, the very lowest echoes observed by the ionosonde are at approximately 90 km at a frequency of 1.5–2.0 MHz). They do not observe absorption around midnight.

Mawson is a unique place to observe auroral and geomagnetic phenomena, having the highest incidence of overhead auroras of any observatory in the southern hemisphere. In fact the original decision of where to site Mawson (established 1954) was partly based upon its position within the auroral zone. Most of the time Mawson is within the region known as the auroral oval. Figure 3.48, from Bond and Paine (1971), shows the mean position of the auroral oval, along with the inner and outer envelopes, for different levels of the geomagnetic Kp index. Mawson's invariant latitude is 70° S (ie. colatitude 20° in figure 3.48) which means that during times of normal geomagnetic activity (Kp=1–3),

[7] i.e. multiple reflections between the ionosphere and the ground

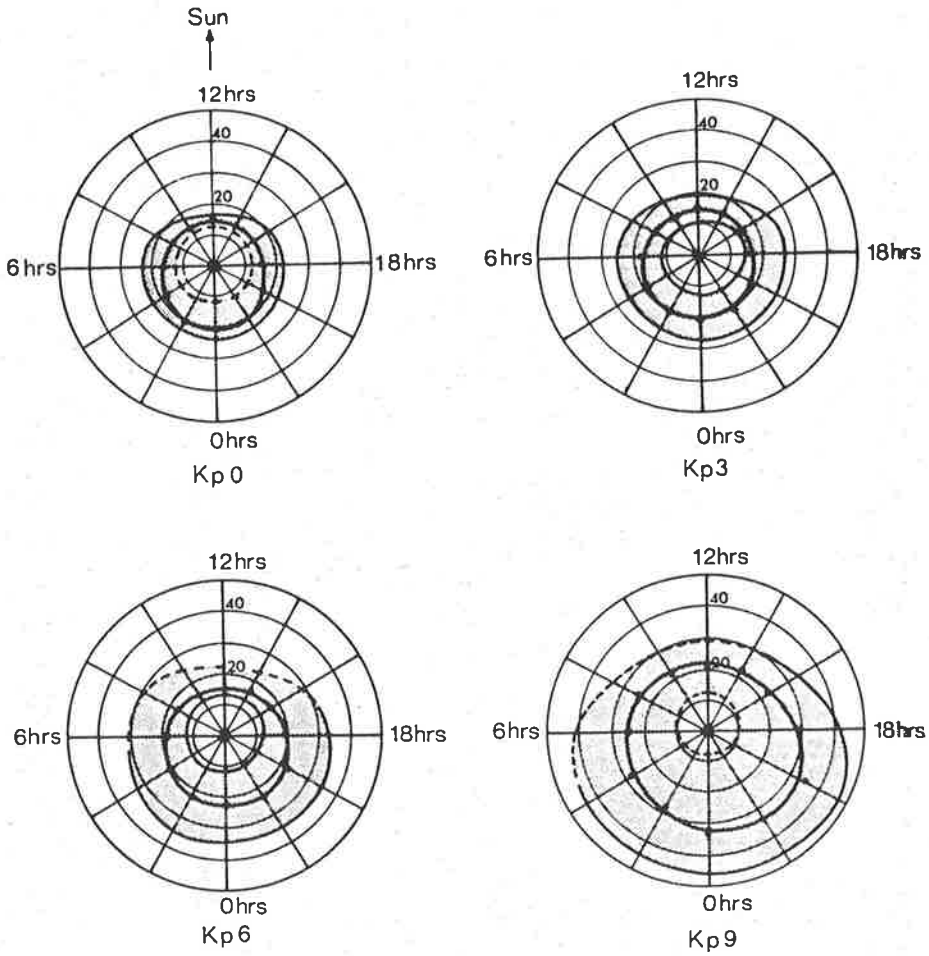

Figure 3.48: **Smoothed mean locations of the austral auroral ovals shown together with the poleward and equatorwards envelopes for Kp=0,3,6 and 9 (Bond and Paine, 1971). Coordinates are invariant co-latitude and local magnetic time. Dotted lines indicate that data are limited and the 'probable' envelopes are shown.**

Mawson will move during the day (relative to the oval) from the outside region to the central region of the oval. During times when Kp=6, Mawson will be completely within the oval at all times and the centre of the oval will pass overhead twice a day. This effect is demonstrated in figure 3.48 where the geomagnetic latitude of the centre of the oval is shown as a function of time, geomagnetic latitude and Kp index.

Comparison of figure 3.48 with figure 3.45 shows that the midday loss of signal is coincident with Mawson being located *northward* of the centre of the oval. (Local midday at Mawson corresponds to approximately 9 h magnetic time.) During normal-to-quiet geomagnetic conditions figure 3.48 shows that this (ie. midday) is the time

when Mawson is near the outside northern edge and is commencing to move inwards (figure A.2 in appendix A.5 is similar to figure 3.48 but shows the diurnal motion of the auroral oval in geographic coordinates) It is clear from this diagram that around local midday and during normal-to-quiet geomagnetic conditions, Mawson is near the outer edge of the auroral oval. Although this is an interesting coincidence, the author cannot find any literature linking this region of the auroral oval to any belt of particle precipitation, or any other effect which might lead to these observations.

In summary, the investigation of possible causes of the semidiurnal variation in S/N ratio considered the following:

- Inappropriate polarization
- Variation of the effect with different levels of geomagnetic disturbance
- Variation in the local (man-made) terrestrial noise
- Energetic particle precipitation
- Vertical forcing by the interaction of tidal winds with the local magnetic field
- The overhead passage of the auroral oval and the possible relationship with the auroral electrojet or a belt of precipitation which retains a constant position with respect to the auroral oval

It is the author's belief that an effect other than inappropriate polarization is leading to the midday loss of signal at Mawson. The most plausible explanation is that energetic particle precipitation is leading to increased absorption in the lower D-region. However, within the limitations of these data, and the absence of corroborative observations, this is speculative.

3.4 A summary of conclusions

Mean winds at Mawson (and in the southern hemisphere generally), in the height range 70–110 km, are significantly stronger than in the northern hemisphere and do not show (obvious) effects of the stratospheric warmings which are apparent in comparable Poker Flat MST wind data. At Mawson, the spring reversal in the zonal wind direction is very abrupt and appears to occur a little later in spring than at Poker Flat. Meridional winds from Poker Flat and Mawson do not show clear annual oscillations, except for a summertime equatorward flow which often peaks at, or just above, 90 km. Current semi-empirical mean wind models are found to be significantly at variance with the radar mean wind observations. In particular, geostrophic winds from Barnett and Corney (1985) and Fleming et al. (1988) have wintertime values which are generally 3–4 times stronger than those observed. Summertime geostrophic winds are in better agreement (including the timing of the zonal wind reversals). Although the model mean winds all tend to show an eastward bias, the magnitude of the annual zonal oscillation (from Fleming et al. 1988) is in good agreement with the radar observations.

Long period wave activity at Mawson is very weak compared with Adelaide, where consistently negative ($\overline{u'v'}$) fluxes imply an equatorward Eliassen-Palm flux. At Adelaide there is a strong increase in wave activity during the wintertime (propagated from below) but this is attenuated strongly in the height range 70–80 km, possibly due to gravity wave drag effects (Miyahara, 1985).

The quasi 2-day wave is a regular feature of the high-latitude summer in the height range 70–108 km, and at its maximum during January wind amplitudes may reach 10–15 ms^{-1}. This appears to be stronger than that observed at similar latitude stations in the northern hemisphere. This is consistent with observations of the wave

being stronger in the southern hemisphere generally (Craig and Elford, 1981; Vincent, 1984). The relative amplitude of the zonal and meridional wind components of the wave at Mawson are sometimes comparable but usually the meridional component is the stronger, whereas at Adelaide the meridional component always predominates. At both Mawson and Adelaide the period is very close to two days (48±2 h) and the phase relationship between Mawson and Adelaide is consistent with a westward travelling, wavenumber 3, Rossby-gravity normal mode of the type proposed by Salby (1981).

At Mawson, the amplitude of the meridional component of both the diurnal and semidiurnal tides is usually significantly larger (up to 100%) than that of the zonal component. This is not the case at Adelaide, where component amplitudes are usually very similar. Observations from Poker Flat and Molodezhnaya suggest that the meridional amplitudes may exceed the zonal. This effect may be due to ion drag, which is preferentially oriented in a N–S direction; a decoupling of electrons in an electric field (leading to a drift of ionized irregularities not related to the wind in the neutral air); a hitherto unrecognized breakdown of full correlation analysis when applied to high-latitude data; or an error in analysis. Comparison with other (non-radiowave) observing techniques, such as Lidar or Fabry-Perot spectrometer observations, is required to confirm the reality of this observation.

The phase structure of the diurnal tide shows that evanescent tidal modes predominate. Comparison between Mawson and Poker Flat suggest that the (1,–2) or (1,–4) modes probably account for most of the observations. Enhancement of the diurnal tide during summer is possible due to increased amplitude of anti-symmetric modes or increased insolation leading to greater in-situ forcing. The phase profile of the meridional component usually undergoes a sudden phase change in the height range 90–100 km. This may be due to mode superposition or mode interference or perhaps interference

due to downward propagation of energy from the thermosphere.

Semidiurnal phase profiles imply that a mixture of modes are present. Pronounced seasonal changes include a tendency for shorter vertical wavelengths in summer and longer during winter. These wavelengths suggest that the summertime tides (in the height range 80–100 km) may be due to the (2,6) or (2,7) tidal modes while the (2,2) or (2,3) may dominate observations during the summer. During the equinoxes the semidiurnal amplitudes increase substantially, reaching maximum velocities of around 20 ms^{-1} at around the 90 km level.

The amplitude and phase of the diurnal tide at Mawson are highly variable on a daily, seasonal and annual basis. By comparison, the semidiurnal tide is considerably more stable and does not show the abrupt phase changes seen at Adelaide during the equinoxes. Comparisons of the radar measured winds (from Mawson) with current tidal models show, at best, only approximate agreement. However the difficulty in obtaining absolute amplitudes and phases when modes are superimposed is quite understandable and, in view of this, the tidal models do form a reasonable description of the tidal nature of the atmosphere in our observing range.

Geomagnetic effects are apparent in the wind data. In particular, the meridional component of the diurnal atmospheric tide is enhanced during times of high Kp. The effect increases with height, and is similar to the findings of Johnson et al. (1987) who have analysed winds from the MST radar at Chatanika, Alaska, and who attribute the effect to ion drag on the neutral wind. It is highly probable that this mechanism is also responsible for the Mawson observations although the possibility of magnetospheric electric fields leading to a systematic drift of the ionospheric irregularities cannot be discounted.

At Mawson there is a significant decrease in the strength of the signals reflected from

the D-region at around midday and, to a lesser extent, midnight. The decrease in signal (compared with that during the morning and evening) is typically 20–30 dB at 90 km. Historical riometer data from 1963 also show a midday/midnight increase in absorption in cosmic radio noise (at 27.6 MHz). The midday attenuation is increased during times of high geomagnetic activity, when reflections may disappear altogether. The root cause of this attenuation is unknown but it is probable that energetic particle precipitation into the D-region is leading to increased absorption at levels at the bottom of (and below) the SAPR radar observing height range. The possibility that the semidiurnal tidal winds were interacting with the geomagnetic field was investigated and was considered an unlikely explanation of the observations. Mawson is usually located on the outside edge of the auroral oval at around local midday. There is the possibility that this region of the oval may be associated with a belt of precipitation but the author knows of no such belt. Another possibility is that the radar may be transmitting an inappropriately polarized signal which is being strongly absorbed during the day. For several reasons this argument appears unlikely though is being further investigated. For the moment the cause of this effect, which is closely related to the data acquisition rate, is unknown.

3.5 Suggestions for further work

Some future directions for the SAPR radar at Mawson are suggested by the present limitations and potential improvements of the instrument. For example, considerably more transmitter power would permit sounding below the current lower limit of approximately 75 km. Mesospheric wind data from the southern hemisphere at high latitude is sparse and urgently needed to form newer and better wind climatologies. Recent suggestions by Von Biel (1988) of a high-latitude layer of increased ionization (centred at about 40 km) holds the promise that winds in the upper stratosphere may be measured by the SAPR technique. An improved time resolution between soundings (currently 5-15 min) would reduce the errors of long-term wind and tidal averages and lead to a considerable improvement in accuracy when studying transient phenomena such as turbulence and short-period gravity waves. This could be achieved by increasing the transmitter PRF and by faster real-time computer processing of data. The implementation of some of these improvements is scheduled for summer (Jan–Feb) 1989, by the replacement of the NOVA computers by considerably faster IBM–XT (clone) computers.

These new computers will also permit extremely rapid acquisition and storage of large amounts of raw data, which could be analysed fully at a later date. Such campaigns would be useful in the study of very short-term phenomena such as the rapid response of the winds to heating which occurs during auroral substorms and impulsive particle precipitation events. Because the radar at Adelaide is very similar to that at Mawson, considerable amounts of software which have been written at Adelaide could be relatively easily installed at Mawson. The addition of a more modern computer will (it is hoped) result in considerably less downtime due to maintenance and faults.

The transmitter will be replaced when the funds become available.

Perhaps the most important requirement, is an improvement in the confidence that the 'winds' being measured by the SAPR radar do actually represent the bulk motion in the upper mesosphere/lower thermosphere. With the absence of co-located measurements by other techniques, there remains a a small but lingering doubt[8] about the reliability of the SAPR wind data (especially that in the height range 100–108 km). This problem is currently being tackled with a program of simultaneous measurements by the Fabry-Perot spectrometer and 3-field photometer at Mawson. It is also hoped that a Lidar, currently under construction at the Mawson Institute (Adelaide) will be able to measure winds and temperatures at heights within the SAPR radar observing range.

Further collaborative studies with northern hemisphere, high-latitude sites (such as the MST radar at Chatanika, Alaska (65° N) and the EISCAT incoherent scatter, northern Scandinavia) are needed to investigate the similarities and differences between the hemispheres. Collaborative work with the SAPR radar at New Zealand's Scott Base (78° S, 166° E) is another area which is potentially very interesting, especially for study of planetary wave propagation (The author is very keen to pursue studies of the quasi 2-day wave at high latitude!). Interestingly, the SAPR transmitting equipment at Scott Base is shared with a differential absorption sounder. The similarity of the hardware for the two techniques also raises the possibility that the Mawson SAPR radar could be configured to measure differential absorption, although some upgrading of the antenna systems would be required.

Despite several years of continuous measurement of the winds at Adelaide, Christchurch and Mawson, there has not yet been a coordinated study of the amplitude and variabil-

[8]not with FCA theory, but the possibility of a programming error or unexpected drift of ionization relative to the neutral wind

ity of the atmospheric tides. One fundamental question that remains unanswered, is whether the variation in the tides is of local or global extent, or whether (for instance) a disturbance is propagating between stations. Between the high-latitude stations, studies could be undertaken to measure the possible changes in the tides which may occur simultaneously during times of intense auroral activity.

Because of the convergence of the Earth's magnetic field lines into the polar regions, and because of the tendency for charged particles to travel along magnetic field lines, observations of the high latitude thermosphere additionally permit a window into the solar/terrestial space environment. The relationship between solar activity and the winds in the upper mesosphere/lower thermosphere is unknown; long-term observations from Mawson (of one solar-cycle or greater) would be a valuable contribution towards the study of this relationship.

Over the time the Mawson radar has been operating, new uses for it have been found. For instance, S/N data have been useful as a measure of auroral activity and these data have been correlated with short-term magnetic and auroral fluctuations (Price, 1988). These data are valuable as the electronically noisy environment at Mawson has rendered the riometer virtually useless, and the IPSO ionosonde lacks the necessary sensitivity and time resolution required for real-time comparison with short-term auroral/magnetospheric observations. It is probable that other phenomena, not currently apparent in the wind (or other) data recorded by the SAPR radar will be of use later on. For the study of small effects there is considerable benefit in having a long-term (ie. several years) unbroken data set. It is hoped that the current upgrading of computer hardware will be followed by the installation of a solid-state transmitter ensuring a viable, low maintenance system that will run for many more years. With the current interest in the 'ozone hole' in the southern polar stratosphere, and its possible impli-

cations, there is a great need for a better understanding of the dynamics of the polar mesosphere.

Appendix A

APPENDIX

A.1 Notes on the Geomagnetic L coordinate system

When referring to magnetic longitude and latitude, the coordinate system used in this thesis is the **Geomagnetic L** coordinate system proposed by Kilfoyle and Jacka (1968) and further discussed, tabulated and plotted by Schaeffer (1970). In this system the L-value of a point on the earth's surface (or more precisely, 100 km above the geoid) is that defined by McIlwain (1961) and is approximately the radius (measured in units of earth's radii) in the equatorial plane, from the centre of the earth to the field line through the point in question. The geomagnetic L latitude Φ is defined by the dipole relationship $\cos\Phi = (\frac{1}{L})^{\frac{1}{2}}$.

Figure A.1 shows the relationship between geographic and geomagnetic coordinates over Antarctica. Lines of constant geomagnetic latitude form ovals that correspond to the shape of the Austral auroral oval. Trying to describe the position and shape of the auroral oval would be difficult in geographic coordinates, but because auroras largely occur at constant geomagnetic latitude, their description is simplified in this system.

Other magnetic data at Mawson (July 1980)

- L=8.7, Invariant L coordinates - 70.2°S, 18.4°E
- Inclination 68° 30.8'S, declination 63° 7.9'W
- Local magnetic field strengths (July 1980)
  - total 50274 nT
  - vertical -46780 nT
  - horizontal 18415 nT
- electron gyro frequency=1.41 MHz

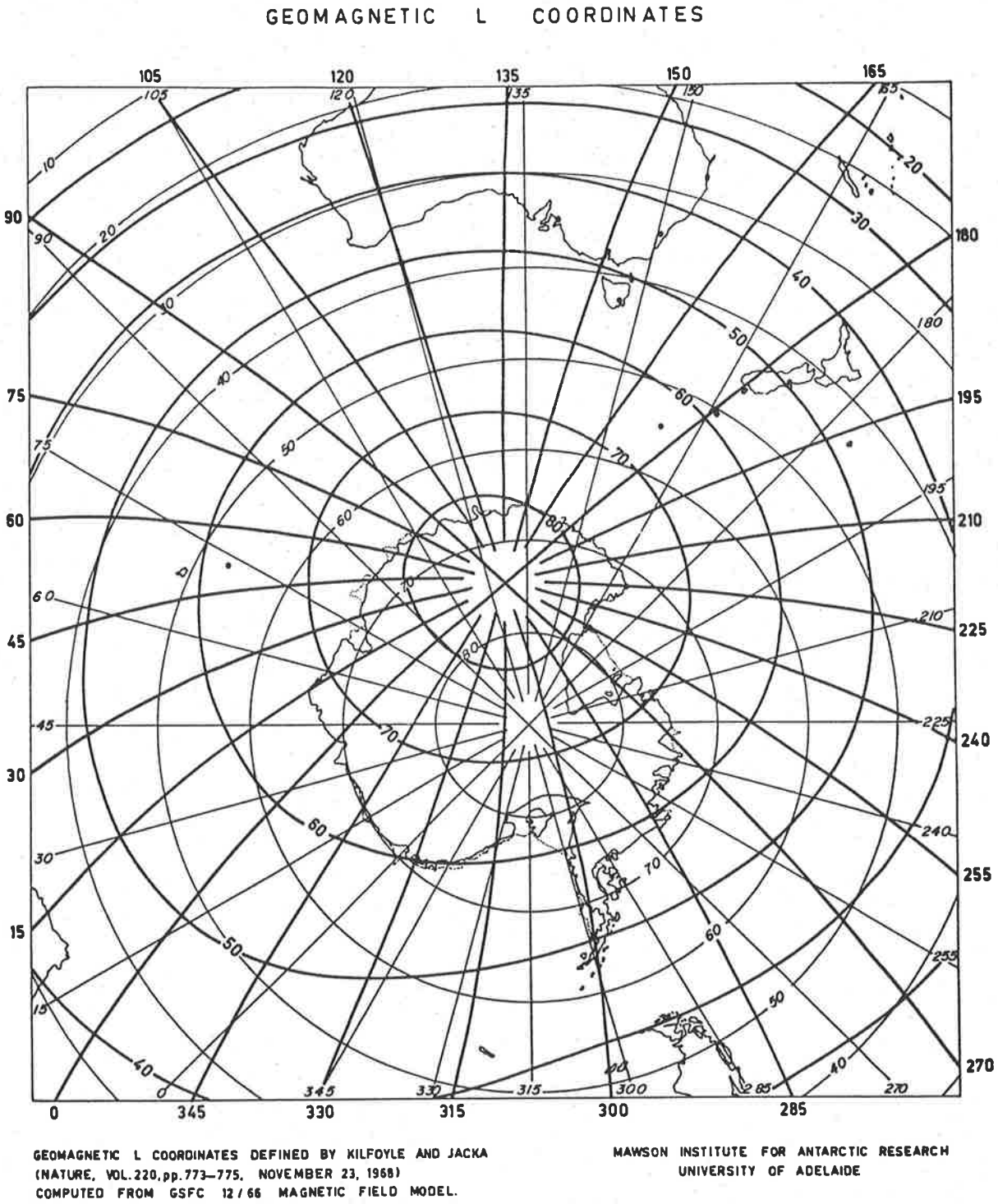

Figure A.1: **The Southern Hemisphere in geographic and geomagnetic L coordinates (Kilfoyle and Jacka 1968), computed by R.C. Schaeffer (1970).**

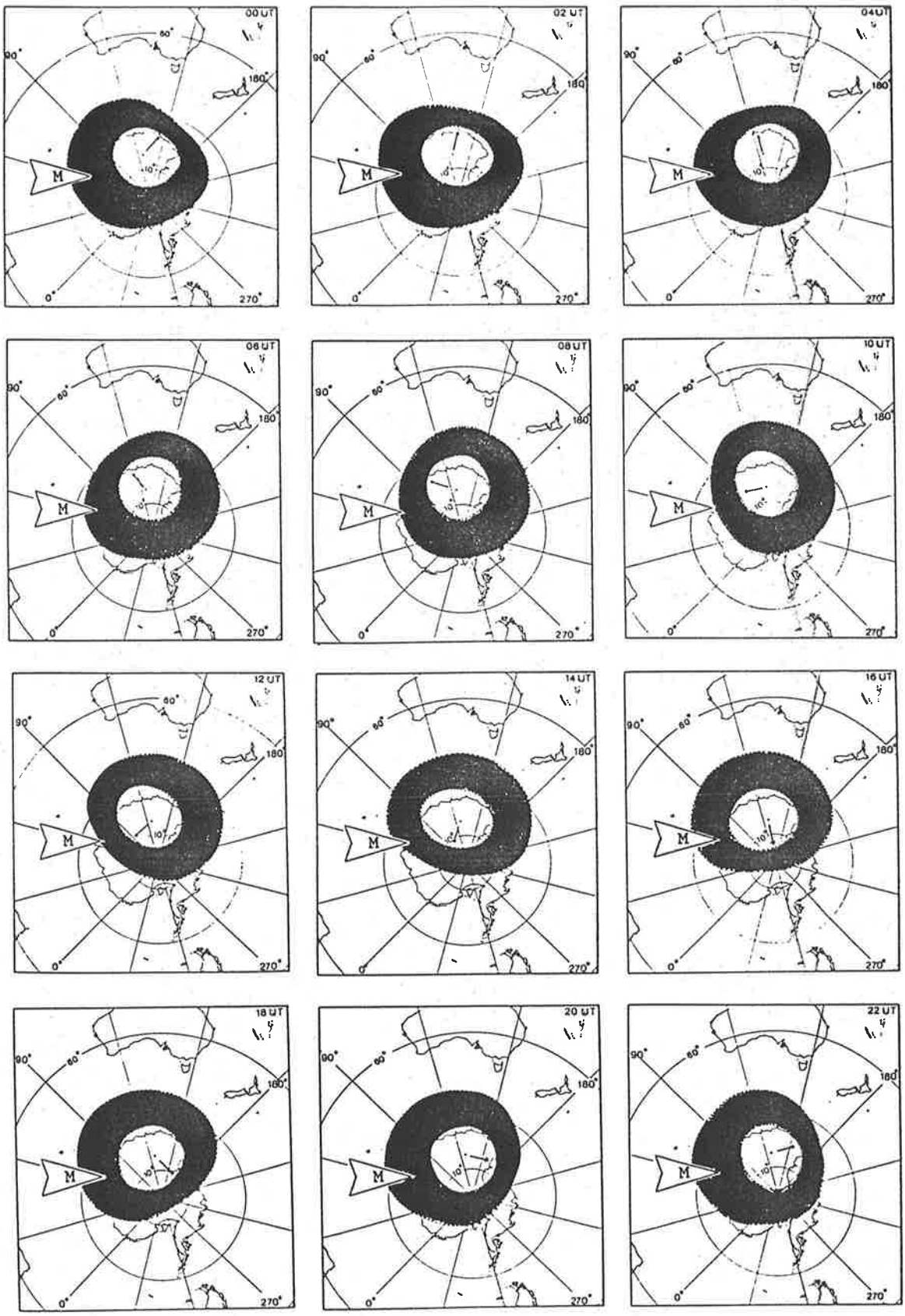

Figure A.2: **The auroral ovals and envelopes at Kp=3 for two-hourly intervals of UT for the southern winter** (Bond and Paine, 1971). The geographic position of Mawson (68° S, 63° E) is arrowed. Note that Mawson local time = UT + 4 h 11 min.

A.2 Notes on the upgrade of the Mawson SAPR radar 1988-89

Although not of direct concern to this thesis, it is worth mentioning that the SAPR radar at Mawson was substantially upgraded during the summer of 1988-89. The ageing Data General NOVA II minicomputer systems were replaced with Olivetti M24 (or 'ATT6300' as they are known in U.S.A.) personal computers; one operational and one for backup. The increased memory capacity and computational speed has resulted in a substantial increase in efficiency and ease of operation.

The work entailed,

- Construction of a receiver system in Adelaide identical to that in Mawson (but only one channel), so that the new hardware and software could be tested in Adelaide prior to shipping to Mawson. This equipment will also be of benefit in the future for training and software testing.

- The design of a personal computer interface board and driver software built to Mawson Institute specification by Genesis Software. The software included drivers for a microprocessor averager which can be added into the experiment hardware to externally average successive soundings prior to the data reaching the computer.

- A complete rewrite of the software. The NOVA software was the result of the efforts of a number of authors and had a number of limitations. For the new program, R.A. Vincent wrote the analysis section and the author wrote the coherent averaging and main program, which ties the acquisition and analysis software together. In addition, on the assumption that future operators may not be familiar with computers and the general theory of the SAPR radar, the program

incorporated a number of features which automatically regulate operation and advise the operator of likely hardware problems. All code was written in the 'C' programming language, except for hardware diagnostics and other utilities which were written in the Pascal programming language.

- Commissioning of the new computer system, a thorough overhaul of all the antenna systems, replacement of damaged co-axial cables and transmitter maintenance.

Funds have been requested to construct a solid-state transmitter similar to the unit operating in the Physics Dept. of the University of Adelaide.

A.3 Appendices to Section 3.1

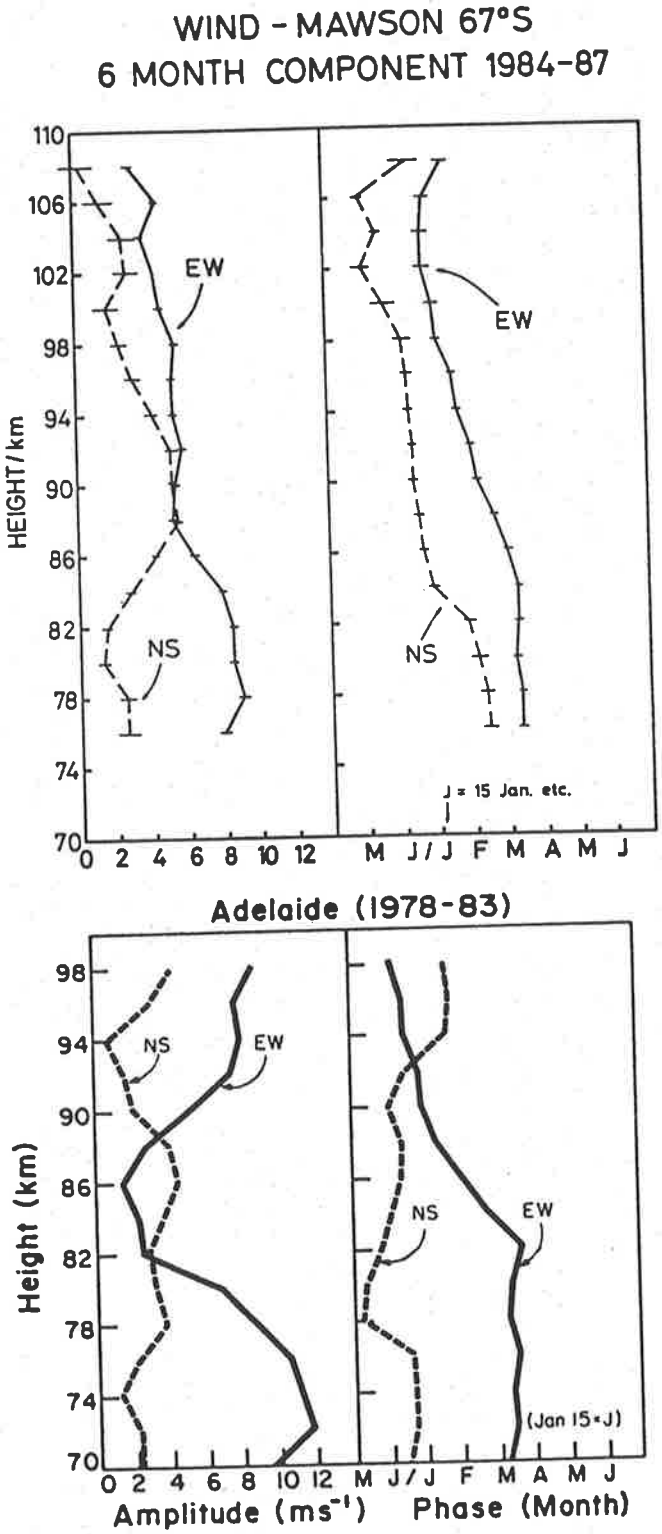

Figure A.3: **Amplitude and phase of the semiannual wind oscillation as a function of height observed at Mawson (top) and Adelaide (bottom).** Note that the 'phase' is the time of maximum northwards or eastward motion. The Adelaide figure was produced by R.A. Vincent and presented in Manson et al. (1985).

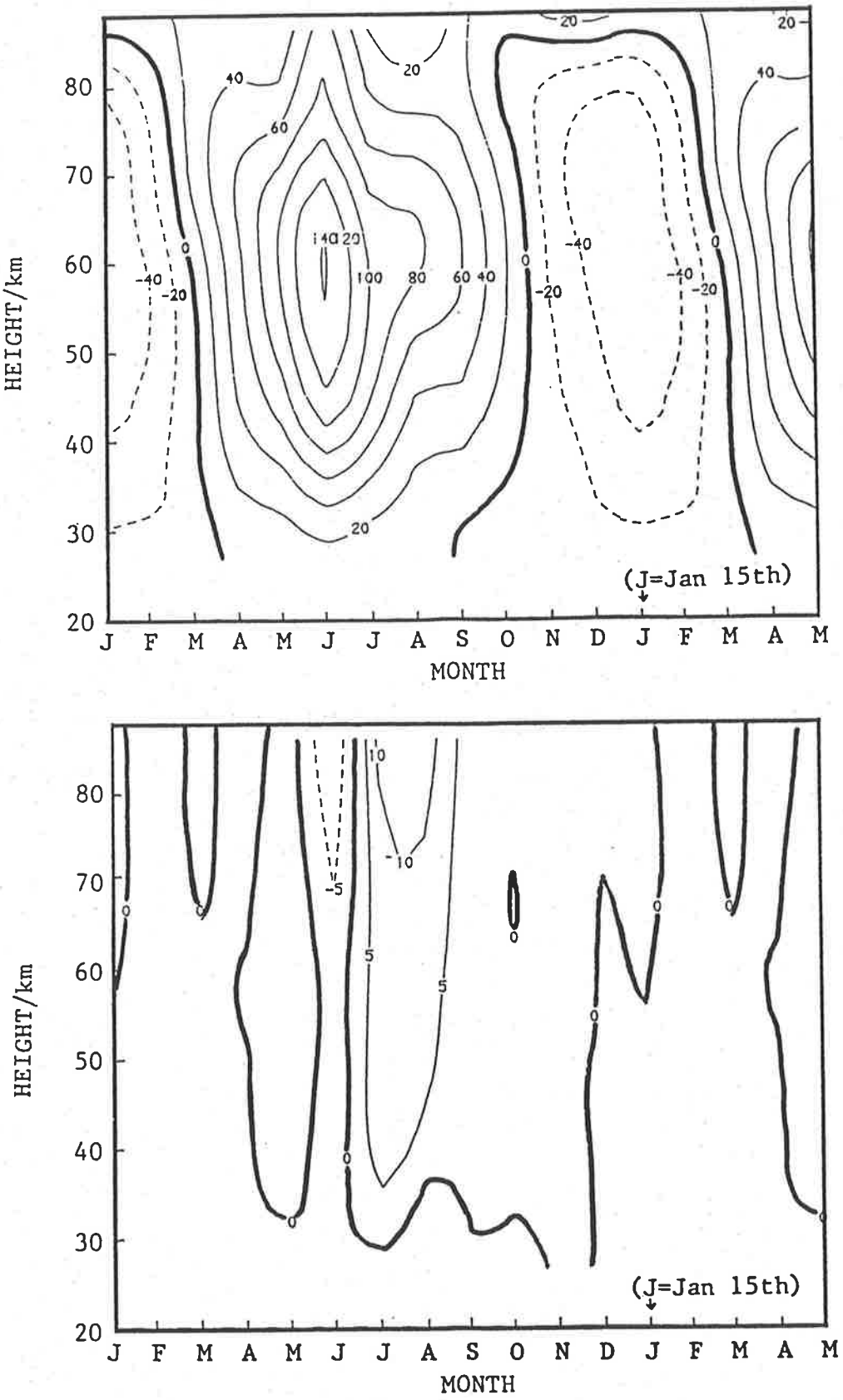

Figure A.4: **Zonal (top) and meridional (bottom) mean winds for Adelaide from the model of Barnett (1987),** in ms^{-1}. These figures were derived from MAP Handbook 16 data using the zonal mean and wavenumbers 1 and 2 to obtain the values at the particular latitude and longitude of Adelaide with the geostrophic wind approximation.

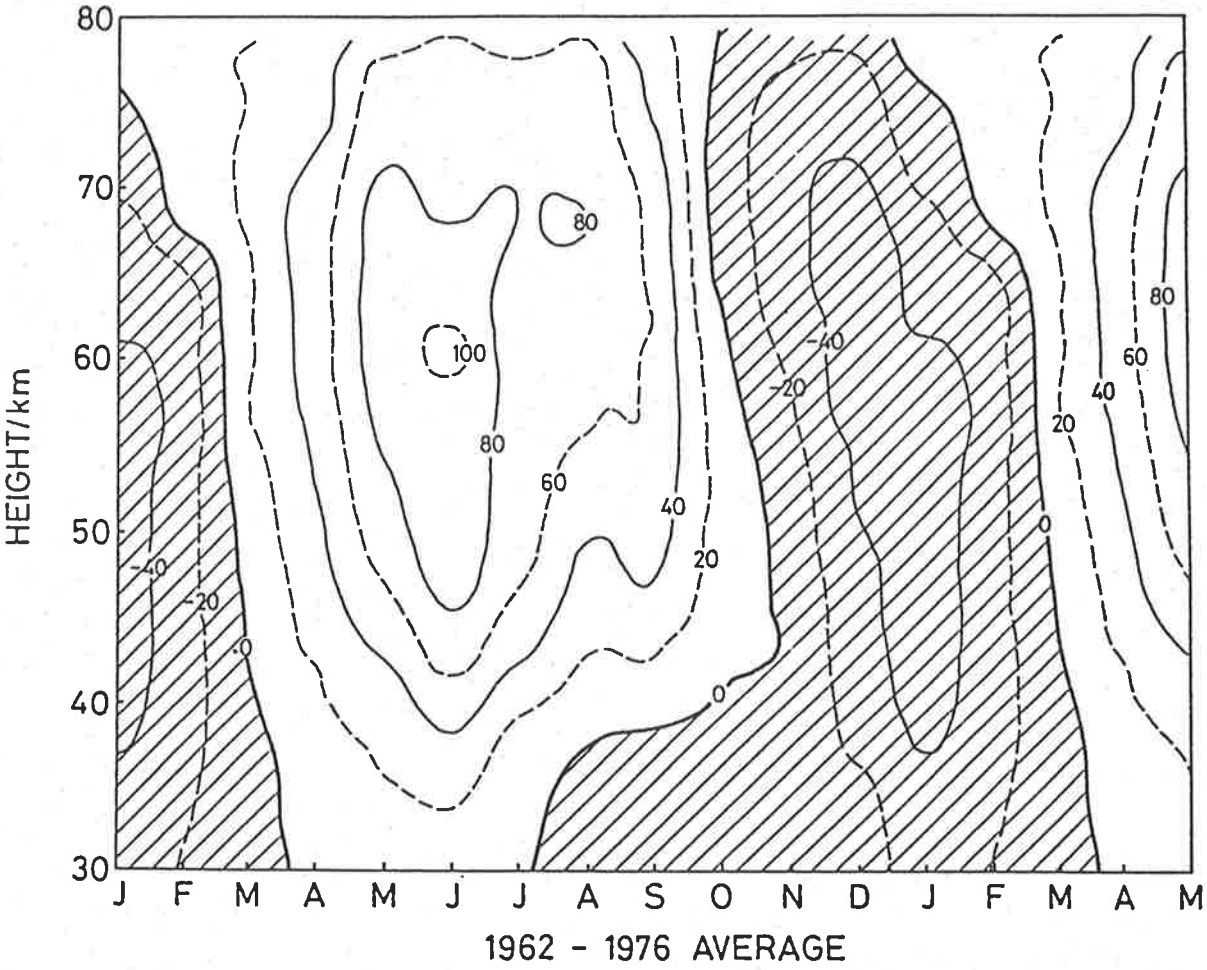

Figure A.5: **Mean zonal winds at Woomera (31° S, 137° S) derived from rocket-borne falling sphere and sonde measurements made between 1962–76** (Data prepared by Eckermann, 1987).

A.4 Appendices to Section 3.2

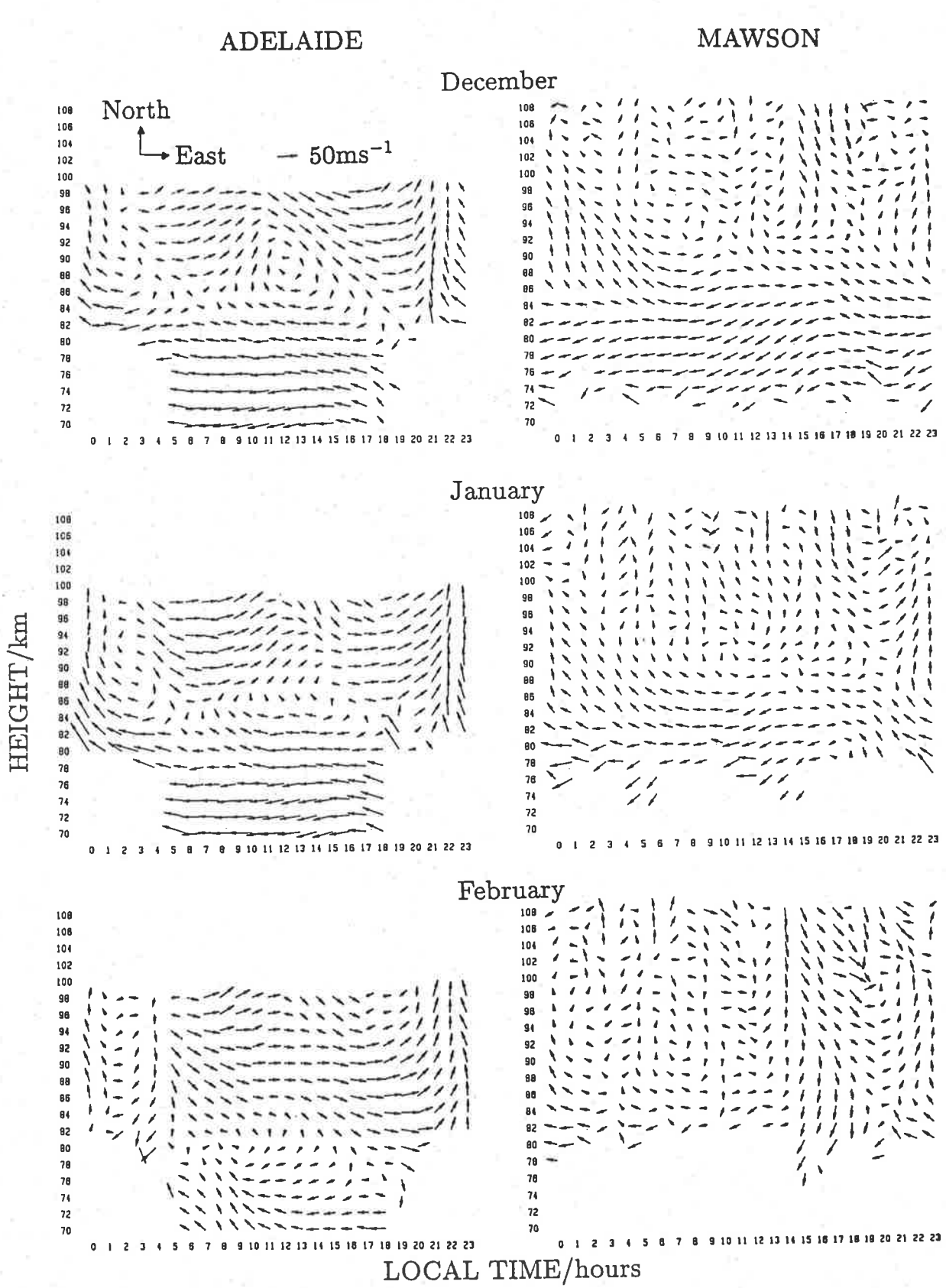

Figure A.6: **Hourly mean winds measured at Adelaide (35° S) and Mawson (67° S).** Winds have been averaged for the **summer months** of 1986. Note that wind values plotted at **12** hours (for example) on the time axis, are the averages taken between 12:00-13:00 hours local time.

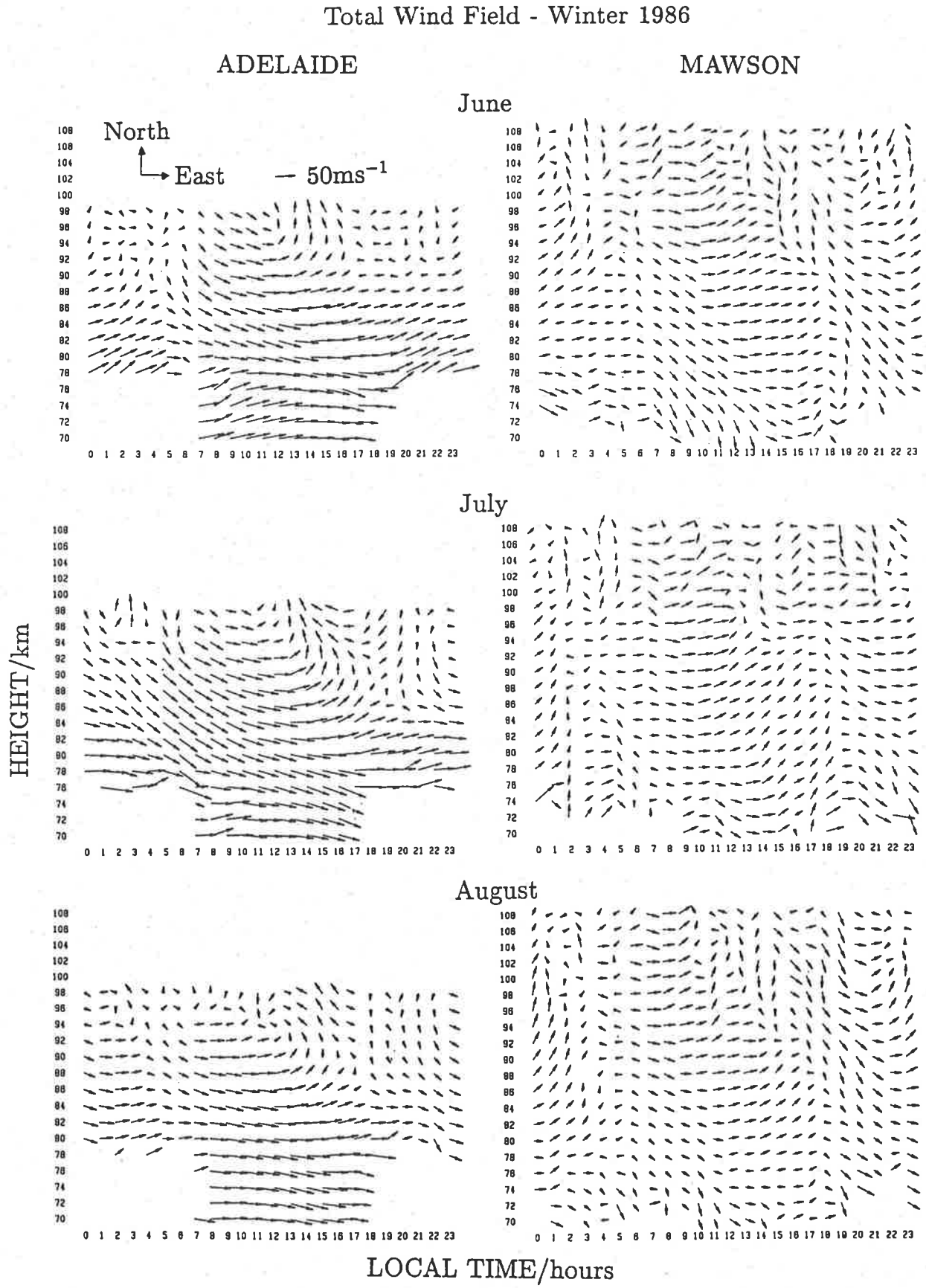

Figure A.7: as for figure A.6 except for the **winter months.**

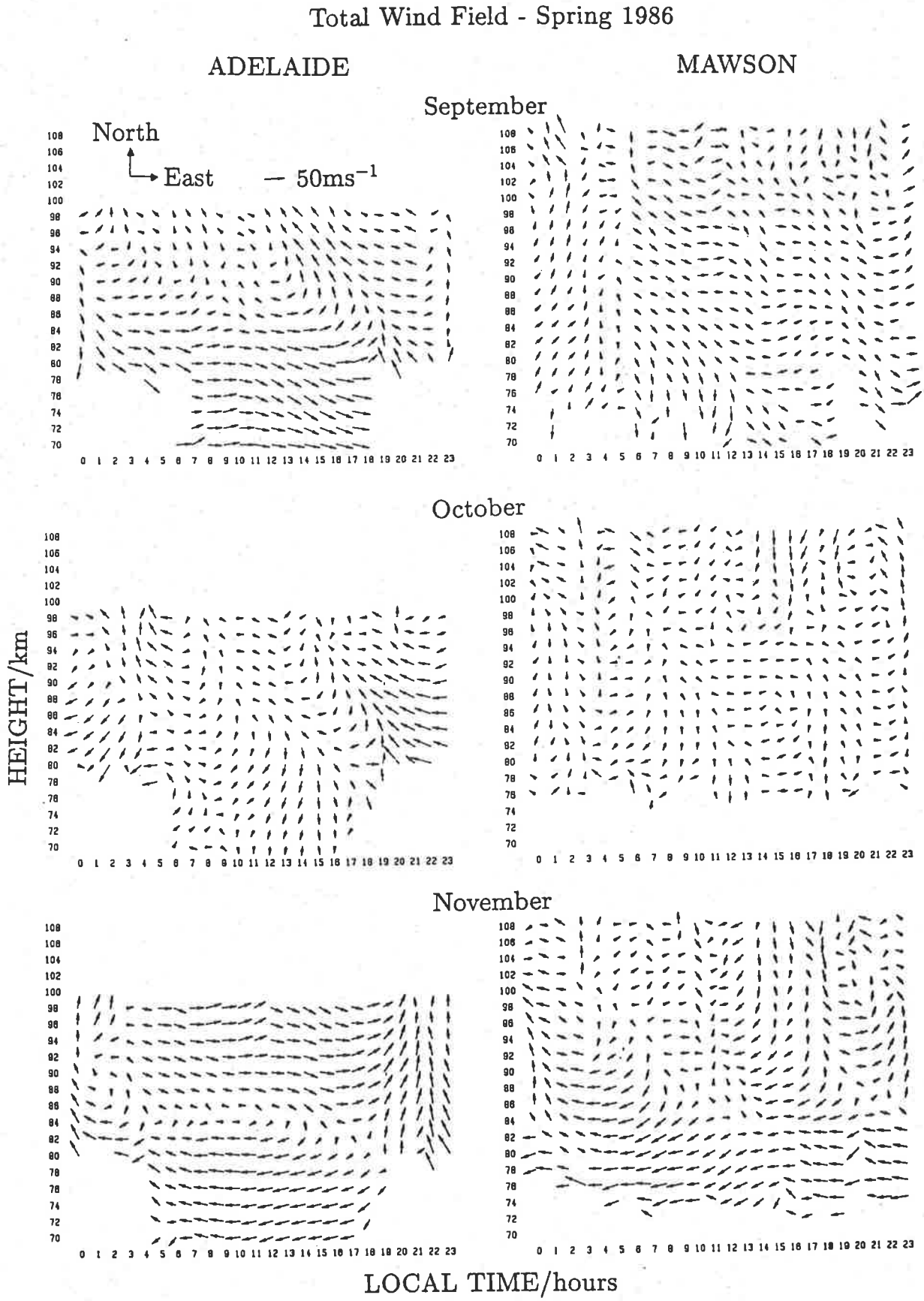

Figure A.8: as for figure A.6 except for the **spring months.**

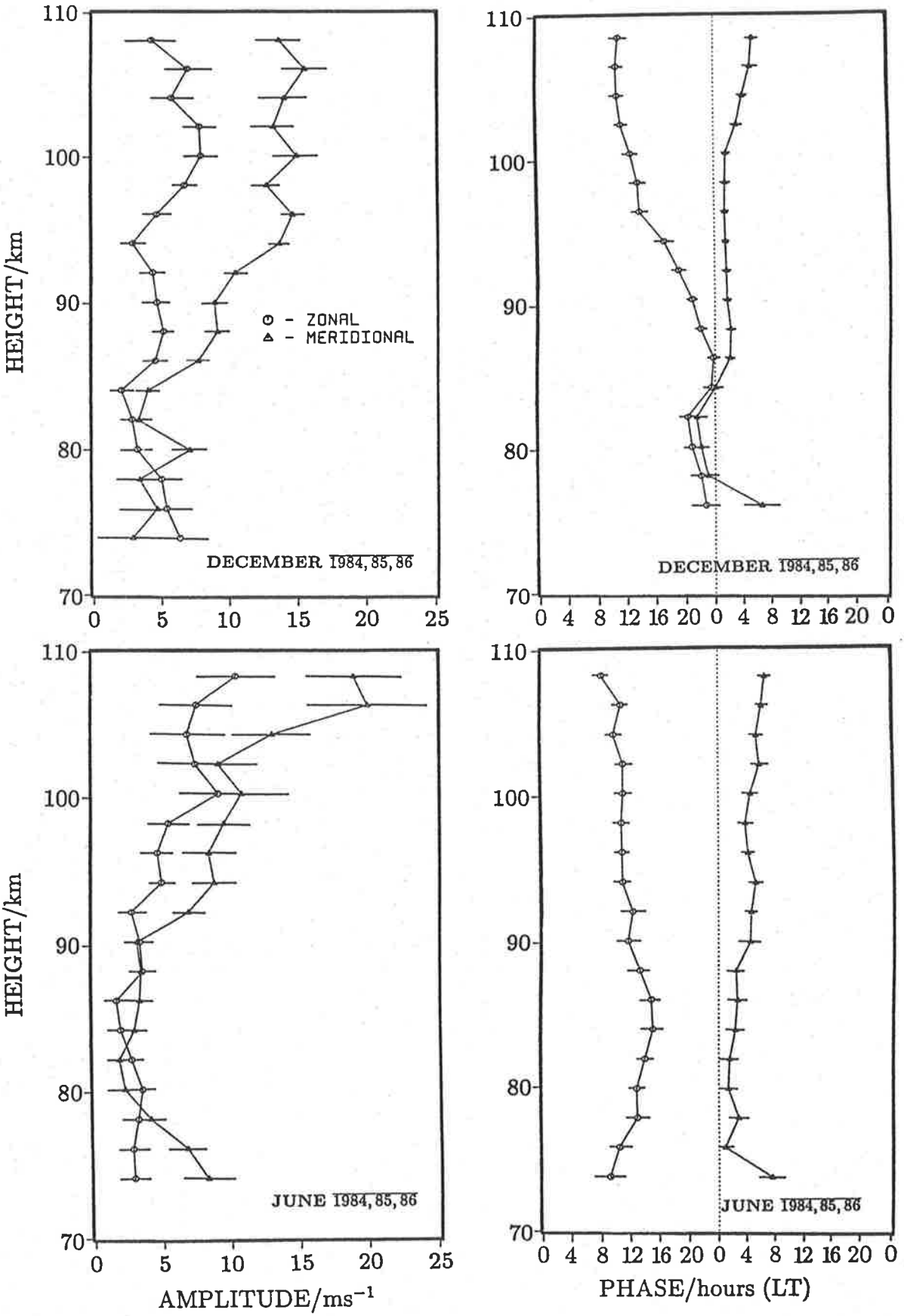

Figure A.9: **Amplitude and phase of the mean diurnal tide at Mawson** during the solstice months of December and June. Data from 1984–86 have been combined to produce a 'mean' December and June.

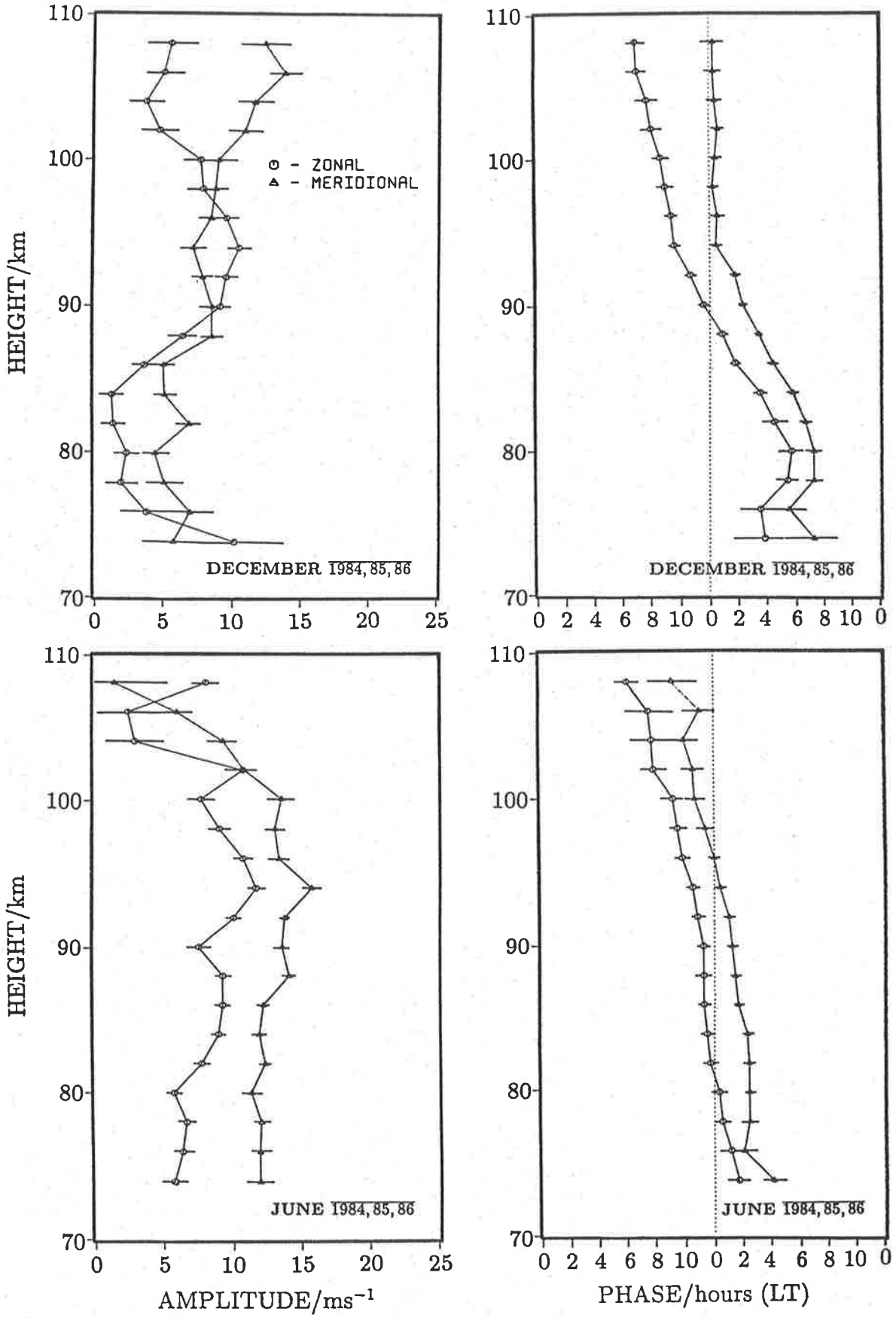

Figure A.10: **Amplitude and phase of the mean semidiurnal tide at Mawson** - details as for figure A.9

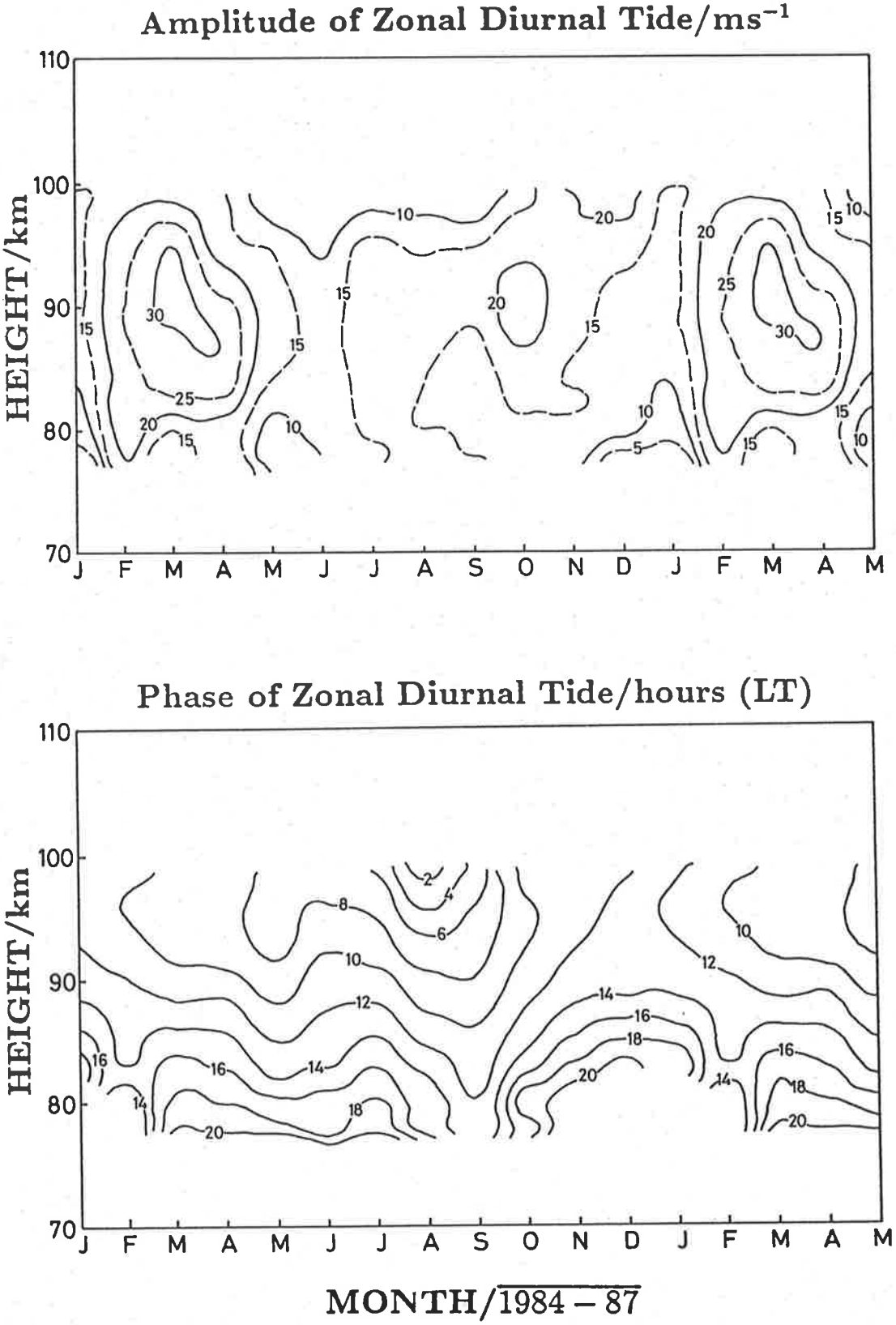

Figure A.11: **Contours of amplitude and phase of the mean zonal diurnal tide at Adelaide (35° S).** 3 years of data (1984-87) have been combined to produce a mean year. Note that the time marks on the x-axis indicate the middle of a month and the months January–May have been repeated on the right hand side of the plot.

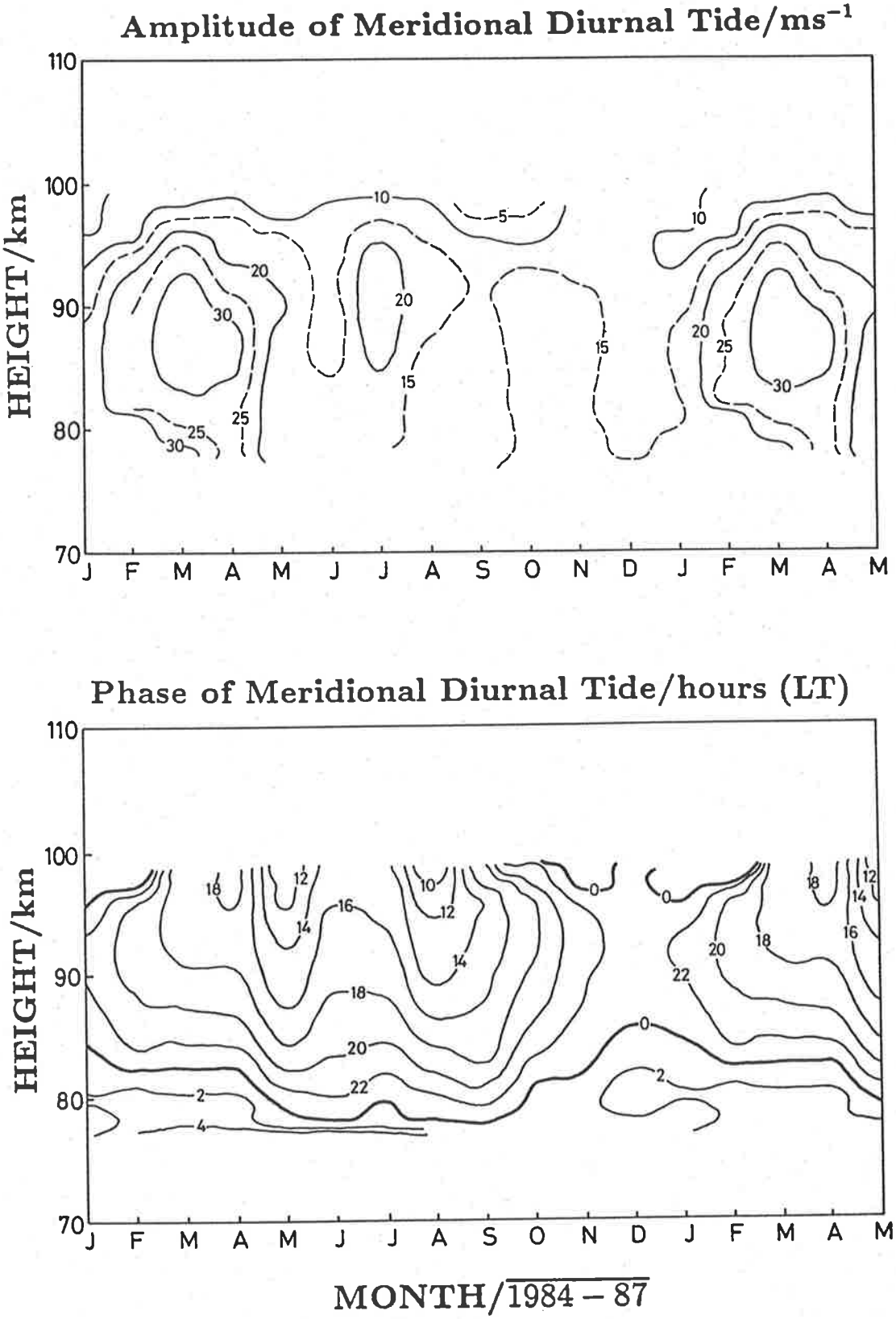

Figure A.12: **Contours of amplitude and phase of the mean meridional diurnal tide at Adelaide (35° S)** - details as for figure A.11.

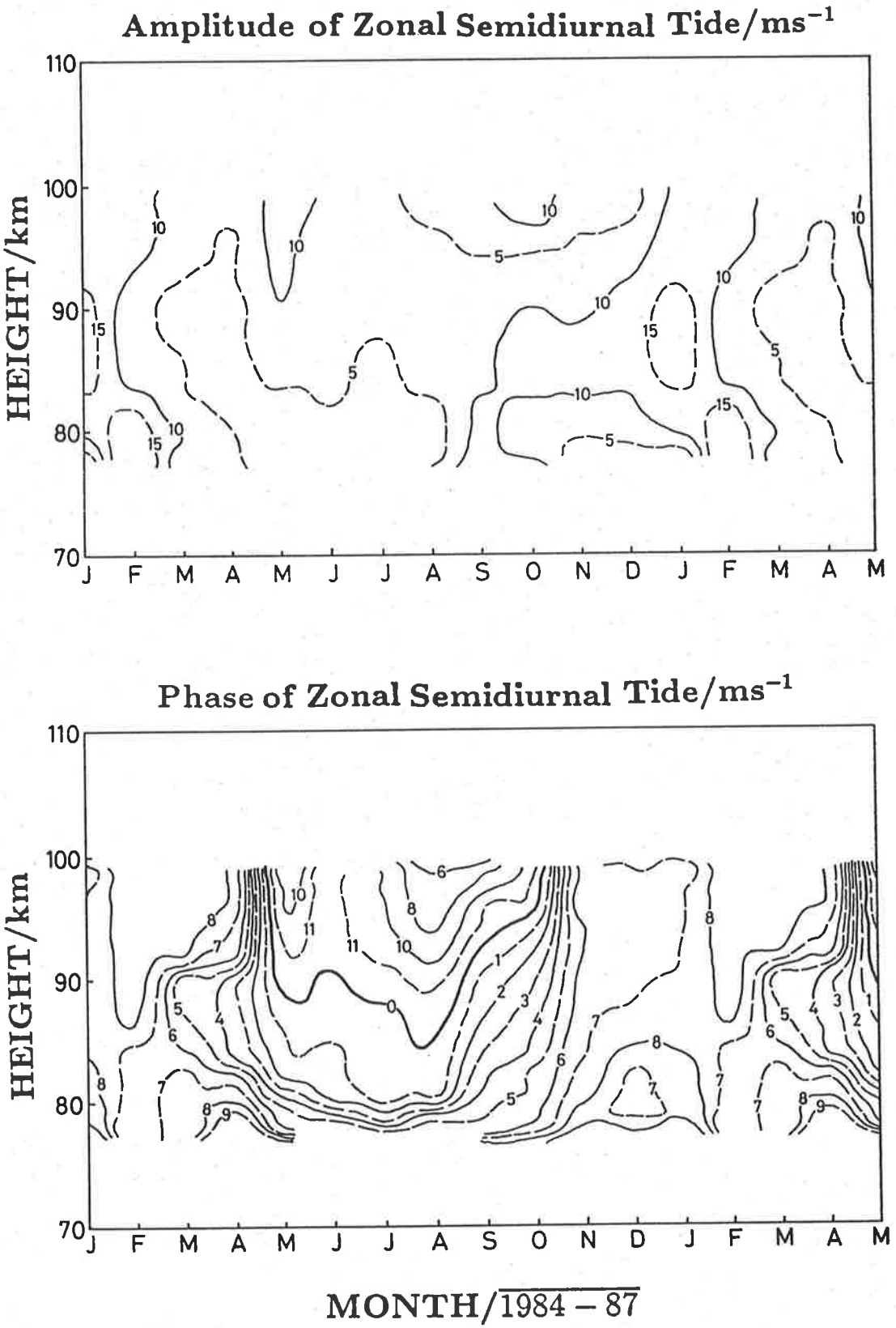

Figure A.13: **Contours of amplitude and phase of the mean zonal semidiurnal tide at Adelaide (35° S).** - details as for figure A.11

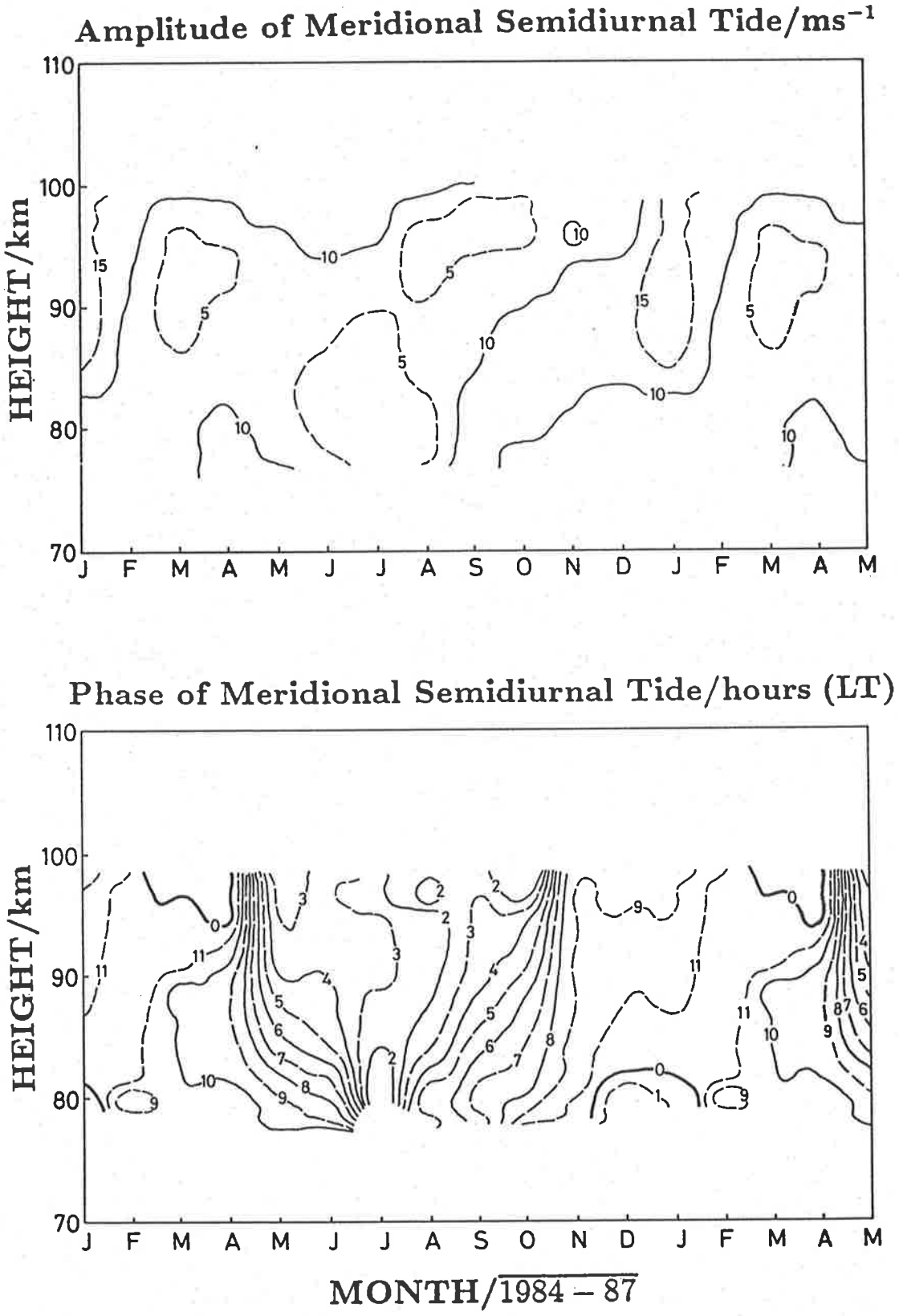

Figure A.14: **Contours of amplitude and phase of the mean meridional semidiurnal tide at Adelaide (35° S)** - details as for figure A.11.

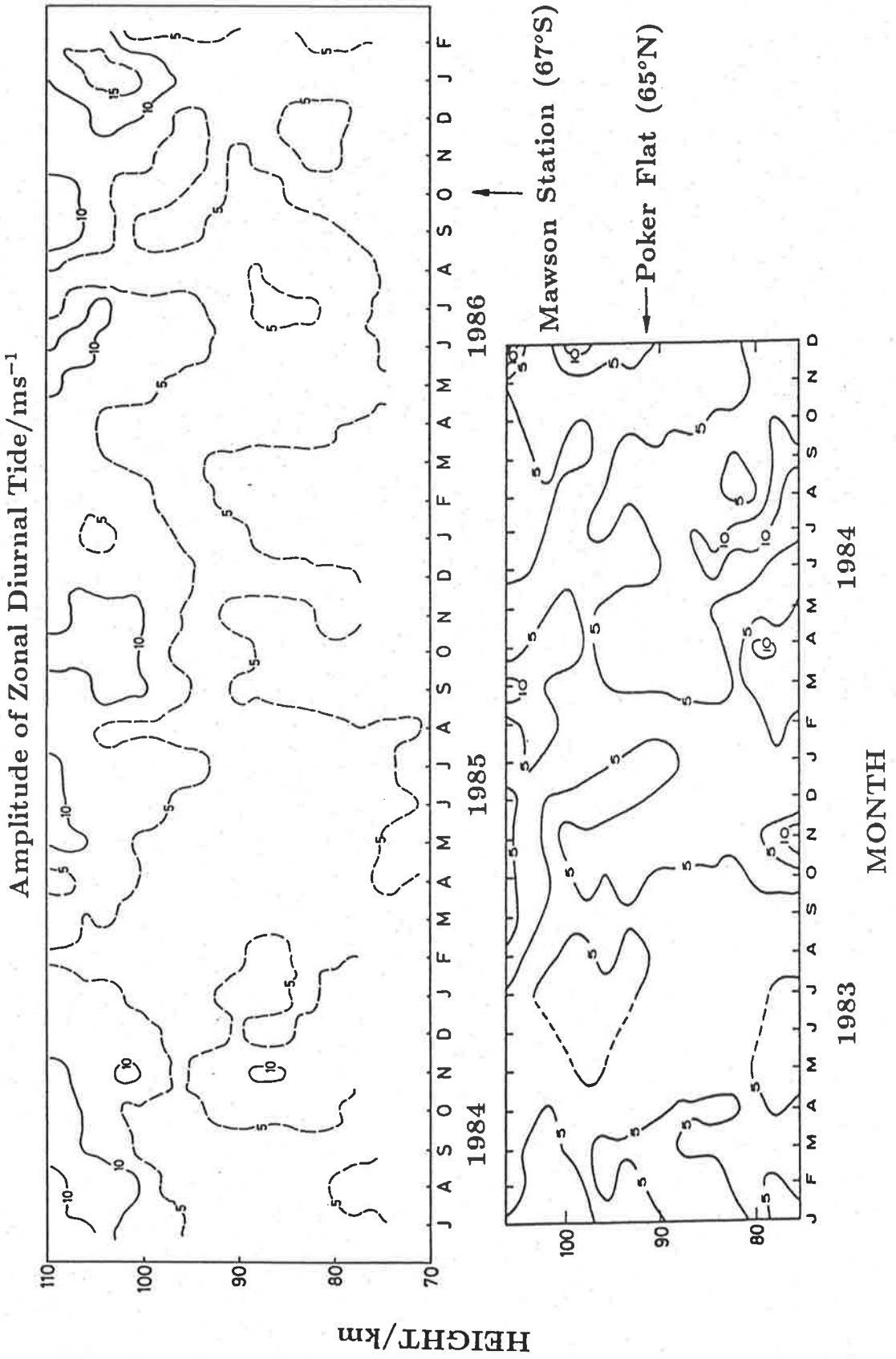

Figure A.15: **Comparison of contours of the amplitude of the zonal diurnal tide at Poker Flat, Alaska (Tetenbaum et al. 1986) and Mawson Antarctica.** Note that the time scales have been displaced by 6 months to assist with recognition of seasonal similarities.

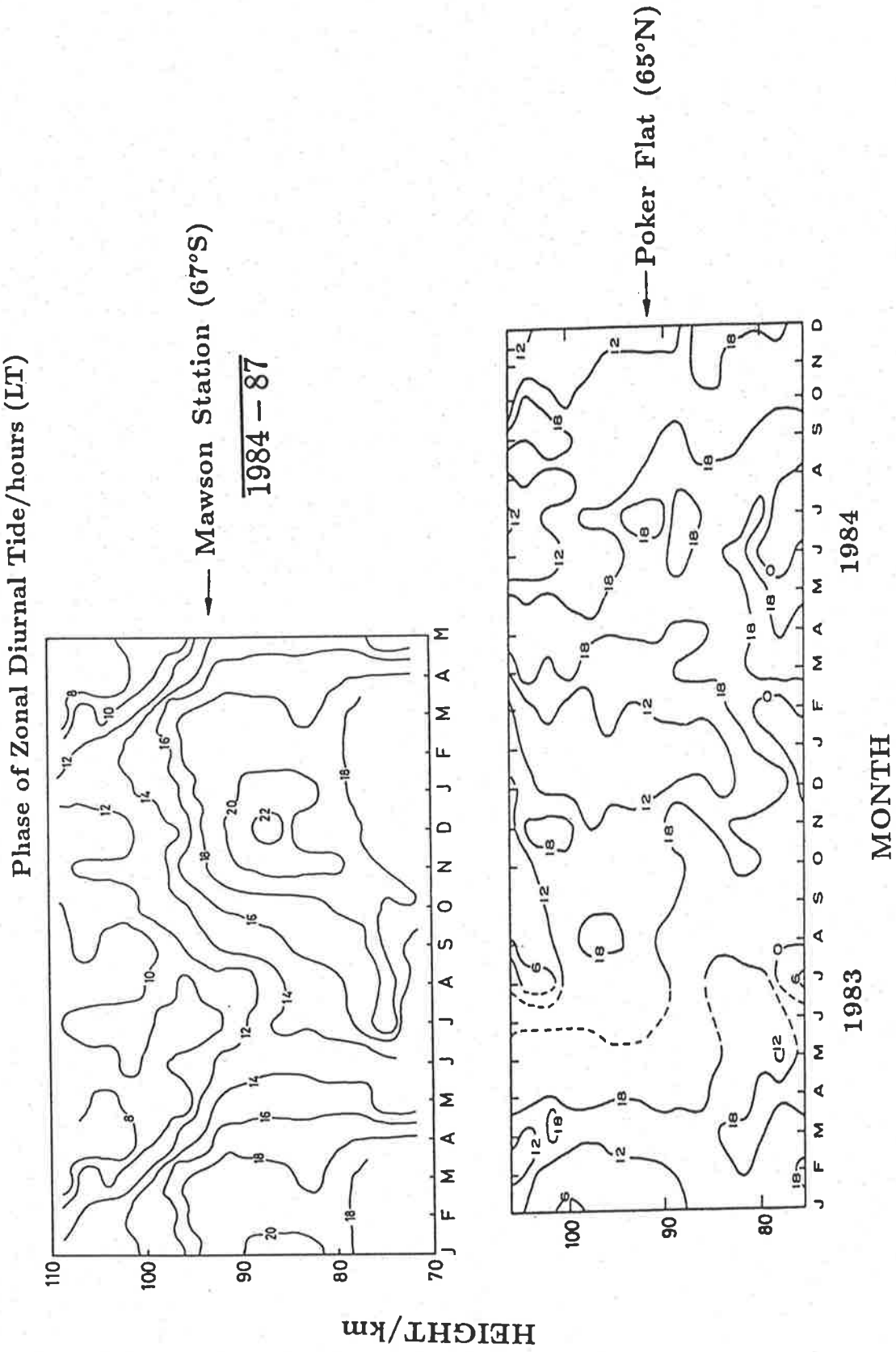

Figure A.16: **Phase of the zonal diurnal tide.** Because of large month-to-month variations in the diurnal phase at Mawson an average of 3 years of data (1984-87) is presented - other details as for figure A.15.

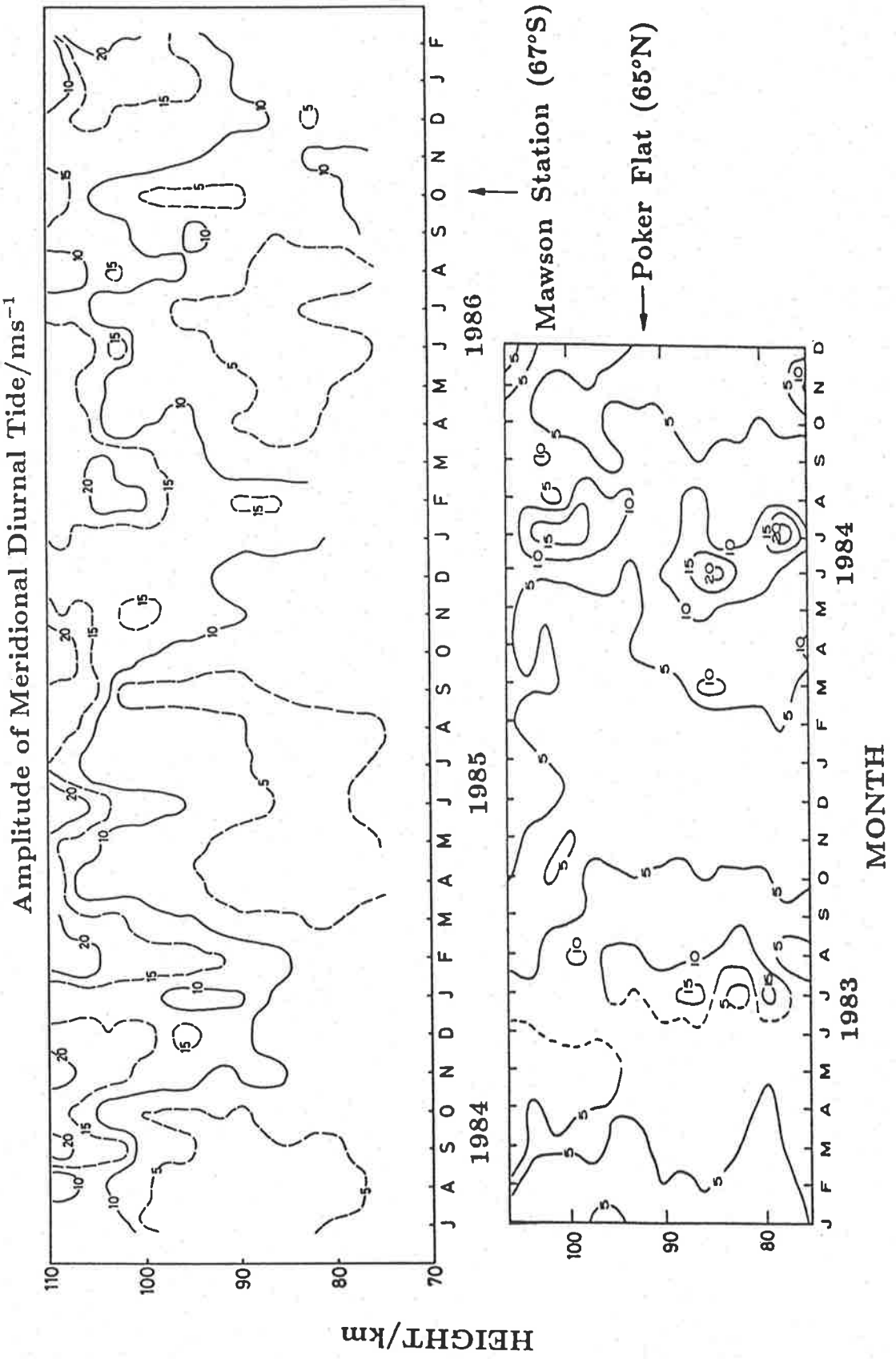

Figure A.17: **Amplitude of the meridional diurnal tide** - details as for figure A.15.

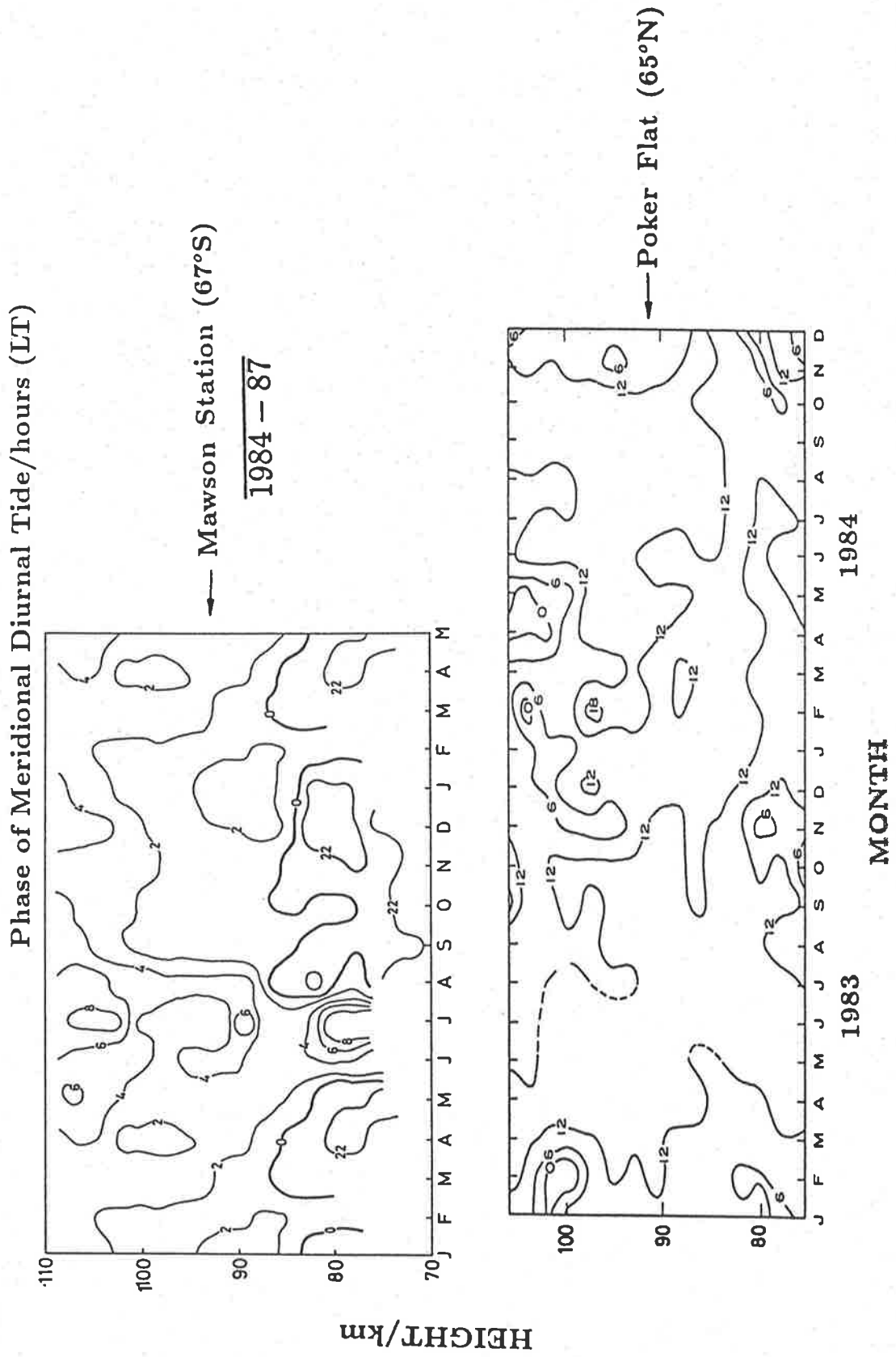

Figure A.18: **Phase of the meridional diurnal tide** - details as for figure A.16.

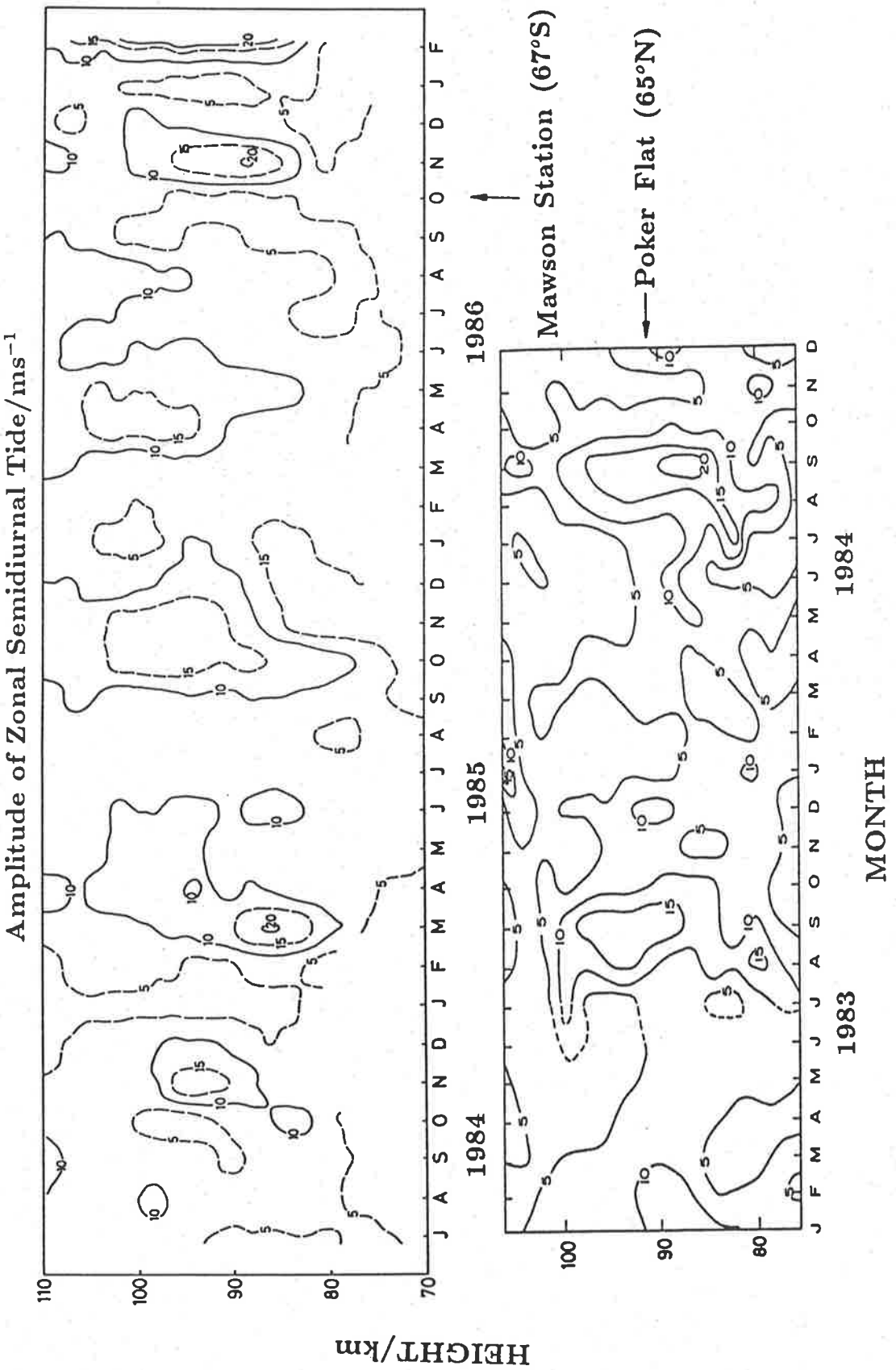

Figure A.19: **Amplitude of the zonal semidiurnal tide** - details as for figure A.15.

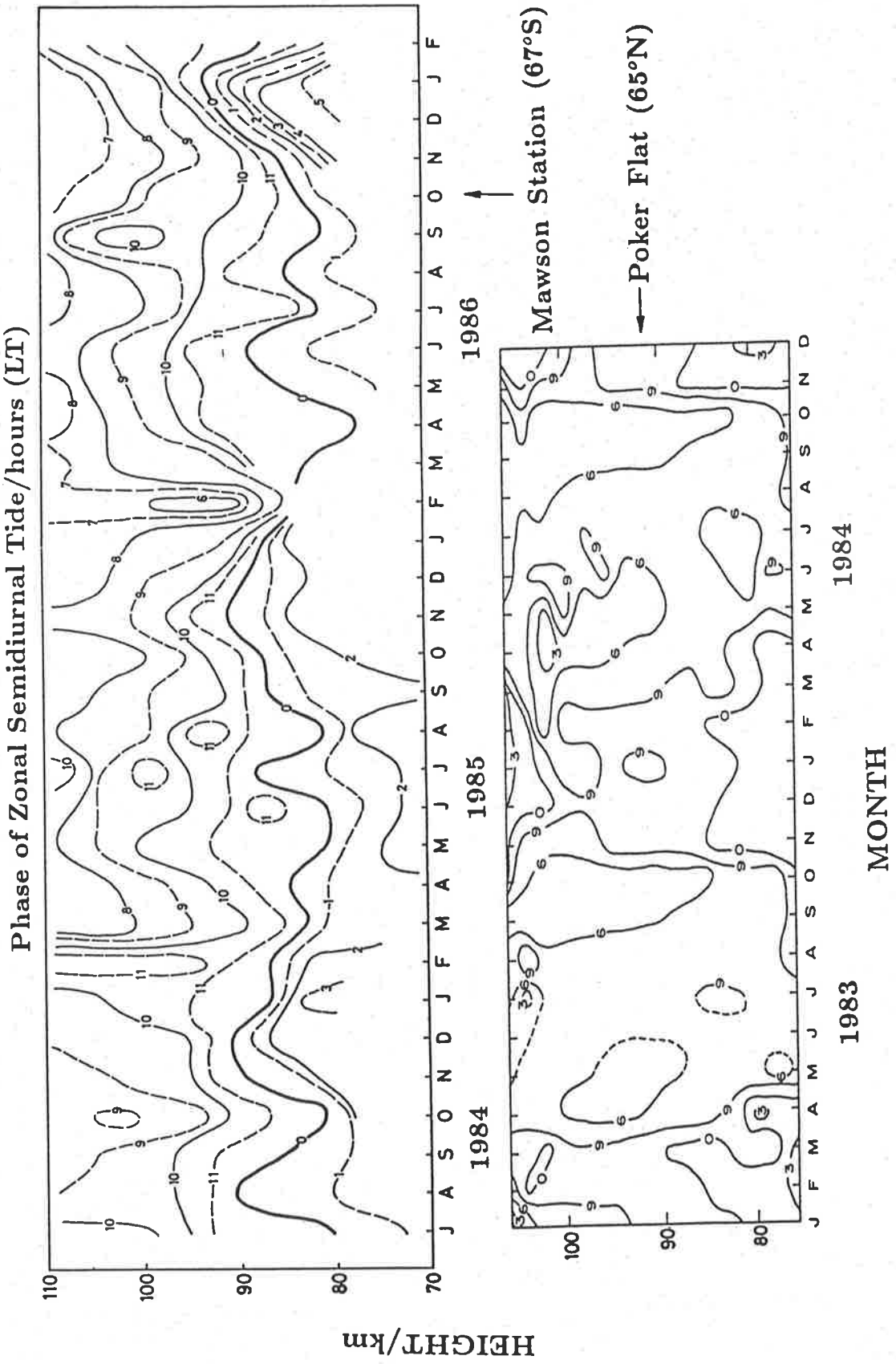

Figure A.20: **Phase of the zonal semidiurnal tide** - details as for figure A.16.

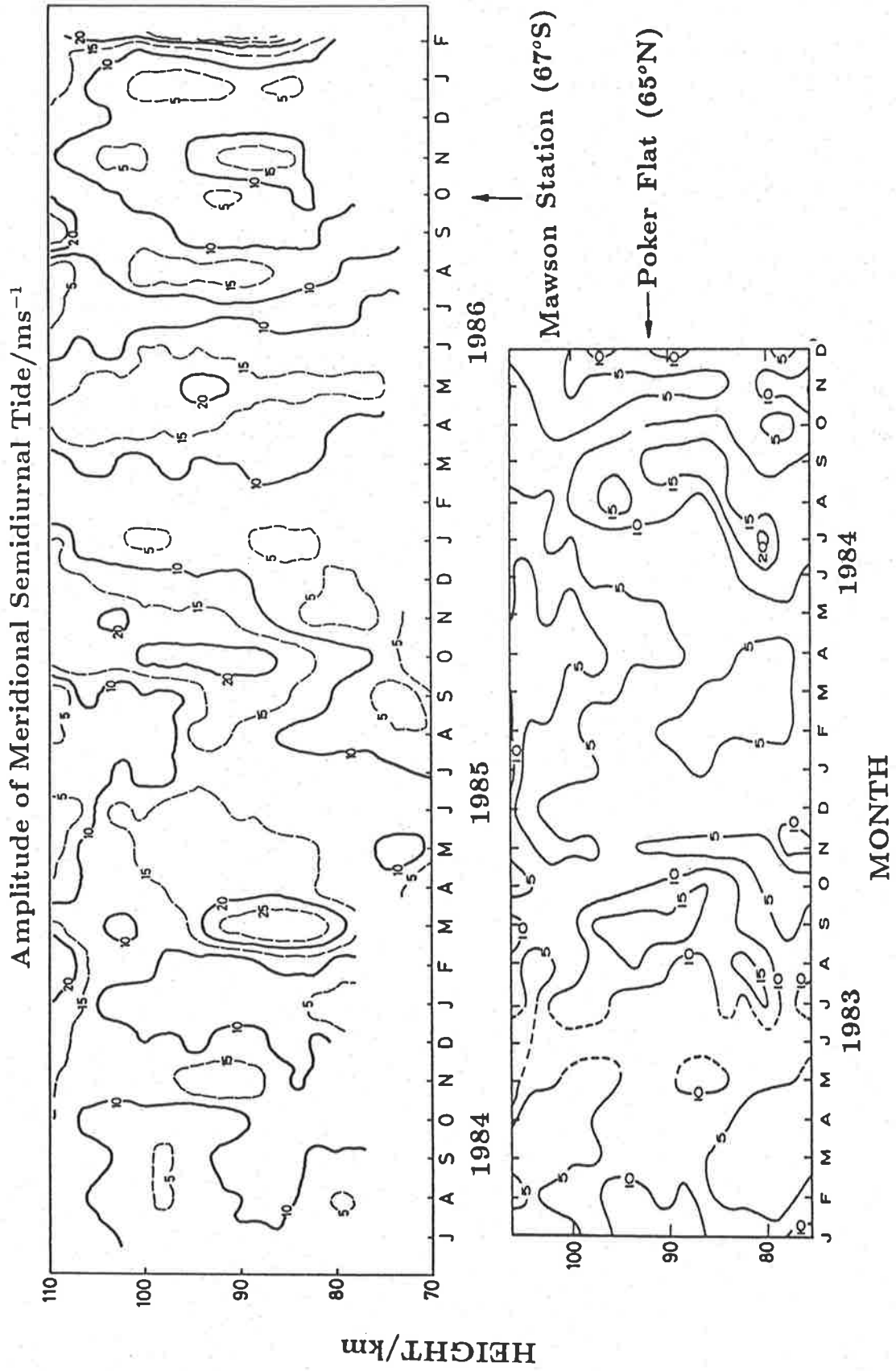

Figure A.21: **Amplitude of the meridional semidiurnal tide** - details as for figure A.15.

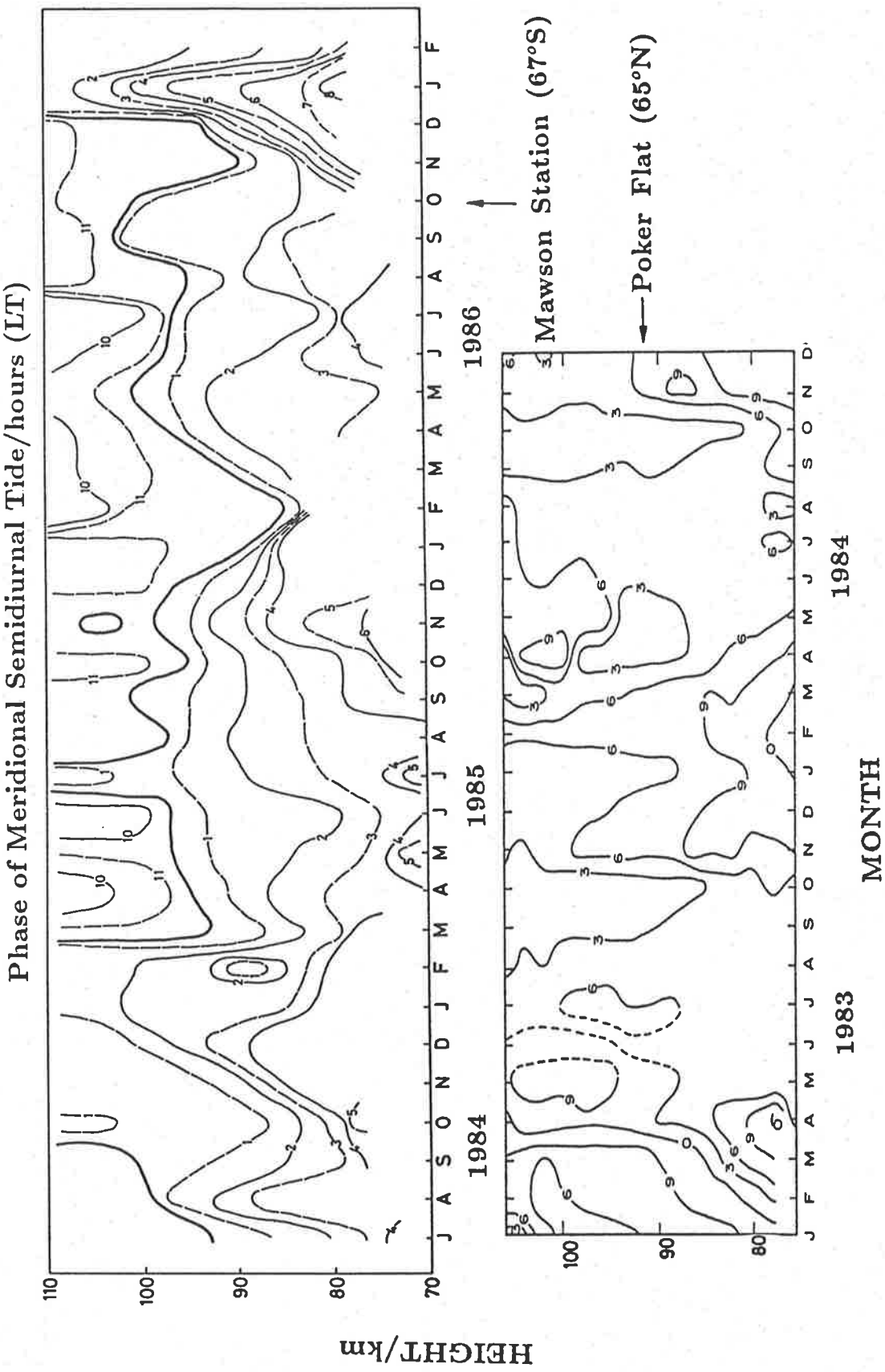

Figure A.22: **Phase of the meridional semidiurnal tide** - details as for figure A.16.

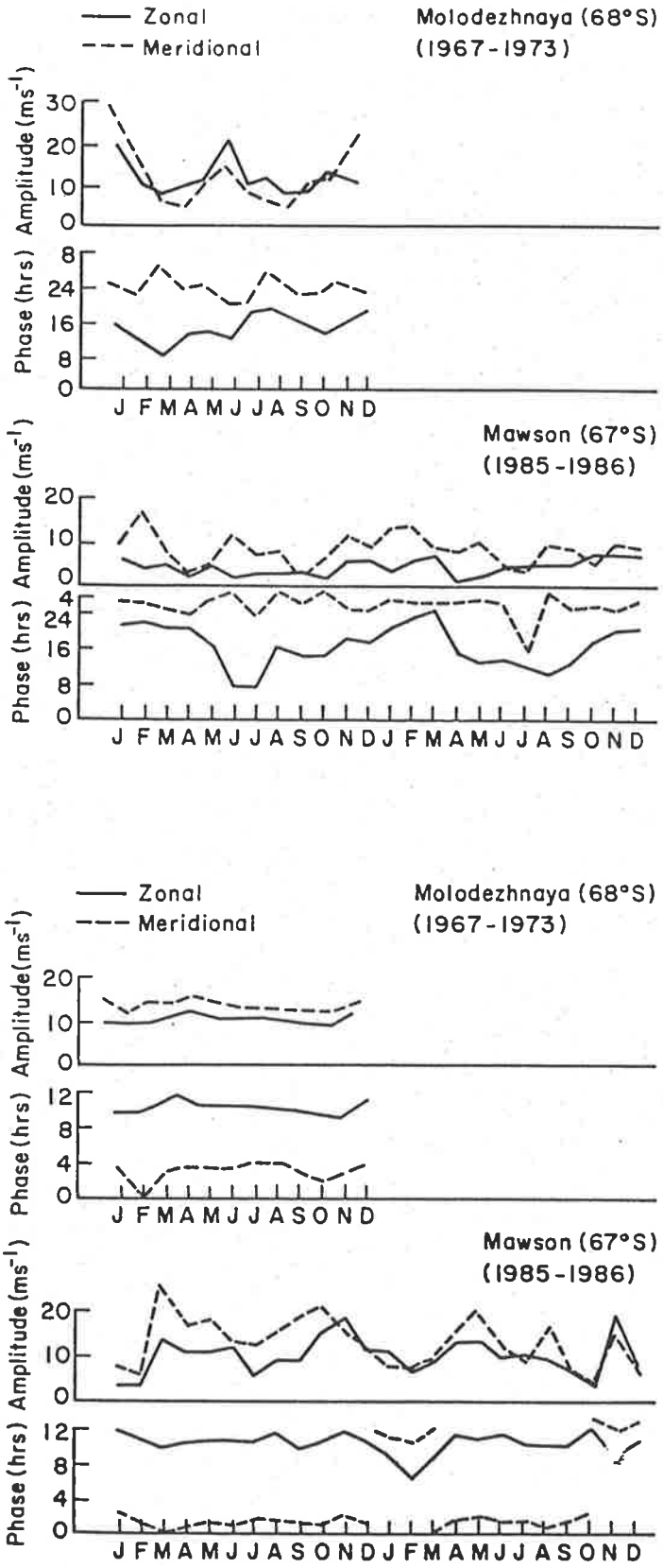

Figure A.23: **Monthly amplitude and phase of the diurnal tide (top) and semidiurnal tide (bottom) in the height range 90–92 km at Mawson (67°S) and Molodezhnaya (68°S), (Avery et al. 1988).**

A.5 Appendix to Section 3.3

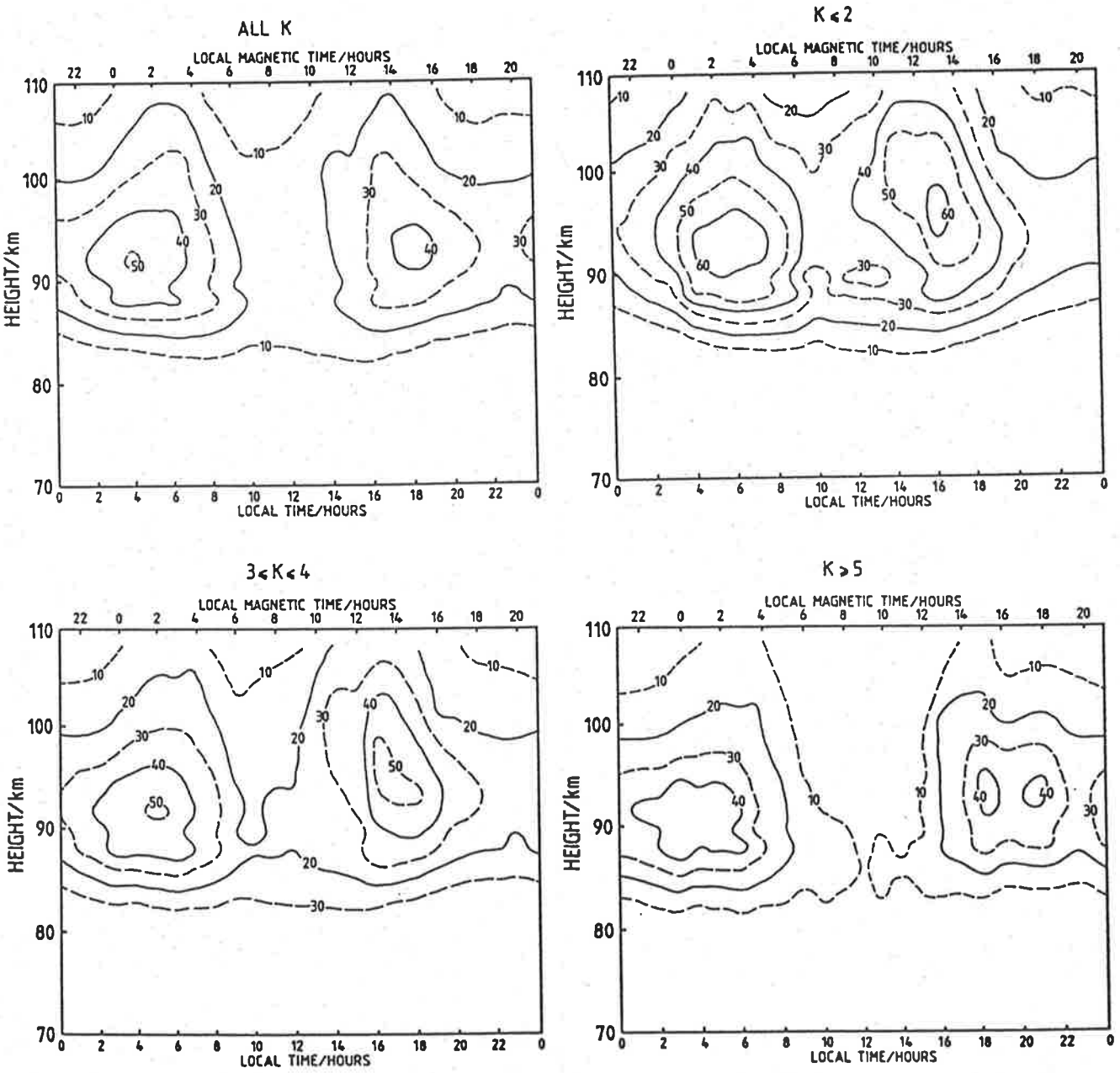

Figure A.24: **Contours of mean signal-to-noise ratio, (at Mawson) for different values of the 3-hour local K index.** A complete year of data (1985) was used to produce these diagrams. Note that the S/N ratio is expressed as a ratio (rather than decibels).

A.6 Reprint of paper: "Simultaneous observations of the quasi 2-day wave at Mawson, Antarctica, and Adelaide, South Australia", by A. Phillips

J. atmos. Terr Phys **1989 51:119–124.**

Journal of Atmospheric and Terrestrial Physics, Vol. 51, No. 2, pp. 119–124, 1989.
Printed in Great Britain.

0021–9169/89 $3.00 + .00
Pergamon Press plc

Simultaneous observations of the quasi 2-day wave at Mawson, Antarctica, and Adelaide, South Australia

A. PHILLIPS

Mawson Institute for Antarctic Research and Department of Physics, University of Adelaide, Adelaide, South Australia

(*Received in final form* 26 *August* 1988)

Abstract—Observations of the Austral quasi 2-day wave at Mawson, Antarctica (67°S, 63°E) are presented and compared with those from Adelaide (35°S, 138°E). The data were obtained from partial-reflection radars which have been measuring winds continuously since mid-1984, and the results presented here are the first to record the 2-day wave in middle atmosphere winds from Mawson. They show that 2-day period oscillations of 10–15 m s^{-1} are a regular feature of the high latitude southern hemisphere summer. The wide longitude and latitude separation of the radar stations permits estimates of propagation velocity and latitude phase structure, and results are consistent with the passage of a westward travelling Rossby-gravity (3, 3) wave.

1. INTRODUCTION

A ubiquitous feature of the summer hemisphere middle atmosphere is the presence of a quasi 2-day period oscillation. This phenomenon has been observed in both hemispheres by rocket, radar and satellite techniques for over 20 years (MULLER, 1972; KINGSLEY *et al.*, 1978; MULLER and NELSON, 1978; ROGERS and PRATA, 1981; CRAIG *et al.*, 1980; CRAIG and ELFORD, 1981; CRAIG *et al.*, 1983; TSUDA *et al.*, 1988) but there is still no universally accepted explanation of the driving force. There is, however, substantial evidence to suggest that the disturbance is due to a westward-propagating Rossby-gravity (3, 3) normal mode (SALBY, 1981). In the northern hemisphere (NH) the period of the wave is frequently given as 51 ± 2 h, whereas in the southern hemisphere (SH), the period is usually very close to (if not exactly) 48 h (MULLER and NELSON, 1978; CRAIG *et al.*, 1980). SALBY (1981) proposed that a combination of weak eastward winds (*relative* to the wave) and an equatorward temperature gradient lead to the amplification of the wave at mesospheric heights. An alternate theory by PLUMB (1982) suggests that the wave is due to a baroclinic instability of the westwards jet in the summer mesosphere.

2. RESULTS

The present study draws mainly on data collected during the SH summer months of December, January and February for the years 1986 and 1987 (i.e. 'summer' 1986 is the period, Dec. 85–Feb. 86). At both Mawson (67° 36′S, 62° 53′E) and Adelaide (34° 36′S, 138° 28′E) 2 MHz spaced-antenna partial-reflection radars continuously measured horizontal winds at heights between 80 and 100 km at 2 km intervals, with a time resolution of 5–15 min between successive wind measurements. For the purposes of the present analysis, the winds were averaged over the height range 87.5–97.5 km in order to minimize errors and reduce the number of record gaps. This should have little effect on the 2-day wave because of its large vertical wavelength, but it may have reduced the tidal amplitudes. Also, one hour averages were formed in Universal Time (UT), and are used throughout the present analysis.

Although the wave is present for most of the summer months (and may have a few 'bursts' of activity lasting for a few cycles) it usually reaches maximum amplitude during the latter part of January, whereupon it may abruptly diminish (as was the case in 1987). Maximum amplitudes in excess of 50 m s^{-1} are often observed in the meridional wind component at Adelaide. Figure 1 shows that the amplitude structure is similar at the two sites (especially in 1987) but the amplitude at Mawson is approximately 0.3 of the amplitude at Adelaide. Note that in Fig. 1, occasional gaps in the wind data were filled (to avoid spurious 'ringing' in the filtered data) by taking an average of the wind 48 h before and after the missing data point. While it may be argued that this process could introduce a fictitious 48 h component, it is acceptable in this case as the true frequency is very close to 48 h, and the data gaps very few.

Figure 2 shows *amplitude* spectra for the last two

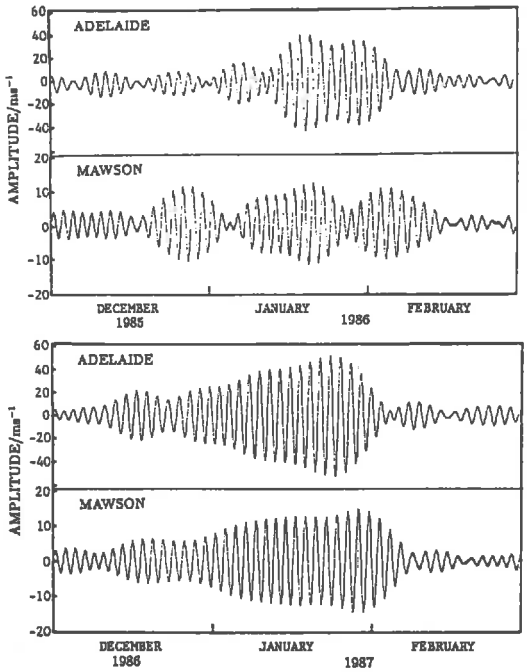

Fig. 1. Comparison of the meridional components of the wind at Adelaide and Mawson during December–January 1986 (top) and 1987 (bottom). Wind data have been band pass filtered by a square filter of period range 1.8–2.2 days.

weeks of January in 1986 and 1987, when the 2-day wave amplitude is a maximum. These diagrams have been arranged to allow comparison of spectral amplitudes between the zonal and meridional wind components of the 2-day wave at each station. At Adelaide the amplitude of the meridional component averaged 33 m s^{-1} in 1986 and 45 m s^{-1} in 1987, with the zonal components approximately 0.3 and 0.5 (respectively) of the meridional. At Mawson, the meridional amplitudes for the two years were both about 12 m s^{-1}, with the zonal amplitudes approximately 0.25 of the meridional in 1986 and 0.9 of the meridional in 1987. During the last two weeks of January 1985 (not shown in Fig. 2) the component amplitudes at Mawson were again comparable, and averaged 10 m s^{-1} for the meridional component and 8 m s^{-1} for the zonal.

The geographic separation of Mawson and Adelaide is 33° 0′ in latitude and 75° 35′ in longitude. If the 2-day wave is assumed to be due to a westward travelling wave of zonal wavenumber 3 (which takes precisely 6 days to traverse the globe), and assuming there is no phase change with latitude, the 2-day wave at Mawson should lag that at Adelaide by 30.23 h. In order to estimate the actual time differences between the stations, cross-spectral techniques were employed. Figure 3 shows a normalized cross-spectrum between the meridional winds at Adelaide and Mawson for January 1–31, 1987. The spectrum has been smoothed with a window of 0.2 cycles day^{-1} to show trends in phase difference. At the 2-day period the phase difference is approximately 215° or 28.6 h. While the 2-day wave dominates the diurnal and semidiurnal tides over this period, in this diagram the tides may be underestimated due to vertical averaging of the data.

Table 1 shows the apparent phase lag between the stations for several independent periods during 1986 and 1987. These estimates were determined by computing a cross-spectrum for the interval and measuring the phase at a frequency of $\frac{1}{2}$ cycle day^{-1}. Given variations in the quality of the data, it is difficult to create a reliable error estimate for the cross-spectral phase. Therefore, phase differences from several independent periods are presented to demonstrate any trends. Intervals were chosen to be at times when the 2-day wave was large (see Fig. 1). Over these periods the phase of the meridional wind component at Mawson lags that at Adelaide by approximately 26 ± 6 h (150°–240°), and the zonal by 24 ± 8 h (120°–240°).

Figure 4 shows a cross-spectrum of the wind components at Mawson. Note that phase is approximately 90° at the $\frac{1}{2}$, 1, 2, $2\frac{1}{2}$ and 3 cycle day^{-1} frequencies (where significant peaks in amplitude occur). Table 2 shows the phase relationship between the zonal and meridional wind components at each station. These figures were obtained by taking the cross-spectrum of the wind components and measuring the phase at a period of 2 cycles day^{-1} and, as with Table 1, several independent periods are presented. In the SH, wave polarization is normally 'anticlockwise' (i.e. the zonal leads meridional by approximately 90°) and, therefore, it may be expected that for the 2-day wave the

Table 1. Phase relationship of 2-day wave components between Mawson and Adelaide. Universal time has been used and figures shown are the number of hours by which Mawson *lags* Adelaide

Interval	Zonal	Meridional
January 17–22, 1986	17.8	21.5
January 1–8, 1987	22.3	24.2
January 9–16, 1987	26.9	26.5
January 17–22, 1987	19.6	24.8
January 23–31, 1987	32.0	32.3
Average	24 ± 8	26 ± 6
January 1–31, 1986	18.7	21.1
January 1–31, 1987	24.6	28.6

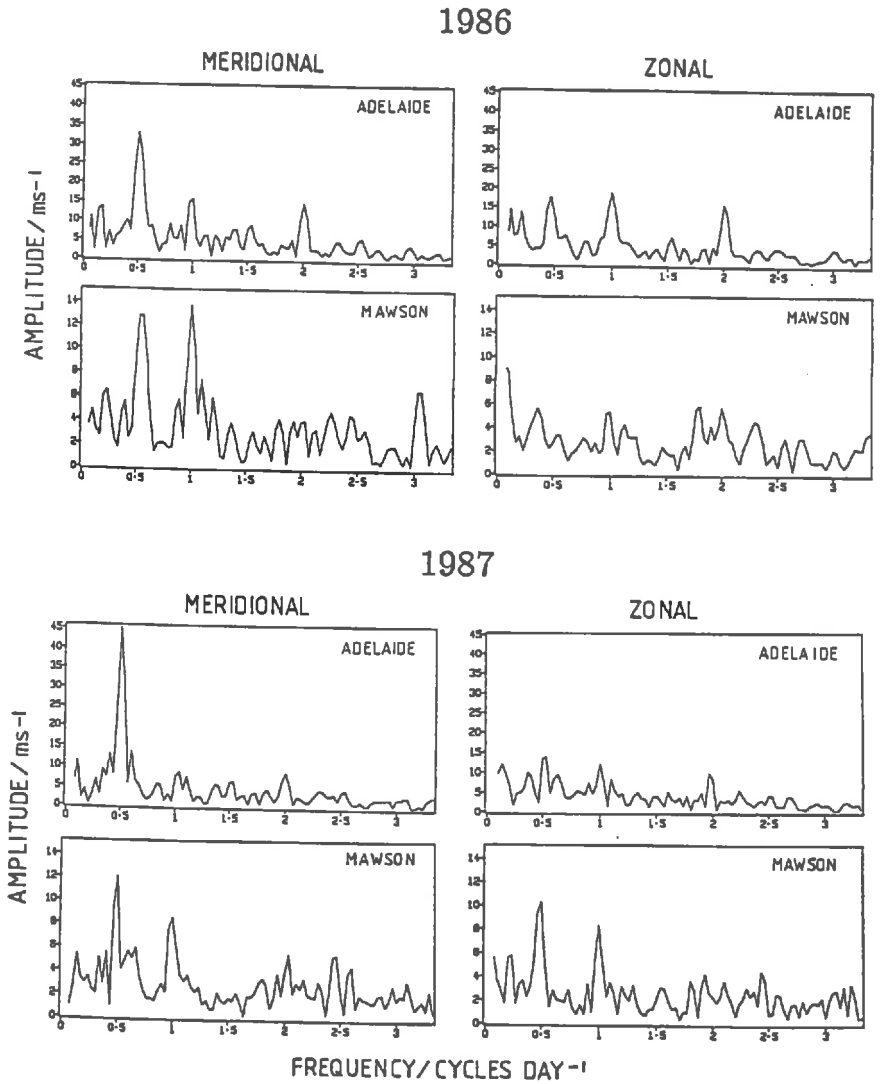

Fig. 2. Spectra for the mean wind components (87.5–97.5 km) for the periods January 15–26, 1986 (top) and January 15–31, 1987 (bottom)—note that the amplitude scale at Mawson has been expanded by three times. The ordinates of the amplitude spectra have dimensions of m s^{-1} Hz^{-1}. However, in these diagrams, they have been multiplied by a normalizing constant (with dimensions of Hz) in such a way that a sinusoid of amplitude A occupying the entire record length will appear in the spectrum as a 'line' of peak height A m s^{-1}, and the spectra may be used to estimate the amplitudes of any purely sinusoidal components which are present in the records analysed.

zonal component will lead the meridional by 12 h. Phase relationships between the 2-day wind components given in Table 2 show that generally this is the case. However, it is interesting to note that at Mawson the phase difference of the components of the 2-day winds is usually close to 90° and at Adelaide often closer to 45° (previous data from Adelaide gave phase differences in the range 6–12 h (Craig *et al.*, 1980).

Figure 5 shows the phase relationship of the (filtered) meridional winds at Mawson and Adelaide during January 1987. The average period of oscillation during this period is 47 ± 1 h at Adelaide and 48 ± 1 h at Mawson. Due to this slight difference in

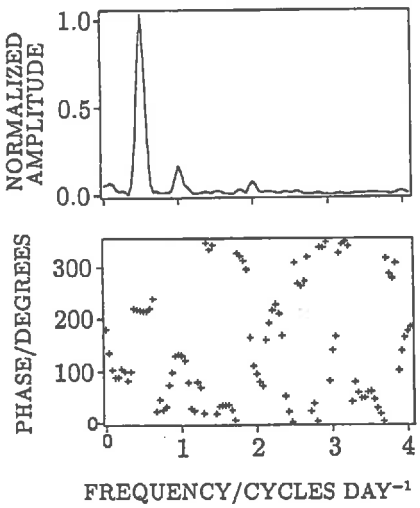

Fig. 3. Normalized cross spectrum of the meridional wind component (averaged over the height range 87.5–97.5 km) between Adelaide and Mawson during January 1987. The *phase* is the number of degrees by which Mawson *lags* Adelaide.

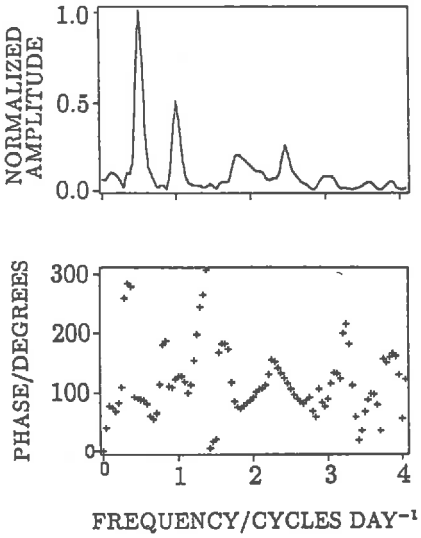

Fig. 4. Normalized cross spectrum of the meridional and zonal wind components (averaged over the height range 87.5–97.5 km) for Mawson during January 1987.

frequency, the two oscillations are approximately in antiphase at the beginning of the month and in quadrature toward the end. While it is clear that the two stations do not have a constant phase relationship, other observations (e.g. Table 1) indicate that the phase usually remains within the range of that shown in Figure 5.

Use of data for individual heights shows that, within the height range being sampled (80–100 km), amplitudes at both stations maximize at 92 ± 6 km with no measurable vertical phase variation, although vertical wavelengths > 60 km are plausible. CRAIG *et al.* (1983) found vertical wavelengths of 50 ± 10 km at low latitude (i.e. Townsville—19°S) but wavelengths > 100 km are usual at Adelaide and are also consistent with the present observations at Mawson.

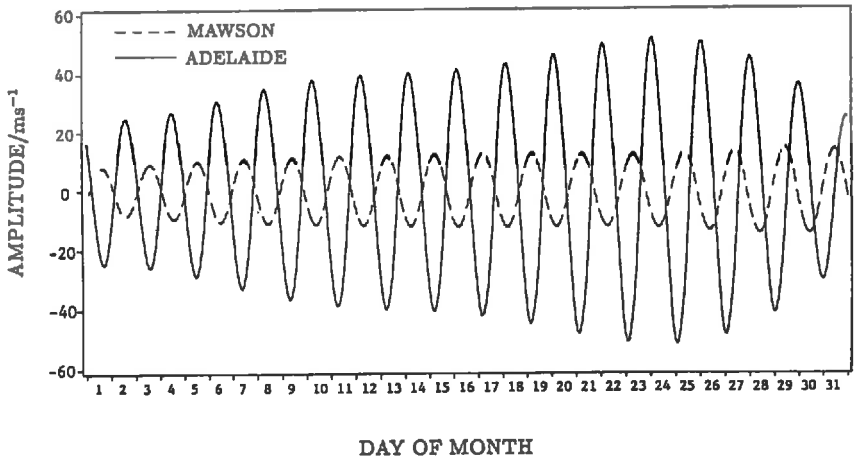

Fig. 5. Comparison of the meridional component of the 2-day oscillation between Mawson and Adelaide during January 1987 (an expanded section of Fig. 1). Wind data have been filtered by a square band pass of period range 1.8–2.2 days.

Table 2. Phase relationship of 2-day wave wind components. Figures show the number of hours by which the zonal leads the meridional component

Interval	Mawson	Adelaide
January 17–22, 1986	11.0	6.9
January 1–8, 1987	10.0	8.2
January 9–16, 1987	7.9	3.4
January 17–22, 1987	10.8	5.3
January 23–31, 1987	13.0	12.1
Average	11 ± 2	7 ± 4
January 1–31, 1986	10.0	5.7
January 1–31, 1987	11.9	7.9

3. DISCUSSION

During all summers (from mid-1984 to the present), 2-day wind oscillations have been measured at Mawson with typical amplitudes (during January) of 10–15 m s^{-1}, and reaching a maximum in late January. The simultaneous onset and development of the 2-day disturbance at Mawson and Adelaide suggests that the wave is global and persistent to high southern latitudes.

In the northern hemisphere, the 2-day wave is also observed at fairly high latitude. A study by meteor winds at Garchy, France (40°N) and Obninsk, U.S.S.R. (55°N) (GLASS *et al.*, 1975) showed 51 h period oscillations of 13 m s^{-1} (at both sites), which persisted for two weeks in July/August. This amplitude compares well with Mawson, but Carter and Balsley (1982) observed only weak 2-day winds with the MST radar at Poker Flat (65°N—the latitude conjugate of Mawson, 67°S). Although more quantitive data is required, a weaker 2-day wave in the high latitude NH is consistent with the generally weaker 2-day wave amplitudes observed in that hemisphere (CRAIG and ELFORD, 1981; VINCENT, 1984).

At Adelaide the disturbance is predominantly meridional with the zonal amplitudes approximately 0.3 of the meridional. During 1985 and 1987 wind component amplitudes at Mawson were comparable but in 1986 the meridional strongly dominated. In 1985 and 1987 the meridional amplitudes were still slightly stronger (10–15%) but further data will be required to positively establish a trend.

Using satellite observations of the stratosphere (40 ± 20 km), ROGERS and PRATA (1981) found a 2-day period temperature perturbation (maximum of 0.6 K) at 20°S. The perturbations become immeasurable outside the latitude range 20°N–50°S, which is interesting as mesospheric wind observations from Mawson showed that the 2-day winds occur with significant amplitude at higher latitudes than these satellite observations would suggest.

Earlier studies by pairs of similar latitude stations show good agreement with the theory of a wave travelling westward at approximately 60° longitude per day (CRAIG *et al.*, 1980). The phase differences of the wind components between Adelaide and Mawson are 24 ± 8 h for the zonal and 26 ± 6 h for the meridional (cf. Table 1). These are less than the 30.23 h which would have been expected if the wave was of a precisely 2-day period and the stations were of comparable latitude. This suggests that the phase may have changed by around 5 h ($\approx40°$) over the 33° latitude separation between the stations. SALBY (1981) has modelled the amplitude and phase structure for the 2-day wave at 'midsummer' (i.e. using a wind model which draws no distinction between the hemispheres) but only up to 12 scale heights (84.5 km—CIRA, 1988). At this level, there is $65\pm20°$ phase difference between the latitudes of Mawson and Adelaide. It is probable that there is a phase variation with latitude and this may account for Mawson's approximate 5 h phase lead (i.e. Mawson is approximately 5 h 'early') seen in both the zonal and meridional wind components. However, because the phase relation is not fixed, times can be found when the phase difference is very close to the 30.23 h which would be expected for similar latitude stations (e.g. January 23–31, 1987).

This variable phase relationship also suggests that the global structure of the wave region may be changing, with the mid- and high latitude parts of the wave propagating at different velocities (in this case, assuming that wave velocity is related to observed frequency, the mid-latitude part of the wave is propagating faster). Similar behaviour has also been observed between mid-NH and low latitude SH parts of the wave. For example, simultaneous observations at Sheffield (53°N) and Townsville (19°S) by CRAIG *et al.* (1983) gave periods of 51 ± 1 h at Townsville and 49 ± 1 h at Sheffield. Also meteor radar observations from Kyoto (TSUDA *et al.*, 1988) showed that the period of the 2-day wave may vary from 2.1–2.5 days during summer and may become 2 days during the autumn. These changes were tentatively correlated with the disappearance of eastward mean winds at around 95 km, which may be related to changes in zonal circulation at a lower level. Considerably improved satellite observations or an array of radars will be required to fully resolve the latitude and time dependent amplitude and phase structure of the mesospheric 2-day wave.

Acknowledgements—I wish to thank Dr B. H. BRIGGS for many useful discussions and for assistance in the preparation of this paper. This research was supported by the Australian Research Grants Scheme and by the Australian Antarctic Division.

REFERENCES

CARTER D. A., BALSLEY B. B.	1982	*J. atmos. Sci.* **39,** 2905.
CRAIG R. L. and ELFORD W. G.	1981	*J. atmos. terr. Phys.* **43,** 1051.
CRAIG R. L., VINCENT R. A., FRASER G. J. and SMITH M. J.	1980	*Nature* **287,** 319.
CRAIG R. L., VINCENT R. A., KINGSLEY S. P. and MULLER H. G.	1983	*J. atmos. terr. Phys.* **45,** 539.
GLASS M., FELLOUS J. L., MASSEBEUF A., SPIZZICHINO A., LYSENKO I. A. and PORTNIAGHIN YU. I.	1975	*J. atmos. terr. Phys.* **37,** 1077.
KINGSLEY S. H., MULLER H. G., NELSON L. and SCHOLEFIELD A.	1978	*J. atmos. terr. Phys.* **40,** 917.
MULLER H. G.	1972	*Phil. Trans. R. Soc.* **A271,** 585.
MULLER H. G. and NELSON L.	1978	*J. atmos. terr. Phys.* **40,** 761.
PLUMB R. A., VINCENT R. A. and CRAIG R. L.	1987	*J. atmos. Sci.* **44,** 3030.
ROGERS C. D. and PRATA A. J.	1981	*J. geophys. Res.* **86,** 9661.
SALBY M. L.	1981	*J. geophys. Res.* **86,** 857.
TSUDA T., KATO S. and VINCENT R. A.	1988	*J. atmos. terr. Phys.* **50,** 225.
VINCENT R. A.	1984	*J. atmos. terr. Phys.* **46,** 961.

A.7 Reprint of paper: "Radar observations of prevailing winds and waves in the southern hemisphere and lower thermosphere", by A. Phillips and R.A. Vincent *Pure Appl. Geophys.* 1989 130:303-318.

Phillips, A., & Vincent, R. A. (1989). Radar observations of prevailing winds and waves in the Southern Hemisphere mesosphere and lower thermosphere. *Pure and Applied Geophysics*, *130*(2), 303-318.

A.8 Reprint of paper: "High-latitude tidal behavior in the mesosphere and lower thermosphere", *J. atmos. Terr Phys* 1989 51:595–608.

Journal of Atmospheric and Terrestrial Physics, Vol. 51, No. 7/8, pp. 595–608, 1989.
Printed in Great Britain.

0021–9169/89 $3.00 + .00
Pergamon Press plc

High-latitude tidal behavior in the mesosphere and lower thermosphere

S. K. AVERY

Cooperative Institute for Research in Environmental Sciences, University of Colorado, Boulder, CO 80309, U.S.A.

R. A. VINCENT and A. PHILLIPS

Physics Department, University of Adelaide, Adelaide, South Australia 5001, Australia

A. H. MANSON

Institute of Space and Atmospheric Studies, University of Saskatchewan, Saskatoon, Saskatchewan, S7N 0W0, Canada

and

G. J. FRASER

Department of Physics, University of Canterbury, Christchurch, New Zealand

(*Received in final form* 24 *July* 1989)

Abstract—The high-latitude structure of the mean winds and tides is described in this paper using climatologies prepared from radar data during the Atmospheric Tides Middle Atmosphere Program. The monthly evolution of the amplitude and phase of the tides is discussed. Comparison between the southern and northern hemispheres indicate that the diurnal tide is stronger in the southern hemisphere and that the antisymmetric diurnal tidal modes are dominant. The semidiurnal tide is larger than the diurnal tide. The vertical wavelength structure is significantly different between the southern and northern hemisphere. Comparisons with recent tidal models show several discrepancies.

INTRODUCTION

Mid-latitude tides have long been studied by continuous measurements from meteor radar and medium frequency radars operating in a spaced antenna mode (MANSON *et al.*, 1989). Until recently there has not been much observational work on tides at latitudes greater than 65 degrees in either hemisphere. During the Atmospheric Tides Middle Atmosphere Program (ATMAP), many high-latitude radar facilities were in operation that provided continuous observations of the mean winds and tides in the upper mesosphere and lower thermosphere. In this paper we present an overview of the high-latitude structure that can be delineated from these climatologies and compare these results with previously taken wind and tidal data. The observational sources for high-latitude tides are summarized in Table 1.

Table 1. Observational sources

Location	Facility	Dates
Heiss Island (81°N, 55°E)	Meteor Radar	1964–1973
Tromso, Norway (69.5°N, 19°E)	EISCAT, UHF	Jan.–Feb., 1984
	Incoherent scatter radar	
	Portable MF/HF (Canada)	June–Dec., 1987
Andenes, Norway (69°N, 16°E)	Portable VHF (Germany)	June, 1984
Kiruna, Sweden (69°N, 20°E)	Meteor Radar (France)	1974–1975
Poker Flat, Alaska (65°N., 147°W)	MST/Meteor VHF (U.S.A.)	1983–1984
Mawson, Antarctica (67°S, 63°E)	MF/HF (Australia)	Dec. 1981–Jan. 1982
		1984–1987
Molodezhnaya (68°S, 45°E)	Meteor Radar	1967–1973
Scott Base, Antarctica (78°S, 170°E)	MF/HF	Dec. 1982, Jan. 1987
	(New Zealand)	Nov. 1987
College, Alaska (65°N)	Meteor Radar	Dec. 1966

Much of these data have not been published (Tromso, Mawson and Scott Base). The rest of the data can be found in TETENBAUM *et al.* (1986), ROTTGER and MEYER (1987), GLASS *et al.* (1978), RUSTER *et al.* (1988), FRASER (1984), CARTER and BALSLEY (1982), LYSENKO *et al.* (1980), and MACLEOD and VINCENT (1985). Note that several different types of radars have been used in studying atmospheric tides and consequently different signal processing techniques most suited to the particular radar have been used. The tides and mean winds that are discussed are the result of analyses of long segments of data that would represent a vector average of the tidal components.

The first reported observations of high-latitude tides in the northern hemisphere were made by HOOK (1970). Using a meteor radar located at College, Alaska (65°N), he was able to describe the main features of the diurnal and semidiurnal tides over an average height interval between 75 and 110 km. However due to the limited height resolution of the radar, it was difficult to delineate the vertical structure of the tides. Observations from Heiss Island (81°N) were made between 1964 and 1973 using a meteor radar (LYSENKO *et al.*, 1980). Due to the lack of height discriminating equipment on the radar, these observations refer to a mean height of 94 km. The French meteor radar facility provided observations of the tides during a four day campaign in August, 1974 at Kiruna, Sweden (69°N) (GLASS *et al.*, 1978). Due to the campaign nature of these observations, there was no information on the seasonal variability of the tides. A more extensive data base was analyzed from the MST radar at Poker Flat, Alaska (65°N) by CARTER and BALSLEY (1982). Their analysis was limited to the summer months due to the lack of mesospheric echoes during the non-summer months. However, because the MST radar has the capability of observing meteor echo returns, it was possible to provide climatologies of the tides and mean winds at Poker Flat during all seasons for the years 1983–1984 (TETENBAUM *et al.*, 1986). These climatologies have been compared with climatologies from the medium frequency radar at Saskatoon, Saskatchewan (52°N). This comparison between a high-latitude site and a mid-latitude site showed many similarities in the tidal structure (MANSON, 1988). There have been additional observational campaigns at high latitudes using the EISCAT incoherent scatter radar during MAP/WINE in January and February of 1984. Recently, climatologies at Tromso, Norway (69.5°N) are available from the portable medium frequency radar provided by the Saskatoon research group (MANSON, 1988).

Less observational work has been done at high latitudes in the southern hemisphere than in the northern hemisphere. First results of the tides were shown by ELFORD and MURRAY (1960) using a meteor radar at Mawson Base, Antarctica (67°S). However, their echo rates were extremely low to provide detailed information about the temporal evolution of the tides. The meteor radar at Molodezhnaya (68°S) provided data from 1967 to 1973 (LYSENKO *et al.*, 1980) but suffers also from the lack of height resolution. A medium frequency radar at Scott Base, Antarctica (78°S) provided some results for December 1982 (FRASER, 1984) and this system has recently been updated and was able to provide some measurements during 1987. MACLEOD and VINCENT (1985) reported some first results from a medium frequency radar operating in the spaced antenna mode at Mawson. These first results compared favorably with Poker Flat. This facility now has run continuously from 1984 and more complete climatologies of the wind field and tides are now available (PHILLIPS and VINCENT, 1988).

MEAN WIND STRUCTURE

The mean wind structure through which tides propagate is important in determining the structure of the tides in the mesosphere. The mean zonal winds from Poker Flat during 1983–1984 (TETENBAUM *et al.*, 1986) and those from Mawson during 1984–1986 (PHILLIPS and VINCENT, 1989) are shown in Figs. 1 and 2. Both locations show winter westerlies and stronger summer easterlies. The winter wind reversals at Poker Flat are associated with stratospheric warmings. These events are not apparent at Mawson. Both locations show an abrupt springtime reversal. This reversal occurs later at Mawson than at Poker Flat. The fall transition is more gradual than the spring transition occurring over a period of several weeks in the 70–100 km height region.

The mean meridional winds for the same locations and periods are shown in Fig. 2. There is more interannual variability in the meridional wind than the zonal wind and less consistency between the two locations. In general, there are equatorward winds during the summer maximizing at approximately 90 km with velocities of 10 m s^{-1}. These summer equatorward winds have also been observed at other high latitudes at Heiss Island, Molodezhnaya, and Scott Base (LYSENKO *et al.*, 1980; FRASER, 1984). The summer mesosphere equatorward winds appear to be a global effect (NASTROM *et al.*, 1982).

The mean winds observed with radars and the winds derived from satellite data show considerable differences at 80 km, especially during the winter months where the satellite winds indicate stronger westerlies

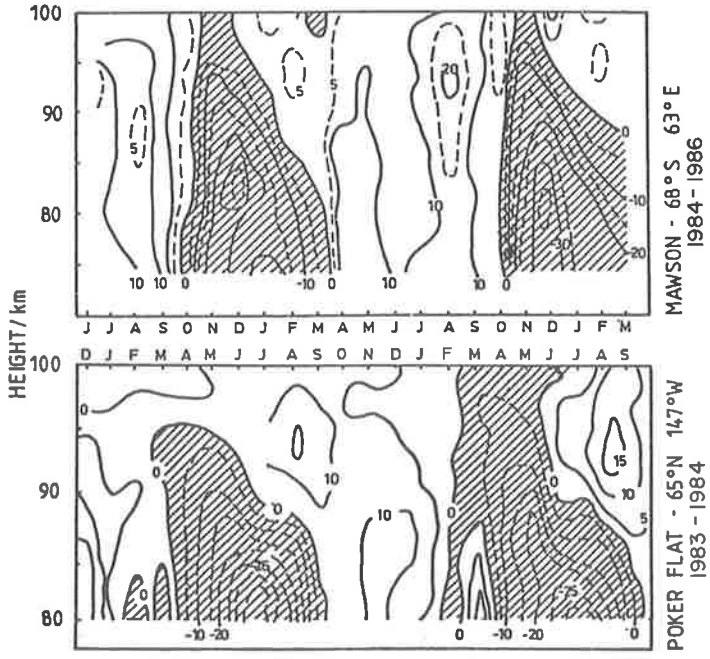

Fig. 1. Height–time contour plots of the monthly mean zonal winds from Mawson 1984–1986 (top) and Poker Flat, 1983–1984 (bottom). Positive values indicate westerlies. Contour units in $m\,s^{-1}$. Zonal winds at Mawson have been shifted by 6 months (PHILLIPS and VINCENT, 1989; TETENBAUM *et al.*, 1986).

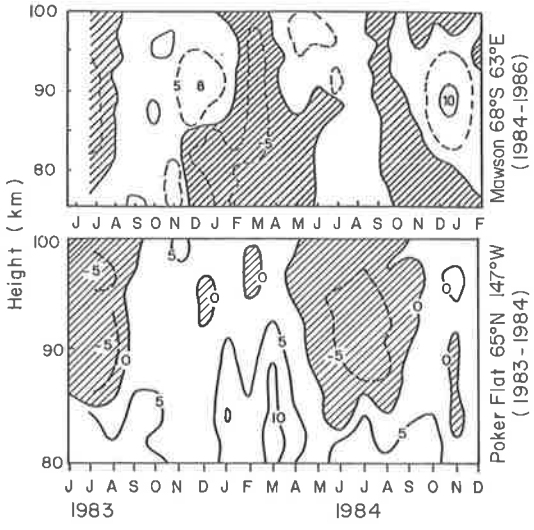

Fig. 2. Same as Fig. 1 except for meridional wind. Positive values indicate southerlies. Contour units in $m\,s^{-1}$ (PHILLIPS and VINCENT, 1989; TETENBAUM *et al.*, 1986).

(MANSON *et al.*, 1987). This discrepancy may be due to the geostrophic assumptions used in deriving the winds from satellite data and/or the fact that the radars provide only a temporal mean and not a temporal and spatial mean that the satellite data provide.

DIURNAL TIDE

The height–time monthly contour plots of the amplitude and phase of the diurnal tide at Mawson (1984–1986), Poker Flat (1983–1984), and Tromso (1987) are shown in Figs. 3 5 (PHILLIPS and VINCENT, 1988; TETENBAUM *et al.*, 1986; MANSON, 1988). The amplitude of the meridional component is generally larger than the zonal component at Poker Flat and Mawson. At Tromso the zonal and meridional components have the same amplitudes. The diurnal tide maximizes during the summer at approximately 85 km with a secondary maximum above 100 km. The first summer maximum is slightly higher at Mawson than at Poker Flat. The secondary maximum in August occurs when the mean wind shifts from easterly to westerly. Amplitudes at Mawson are generally greater than those at Poker Flat and Tromso above 100 km.

The phase structure at all three locations is indicative of evanescent or long vertical wavelength behavior during the spring, summer, and fall. During the winter months the phase structures are less regular with gradients equivalent to vertical wavelengths as short as 20–40 km. The meridional and zonal components are not necessarily in quadrature nor do they necessarily exhibit the same phase gradients. However, during the summer the phases are similar

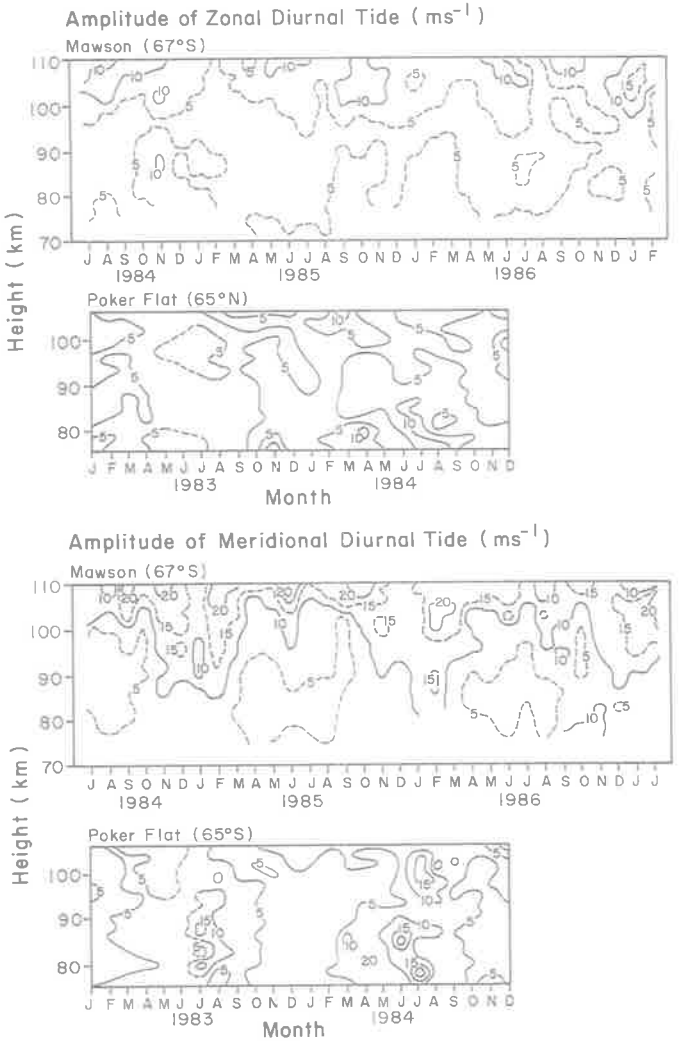

Fig. 3. Height–time monthly contour plots of the amplitude of the diurnal tide at Mawson and Poker Flat. Zonal (top); meridional (bottom). Units are in m s^{-1} (PHILLIPS and VINCENT, 1989; TETENBAUM *et al.*, 1986).

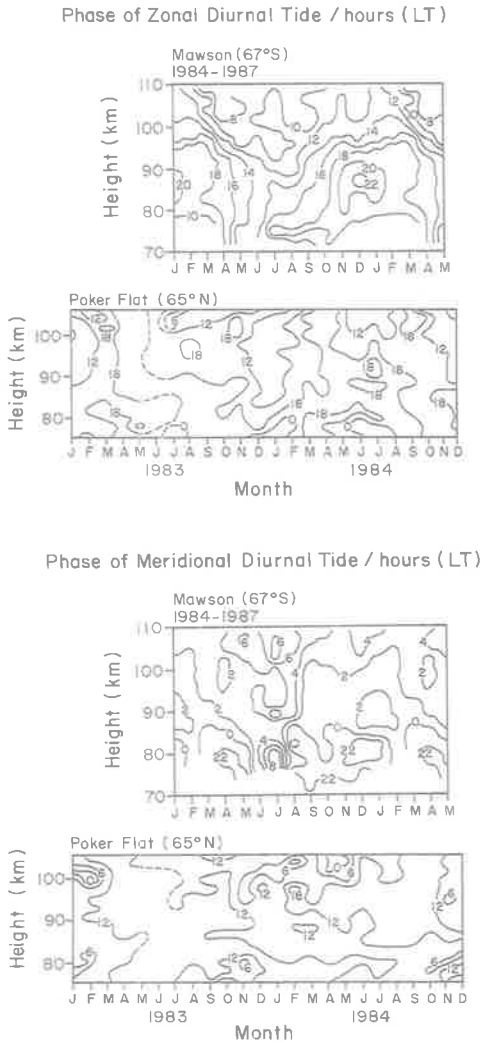

Fig. 4. Height–time monthly contour plots of the phase of the diurnal tide at Mawson and Poker Flat. Zonal (top); meridional (bottom). Units are the hour of maximum westerlies or southerlies relative to local midnight (PHILLIPS and VINCENT, 1989; TETENBAUM *et al.*, 1986).

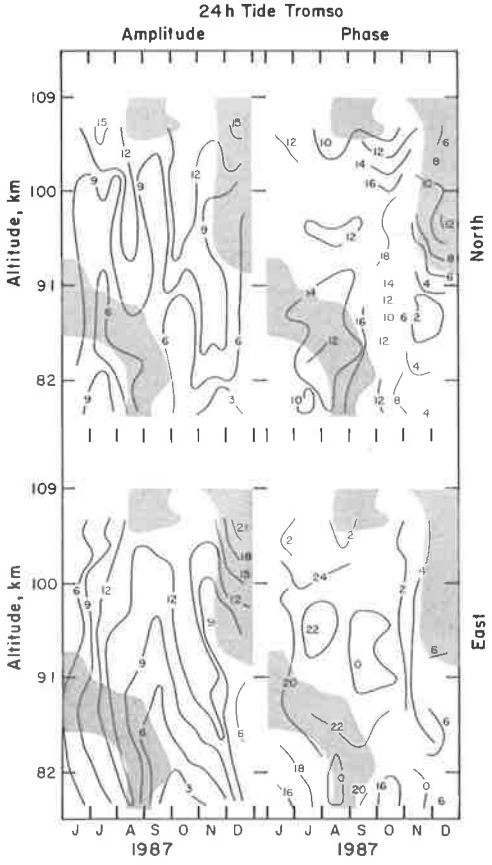

Fig. 5. Height–time monthly contour plots of the amplitude and phase of the zonal and meridional diurnal tide at Tromso during 1987. Amplitude in $m\,s^{-1}$; phase is the hour of maximum westerlies or southerlies relative to local midnight.

at Poker Flat and Tromso and the components are in quadrature. The phase transition from evanescent behavior to propagating wave structure is quite smooth beginning in the fall. The meridional components at Mawson and Poker Flat are in antiphase suggesting that symmetrical modes are important at these latitudes. The August results at Mawson, Poker Flat, and Tromso are similar to earlier results at Kiruna, Sweden taken by the French meteor radar facility during 11–14 August 1974 (Glass *et al.*, 1978).

The behavior of the diurnal tide during the winter months is slightly different at the three locations. At Mawson, the meridional phase indicates an upward propagating wave below 90 km, an evanescent structure between 90 and 100 km, and a downward propagating wave above 100 km as shown by the positive phase slope. The zonal component has a much smoother phase structure with a change of 6–8 h between 85–95 km with earlier times at greater height suggesting mode superposition or reflection. Above 100 km the zonal component at Mawson also shows an upward phase progression. At Poker Flat the diurnal phase structure is quite irregular. Upward propagating waves with short vertical wavelengths are observed below 100 km. The vertical wavelengths are shorter at Mawson than at Poker Flat. Above 100 km, upward phase progressions are observed. At Tromso, the phase structure shows an upward propagating wave above 100 km. The height behavior is suggestive of the combination of forcing in the troposphere/stratosphere and *in-situ* forcing in the upper mesosphere/lower thermosphere or mode superposition and reflection. At Tromso the *in-situ* forcing would appear to be centered around 100 km altitude.

The temporal evolution of the phase at 92 km shows that at Mawson the meridional component lags the zonal component by approximately 6 h. The phase slope with height is negative, hence the tidal components rotate counterclockwise which is indicative of an upward propagating tide. At Poker Flat and Tromso, the meridional component leads the zonal component by 6 h; the phase slope is positive giving a clockwise rotation of the tide suggestive of a downward propagating wave. Similar results are indicated in Lysenko *et al.* (1980).

Specific comparisons can also be made between observations at locations during simultaneous times. Figure 6 shows a comparison of data taken at Scott Base during November 1987 (Fraser, 1988) with that taken at Tromso (Manson, 1988) during the same period. At Scott Base, the meridional component has a long vertical wavelength whereas the zonal component has a short effective vertical wavelength (34 km) with a phase slope reversal at 85 km. At Tromso the zonal component exhibits more of an evanescent structure and the meridional component has a short vertical wavelength with a similar phase slope reversal at 85 km. In both cases, the zonal component leads the meridional component. Also shown in this figure are the results from Scott Base during January 1987. Unlike the winter months at Mawson, Poker Flat, and Tromso, Scott Base shows that the meridional and zonal components are in quadrature with a propagating wave having a vertical wavelength of approximately 90 km.

Another diurnal tide comparison that can be made is between the Sousy portable radar at Andenes, Norway (Ruster *et al.*, 1988) and Poker Flat, Alaska during June 1984. This comparison is shown in Fig. 7. Note that both zonal components decrease with increasing height and both meridional components increase with increasing height at lower heights then

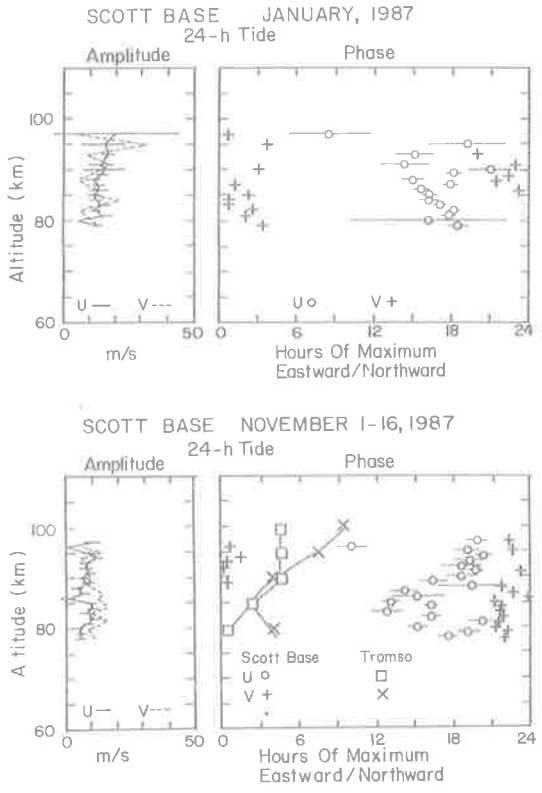

Fig. 6. Comparison of the amplitude and phase of the diurnal tide at Scott Base and Tromso during November 1987 (bottom). Also shown is the tidal structure at Scott Base during January 1987 (top).

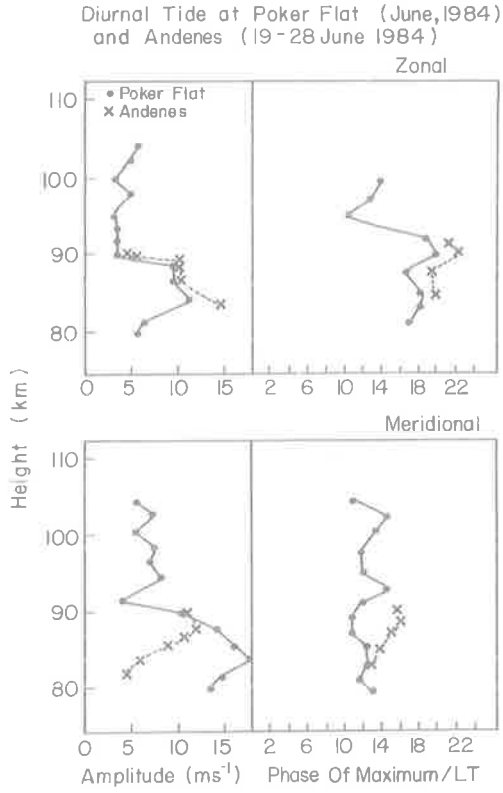

Fig. 7. Amplitude (m s^{-1}) and phase (hour/LT) of the diurnal tide at Poker Flat and Andenes during June 1984.

decrease with increasing height. The meridional amplitude peaks at Poker Flat at a lower height than at Andenes. Both locations show long vertical wavelength (70 km) structure and the absolute phases agree quite well. The meridional component leads the zonal component with a slightly positive phase slope indicating downward propagation. This tide is in quadrature up to 92 km.

Figure 8 shows the zonal diurnal tide at Mawson compared with model results of VIAL (1986) and FORBES and HAGAN (1988). Both of these models include the effects of diffusion which latitudinally broadens the diurnal tide. Model amplitudes for summer solstice are too large. The vertical wavelengths compare favorably with the Vial model being slightly better than the Forbes and Hagan model. The models do not show the observed seasonal phase shift of 8 h. In both cases the meridional diurnal tide compares more favorably with these models than the zonal diurnal tide.

SEMIDIURNAL TIDE

The monthly height–time contour plots of the semidiurnal tide for Mawson, Poker Flat, and Tromso are shown in Figs. 9–11 (PHILLIPS and VINCENT, 1988; TETENBAUM *et al.*, 1986; MANSON, 1988). The first fact to note is that the semidiurnal tide is larger than the diurnal tide which is expected from theory since the diurnal tidal modes decay away from the equator. The amplitudes of the meridional component are comparable to those of the zonal component. The amplitudes are greater at Mawson than at Poker Flat and Tromso especially above 100 km and during the equinoxes although it is difficult to make a direct comparison due to the interannual variability of the tide. A summer/early fall maximum is observed at all three locations. This jet maximizes later at Mawson than at Poker Flat and Tromso which is consistent with a later zonal wind reversal at Mawson. There is also an enhancement during spring at Mawson which is not observed at Poker Flat.

The phase structure at Mawson, Poker Flat, and Tromso is quite different which may be due to different

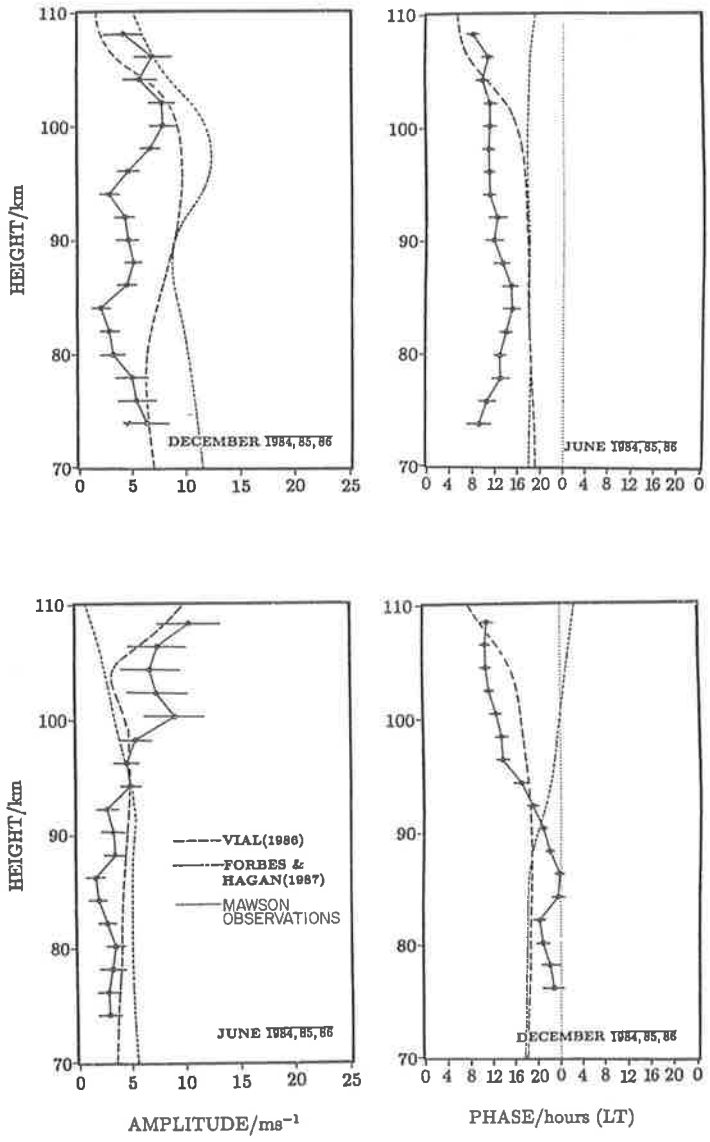

Fig. 8. Zonal diurnal tide at Mawson at winter and summer solstice compared with recent tidal models (PHILLIPS and VINCENT, 1988).

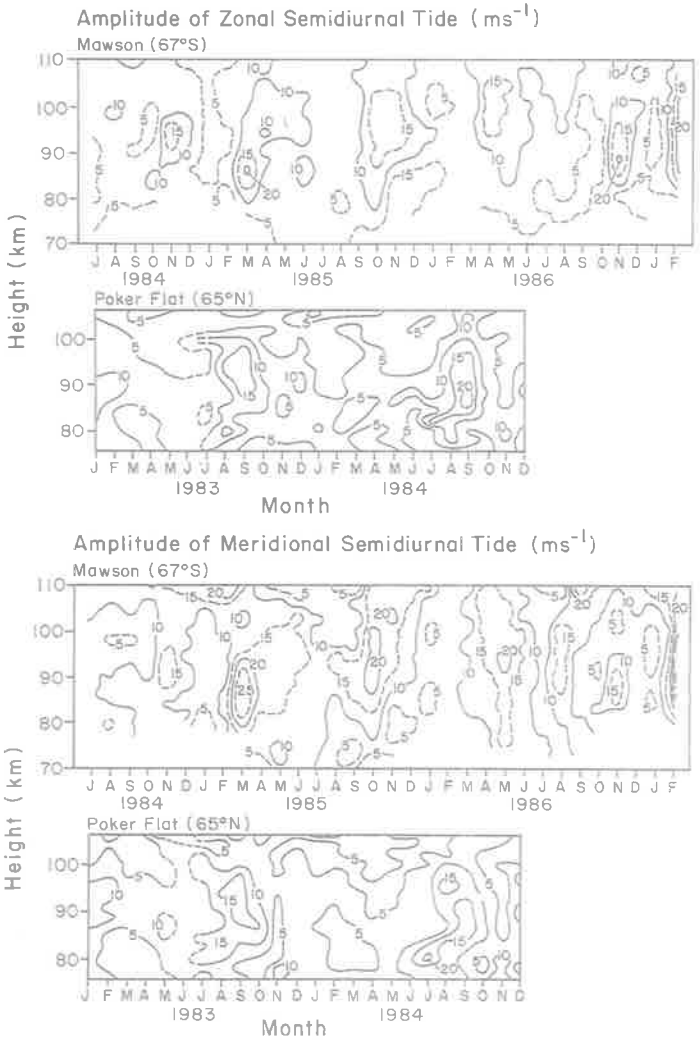

Fig. 9. Same as Fig. 3 except for semidiurnal tide.

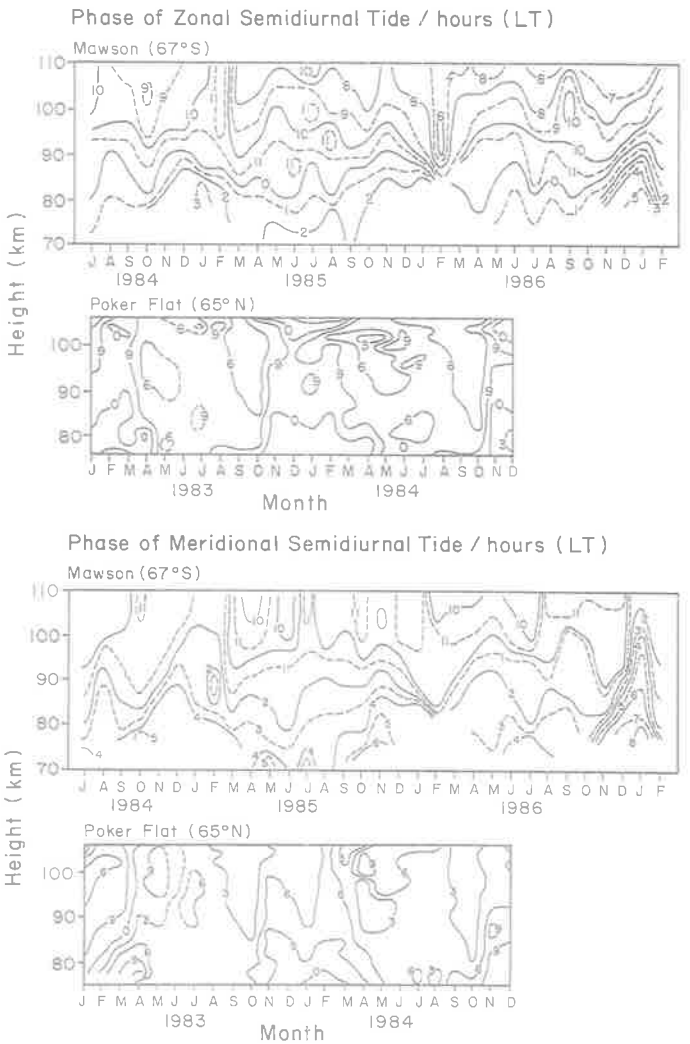

Fig. 10. Same as Fig. 4 except for semidiurnal tide.

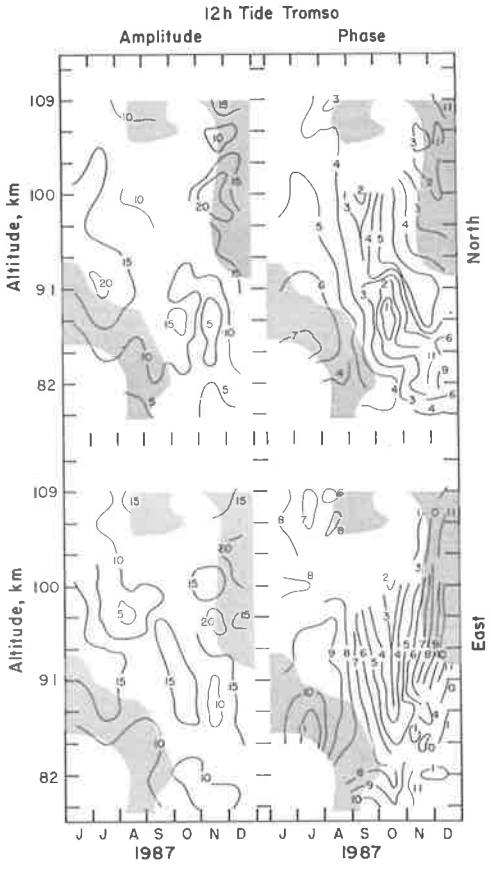

Fig. 11. Same as Fig. 5 except for semidiurnal tide.

mode superposition at the three locations. One obvious feature in these phase plots is the strong positive phase progression during October and November at Poker Flat, Tromso, and Mawson. During July–August at Tromso and January–February at Mawson, a rapid negative phase progression is observed. This negative phase progression is not observed at Poker Flat. The phases at the three locations go through a 180 degree shift in approximately 2 months. Note that these rapid phase progressions occur in the summer–fall period in the northern hemisphere and the spring–summer period in the southern hemisphere. The standard deviation of the weekly zonal mean winds and tides at Poker Flat during 1984 in each of the seasons is shown in Fig. 12. These results clearly show the variability of the semidiurnal tide during the fall season and make it difficult to compare with seasonal models of the semidiurnal tide.

Because the phase structure for the semidiurnal tide is much smoother than the diurnal tides it is possible to fit the phase slope and thus obtain a measure of the vertical wavelengths. The mean vertical wavelengths at Mawson and Poker Flat are shown in Fig. 13. At Mawson propagating modes are definitely present since the zonal component leads the meridional component and there is a negative phase slope with height. The vertical wavelengths during the summer are 20–30 km suggestive of the S(2, 6) or S(2, 7) modes. In winter the vertical wavelengths are 70–80 km suggestive of the S(2, 3) mode. Above 100 km the meridional and zonal phase structures become more evanescent indicating the dominance of the S(2, 2) mode. The vertical wavelengths at Poker Flat have the opposite trend of that at Mawson. Long vertical wavelengths (greater than 150 km) or evanescent structure is observed during the summer. Short vertical wavelengths (20–40 km) are observed during winter and spring and 80 km vertical wavelengths are observed during fall. At Tromso the structures are more similar to Poker Flat. The vertical wavelengths can be estimated to be approximately 50–100 km during summer, evanescent/irregular in the zonal/meridional component during fall, and 40–45 km in both components below 100 km during winter with much longer wavelengths above 100 km. Long vertical wavelengths during the summer have previously been observed at Kiruna, Sweden (Glass *et al.*, 1978). Significant differences are also apparent when comparing tides observed at Scott Base and Tromso during November 1987 (not shown). There is an abrupt phase reversal at Tromso at 87 km in the meridional component, whereas the zonal component compares favorably.

The comparison between Poker Flat and Andenes during June 1984 is shown in Fig. 14. The data from Andenes were taken from Ruster *et al.* (1988). The amplitudes are much larger at Andenes than at Poker Flat. Shorter vertical wavelengths (30 km) are also observed at Andenes making it more similar to Tromso observations during the summer of 1987 than to Poker Flat.

During January and February 1984 the EISCAT 933 MHz radar was operating as part of the MAP/WINE campaign. Results from this campaign have been reported in Rottger and Meyer (1987). Figure 15 is taken from that reference and has had the Poker Flat January 1984 semidiurnal tidal results superposed for a comparison. Although the EISCAT data can be spotty some qualitative conclusions can be drawn from this figure. The amplitudes are weaker at Poker Flat than at Tromso during this period. The phases are in good agreement with Poker Flat leading Tromso by approximately 2–3 h. The vertical phase structure indicates a propagating wave that is the same at both locations.

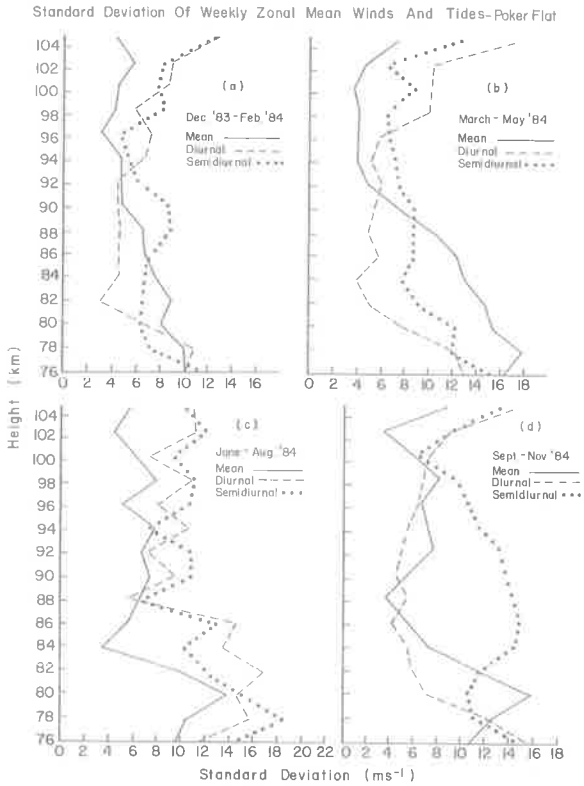

Fig. 12. Standard deviation of the weekly zonal mean winds, diurnal and semidiurnal tides at Poker Flat as a function of season.

Semidiurnal tidal results obtained from the EISCAT UHF radar at high altitudes during 1985 have been reported by KIRKWOOD (1986). The amplitude of the semidiurnal tides are much larger at higher altitudes peaking at 70–140 m s^{-1} at 105 km altitude. The amplitudes below 100 km should be treated with caution due to the height resolution of the UHF radar. During May, November, and January upward propagating tides are seen with wavelengths of 22–50 km. During August 120 km vertical wavelengths are seen. This seasonal pattern is more in line with what was observed at Poker Flat during 1983–1984 than with the Tromso 1987 or the Mawson 1984–1986 results.

MODEL RESULTS

Recently VIAL and FORBES (1989) have developed a tidal model that computes the monthly evolution of the semidiurnal tide. Contour plots of the meridional amplitude and phase at 66°N are compared with the Poker Flat results in Figs. 16 and 17. The model amplitudes are stronger at winter solstice than that observed by a factor of 10. The observations at summer solstice are stronger than what the model predicts. The model predicts the September jet at 90–95 km but the jet is slightly higher than that observed and about 10 m s^{-1} stronger than that observed.

The model phases predict longer vertical wavelengths (60 km) during the winter months whereas the observations show shorter vertical wavelengths. The model wavelengths are shorter in summer when the observations show evanescence. The model does correctly predict the rapid positive phase transition in October–November which is observed to occur regularly at Poker Flat. It does not predict the negative phase transition observed during July–August at Tromso. Although not shown here, the meridional component leads the zonal component in both model and observations.

Similar plots are shown for Mawson and the model in Figs. 18 and 19. The model does not predict the summer jet that is observed. The observed amplitudes during the summer are stronger than the model shows. The model amplitudes increase with increasing height which is also observed. However, the observed ampli-

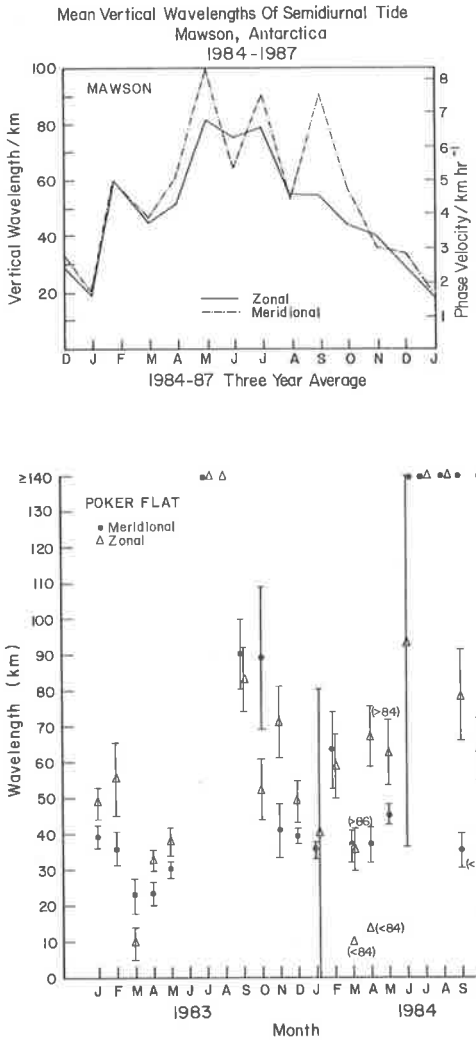

Fig. 13. Three year averaged vertical wavelengths of the semidiurnal tide at Mawson (top) and monthly mean vertical wavelengths of the semidiurnal tide at Poker Flat (bottom).

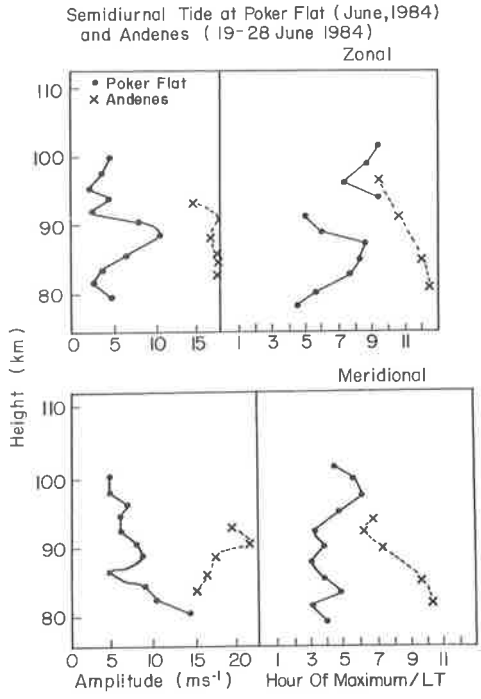

Fig. 14. Amplitude ($m\,s^{-1}$) and phase (hour/LT) of the semidiurnal tide at Poker Flat and Andenes during June 1984.

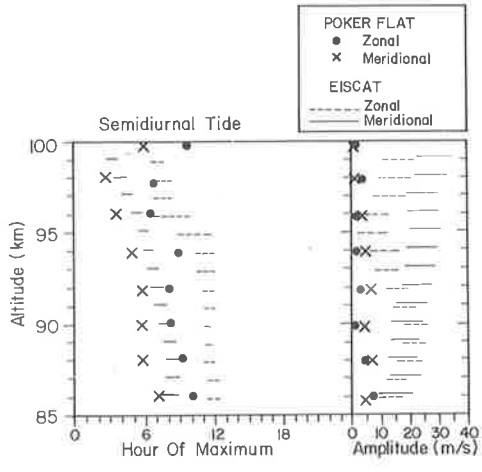

Fig. 15. Amplitude and phase of the semidiurnal tide at EISCAT (ROTTGER and MEYER, 1987) and Poker Flat during January 1984.

tudes above 100 km are weaker than the model amplitudes.

The observed rapid negative phase transition during January–March is predicted by the model, however, the model predicts a longer vertical wavelength during this period than that observed. The model does predict shorter wavelengths in summer than in winter which is in agreement with the observations. The rapid positive phase shift observed during October–November at Mawson is not predicted by the model. The model zonal component leads the meridional component as observed.

SUMMARY

At latitudes above 60° the amplitude of the observed meridional diurnal tide is larger than the zonal component. Below 100 km, the tide maximizes during summer. The amplitudes in the southern hemi-

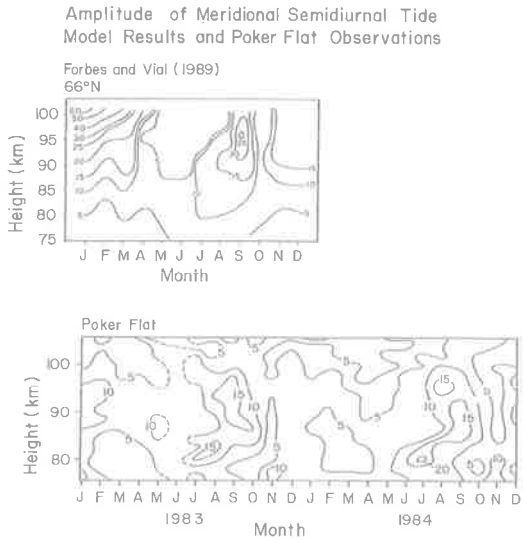

Fig. 16. Comparison of height–time monthly contours of the amplitude of the meridional semidiurnal tide between model results (FORBES and VIAL, 1989) and Poker Flat observations (TETENBAUM *et al.*, 1986).

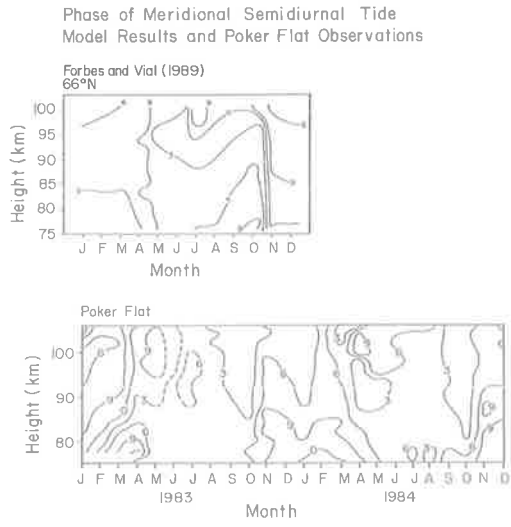

Fig. 17. Same as Fig. 16 except for the phase of the meridional semidiurnal tide.

sphere are greater than those in the northern hemisphere, especially above 100 km. The tide exhibits evanescent or long vertical wavelength structure during spring, summer and fall. During winter, strong phase gradients equivalent to 20–40 km vertical wavelengths are observed and *in-situ* forcing or mode superposition of the tide is apparent. Symmetric tidal modes appear to be dominant due to the antiphase structure between the southern and northern hemisphere meridional components. Dissipation and antisymmetric modes are also important in correctly modelling the diurnal tide.

The observations of the semidiurnal tide show that

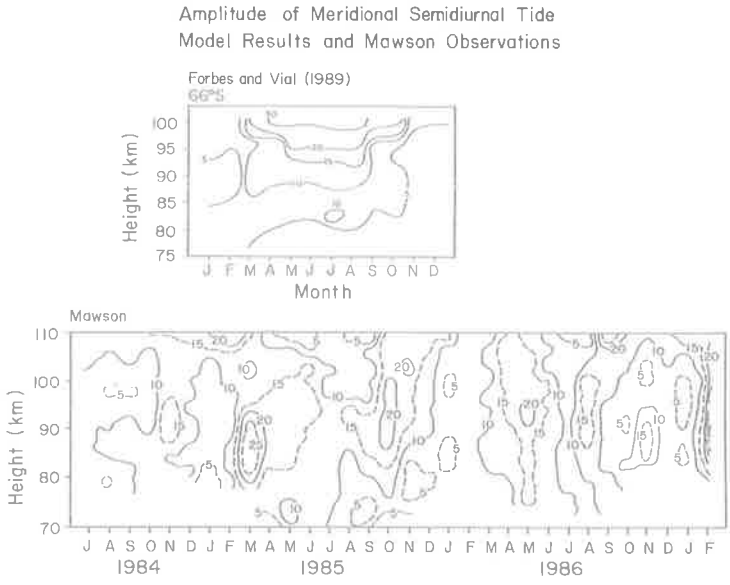

Fig. 18. Comparison of height–time monthly contours of the amplitude of the meridional semidiurnal tide between model results (FORBES and VIAL, 1989) and Mawson observations (PHILLIPS and VINCENT, 1988).

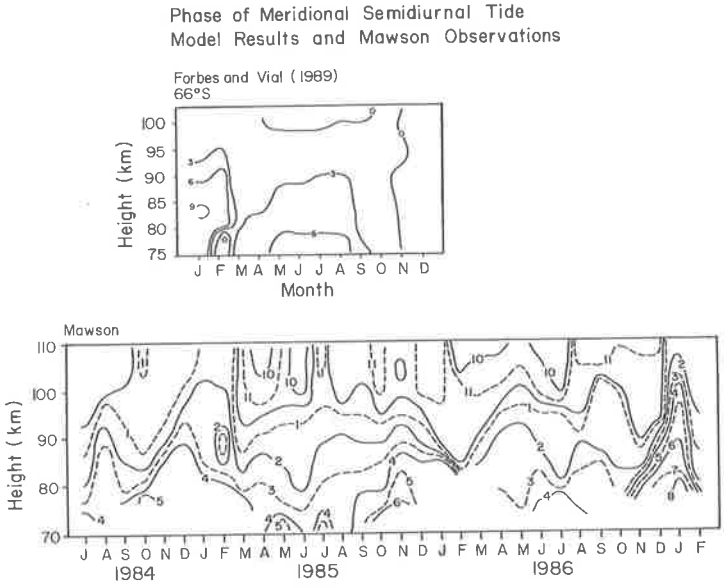

Fig. 19. Same as Fig. 18 except for the phase of the meridional semidiurnal tide.

it is larger than the diurnal oscillation. There is an enhancement of the semidiurnal tide during autumn below 100 km. A similar enhancement is observed during spring in the southern hemisphere but not in the northern hemisphere. There is a rapid positive phase shift of 180 degrees in 2 months during October–November. There is a corresponding negative phase shift during July–August in the northern hemisphere at European longitudes and January–February in the southern hemisphere. The vertical wavelengths in the northern hemisphere have opposite seasonal trends to that in the southern hemisphere. Short vertical wavelengths are observed during the southern hemisphere summer and the northern hemisphere winter. Long vertical wavelengths are observed during the southern hemisphere winter and the northern hemisphere summer. Comparison of results from different locations during different years can be misleading due to the interannual variability of the semidiurnal tide. Comparisons between model results and Poker Flat observations show that model amplitudes are significantly stronger than observed amplitudes during the winter and observed amplitudes are stronger than model amplitudes during the summer. Longer vertical wavelengths during winter than summer are predicted by the model whereas short vertical wavelengths are observed in winter and evanescent or long vertical wavelengths are observed in summer. The model correctly predicts the rapid positive phase transition during October–November but does not predict the rapid negative phase transition in July–September observed at Tromso. Model comparisons with Mawson data show that the model does not predict the observed summer/fall jet, the observed amplitudes above 100 km are weaker than the model, but the wavelengths are reproduced. The rapid negative phase transition during January–March is predicted by the model but the rapid positive phase transition in October–November is not predicted.

Acknowledgements—This work was supported in part by the National Science Foundation under grant NSF ATM 86-10357.

REFERENCES

Forbes J. M.	1982	*J. geophys. Res.* **87,** 5222.
Forbes J. M. and Hagan M. E.	1988	*Planet. Space Sci.* **36,** 579.
Fraser G. J.	1984	*J. atmos. terr. Phys.* **46,** 143.
Fraser G. J.	1988	Private communication.
Glass M., Bernard R., Fellous J. L. and Massebeuf M.	1978	*J. atmos. terr. Phys.* **40,** 923.
Kirkwood S.	1986	*J. atmos. terr. Phys.* **48,** 817.

LYSENKO I. A., ORLYANSKY A. D. and PORTNYAGIN YU. I.	1980	*Electric Current and Atmospheric Motion* (KATO, S. and ROPER, R. G., Eds), Center for Academic Publications, Tokyo.
MANSON A. H.	1988	Private communication.
MANSON A. H., MEEK C. E., MASSEBEUF M., FELLOUS J. L., ELFORD W. E., VINCENT R. A., CRAIG R. L., ROPER R. G., AVERY S., BALSLEY B. B., FRASER G. J., SMITH M. J., CLARK R. R., KATO S. and TSUDA T.	1987	*Adv. Space Res.* **7,** 143.
MANSON A. H., MEEK C. E., TEITELBAUM H., VIAL F., SCHMINDER R., KÜRSCHNER D., SMITH M. J., FRASER G. J. and CLARK R. R.	1989	*J. atmos. terr. Phys.* **51,** 579.
NASTROM G. D., BALSLEY B. B. and CARTER D. A.	1982	*Geophys. Res. Lett.* **9,** 139.
PHILLIPS A. and VINCENT R. A.	1988	Mawson Institute Report, University of Adelaide.
PHILLIPS A. and VINCENT R. A.	1989	*Pure app. Geophys*, in press.
ROTTGER J. and MEYER W.	1987	*J. atmos. terr. Phys.* **49,** 689.
RUSTER R., CZECHOWSKY P. and SCHMIDT G.	1988	*J. atmos. terr. Phys.* **50,** 1041.
TETENBAUM D., AVERY S. K. and RIDDLE A. C.	1986	*J. geophys. Res.* **91,** 14359.
VIAL F.	1986	*J. geophys. Res.* **91,** 8955.
VIAL F. and FORBES J. M.	1989	*J. atmos. terr. Phys.* **51,** 663.

REFERENCES

Andrews, D.G., and McIntyre, M.E. (1976), Planetary waves in horizontal and vertical shear: The generalized Eliassen-Palm relation and the mean zonal acceleration. *J. Atmos. Sci.* **33**:2031–2048.

Avdyushin, S.I., et al. (1981), Experimental testing of 'corpuscular' hypothesis of night-time mid-latitude ionosphere. Results of simultaneous rocket–satellite investigations. *Adv. Spac. Res.* **1**:107–110.

Avery, S.K., Vincent, R.A., Phillips, A., Manson, A.H., Ruster, R., Röttger, J., Fraser, G.J., Vial, F., and Forbes, J.M. (1989), High latitude tidal behaviour in the mesosphere and lower thermosphere. Paper presented at COSPAR meeting, Helsinki 1988. *J. Atmos. Terr. Phys.* **51**:595–608.

Ball, S.M. (1983), Upper atmosphere tides and gravity waves at mid-latitudes. Ph.D. thesis, The Adelaide University.

Barnett, J.J. (1987), Private communication.

Barnett, J.J. and Corney, M. (1985), Middle atmosphere reference model derived from satellite data. *Handbook for MAP.* **16**:47–85.

Belrose, J.S. (1970), Radio wave probing of the ionosphere by the partial reflection of radio waves (from heights below 100 km). *J. Atmos. Terr. Phys.* **32**:567–596.

Bernard, R. (1981), Variability of the semi-diurnal tide in the upper mesosphere. *J. Atmos. Terr. Phys.* **43**:663–674.

Bond, F.R. and Paine, R.L. (1971), Geographical maps of the auroral ovals for different levels of geomagnetic disturbance. Australian Antarctic Division Technical Note 7.

Boville, A. B. (1987), The validity of the geostrophic approximation in the winter stratosphere and troposphere. *J. Geoph. Res.* **44**:443–457.

Brekke, A. (1983), Joule Heating and Particle Precipitation. *Adv. Spac. Res.* **2**:45–53.

Briggs, B. H. (1984), The analysis of spaced sensor records by correlation techniques. *Handbook for MAP.* **13**:166–186.

Briggs, B. H., Phillips, G. J., and Shinn, D. H. (1950), The analysis of observations on spaced receivers of the fading of radio signals. *Proc. Phys. Soc. London.* **63**:106–121.

Carter, D.A., Balsley, B.B. (1982), The summer wind field between 80 and 93 km observed by the MST radar at Poker Flat, Alaska (65°N). *J. Atmos. Sci.* **39**:2905–2915.

Chamberlain, M.T. and Jacka, F. (1979), Optical evidence for mid-latitude charged particle precipitation. *J. Atmos. Terr. Phys.* **41**:111–118.

Chanin, M.L. (1984), Review of lidar contributions to the description and understanding of the middle atmosphere. *J. Atmos. Terr. Phys.* **46**:987–993.

Chapman, S. and Lindzen, R.S. (1970), Atmospheric tides. D. Reidel Pub. Co.

Charney, J.G. and Drazin, P.G. (1961), Propagation of planetary-scale disturbances from the lower into the upper atmosphere. *J. Atmos. Sci.* **66**:83–109.

CIRA (1988), Figures from CIRA 1988 are contained in a computer program held by the Atmospheric Physics Group at Adelaide. CIRA 1988 data displayed in this thesis were computed from this program by S. Eckermann.

Cocks, T.D., Creighton, D.F., and Jacka, F. (1980), Application of a dual Fabry-Perot spectrometer for daytime studies. *J. Atmos. Terr. Phys.* **42**:499–511.

Collis, P.N., et al. (1986), Experimental determination of effective recombination rates in the disturbed high latitude ionosphere. *Annales Geophysicae* 4:211–218.

Craig R. L. and Elford W. G. (1981), Observations of the quasi 2–day wave near 90 km altitude at Adelaide (35°S). *J. Atmos. Terr. Phys.* **43**:1051–1056.

Craig, R.L., Vincent, R.A., Fraser, G.J. and Smith M.J. (1980), The quasi 2-day wave in the southern hemisphere mesosphere. *Nature:Phys. Sci.* **287**:319–320. 1980.

Craig, R.L., Vincent, R.A., Kingsley, S.P. and Muller, H.G. (1983), Simultaneous observations of the quasi 2-day wave in the northern and southern hemispheres. *J. Atmos. Terr. Phys.* **45**:539–541.

Eather, R.H. and Jacka, F. (1966), Auroral absorption of cosmic radio noise. *Aust. J. Phys.* **19**:215–239.

Edmon, H.Jr., Hoskins, B.J. and McIntyre, M.E. (1981), Eliassen–Palm cross sections for the troposphere. *J. Atmos. Sci.* **37**:2600–2616.

Eliassen, A. and Palm, E. (1960), On the transfer of energy in stationary mountain waves. *Geophysica Norvegica* **12**:1–23.

Felgate, D.G. (1970), On the point source effect in the measurement of ionospheric drifts. *J. Atmos. Terr. Phys.* **32**:241–245.

Fleming, E.L.,Chandra, S.,Shoeberl M.R. and Barnett, J.J. (1988), Monthly mean global climatology of temperature, wind, geopotential height and pressure for 0–120 km. *NASA Technical Memorandum 100697, February 1988.*

Forbes, J.M. (1982a), Atmospheric tides **1.** Model description and results for the solar diurnal tide. *J. Geoph. Res.* **87**:5222–5240.

Forbes, J.M. (1982b), Atmospheric tides **2.** The solar and lunar semidiurnal components. *J. Geoph. Res.* **87**:5241–5252.

Forbes, J.M. (1984), Middle atmosphere tides. *J. Atmos. Terr. Phys.* **46**:1049–1067.

Forbes, J.M. (1985), Middle Atmosphere Tides Between 80 and 120 km. *Handbook for MAP.* **16**:278–289.

Forbes, J.M. and Garrett, H.B. (1979), Theoretical studies of atmospheric tides. *Rev. Geophys.* **17**:1951–1981.

Forbes, J.M. and Hagan M.E. (1982), Thermospheric extensions of the classical expansion functions for semidiurnal tides. *J. Geoph. Res.* **87**:5253–5259.

Forbes, J.M. and Hagan M.E. (1988), Diurnal propagating tides in the presence of mean winds and dissapation: a numerical investigation. *Planet. Spac.* **36**:579–590.

Forbes, J.M. and Vial, F. (1989), Private communication. *J. Atmos. Terr. Phys.* in press.

Francis, R.J. and Jacka, F. (1969), Studies on auroral hydrogen emission using an image intensifier. *J. Atmos. Terr. Phys.* **31**:321–337.

Fraser G. J. (1984), Summer circulation in the Antarctic middle atmosphere. *J. Atmos. Terr. Phys.* **46**:143–146.

Fraser G. J. (1984), Partial-reflection spaced antenna wind measurements. *Handbook for MAP.* **13**:233–247.

Fritts D. C. (1984), Gravity wave saturation in the middle atmosphere: a review of theory and observations. *J. Geoph. Res.* **22**:275–308.

Garcia, R.R., Susan, S., Avery S.K. and Reid, G. (1987), Transport of nitric oxide and the D region winter Anomaly. *J. Geoph. Res.* **92**:977–994.

Glass, M., Fellous, J.L., Massebeuf, A., Spizzichino, A., Lysenko, I.A., and Portniaghin, Yu.I. (1975), Comparison and interpretation of the results of simultaneous wind measurements in the lower thermosphere at Garchy (France) and Obninsk(U.S.S.R.) by meteor radar technique. *J. Atmos. Terr. Phys.* **37**:1077-1087.

Gregory, J.B. and Manson, A.H. (1970), Seasonal variations of electron densities below 100 km at mid-latitudes–III. Stratospheric–ionospheric coupling. *J. Atmos. Terr. Phys.* **32**:837–852.

Grose, W.L. and O'Neill (1989), Comparison of data and derived quantities for the middle atmosphere of the southern hemisphere. *Pure Appl. Geophys.* **130**:195–212.

Groves, G.V. (1983), Thermospheric energy flux of the semidiurnal tide. *Planet. Spac.* **31**:1183–1186.

Groves, G. V. (1985), A global reference atmosphere from 18 to 80 km. U.S. Air Force surveys in geophysics. AFGL-TR-85-0129.

Hartmann, D. L. (1976), The structure of the stratosphere in the southern hemisphere during late winter 1973 as observed by satellite. *J. Atmos. Sci.* **33**:1141–1154.

Hedin, A.E. (1983), A revised thermospheric model based on mass spectrometer and incoherent scatter data: MSIS-83. *J. Geoph. Res.* **88**:10170–10185.

Heelis, R.A., Lowell, J.K. and Spiro, R.W. (1982), A model of the high-latitude ionospheric convection pattern. *J. Geoph. Res.* **87**:6339–6345.

Hirota, I., Hirooka T. and Shiotani M. (1983), Upper stratospheric circulations in the two hemispheres observed by satellites. *Roy. Meteorol. Soc. Q. J.* **109**: 443–454.

Hocking, W.K. (1981), Investigations of the movement and structure of D-region ionospheric irregularities. Ph.D. Thesis, The University of Adelaide.

Hocking, W.K., May, P. and Röttger, J. (1989), Interpretation, reliability and accuracies of parameters deduced by the spaced antenna method in middle atmosphere applications. *Pure Appl. Geophys.* **130**:571–604.

Hocking, W.K. and Vincent, R.A. (1982), A comparison between HF partial reflection profiles from the D-region and simultaneous Langmuir probe electron density measurements. *J. Atmos. Terr. Phys.* **44**:843–854.

Holton, J.R. (1982), The role of gravity wave induced drag and diffusion in the momentum budget of the mesosphere. *J. Atmos. Sci.* **39**:791–799.

Houghton, J.T. (1977), The physics of atmospheres. Cambridge University Press.

Jacka, F. (1984), Application of Fabry-Perot spectrometers for measurement of upper atmosphere temperatures and winds. *Handbook for MAP.* **13**:19–40.

Jacob, P.G. and Jacka, F. (1985), Internal gravity waves at the 95 km level. *Handbook for MAP.* **18**:248-252.

Johnson, R.M. and Luhmann, J.G. (1985a), Neutral wind spectra of the auroral zone mesopause: geomagnetic effect? *J. Geoph. Res.* **90**:1735-1743.

Johnson, R.M. and Luhmann, J.G. (1985b), High latitude mesopause neutral winds and geomagnetic activity: A cross-correlation analysis. *J. Geoph. Res.* **90**:8501-8506.

Johnson, R.M., Wickwar, V.B., Roble, R.G. and Luhmann, J.G. (1987), Lower-thermospheric winds at high latitude: Chatanika radar observations. *Annales Geophysicae* **5A**:383–404.

Jones, N.D. and Jacka, F. (1987), Dynamics of the thermosphere over Mawson, Antarctica. IV The lower thermosphere. *ANARE Research Notes.* **48**:138–147.

Kawahira, K. (1982), An observational study of the D-region winter anomaly and sudden stratospheric warmings. *J. Atmos. Terr. Phys.* **44**:947–955.

Kelly, M.C.,Farley, D.T. and Röttger, J. (1987), The effect of cluster ions on anomalous VHF backscatter from the summer polar mesosphere. *Geophys. R. L.* **14**:1031–1034.

Kilfoyle, B.P. and Jacka, F. (1968), Geomagnetic L coordinates. *Nature:Phys. Sci.* **220**:773–775.

Kingsley, S.H., Muller, H.G., Nelson, L. and Scholefield, A. (1978), Meteor winds over Sheffield. *J. Atmos. Terr. Phys.* **40**:917–922.

Kopp, E., et al. (1985), Positive ion composition and derived particle heating in the lower auroral ionosphere. *J. Atmos. Terr. Phys.* **47**:301–308.

Koshelkov, V.V. (1987), The winter anomaly in the ionospheric D-region – some numerical calculations. *J. Atmos. Terr. Phys.* **49**:81–97.

Koshelkov, Yu. P. (1985), Observed winds and temperatures in the southern hemisphere. *Handbook for MAP.* **16**:15–35.

Koshelkov, Yu. P. (1986), Mean geopotential fields for the lower thermosphere of the southern hemisphere. *J. Atmos. Terr. Phys.* **48**:1121–1143.

Labitzke, K., Manson, A.H., Barnett, J.J. and Corney, M. (1987), Comparison of geostrophic and observed winds in the upper mesosphere over Saskatoon, Canada. *J. Atmos. Terr. Phys.* **49**:987–998.

Lindzen, R.S. (1978), Effect of daily variations of cumulonimbus activity on the atmospheric semidiurnal tide. *Mon. Wea. Rev.* **106**:526–533.

Lindzen, R. S. (1981), Turbulence and stress owing to gravity wave and tidal breakdown. *J. Geoph. Res.* **86**:9707–9714.

Lindzen, R.S. and Hong, S-S (1974), Effects of mean winds and horizontal temperature gradients on solar and lunar semidiurnal tides in the atmosphere. *J. Atmos. Sci.* **31**:1421–1446.

Macleod, R. (1986), Dynamics of the Antarctic middle atmosphere. Ph.D. thesis, The University of Adelaide.

MacLeod, R. and Vincent, R. A. (1985), Observations in the Antarctic summer mesosphere using the spaced antenna technique. *J. Atmos. Terr. Phys.* **47**:567–574.

Manson, A.H., Meek, C.E., Vincent, R.A. and Smith (1985), Mean winds of the mesophere (60–80 km) measured by MF radars. *Handbook for MAP.* **16**:36–46.

Manson et al. (1985), Mean winds of the upper middle atmosphere (60-100 km): A global distribution of radar systems. *Handbook for MAP.* **16**:239–268.

May, P.T. (1988), Statistical errors in the determination of wind velocities by the spaced antenna technique. *J. Atmos. Terr. Phys.* **50**:21–32.

McIlwain, C.E. (1961), Coordinates for mapping the distribution of magnetically trapped particles. *J. Geoph. Res.* **66**:3681–91.

Miyahara, S. (1985), Suppression of stationary gravity waves by internal gravity waves in the mesosphere. *J. Atmos. Sci.* **42**:100–107.

Muller, H.G. (1972), Long-period meteor wind oscillations. *Phil. Trans. R. Soc.* **271**:585–598.

Muller, H.G. and Nelson, L. (1978), A travelling quasi 2-day wave in the meteor region. *J. Atmos. Terr. Phys. 40*:761–766.

Offermann, D. (1979), Recent advances in the study of the D-region winter anomaly. *J. Atmos. Terr. Phys.* **41**:735–752.

Olsson-Steel, D. and Elford W. G. (1987), The height distribution of radio meteors: observation at 2 MHz. *J. Atmos. Terr. Phys.* **49**:243–258.

Ono, T. and Hirasawa, T. (1987), Proton auroras observed at the equatorward edge of the duskside auroral oval. *Geophys. R. L.* **14**:660–663.

Phillips, A. and Jacka, F. (1987), Winds in the middle atmosphere at Mawson, Antarctica. III. Geomagnetic and 'meteorological' effects. *ANARE Research Notes.* **48**:107–113.

Plumb , R.A. (1983), Baroclinic instability of the summer mesosphere: A mechanism for the quasi-two-day Wave? *J. Atmos. Sci.* **40**:262–270.

Plumb R. A., Vincent R. A. and Craig R. L. (1987), The quasi-two-day wave event of January 1984 and its impact on the mean mesospheric circulation. *J. Atmos. Sci.* **44**:3030–3036.

Price, G.D. (1988), Upper atmosphere dynamics in the auroral zone. Ph.D. thesis, sumitted October 1988. The University of Adelaide.

Ranta, H. and Ranta, A. (1977), Daily variation of absorption in the D-region using riometer data at high latitudes. *J. Atmos. Terr. Phys.* **39**:309–312.

Reid, G.C. (1983), The influence of electric fields on radar measurements of winds in the upper mesosphere. *Radio Sci.* **18**:1028–1034.

Reid, I.M. (1984), Radar studies of atmospheric gravity waves. Ph.D. thesis, The University of Adelaide.

Rogers, C.D., and Prata, A.J. (1981), Evidence for a travelling two-day wave in the middle atmosphere. *J. Atmos. Terr. Phys. 86*:9661–9664.

Salby, M.L. (1981), The 2-day Wave in the middle atmosphere: observations and theory. *J. Geoph. Res. 86*:9654–9660.

Salby, M.L. (1984), Survey of planetary-scale travelling waves: theory and observations. *Rev. Geophys.* **22**:209–236.

Schaeffer, R.C. (1970), Computation of geomagnetic L coordinates. *Aust. J. Phys.* **23**:941–946.

Schwentek, H. (1963), The variation of ionospheric absorption from 1956 to 1963. **25**:733–734.

Shiotani, M. and Hirota, I. (1985), Planetary wave-mean flow interaction in the stratosphere; a comparison between northern and southern hemispheres. *Roy. Meteorol. Soc. Q. J.* **111**:309–335.

Stamnes, K., et al. (1986), Ionospheric response to daytime auroral electron precipitation. *Annales Geophysicae* 4:235–240.

Tetenbaum, D., Avery S.K., Riddle A.C. (1986), Observations of mean winds and tides in the upper mesosphere during 1980-1984, using the Poker Flat, Alaska, MST radar as a meteor radar. *J. Geoph. Res.* **91**:14539–14556.

Teitelbaum, H. and Cot, C. (1979), Anti-symmetric tidal modes under equinoctal conditions induced by ozone heating. *J. Atmos. Terr. Phys.* **41**:33–41.

Tsuda, T., Kato, S. and Vincent, R.A. (1988), Long period wind oscillations observed by the Kyoto meteor radar and comparison of the quasi-2-day wave with Adelaide HF radar observations. *J. Atmos. Terr. Phys. 50*, 225–230.

Tsuda, T., Nakamura T.and Kato S. (1987), Mean winds observed by the Kyoto meteor radar in 1983-1985. *J. Atmos. Terr. Phys.* **49**:461–466.

Torkar, K.M., et al. (1985), Energy deposition rates by charged particles. *J. Atmos. Terr. Phys.* **47**:61–71.

Vial, F. (1986), Numerical simulations of atmospheric tides for solstice conditions. *J. Geoph. Res.* **91**:8955–8969.

Vial, F., Fellous, J.L. and Teitelbaum, H. (1985), Tidal vertical structure and temperature profiles in the lower thermosphere. *Annales Geophysicae* **3**:313–318.

Vial, F. (1988), Private communication.

Vincent, R. A. (1984), MF/HF radar measurements of the dynamics of the mesopause region - a review. *J. Atmos. Terr. Phys.* **46**:961–974.

Vincent, R.A. (1985), Planetary and gravity waves in the mesosphere and lower thermosphere. *Handbook for MAP.* **16**:269–277.

Vincent, R.A. and Reid, I.M. (1983), HF Doppler measurements of mesospheric gravity wave momentum fluxes. *J. Atmos. Sci.* **40**:1321–1333.

Vincent, R. A., T. Tsuda and S. Kato. (1988), A comparative study of mesospheric solar tides observed at Adelaide and Kyoto. *J. Geoph. Res.* **93**:699-708.

Von Biel, A. (1988), Report at SCAR working group on upper atmospheric physics, Hobart 1988.

Wagner, C.U and Ranta H. (1983), The midlatitudinal post-storm electron precipitation belt. *J. Atmos. Terr. Phys.* **45**:811–822.

Wardill, P., Jones, N.D. and Jacka, F. (1987), Dynamics of the thermosphere over Mawson, Antarctica. I. Diurnal variation and geomagnetic dependence. *ANARE Research Notes.* **48**:114–120.

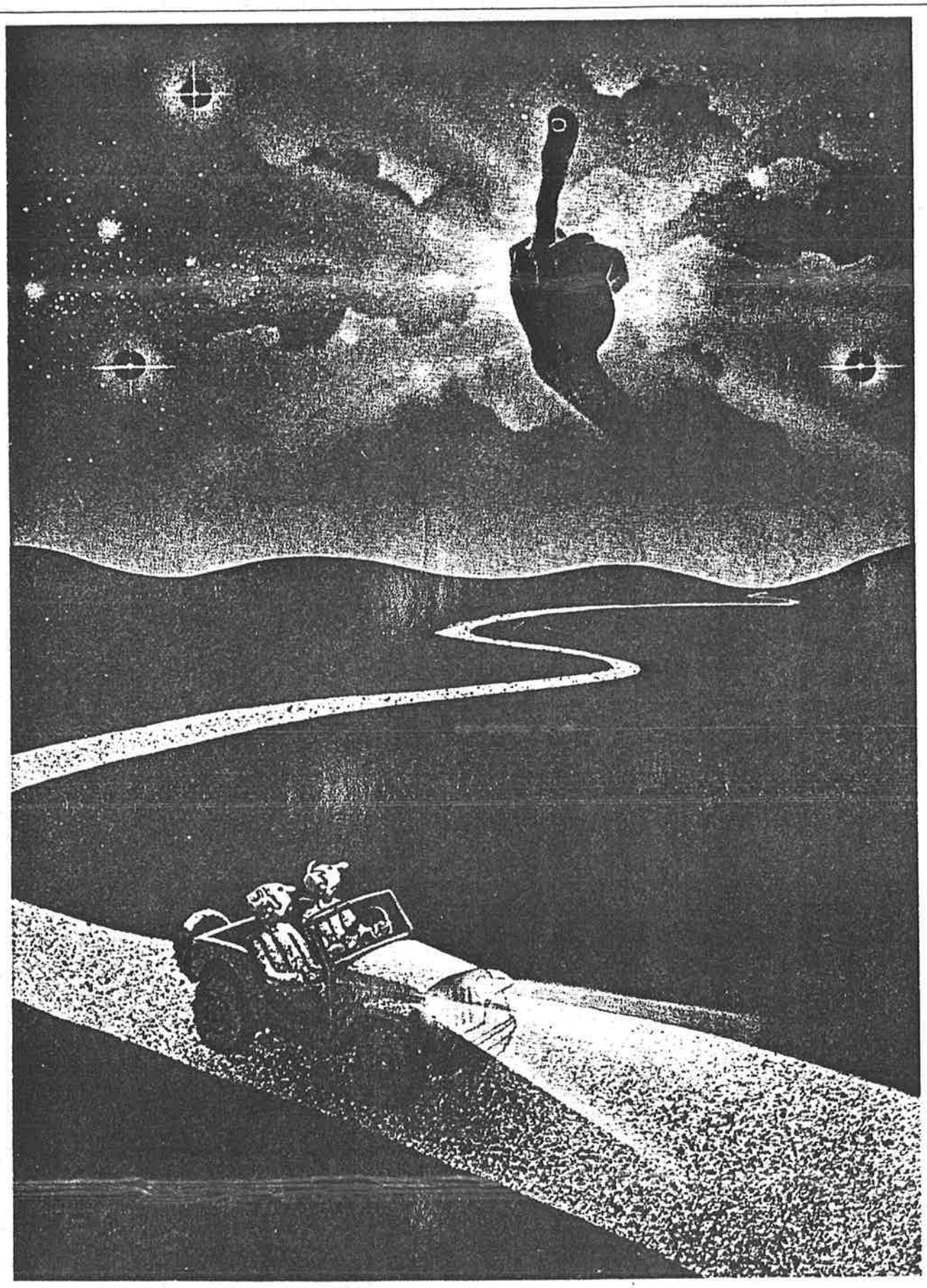

"It's either a subtle interaction between charged solar particles and the magnetosphere — or else the gods are angry!"

Well known cartoon affixed to the door of the aeronomy laboratory, Mawson Antarctica 1983–89.